Lateral tunnelling in two-dimensional electron systems

Peck, Andrew John

Award date:
1994

Awarding institution:
University of Bath

Lateral Tunnelling in Two-Dimensional Electron Systems

Submitted by Andrew John Peck
for the degree of Ph.D
of the University of Bath
1994

A. J. Peck

ProQuest LLC
789 East Eisenhower Parkway
P.O. Box 1346
Ann Arbor, MI 48106-1346

Abstract

The electrical properties of lateral tunnelling devices have been investigated, in zero and quantising magnetic fields. The devices were fabricated on modulation doped GaAs/AlGaAs heterostructures, with the tunnelling barriers situated in the plane of the two-dimensional electron system (2DES). Measurements were performed on two types of device, in which the potential barriers were induced either by shallow etching a nanometre-scale trench into the surface of the heterostructure, or by the influence of a reverse-biassed Schottky gate.

A range of characteristation data are presented for the single barrier etched diodes, which is a new structure with the potential for ultra-high frequency (THz) applications. The devices were successfully modelled using a numerical solution to the Poisson equation, and good agreement was obtained between experimental and theoretical current-voltage characteristics.

Experiments on single barrier gated diodes indicated that the device properties are strongly influenced by disorder. Additional measurements demonstrated a novel hot electron effect in the conducting regime, which is a 2D analogy of the Gunn effect. Double barrier gated diodes were also studied and displayed both negative transconductance and negative differential resistance. The results are discussed within the accepted picture of resonant tunnelling.

In a strong magnetic field, applied perpendicular to the 2DES, both types of single barrier device displayed a detailed spectrum of sharp resonances in the conductivity as a function of the bias voltage. The data are explained in terms of tunnelling between magnetic edge states on each side of the barrier. Calculated fan diagrams of the expected resonance positions, derived from a numerical solution to the Schrödinger equation, produced qualitative agreement with the experimental data. The results add strong support to the edge state picture of a 2DES in a perpendicular magnetic field.

Acknowledgements

The work presented in this thesis was carried out at the Max-Planck-Institut für Festkörperforschung in Stuttgart, Germany with financial support from the Wingate Foundation and the SCIENCE research programme of the Commission of the European Economic Community.
I would like to thank everyone who has been involved in the preparation of this thesis, in particular;
Prof. Klaus von Klitzing for giving me the opportunity to work in his department, and for making available to me the facilities of the Max-Planck-Institut.
Simon Bending, for excellent supervision, including the application for numerous research stipendia, continuous support and advice *per e-mail*, and for many of the ideas on which this work is based.
Prof. Klaus Ploog, for excellent samples.
Carlos Tejedor for advice and ideas and example calculations on resonant tunnelling between edge states.
Frank Stern for calculations and discussions on problems concerning electrostatic potentials and transport in 2D systems.
Daniela Pfannkuche for explaining many areas of theory to me and for large amounts of time donated to the overcoming of computer problems.
Daniela Pfannkuche, Rolf Haug and Jürgen Weis for a critical reading of parts of the manuscript.
Nick Pulsford for offering his apartment for use in numerous parties, and for being a fairly worthy opponent on the squash court.
Manfred Roßmanith and Peter Schultz for a great deal of advice and help on tunnelling experiments and theory.
Jürgen Weis for the use of his characterisation apparatus, and Jürgen Weis, Robert Blick and Rolf Haug for help with running the dilution refrigerator.
Bernd Schönherr, Astrid Gollhardt, Claudia Lange and Monika Riek, for professional technical support in sample processing.

Frank Schartner for bonding countless samples.
The technical staff at MPI, in particular, Susanne Demel, Jürgen Behring, Manfred Schmidt and Günther Wilk.
My research colleagues, in random order: Arno Lehman, Rolf Menne, Herbert Lage, John Cooper, Gerd Lütjering, Bernd Meurer, Yvonne Kershaw, Peter Grambow, Johannes Nieder, Thomas Bever, Holgar Grahn, Wolfgang Müller, Dieter Weiss, Elizabeth Vasiliadou, Gerhard Müller, Hugues Pothier, Matthias Tewordt, Gabi Ernst and Ramesh Mani.
Finally, a special thanks goes to my parents, for their support and encouragement over the years. Parhaat kiitokseni Christinelle suuremmoisesta tuesta ja rakkaudesta.

Contents

1 Introduction

1.1 Motivation

Research into low-dimensional-electron-systems (LDES), where the electron motion is confined in one or more physical directions, has seen a dramatic increase in the last twenty years since Chang, Esaki and Tsu [1] demonstrated resonant tunnelling through quasi-two-dimensional (2D) bound states in a GaAs/AlGaAs quantum well structure. The motivation for this research effort has been twofold; from a commercial standpoint, LDES promise a new generation of high performance, nanometre-scale electronic devices for the electronics and computer industries. From an academic standpoint they provide an unrivaled opportunity to study experimentally, many of the physical phenomena predicted by theorists since the early parts of this century.

Initial success in reducing the dimensionality of electronic systems was achieved through the development of atomically precise, epitaxial crystal growth techniques such as molecular-beam-epitaxy (MBE) [2] and metal-organic-chemical-vapour-deposition (MOCVD) [3], which enable the growth of multiple layers of differing semiconductor materials within a vertical space of a few nanometres. Electrons confined to a single layer, by the larger conduction band energy of neighbouring materials will exhibit 2D properties if the thickness of the layer is comparable to the extent of the electron wavefunction. The most common material system used in studying this type of structure is GaAs/$Al_xGa_{1-x}As$, where the size of the conduction band offset between the two materials is controlled via the Al fraction x. Chang, Esaki and Tsu's resonant tunnelling diode thus provided an elegant demonstration of the 2D nature of a thin GaAs layer sandwiched between $Al_xGa_{1-x}As$ barriers.

Semiconductor devices based on LDES can be categorised quite simply in terms of the direction of current flow in the active region of the

structure. Devices such as the resonant tunnelling diode are generally classified as *vertical* structures, which implies that the electron motion occurs in a direction perpendicular to the sample layers. An equally large family of low dimensional structures, and one with which this work is concerned, are based on *lateral* transport, which as the name suggests rely on electron motion in the plane, parallel to the to the sample layers. Recently, a technique known as *modulation doping*, in which electrons are spatially separated from their parent donors, has enabled the fabrication of high mobility quasi-2D sheets of electrons, confined at the interface of a single GaAs/$Al_xGa_{1-x}As$ heterojunction. Such two-dimensional electron systems (2DES), where the electron motion is free in the directions parallel to the crystal interface, have provided an ideal basis for the realisation of a wide range of lateral devices such as the high-electron-mobility-transistor (HEMT) [4] and for the study of numerous important physical phenomena of which the quantum Hall effect [5] and more recently, quantised conduction in one-dimensional (1D) point contact devices [6] are two commonly cited examples.

This thesis presents an investigation of lateral *tunnelling* in a 2DES, which is a subject that has received relatively little attention in its own right from previous authors. In lateral tunnelling devices, current flow occurs through narrow (< 100nm wide) electrostatic potential barriers separating adjacent regions of the 2DES which act as the emitter and the collector electrodes. The majority of reported devices to-date have used nanometre-scale, field-effect Schottky gates on the heterostructure surface to induce electrostatic barriers in the plane of the 2DES. To fabricate such structures requires the use of ultra-high resolution technologies such as electron beam or X-ray lithography.

Research interest in lateral tunnelling has been partly encouraged by the promise of high frequency device applications owing to the short length scales involved in tunnelling processes, and the minute capacitance values (<10fF) [7] associated with devices based on adjacent *edge-*

on 2D systems of electrons. Although the requirements of low temperature operation will restrict the use of such devices, advances in closed cycle refrigeration technology mean that applications in highly specialised areas are becoming more realistic. Commonly proposed applications are in the sub-millimeter band of the electromagnetic spectrum (THz regime) which are important for example in astronomy and in remote sensing for environmental research and pollution monitoring.

From a purely academic point of view, lateral tunnelling represents a useful technique for studying the electrical properties of a 2DES. Electron tunnelling is a phenomenon which is intrinsically highly sensitive to the energy scales involved, and hence tunnelling devices have often been used in the role of electron spectrometers. For this reason, lateral tunnelling experiments can provide useful information about many aspects of 2D physics, which are not available using other techniques.

In the work described in the following chapters, an attempt has been made to consider both the applications and the pure research aspects of lateral tunnelling devices. After introducing the relevant physics and technology associated with the field, results are presented for a new type of single barrier lateral tunnelling device in which the electrostatic potential barrier is induced by etching a tiny trench into the surface of the heterostructure, in place of the more conventional Schottky gate. It is proposed that owing to the absence of parasitic capacitances between the gate and 2DES in such an etched structure, its high frequency performance should be enhanced. Chapters 5 and 6 detail a range of characterisation experiments and numerical modelling data on the devices, and future work to assess their high frequency performance is planned. The remainder of the thesis is concerned purely with the physics of lateral tunnelling in a 2DES for which more conventional gated devices are used. Chapter 7 discusses the zero magnetic field behaviour of both single and double barrier diodes, from which one of the major conclusions is that despite the impressive quality of crystal growth and lateral pat-

terning techniques, the properties of lateral devices are still dominated by disorder. Chapter 8 concentrates on lateral tunnelling through single barrier diodes in a perpendicular magnetic field, where the tunnelling barriers are used to perform spectroscopy on a 2DES, quantised into magnetic Landau levels. In contrast to previous experiments [8,9] in which spectroscopy was performed by studying vertical tunnelling between two parallel 2D electron systems, separated by an AlGaAs barrier, the lateral geometry enables an interpretation of the data in terms of the edge state picture of a 2DES in a perpendicular magnetic field.

A more detailed summary of the content and conclusions of the thesis is presented in the following section.

1.2 Scope and Summary of the Thesis

In a sense, the subject of lateral tunnelling forms an interesting link between vertical tunnelling experiments, to which there exist strong analogies, and the purely 2D physics associated with the 2DES on which lateral devices are based. The work described in this thesis reflects this link between the two fields, and in the interpretation of many of the experimental results, parallels are drawn with known results for both vertical and lateral structures.

The theoretical background for the thesis begins in Chapter 2 which reviews some of the basic physics of quantum tunnelling. After a brief summary of the early history of the field, which began in earnest in the late 1920's with field emission in metals, the discussion concentrates on tunnelling in semiconductor devices. Particular attention is paid to tunnelling in semiconductor heterostructures, which often provide an elegant experimental demonstration of some of the fundamental principles of quantum mechanics. The mathematics begins with a simple discussion of the equations determining current flow in solids which are then applied to tunnelling with the introduction of the momentum and

energy conservation laws and the concept of transmission coefficients. Approximate methods for calculating the transmission coefficients for arbitrary potential barriers are briefly discussed and used to demonstrate the non-linear current-voltage properties which make tunnelling devices attractive for many commercial applications. The latter parts of the chapter are devoted to an outline of both the theory of resonant tunnelling in double barrier systems, and the experimental properties of double barrier resonant tunnelling diodes based on semiconductor heterostructures.

In Chapter 3, attention is focussed on the physical properties of low dimensional systems and the discussion begins with an overview of the historical development of two-dimensional electron systems in modulation doped semiconductor heterostructures. The electronic structure of a 2DES is briefly described with solutions to the Schrödinger equation and simple expressions are derived for intrinsic physical properties such as the 2D density of states. The chapter goes on to discuss the classical Hall effect, and the modifications made to the electronic structure of a 2DES by the presence of a strong magnetic field, applied perpendicularly to the sample layers. Two of the most widely studied effects in semiconductor physics, the Shubnikov-de Haas and the quantum Hall effects are then introduced and initially explained within the picture of localised and extended electronic states. The final part of the chapter concentrates on the edge state model of the quantum Hall effect which remains the most complete interpretation of von Klitzing's original experiments from the late 1970's.

Few of the recent developments in low dimensional semiconductor research could have been achieved without the corresponding development of crystal growth and lithographic technologies, and these are discussed in some detail in Chapter 4. Beginning with a description of crystal epitaxy, details of the crystal structure of the samples used in the experiments are listed. Techniques for optical and electron beam

lithographies are subsequently introduced and details are given for the parameters used in the fabrication of Hall bar samples. The realisation of nanometre-scale lateral devices relies heavily on controlled lithography and lateral patterning methods and some of the pitfalls encountered in the early parts of the work are explained, with particular reference to the respective merits of wet etching and reactive ion etching. The remaining part of the chapter concentrates on evaporation and lift-off techniques for the fabrication of nanometre-scale Schottky gates.

Chapter 5 introduces the principles of a novel type of single barrier lateral tunnelling diode in which the potential barrier in the plane of the 2DES is induced by etching a nanometre-scale *quantum trench* into the surface of the heterostructure. The motivation for fabricating such a device is partly based on the fact that the parasitic capacitances that exist in field effect gated devices are absent in quantum trench structures which should display enhanced high frequency properties. Experimental data are presented for a range of different devices which at low temperature (4.2K) display the highly non-linear current-voltage characteristics associated with tunnelling phenomena. The tunnelling barrier heights were successfully determined by a measurement of thermally activated current, which is a novel use for a technique more commonly applied to vertical devices such as Schottky diodes and heterostructure tunnelling diodes. The results indicate that the size of the tunnelling barrier can be controlled quite simply via the depth of the etched trench. A further experiment showed that the diode characteristics are extremely sensitive to illumination at low temperature, a fact which is assigned to the influence of D-X centre donor impurities in the AlGaAs layer of the heterostructure. An overall conclusion from this chapter is that quantum trench tunnelling diodes represent a robust and practical alternative to field-effect gated devices, and may have significant advantages for high frequency applications. Future work to asses this proposal is planned.

Chapter 6 presents a detailed discussion of a numerical model of

the quantum trench structure, from which a direct comparison between experimental and calculated current-voltage properties is made. The model uses a finite difference solution to the Poisson equation to calculate the conduction band edge potential of the heterostructure, which in turn gives the electrostatic potential barrier to electrons in the 2DES. To ensure simplicity and modest computing requirements, a full quantum mechanical treatment of the 2DES, was avoided, and instead the electronic charge in the 2DES was distributed using a Fang-Howard variational approach. The influence of an inhomogeneous occupation of donor impurities in the AlGaAs layer of the devices was also taken into account. An interesting feature of the model involves the application of a bias voltage across the barrier, which is achieved using a self-consistent method of adjusting the boundary conditions such that the calculated electrostatic potential remains a solution to the Poisson equation. Current-voltage characteristics for the model barriers were obtained using both the WKB approximation and standard tunnelling theory.

Using the trench depth to fit the calculated barrier heights to values obtained from thermal activation experiments enabled a direct comparison between calculated and experimental current-voltage characteristics. The agreement between experiment and theory was good, providing support for the range of approximations used in the model. One of the main features of this model is its simplicity, and the fact that with minor alterations it could be applied to structures with arbitrary geometry.

Chapter 7 represents a move away from the device applications side of lateral tunnelling, and concentrates on the physics of lateral tunnelling in devices employing field-effect Schottky gates. One of the first results presented is that single barrier devices show quantised conductance in units of $2e^2/h$ in the gate voltage regime just before pinch-off. This implies that the electrostatic potential barriers are strongly inhomogeneous and that transport in this gate voltage regime occurs via 1D subbands,

confined by fluctuations in the barrier potential. A simple analysis of the curves suggests that the origin of the potential fluctuations arises from the random positions of donor impurities in the AlGaAs layer of the heterostructure. This is an important result in that it implies that despite the impressive quality of crystal growth and lateral patterning technologies, the characteristics of lateral, low-dimensional devices are still dominated by disorder.

One of the more unexpected effects observed for the single barrier gated devices occurred in the low gate voltage, conducting regime, where strong minima were found to exist in the conductivity as a function of the bias voltage. The minima were associated with the onset of strong interband scattering and reduced carrier velocity, due to the transfer of *hot* electrons to the second subband of the 2DES in the collector of the device. In principle, this kind of effect, which is a 2D analogue of the Gunn effect, could be used to study electrically, the interband scattering mechanisms present in 2D electron systems.

The second part of Chapter 7 discusses experimental results for a *double barrier* lateral tunnelling diode. A range of sharp current resonances were observed for the device as a function of the gate voltage, which are assigned to resonant tunnelling through different quasi-bound states in the 1D quantum well between the barriers. In addition, resonant tunnelling was also observed in the current-voltage properties of the device, which exhibit pronounced negative differential resistance. Owing to the small energy spacing of the quasi bound states in the 1D quantum well, it has been proposed [10] that such a lateral resonant tunnelling device could be used as a sensitive detector for acoustic phonons. Work to adapt this kind of device for application as an in-situ phonon detector is already advanced.

The final chapter of the thesis presents a detailed experimental and theoretical investigation of lateral tunnelling through single barriers in a strong magnetic field, applied perpendicular to the plane of the 2DES.

This is an interesting geometry, in that within the framework of recent theories and experiments, current carrying electrons near the barrier are believed to be confined to 1D magnetic *edge states.* A theoretical analysis of the problem, based on the edge state model, indicates that only a discrete set of tunnelling channels exist between edge states in the emitter and collector, due to the requirements of energy and parallel momentum conservation in the tunnelling process. The theory predicts that a sharp peak in the conductivity of the devices should be measured whenever a tunnelling channel passes the Fermi energy in the emitter. In the experiments for the gated tunnelling devices, a highly detailed range of sharp resonances were observed in the conductivity, which are interpreted in terms of tunnelling between edge states. Moreover, tunnelling between edge states with different Landau level indices is observed in different ranges of the magnetic field, which can be attributed to the influence of the individual transmission coefficients of the various tunnelling channels. A calculation of the expected resonance positions gave some qualitative agreement with the experiment, and provided strong support for the interpretation of the data. Comparable results were also obtained from similar experiments on the quantum trench devices, although the resonant effects were much weaker. It is proposed that the combined results for the two types of device add strong support to the edge state model of a 2DES in a strong perpendicular magnetic field.

Finally, a major direction for future work must be to reduce the tunnelling barrier widths of lateral devices still further; perhaps ultimately into the sub-10nm range which is currently occupied almost exclusively by devices based on vertical tunnelling. This would enable the more successful realisation of lateral versions of devices such as the resonant tunnelling diode, and also allow the use of much higher barriers, which is important if such devices are to find applications other than at liquid helium temperatures. In addition, the study of tunnelling phenomena, such as tunnelling between magnetic edge states would benefit enor-

mously from the use of thin barriers, where the stronger wave function overlap would enhance resonant effects.

Two methods of reducing the barrier lateral dimensions are foreseen. Firstly, the use of high energy electron beam lithography and perhaps new resist materials will enable the routine lateral patterning of features in the sub-10nm range in the near future. Secondly, the continual refinement of MBE techniques has meant that the fabrication of heterostructure samples where the 2DES is positioned to within a few nanometres of the sample surface has recently become possible. For the case of gated structures in particular, this will enable the realisation of narrower and sharper potential barriers.

Combining these two approaches will lead to a drastic improvement in the performance of lateral tunnelling devices, which will surely be the subject of significant research in future years.

2 Theory and Applications of Quantum Tunnelling

2.1 Introduction

The phrase "quantum mechanical tunnelling" is used to describe the transmission of a particle through a barrier, impenetrable when considered purely in terms of Newtonian mechanics. The concept arises from the wave-like nature of microscopic particles, where the wave may propagate in attenuated form, through a region which is classically forbidden. Thus a particle in a state on one side of a potential barrier always has a finite probability of tunnelling into an empty state on the other side. The effect is characterised by an exponential dependence of the tunnelling probability on both barrier height and barrier width. It is this non-linear behaviour that makes tunnelling phenomena both a very sensitive method for studying many problems in solid state physics and has allowed tunnelling devices to play an important role in many areas of modern day microelectronics.

One of the earliest observations of tunnelling effects was of field emission in metals by Lillenfield in 1922 [11], although it was not until 1928 [12] that Fowler and Nordheim described the main features of the experiment in terms of tunnelling. Other fundamental experiments such as the ionisation of hydrogen atoms (Oppenheimer 1928 [13]) and alpha particle decay (Gamow 1928 [14]) were also explained by tunnelling models at about the same time. For the next 30 years the general understanding and application of the phenomenon increased gradually with work by for example Zener [15] on the theory of inter-band tunnelling in solids and by Muller [16] with the invention of the field effect microscope. It was not until 1957 however that the present generation of electronics orientated tunnelling devices was conceived with the invention of the *p-n* tunnel diode by Esaki [17].

The Esaki diode is basically a reverse biased p^+-n^+ junction, where the p- and n-type regions are degenerately doped ($> 10^{19}\text{cm}^{-3}$). Under appropriate bias conditions, electrons tunnel across the depletion layer from the conduction band in the n-type region to the valance band in the p-type region. The tunnelling process is however only allowed for the bias condition such that occupied states in the n-type region are energetically aligned with holes in the p-type region, and the device displays a negative resistance feature at higher bias voltages. This property has found numerous applications in high speed electronics where for example the Esaki diode is used as a high speed switch [4].

Soon after this invention, developments in materials technology allowed the realisation of structures based on tunnelling between metals and between semiconductors through ultra thin insulating films (the so called metal-insulator-metal (MIM) diode and metal-insulator- semiconductor (MIS) diode [18,19]). With this basis, research into tunnelling devices branched into two categories; devices based on inter-band tunnelling within a single semiconductor such as Esaki's tunnel diode, and multi-layer structures such as MIM diodes, Schottky diodes, and more recently semiconductor heterostructures.

In semiconductor heterostructures, the potential barriers for tunnelling are formed by the sandwiching of a wide gap material between narrow gap electrodes. The most commonly studied systems are based on III/V semiconductors and in particular GaAs/AlGaAs where advances in growth techniques such as molecular-beam-epitaxy (MBE) [2] and metal-organic-chemical-vapour-deposition (MOCVD) [3] since the early 1970's have enabled the fabrication of atomically precise layered systems. The near perfect crystal quality of devices grown with these methods has allowed the observation of a whole range of tunnelling effects predicted by quantum mechanics. In 1974, Chang, Esaki and Tsu [1] observed resonant tunnelling through a double barrier semiconductor heterostructure, a manifestation of confined states in the quantum

well between the barriers. Chang and Esaki were also the first to report the observation of miniband transport in a multibarrier superlattice[20]. More complicated three terminal devices have also been reported, for example the hot electron transistor in 1985 [21] which utilises the fast base transit times of high energy electrons tunnelling through an emitter barrier to achieve high speed.

A number of very comprehensive reviews have been published [22–24] which discuss many aspects of the physics of tunnelling in solids. In the following sections, a brief outline of the principles and theory of tunnelling is given as a basis for calculations and experiments described later in the thesis.

2.2 Tunnelling Through Single Potential Barriers

2.2.1 Tunnelling Current

A useful starting point in a discussion of quantum mechanical tunnelling is the Drude model for the conductivity of a free electron gas [25]. In the Drude model, the electron current density flowing in a direction x is described as the product of the charge density ne and the electron drift velocity v_x,

$$J_x = nev_x \tag{2.1}$$

for an electron density $n = N/L^3$ where N is the number of electrons and L^3 is the crystal volume. Assuming the i^{th} electron has an instantaneous velocity v_{xi} and a probability of transmission through the crystal t_i, the expression for the current can be re-written as a sum over all electrons,

$$J_x = \frac{e}{L^3}\sum_{i=1}^{N} v_{xi}t_i. \tag{2.2}$$

Integrating over all states in $k-$space , where the volume of a state is $(2\pi/L)^3$ gives,

$$J = \frac{e}{(2\pi)^3}\int_0^\infty\int_0^\infty\int_0^\infty f(E)v_xT(E_x)dk_xdk_ydk_z \tag{2.3}$$

for an energy dependent transmission coefficient $T(E_x)$ which, for tunnelling problems, becomes the probability that an electron with an energy E_x will tunnel through the potential barrier. $f(E)$ is the Fermi-Dirac distribution function which gives the probability of a state with energy E being occupied at a temperature T where,

$$f(E) = \frac{1}{1 + exp\left[\frac{(E-\mu)}{k_B T}\right]} \tag{2.4}$$

and μ is the electrochemical potential. Eqn.2.3 must be modified further to take into account the fact that in the absence of scattering during the tunnel process, the total energy has to be conserved and the Pauli principle has to be obeyed. Thus, for tunnelling to be possible from the emitter to the collector, an occupied state in the emitter must be coincident in energy with an empty state in the collector. i.e.

$$J_{ec} = \frac{e}{(2\pi)^3} \int_0^\infty \int_0^\infty \int_0^\infty [f_e(E)(1 - f_c(E))]\, v_x T(E_x) dk_x dk_y dk_z. \tag{2.5}$$

Here, $f_e(E)$ and $(1 - f_c(E))$ are the probabilities of states with an energy E being occupied and unoccupied in the emitter and collector respectively and v_x is the electron group velocity.

For net current to flow, a difference in the occupation probabilities in the emitter and collector must exist. This condition is fulfilled by the application of a bias voltage to the barrier, which serves to lower the Fermi level on one side of the barrier by an amount eV relative to the other side. Although the current will then be dominated by tunnelling in the direction of the applied bias, the current flowing in the reverse direction cannot be ignored and the total current density is,

$$J_T = J_{ec} - J_{ce} \tag{2.6}$$

Furthermore, the Fermi function in the collector can be written $f_c(E) = f_e(E + eV) \equiv f(E + eV)$ which gives the total current density,

$$J_T = \frac{e}{(2\pi)^3} \int_0^\infty \int_0^\infty \int_0^\infty [f(E) - f(E - eV)]\, v_x T(E_x, eV) dk_x dk_y dk_z. \tag{2.7}$$

A further development of the formula for the current density is given in Chapter 6 for the specific case of lateral tunnelling between 2D electrodes. For the more commonly studied problem of tunnelling between 3D electrodes, the current density formula for the zero temperature limit is derived by Mendez [26] as,

$$J_T = \frac{em^*}{2\pi^2\hbar^3}\left[eV\int_0^{E_F-eV} T(E_x,eV)dE_x + \int_{E_F-eV}^{E_F}(E_F-E_x)T(E_x,eV)dE_x\right] \quad eV \leq E_F \qquad (2.8)$$

$$J_T = \frac{em^*}{2\pi^2\hbar^3}\left[\int_0^{E_F}(E_F-E_x)T(E_x,eV)dE_x\right] \quad eV \geq E_F \qquad (2.9)$$

Where E_F is the Fermi energy in the emitter, m^* is the effective electron mass ($m^* = 0.067m_0$ where m_0 is the free electron mass) and $\hbar$ is Plancks constant ($\hbar = h/2\pi$). The two energy regimes $eV < E_F$ and $eV > E_F$ correspond to the situation where partial or no overlap respectively exists between the Fermi seas in the emitter and collector of the device (see Chapter 6).

2.2.2 Transmission Coefficients

A large fraction of practical tunnelling problems are characterised by a one-dimensional (1D) barrier potential and, as a result the functional dependencies of the electron wavefunction parallel and perpendicular to the barrier are separable. For a potential barrier in the x-direction, choosing the electron wave function,

$$\Psi(x,y,z) = \psi(x)exp(ik_y y + ik_z z) \qquad (2.10)$$

means that solutions to the Schrödinger equation (SE) both parallel to and on both sides of the barrier are plane waves with energy eigenvalues,

$$E_{\|} = \frac{\hbar^2 k_{\|}^2}{2m^*} \qquad (2.11)$$

where $k_{||} = \sqrt{k_y^2 + k_z^2}$ is the parallel momentum. The fact that for a 1D potential barrier, the wave functions parallel to the barrier remain unchanged during the tunnelling process leads to an important criterion for tunnelling, namely that parallel momentum is conserved.

Fig.2.1 shows a sketch of an ideal single rectangular barrier with

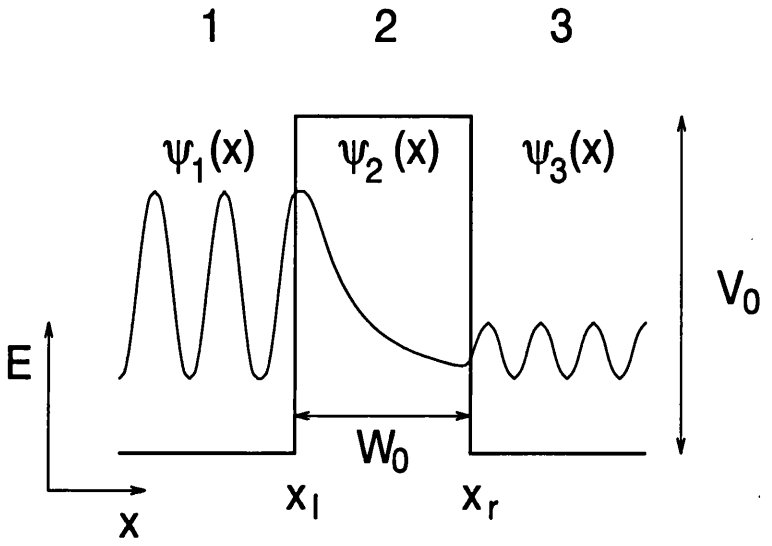

Figure 2.1: *Sketch of the electron wavefunction $\psi(x)$ across a rectangular tunnelling barrier. $\psi(x)$ and $1/m^*(\partial\psi(x)/\partial x)$ are both continuous at the boundaries x_l and x_r.*

height V_0 and width W_0. Within the effective mass approximation, the 1D SE for an electron wave travelling in the $x-$direction is,

$$\left[-\frac{\hbar^2}{2m^*}\frac{\partial^2}{\partial x^2} - V_0\right]\psi(x) = E_x\psi(x). \tag{2.12}$$

Solutions to the SE in the regions 1, 2 and 3 are,

$$\begin{aligned}
\psi_1(x) &= e^{ik_{x1}x} + re^{-ik_{x1}x} && -\infty < x < x_l \\
\psi_2(x) &= Ae^{ik_{x2}x} + Be^{-ik_{x2}x} && x_l < x < x_r \\
\psi_3(x) &= te^{ik_{x3}x} && x_r < x < \infty
\end{aligned} \tag{2.13}$$

(2.14)

where r and t are the reflected and transmitted amplitudes of the electron wavefunction incident on the barrier respectively, and A and B are

constants. Outside the barrier (regions 1 and 3), solutions to the SE are plane waves with $k_{x1}^2 = k_{x3}^2 = (2m^*E_x/\hbar^2)$ whereas in the barrier region,

$$k_{x2}^2 = \frac{2m^*}{\hbar^2}(E_x - V_0). \tag{2.15}$$

If $E_x < V_0$ then k_{x2} is imaginary and the wavefunction $\psi_2(x)$ will decay exponentially in region 2.

Matching the wavefunctions and their first derivatives $1/m^*(\partial\psi(x)/\partial x)$, both of which are continuous at the boundaries x_l and x_r results in an expression for the transmission coefficient ($T \sim |t|^2$) [24],

$$T(E_x) \sim exp(-2\chi W_0) \tag{2.16}$$

where $\chi = -ik_{x2}$. Eqn.2.16 shows clearly that the transmission coefficient (tunnelling probability) and hence the tunnelling current are exponentially sensitive to the barrier dimensions.

2.2.3 WKB Methods

Analytical solutions to the SE such as the above can however only be obtained for tunnelling problems where the barrier potential $V(x)$ has a simple analytical form. Although the SE can be solved numerically, more simple methods such as the Wenzel-Kramers-Brillouin (WKB) [27] semi-classical approximation usually provide sufficiently accurate information about $T(E_x)$. The WKB method is valid for tunnelling problems where the change in the barrier potential within an electron wavelength is small compared to the electrons kinetic energy. The expression for the transmission coefficient is derived in [27] and is generally written,

$$T(E_x) \sim \exp\left(-2\int_{x_l}^{x_r} \chi(x)dx\right) \tag{2.17}$$

where

$$\chi(x) = \sqrt{\frac{2m^*}{\hbar^2}(V(x) - E_x)}. \tag{2.18}$$

The value of the WKB expression is illustrated by applying it to the case of a single rectangular barrier with an applied bias voltage V. The barrier potential, which is trapezoidal for $eV < V_0$ and triangular for $eV > V_0$ becomes,

$$V(x) = V_0 - \frac{(x - x_l)}{W_0} eV. \tag{2.19}$$

Substituting Eqn.2.19 into the WKB formula leads to an expression for

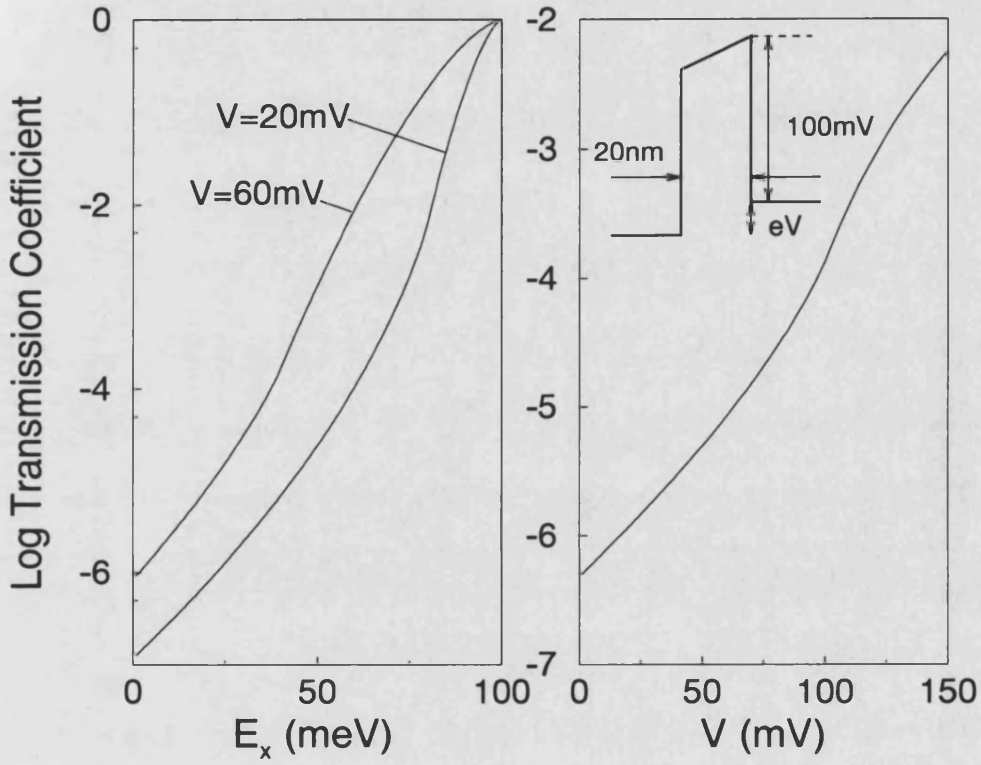

Figure 2.2: *Transmission coefficient T calculated using the WKB expression for a rectangular barrier as a) a function of incident electron energy for fixed applied bias V, and b) as a function of bias voltage for an electron energy at the conduction band edge*

the transmission coefficient for the case $eV < V_0$,

$$T(E_x, eV) \approx \exp\left[-\frac{3}{4}\left(\frac{2m^*}{\hbar^2}\right)^{\frac{1}{2}} \frac{W_0}{eV}\left((V_0 - E_x)^{\frac{3}{2}} - (V_0 - eV - E_x)^{\frac{3}{2}}\right)\right] \tag{2.20}$$

whereas for $eV > V_0$,

$$T(E_x, eV) \approx \exp\left[-\frac{3}{4}\left(\frac{2m^*}{\hbar^2}\right)^{\frac{1}{2}} \frac{W_0}{eV}(V_0 - E_x)^{\frac{3}{2}}\right] \tag{2.21}$$

Fig.2.2a) and b) show the transmission coefficient $T(E_x, eV)$ for a 100meV high, 20nm wide barrier, calculated as a function of both E_x at constant V and as a function of V for a single incident energy E_x. Note that although the WKB expression predicts that $T(E_x, eV)$ will increase monotonically in the triangular barrier regime ($eV > V_0$), the transmission coefficient actually oscillates in this region as the effective barrier width decreases. These oscillations, termed Fowler-Nordheim resonances are due to constructive and destructive interference between waves incident on and reflected from the collector interface [26]. These interference effects are not taken into account in the WKB approximation.

When, as is usually the case for lateral tunnelling problems, the tunnelling barrier potential $V(x)$ cannot be described analytically, the most effective technique for obtaining $T(E_x, eV)$ is to solve the integral in the WKB exponent numerically. Dividing the potential barrier into a large number of thin rectangular components with heights ξ_l (shown in Fig.2.3) means that $T(E_x, eV)$ can be calculated from a product of the individual transmission coefficients $T_l(E_x)$, i.e. for p component barriers,

$$T(E_x) = \prod_{l=1}^{p} T_l(E_x) \tag{2.22}$$

which can be re-written,

$$T(E_x) \approx \exp\left(-2\sum_{l=1}^{p}\int_0^d \chi_l dx\right) \tag{2.23}$$

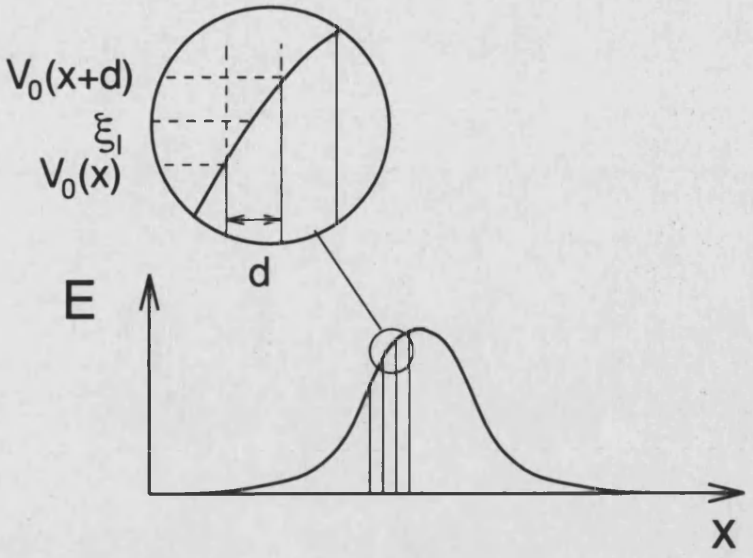

Figure 2.3: *Notation used for numerical integration of the exponent in the WKB approximation. The potential barrier is divided into p rectangular components with heights ξ_l and individual transmission coefficients T_l.*

where d is the width of the component barriers,

$$\chi_l = \sqrt{\frac{2m^*}{\hbar^2}(\xi_l - E_x)} \tag{2.24}$$

and

$$\xi_l = \frac{V_0(x) + V_0(x+d)}{2}. \tag{2.25}$$

Integrating for each square barrier gives the following expression for the transmission coefficient for a potential barrier $V(x)$ for any incident electron energy E_x.

$$T(E_x) \approx \exp\left(-2d\left(\frac{2m^*}{\hbar^2}\right)^{\frac{1}{2}} \sum_{l=1}^{p} (\xi_l - E_x)^{\frac{1}{2}}\right) \tag{2.26}$$

2.2.4 Current-Voltage Properties

With a knowledge of the transmission coefficient $T(E_x, eV)$, it is straightforward to calculate the tunnelling current density J from Eqn.2.8 and 2.9. Fig.2.4 shows calculated current-voltage (I-V) characteristics for

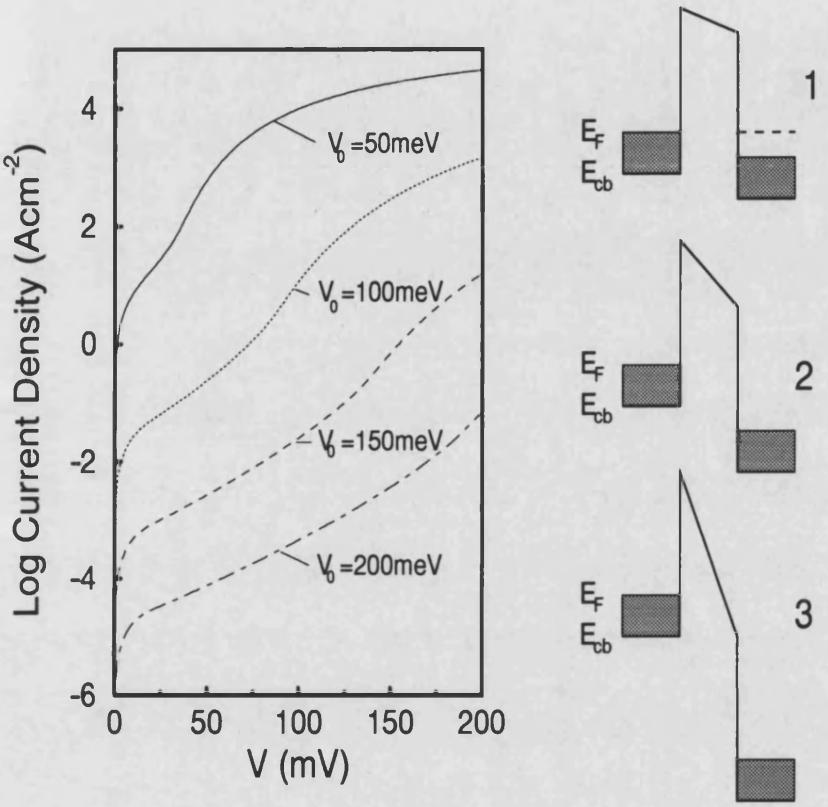

Figure 2.4: *Calculated I-V characteristics for four rectangular tunnelling barriers with 3D electrodes. The transmission coefficients were calculated using the WKB approximation (Eqn.2.20 and 2.21) and the current density was obtained from Eqn.2.8 and 2.9 for a temperature $T = 0K$ and a Fermi energy $E_F = 20meV$. The right-hand part of the figure shows the energy profiles of the tunnelling barriers for the bias regions described in the text.*

four, 20nm wide rectangular tunnelling barriers with barrier heights of 50, 100, 150 and 200meV respectively. Three distinct regions can be seen on the figure; firstly at low bias ($eV < E_F$), the current is van-

ishingly small and roughly proportional to the applied voltage. In the range $E_F < eV < V_0$ the current increases rapidly as the transmission coefficient increases exponentially with decreasing barrier height. In the Fowler Nordheim regime ($eV > V_0$) the rate of current increase is most rapid as both the barrier height *and* the effective barrier width decrease.

2.3 Resonant Tunnelling

2.3.1 Transmission Coefficients

The term "resonant tunnelling" is generally applied to any situation where tunnelling can occur via bound states in a confined system. Experimental observations of the phenomenon are numerous with the most common example being the double barrier heterostructure diode, but resonant tunnelling has been seen through systems of lateral barriers, quantum dots, and a range of other devices.

The concept of resonant tunnelling is most simply demonstrated by the ideal case of a pair of rectangular potential barriers, separated by a narrow quantum well. For the case of symmetric barriers, if the energy of an electron impinging on the barrier is coincident with the energy of a quasi-bound state in the well, then the electron will be transmitted without attenuation; i.e. the transmission coefficient is unity if the electron retains phase coherence during the tunnelling process. This resonance condition corresponds to constructive interference occurring between the electron wave fronts in the well between the barriers and indeed a classical analogue of the device is the Fabry-Pérot resonant optical cavity. For all other incident energies, the transmission coefficient is approximately determined by the transmission coefficients of the individual barriers and the incident electron wavefunction will be strongly attenuated.

Fig.2.5 shows a sketch of the transmission coefficient $T(E_x)$ for a symmetric double barrier system with four quasi-bound states in the

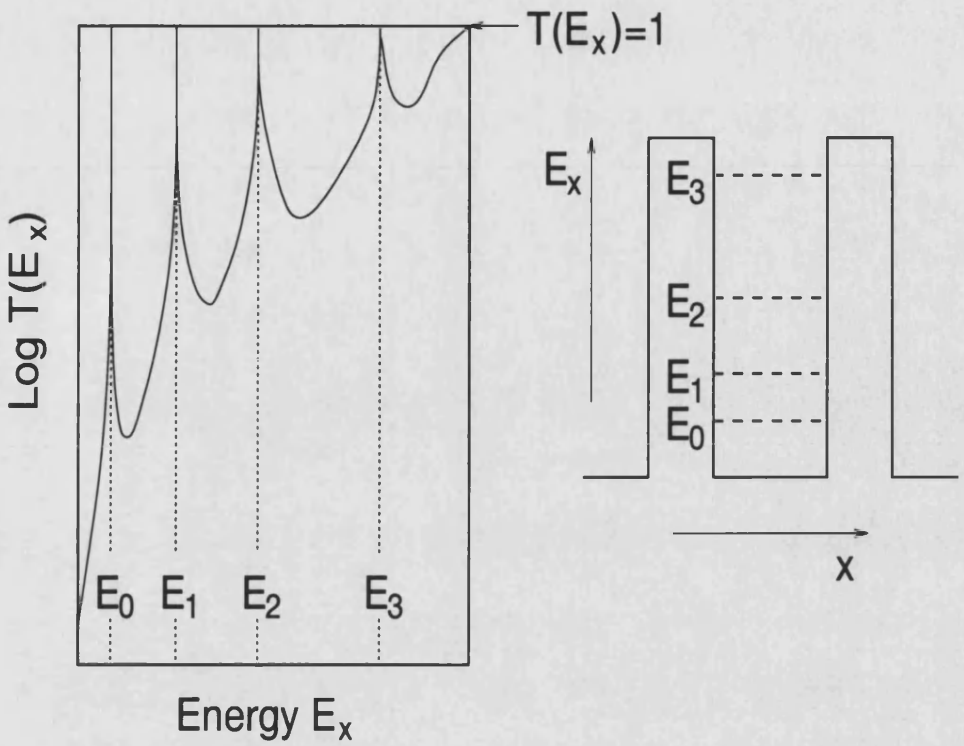

Figure 2.5: *a). Sketch of the transmission coefficient $T(E_x)$ for a symmetric double barrier structure as a function of the incident electron energy. The transmission coefficient reaches unity for electron energies which coincide with the bound state energies E_n. b). Energy profile for an ideal double barrier system with four quasi-bound states*

quantum well. For this ideal case, $T(E_x)$ reaches unity when $E_x = E_n$ $(n = 0, 1, ..)$. Each quasi-bound state is characterised by a lifetime τ_n which is due to the finite probability of an electron leaking out from the well. The energy width of each resonance ΔE_n is related to the lifetime via the uncertainty principle, $\Delta E_n \simeq \hbar/2\tau_n$ and thus the longer lifetimes of the lower, more strongly confined states are reflected by sharper resonances.

2.3.2 *I-V* Characteristics

In real devices, the symmetry condition is usually broken by the application of a bias voltage across the barriers. The right hand side of Fig.2.6 shows a sketch of the conduction band edge profile of a commonly studied device which consists of undoped AlGaAs barriers and an undoped GaAs well, sandwiched by heavily doped GaAs electrodes. For simplicity, the device is taken to have only a single quasi-bound state. Assuming that any applied bias voltage falls linearly across the active region of the structure, both barriers will become trapezoidal and the quasi-bound state energy E_0 will fall with increasing bias (region A on the figure). As E_0 falls below the Fermi energy in the emitter, resonant current can flow while still conserving parallel momentum and total energy during the tunnelling process, causing a sharp rise in the total current (region B). The resonant current will then increase further as E_0 moves down through the Fermi sea, due to the increase in the number of 2D states available in the well for tunnelling. This idea can be seen more clearly in the inset of Fig.2.6 which shows the intersection in momentum space of the Fermi sphere in the emitter electrode and the Fermi disc in the 2D quantum well. The (momentum conserving) resonant current is proportional to the shaded area of the figure, and since $k_0 = 1/\hbar\sqrt{2m^*E_0}$, the area increases with increasing bias i.e. as E_0 falls. When E_0 drops below the conduction band edge energy in the emitter, parallel momentum and total energy can no longer be conserved and the resonant current will drop sharply (region C), giving rise to negative differential resistance (NDR) which is exploited in device applications. At very high bias, the total current increases exponentially due to non resonant tunnelling through the two barriers.

In practice, the magnitude of the valley current I_v is always larger than values predicted by resonant tunnelling theories. This is largely due to the presence of scattering mechanisms in real devices such as

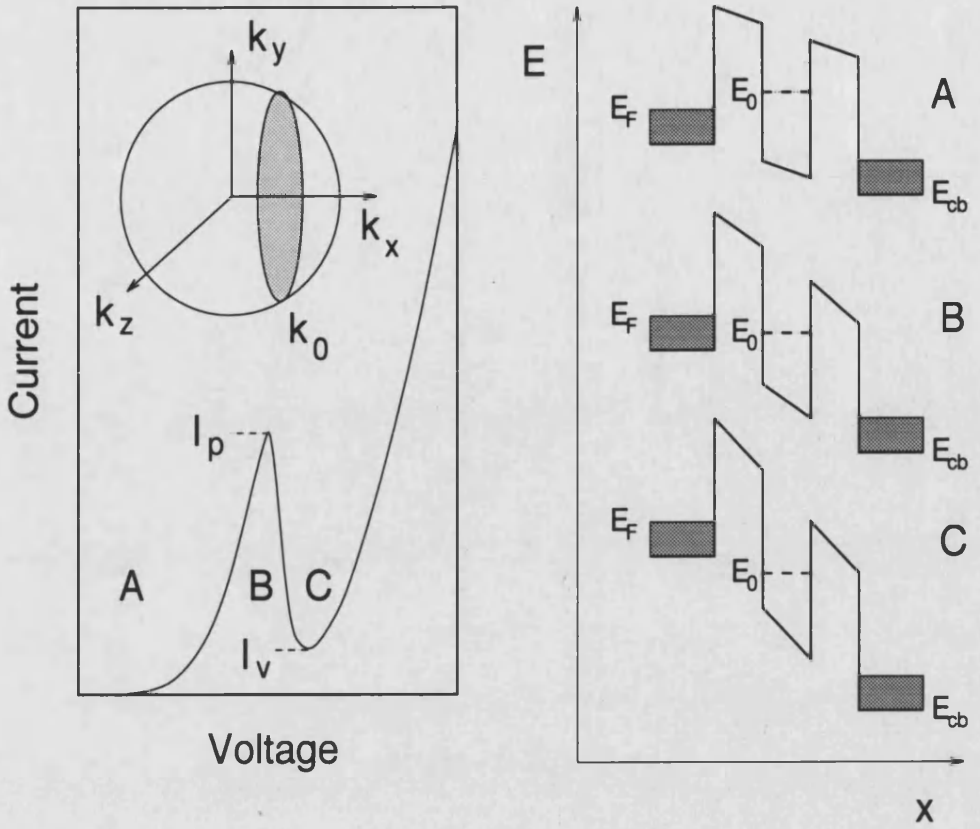

Figure 2.6: *Sketch of a typical I-V characteristic for a double barrier resonant tunnelling diode with a single bound state in the quantum well. The right-hand side of the figure indicates the energy profiles of the device for different bias regimes.*

phonon emission or impurity scattering which destroy the coherence of the electron wave function through the device. In this context, the resonant tunnelling process can be considered as being sequential [28], i.e. the electron tunnels resonantly into the well, is scattered and loses phase coherence, and then tunnels out through the second barrier. This means that perfect cancellation of the back scattered waves no longer occurs and the transmission coefficient is not unity as predicted in the coherent model.

The NDR region, characteristic of resonant tunnelling devices (RTD's) is the basis for what have become significant high frequency electronic

applications, for example as oscillator diodes. Important parameters for such applications are both the value of the high frequency cut-off and the maximum available power, which are both maximised by a broad NDR region and a large difference in the peak and valley currents (I_p-I_v) [29]. Heterostructure based RTD's are the most suitable structures yet developed for these applications, and indeed one of the fastest electronic devices reported to date was an InGaAs/AlAs RTD which achieved a frequency of 420GHz at an output power of 0.2μW [30].

Chapter 7 describes experimental data from a lateral RTD, in which the potential barriers are induced in the plane of a 2D electron gas with a pair of nanometre scale Schottky gates. Although due to reduced electrode charging times, lateral devices have the potential for improved high frequency performance over their 3D counterparts, it is unlikely that such a device would achieve the current densities and room temperature operation requirements necessary for commercial exploitation. Other potential research applications do exist however and are briefly discussed in Chapter 7.

3 Properties of Two-Dimensional-Electron-Systems

3.1 Modulation Doped GaAs/AlGaAs Heterostructures

The physical properties of two-dimensional-electron-systems (2DES)[1] have been the subject of wide ranging research interest for over 20 years. Most of the early studies in the field, right up to the discovery of the quantum Hall effect in 1980 [31] were made on Si MOSFET (Metal-Oxide-Semiconductor-Field-Effect-Transistor) samples in which the 2DES is induced at the Si-SiO_2 interface by the application of a positive bias voltage to the gate electrode on the sample surface. Although Si MOSFET's have been hugely successful for integrated circuit applications, the inherently poor interface quality produced by thermal oxide growth and the large effective mass m^* results in only modest 2D electron mobilities. This makes them non-ideal for use in many research problems, where electron scattering can obscure quantum phenomena, and also limits the device performance in high frequency applications, since electron mobility is of critical importance for fast switching times. A major breakthrough for both research and industry came in the late 1970's with the switch from Si to *III-V* semiconductor materials and in particular with the realisation of the modulation doped GaAs/AlGaAs heterostructure[2] (more commonly known as the high-electron-mobility transistor or HEMT) [33].

Modulation doping is a technique in which donor electrons are spatially separated from their parent impurity atoms. This physical separation, which results in a drastic reduction in impurity scattering can

[1] A system of electrons is generally described as two-dimensional if a discrete spectrum of electronic subbands, each with a constant density of states exists (see section 3.2.1). In reality, a 2DES will have a finite extent in the direction of confinement, which depends on the electron concentration but is generally less than 50nm.

[2] It should be noted that very recently, modulation doped SiGe heterostructures have also attained ultra-high electron mobilities at low temperature [32]

lead to ultra-high electron mobilities ($> 10^7 V^{-1}s^{-1}\text{cm}^2$ at 4.2K) [34] and consequently long electron mean free paths ($> 10\mu$m). Modulation doped heterostructures usually consist of a single junction of two lattice matched semiconductor materials with differing forbidden gaps E_{g1} and E_{g2} (for this work $Al_xGa_{1-x}As$ and GaAs) of which only the wide gap material ($Al_xGa_{1-x}As$) is heavily doped. At equilibrium, charge transfer

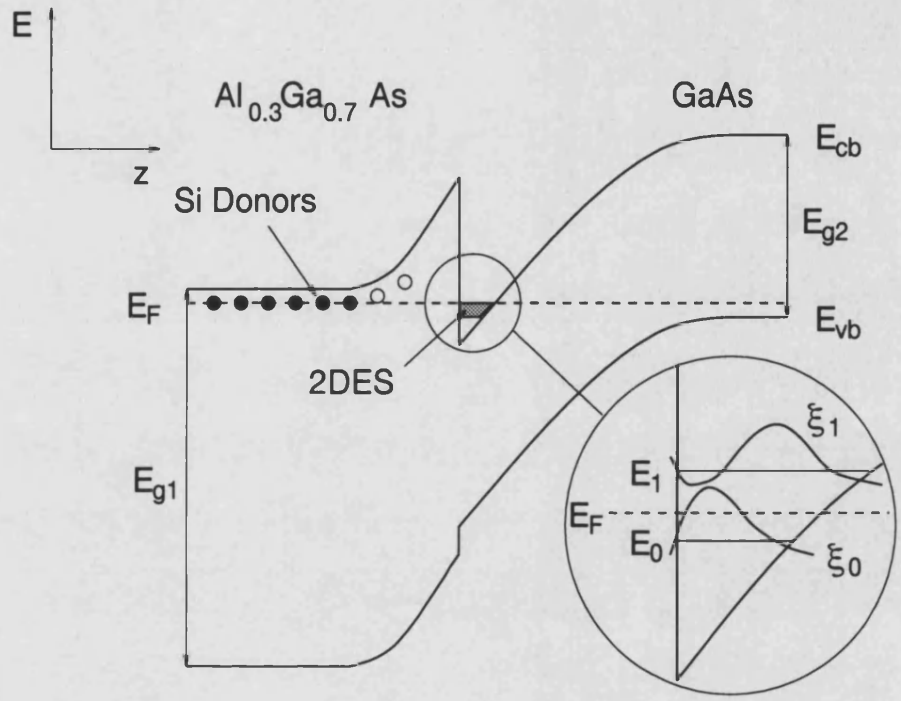

Figure 3.1: *Schematic diagram of the band structure of a GaAs $Al_xGa_{1-x}As$ single heterojunction. The full and empty circles show the positions of occupied and unoccupied Si donors ions respectively in the $Al_xGa_{1-x}As$ layer. The Fermi energy is indicated by the dashed line.*

occurs across the heterojunction in order to create a uniform Fermi energy (E_F) throughout the sample and a 2D gas of electrons builds up in the GaAs at the interface, confined both by the conduction band offset between the two materials and the attractive electrostatic potential produced by the ionised donors. In most devices, the mobility is enhanced by the inclusion of a thin, undoped $Al_xGa_{1-x}As$ spacer layer at the in-

terface which reduces the Coulomb interaction between electrons and donors still further. Any roughness at the GaAs/AlGaAs will induce interface scattering in the 2DES and strongly reduce the mobility. For this reason, only the most precise crystal growth technologies such as MBE or MOCVD can be used to fabricate ultra-high mobility HEMT's.

Fig.3.1 shows a sketch of the energy band structure at the interface of a typical device. Chapter 4 gives a more detailed description of the material and crystal growth parameters of the samples used in this work, and a discussion of the physics of electron transport in a 2DES is given below.

3.1.1 Zero Magnetic Field Properties

The confining potential well $V(z)$ for 2D electrons in a modulation doped heterostructure arises principally[1] from the electrostatic potential $\phi(z)$ of the conduction band edge of the sample in the growth direction. $\phi(z)$ can be calculated from the Poisson equation (PE) which states that the *curvature* of the potential is a function of both the charge density and the dielectric properties of the system. i.e.

$$\frac{\partial^2\phi(z)}{\partial z^2} = -\frac{\rho(z)}{\epsilon_0\epsilon(z)} \tag{3.1}$$

where $\rho(z)$ is the charge per unit volume (charge density), and $\epsilon_0\epsilon(z)$ is the dielectric constant. Since the charge density is proportional to the square of the electron wave function, a calculation of the energy eigenvalues of the well requires a self-consistent solution to both the PE and the Schrödinger equation (SE),

$$\hat{H}\Psi(x,y,z) = E\Psi(x,y,z) \tag{3.2}$$

[1]Strictly speaking, $V(z)$ depends not only on the electrostatic potential $\phi(z)$, but also contains terms originating from the Coulomb interaction between the electrons, the potential associated with the band-edge discontinuity at the interface, and the change in dielectric constant of the materials over the interface [35].

The single particle Hamiltonian $\hat{H}$ for an electron at the boundary between GaAs and AlGaAs takes the form,

$$\hat{H} = \frac{1}{2m^*}\left[(\vec{P} - e\vec{A}(x,y,z))\right]^2 - eV(x,y,z) \tag{3.3}$$

where $\vec{P} = -i\hbar(\vec{i}\partial/\partial x + \vec{j}\partial/\partial y + \vec{k}\partial/\partial z)$ is the momentum operator for the orthogonal set of unit vectors $(\vec{i},\vec{j},\vec{k})$. $\vec{A}(x,y,z)$ is the vector potential and for zero magnetic field $\vec{A}(x,y,z)$ is a constant. Assuming the electron motion to be free in the x-y plane (plane waves), the Hamiltonian can be separated using the wave function $\Psi(x,y,z) = \xi(z)exp(ik_x x + ik_y y)$. Working within the effective mass approximation ($m^* = 0.067m_0$ where m_0 is the free electron mass), solutions to the SE in the x-y plane are $E(k_x) = \hbar^2 k_x^2/2m^*$ and $E(k_y) = \hbar^2 k_y^2/2m^*$. In the z-direction, the SE becomes,

$$\left[-\frac{\hbar^2}{2m^*}\frac{\partial^2}{\partial z^2} - \phi(z)\right]\xi_i(z) = E_i\xi_i(z) \tag{3.4}$$

for the set of energy eigenvalues E_i. Self-consistent solutions to Eqn.3.1 and 3.4 can only be obtained numerically [36], although a useful simplification can be obtained by replacing $\phi(z)$ with a simple triangular potential, in which case the SE can be solved exactly [37].

Solving Eqn.3.1 and 3.4 reveals a discrete set of energy eigenvalues E_i more commonly termed *electronic subbands.* The complete energy spectrum in k-space is given therefore by,

$$E_i(k_x,k_y) = E_i + \frac{\hbar^2 k_x^2}{2m^*} + \frac{\hbar^2 k_y^2}{2m^*} \tag{3.5}$$

and is sketched in Fig.3.2.

For a 2-dimensional system of electrons, the Fermi sphere becomes a Fermi disc of radius k_F. Assuming each electronic state occupies an area $(2\pi/L)^2$ in $k-$space, the total number of states in the disc,

$$N = 2\frac{\pi k_F^2 L^2}{(2\pi)^2} \tag{3.6}$$

where the factor of 2 is included to account for the electron spin. The electron density $n_{2D} = N/L^2$ and hence the Fermi radius is given by,

$$k_F = \sqrt{2\pi n_{2D}} \tag{3.7}$$

Assuming only a single occupied subband, the Fermi energy can then

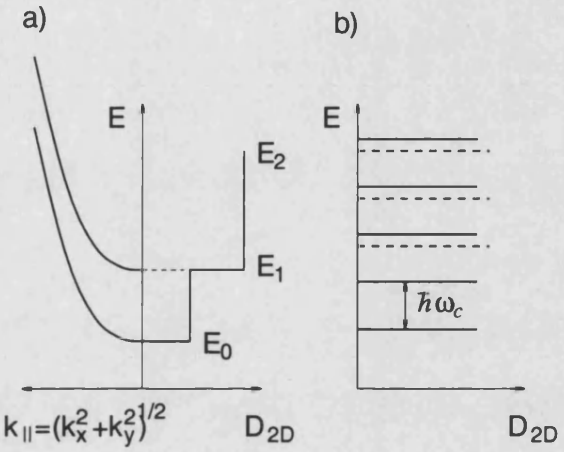

Figure 3.2: *a) Left: Parabolic energy dispersion in k-space in the plane of the 2DES. E_0, E_1 and E_2 indicate the energies of the first three occupied electronic subbands. a) Right: Schematic representation of the density of states of the 2DES per unit area and per unit energy with zero applied magnetic field. b) Un-broadened DOS for a 2DES in a perpendicular magnetic field. The solid and dashed lines indicate Landau levels in the first and second subbands respectively*

be obtained from Eqn.3.5,

$$E_F = E_0 + \frac{\pi\hbar^2 n_{2D}}{m^*} \tag{3.8}$$

where E_0 is the energy of the bottom of the first subband. The density of states (DOS) (number of states per unit area and unit energy) $D_{2D}(E)$ is the sum of the DOS of each subband $D_i(E)$, i.e.,

$$D_{2D}(E) = \sum_i D_i(E) = \sum_i \frac{\partial n_i}{\partial E_i}. \tag{3.9}$$

Therefore,

$$D_{2D}(E) = \frac{m^*}{\pi\hbar^2} \sum_i \Theta(E - E_i) \tag{3.10}$$

where Θ is the Heaviside step function. Thus the DOS in each subband is a constant (if m^* is constant), and the total DOS is a step-like function with increasing energy which is sketched in Fig.3.2.

3.2 The Hall Effect and Magnetoresistance

Electrons travelling through a wire under the influence of an electric field E_x in a perpendicular magnetic field B_z are subject to a Lorenz force $F_y = E_x \times B_z$. As a result, electrons are deflected to one side of the wire, producing an electric field E_y, which under equilibrium conditions will exactly oppose the Lorenz force. This result was first observed by E. H. Hall in 1879 [38]. Hall's experiment is generally reproduced using

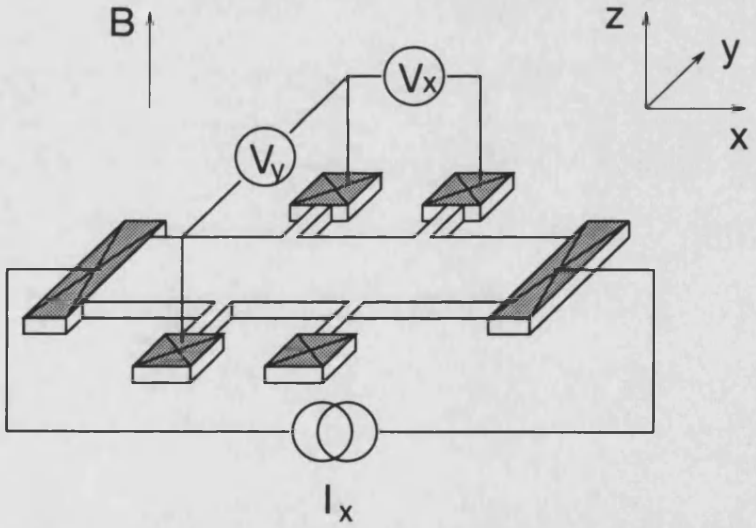

Figure 3.3: *Hall bar geometry used in measurements of the transport properties of a 2DES. The same geometry is also used as a basis for lateral tunnelling devices described in Chapters 4-8.*

the so-called Hall bar geometry which consists of a long thin sample with current contacts at each end and voltage probes on each side (see

Fig.3.3). The voltage probes can be used to obtain either the Hall resistance $R_H = V_y/I_x$ or the magnetoresistance $R_x = V_x/I_x$ by measuring the transverse or longitudinal voltage drops on the sample respectively. Hall found V_x to be magnetic field independent to first order, in contrast to V_y which is given for electrons by,

$$V_y = V_H = -\frac{B_z I_x}{nde} \tag{3.11}$$

where n is the carrier density, d the sample thickness and e the electronic charge. For a 2D sample, the product of carrier density and sample thickness is equivalent to a 2D charge density n_{2D}, hence the surprising result that the Hall voltage for a 2D sample is independent of the sample dimensions. The Hall resistance (for a 2D sample) is therefore given by,

$$R_H = \frac{B_z}{n_{2D}e}. \tag{3.12}$$

A more common notation used to describe magnetotransport in a 2D electron system is obtained from a generalisation of Ohms law involving the 2D magnetic field dependent resistivity tensor $\rho(B)$. The current density is then related to the electric field strength by the relation,

$$\vec{E} = \rho(B)\vec{J} \qquad \rho(B) = \begin{bmatrix} \rho_{xx} & \rho_{xy} \\ -\rho_{xy} & \rho_{xx} \end{bmatrix}. \tag{3.13}$$

Applying Eqn.3.13 to the Hall effect problem with current in the x-direction gives,

$$\begin{pmatrix} E_x \\ E_y \end{pmatrix} = \begin{bmatrix} \rho_{xx} & \rho_{xy} \\ -\rho_{xy} & \rho_{xx} \end{bmatrix} \begin{pmatrix} j_x \\ 0 \end{pmatrix} = \begin{pmatrix} \rho_{xx} j_x \\ \rho_{xy} j_x \end{pmatrix} \tag{3.14}$$

Hence the Hall resistance can be directly related to the ρ_{xy} component of the resistivity tensor,

$$\rho_{xy} = R_H = \frac{B_z}{n_{2D}e} \tag{3.15}$$

The diagonal component ρ_{xx} can be calculated using the Drude theory of conductivity [25] which describes the resistivity of a material in terms of an average scattering time τ,

$$\rho_{xx} = \frac{m^*}{e^2 n_{2D} \tau} = \frac{1}{e n_{2D} \mu} \tag{3.16}$$

where m^* in the effective electron mass. Alternatively, ρ_{xx} can be written in terms of the electron mobility $\mu = \tau e/m^*$,

$$\rho_{xx} = \frac{1}{e n_{2D} \mu}. \tag{3.17}$$

The relations 3.16 and 3.17 for 2D samples are in fact only valid for small values of the magnetic field where the additional quantising influence of the magnetic field is small. This is discussed in detail in the following section.

3.2.1 Properties in a Perpendicular Magnetic Field

Application of a magnetic field to a 2DES imposes a Lorenz force on the electrons in a direction perpendicular to both the field and the direction of motion. If the field direction is perpendicular to the plane of the 2DES, at strong magnetic fields the electrons will follow closed circular orbits in the x-y plane known as *cyclotron* orbits. For finite magnetic field, the vector potential $\vec{A}$ is no longer constant, and the SE for motion in the x-y plane of an ideal 2DES,

$$\frac{1}{2m^*}\left[\vec{P} - e\vec{A}(x,y,z)\right]^2 \Psi(x,y) = (E - E_i)\Psi(x,y) \tag{3.18}$$

where $(E - E_i)$ is the energy in the x-y plane. Choosing a vector potential of the form $\vec{A}(x,y,z) = (0, Bx, 0)$ (termed the Landau gauge) means that the Hamiltonian is separable using wave functions of the form,

$$\Phi(x,y) = exp(ik_y y)\phi_N(x - x_0). \tag{3.19}$$

After some manipulation [39], the SE can be written,

$$\left[\frac{-\hbar^2}{2m^*}\frac{\partial^2}{\partial x^2} + \frac{m^*\omega_c^2}{2}(x - x_0)^2\right]\phi_N(x - x_0) = (N + \frac{1}{2})\hbar\omega_c\phi_N(x - x_0) \tag{3.20}$$

This is simply the differential equation governing the motion of a harmonic oscillator with the central coordinate $x_0 = \hbar k_y/eB$ and a cyclotron frequency $\omega_c = eB/m^*$. The energy eigenvalues are discrete and for each subband, i,

$$E_{i,N} = E_i + \hbar\omega_c(N + \frac{1}{2}) \tag{3.21}$$

where N is the index of the energy level or *Landau level.* A further quantisation occurs within each Landau level due to the presence of spin-up and spin-down electron states. Hence the Zeeman energy must be included in the the complete energy spectrum,

$$E_{i,N,s} = E_i + \hbar\omega_c(N + \frac{1}{2}) + sg^*\mu_B B \tag{3.22}$$

where μ_B is the Bohr magneton and $s = +\frac{1}{2}$ and $-\frac{1}{2}$ for spin up and spin down states respectively. The effective Landé g-factor g^*, which contains many-body corrections, is dependent on the occupation of spin-up and spin-down states within each Landau level N and is therefore also strongly dependent on the magnetic field (see Chapter 8).

Each spin resolved Landau level contains $n_L = eB/h$ states and the density of states, which is sketched in Fig.3.2 is a set of delta functions with energies $E_{i,N,s}$,

$$D_{2D}(E) = n_L \sum_{i,N,s} \delta(E - E_{i,N,s}). \tag{3.23}$$

It is convenient to characterise the system in terms of the number of occupied Landau levels or filling factor

$$\nu = \frac{n_{2D}}{n_L} = \frac{hn_{2D}}{eB}. \tag{3.24}$$

So far, this discussion has concentrated on *ideal* 2D electron systems, ignoring any influence of the disorder which exists in real crystal structures. The effect of disorder, which may for example arise from the presence of impurity atoms near the crystal interface, is to cause an energy broadening of the Landau level DOS. Numerical calculations [40]

have shown an important difference between states in the centre of the levels and those at the edges (or tails), namely that those at the centres are extended (i.e. they can carry current) whereas those in the tails are strongly localised. This can be visualised by considering the long range potential of the 2DES as a landscape of hills and lakes produced by the influence of repulsive and attractive impurities. Cyclotron orbits at the centre of the Landau levels follow equipotential paths between the landscape features, whereas those in the high or low energy tails are closed around hills or within lakes respectively. The first model of the broadened DOS was published by Ando [41] who proposed a sum of half ellipses. A range of subsequent experiments however ([42,43] and references therein) demonstrated that a significant DOS exists between the levels, and a more realistic model, based on a sum of Gaussian functions was developed by Gudmundsson and Gerhardts [44]. They gave the DOS as,

$$D_{2D}(E) = n_L \sum_N \frac{1}{\sqrt{2\pi\Gamma^2}} exp\left[-\frac{1}{2}\left(\frac{E - E_{N,s}}{\Gamma}\right)^2\right]. \qquad (3.25)$$

The term Γ is a measure of the broadening of each Landau level and depends on the type of disorder present in the crystal. Assuming the impurity potential acts over a short range, Γ can be obtained from the expression,

$$\Gamma = \hbar\sqrt{\frac{2eB}{\pi m^* \tau_B}} \qquad (3.26)$$

where τ_B is the mean time between scattering events and importantly is not the same as the τ obtained from the zero field magnetoresistance (Eqn.3.16). Fig.3.4 shows the DOS calculated from Eqn.3.25 at a magnetic field B=3.1T. The approximate energy positions of the localised and extended states are also sketched on the figure.

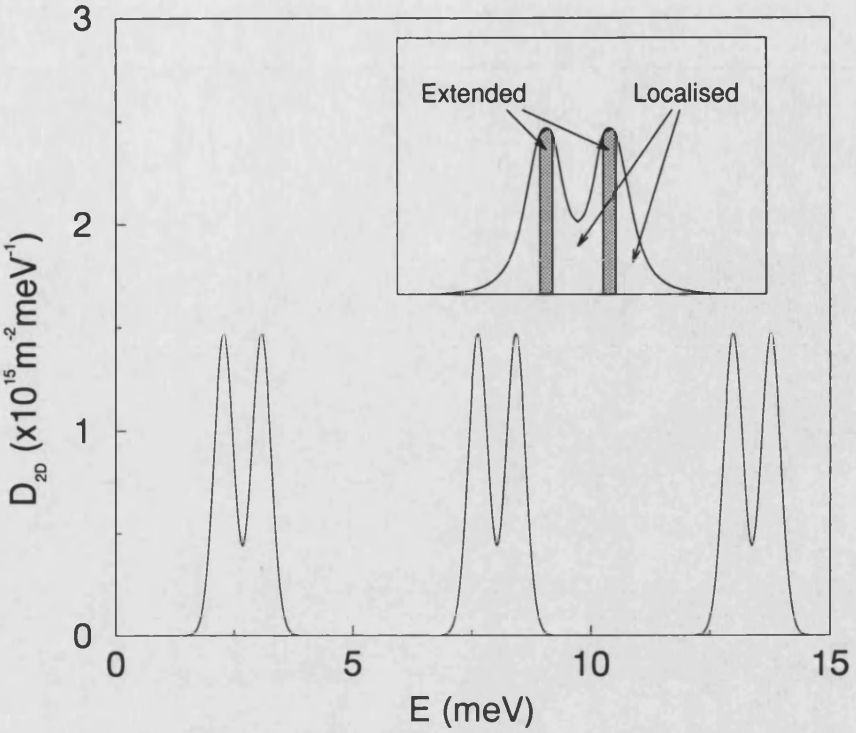

Figure 3.4: *Calculated density of states per unit area and energy D_{2D} as a function of energy for a 2DEG in a perpendicular magnetic field $B = 3.1T$. The calculation includes the enhanced g-factor and assumes g^* is the same for each Landau level. Spin splitting of the Landau levels is clearly observed at this magnetic field. Inset shows a representation of the energy positions of localised and extended states within each level.*

3.3 The Shubnikov-de Haas and Quantum Hall Effects

A measurement of the transport properties of a 2DES at high magnetic fields and low temperatures ($T < 10K$) reveals striking oscillations in the magnetoresistance ρ_{xx} which are periodic in $1/B$. These *Shubnikov-de Haas* (SdH) oscillations are in direct contrast to Hall's observation (at room temperature) that the magnetoresistance of a 3D sample is a constant, and are a consequence of the discrete nature of the DOS

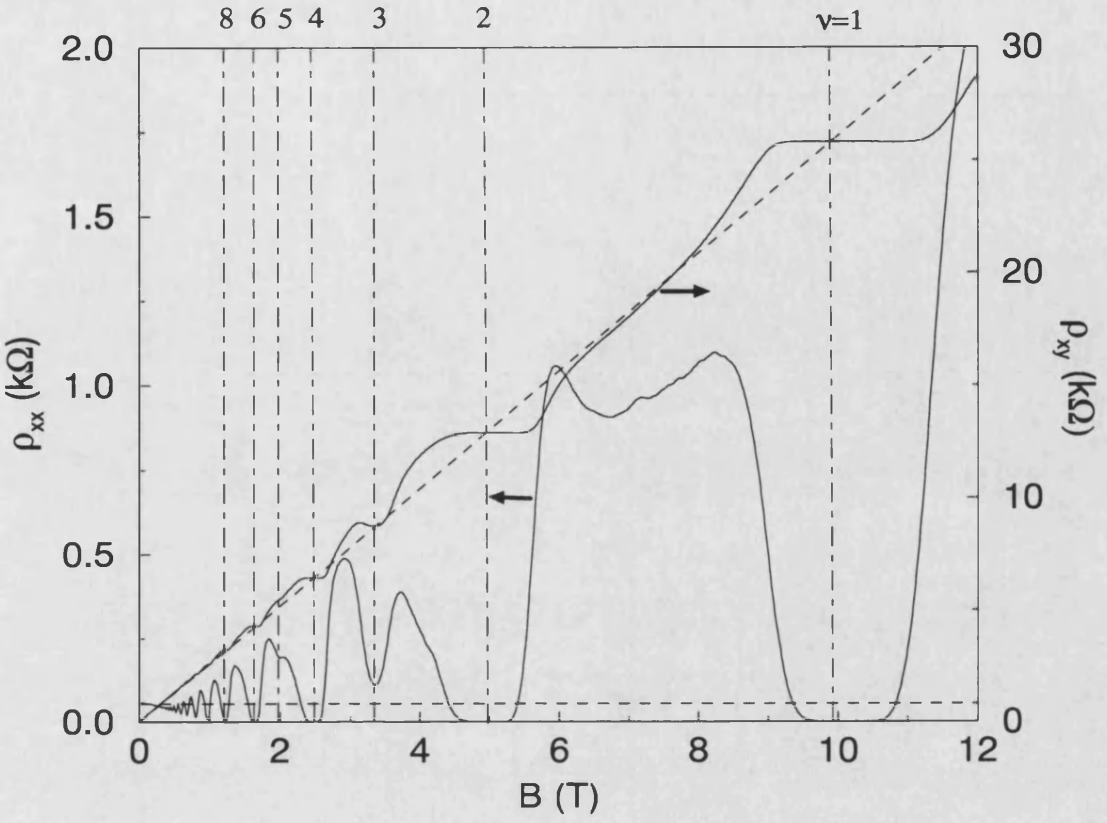

Figure 3.5: *Magnetoresistance ρ_{xx} and Hall resistance ρ_{xy} as a function of magnetic field for a GaAs/AlGaAs heterojunction sample at a temperature T=1.3K. The dashed lines indicate the classical values. The 2DEG mobility $\mu \approx 600000 cm^2 V^{-1} s^{-1}$ and the electron concentration $n_{2D} = 2.52 \times 10^{11} cm^{-2}$. Dot-dashed lines show the positions of integer filling factors up to $\nu = 8$.*

of a 2DES in a magnetic field at low temperature. Fig.3.5 shows ρ_{xx} measured as a function of B for a GaAs/AlGaAs heterojunction sample. The maxima in ρ_{xx} occur at magnetic fields where the Fermi energy lies at the centre of a Landau level (half integer filling factors), whereas minima in ρ_{xx} occur when E_F lies exactly between two Landau levels (integer filling factors). At first glance this observation appears contradictory, as one might expect a lower resistance when E_F lies in a region with a high DOS (Landau level centre) than in a region with a low DOS

(between Landau levels). The explanation lies in the way in which ρ_{xx} is related to the conductivity σ_{xx} via the tensor relation between $\vec{J}$ and $\vec{E}$ (Eqn.3.13). The conductivity tensor $\sigma(B) = 1/\rho(B)$, and it is simple to show that

$$\rho_{xx} = \frac{\sigma_{xx}}{\sigma_{xx}^2 + \sigma_{xy}^2}. \tag{3.27}$$

If σ_{xx} is small compared to σ_{xy} then $\rho_{xx} \sim \sigma_{xx}/\sigma_{xy}^2$ i.e. the resistivity is proportional to the conductivity. Oscillations in ρ_{xx} will therefore be in phase with those in σ_{xx} which are characteristic of the density of states at the Fermi level. This picture of SdH oscillations, based on the modulation of the DOS at E_F cannot however explain why ρ_{xx} *vanishes* at low filling factors (large magnetic fields) over significant ranges of the magnetic field. For that it is necessary to return to the idea of localised and extended states discussed in the previous section. The lack of conducting states available when E_F lies in the localised Landau level tails (near integer values of ν) results in zero conductivity σ_{xx} and hence zero magnetoresistance. The finite DOS that exists between the levels extends this condition over a range of magnetic field values.

Shubnikov-de Haas oscillations provide an accurate experimental way of determining the electron density of a 2DES. Since the minima in ρ_{xx} indicate magnetic field positions of integer filling factors, n_{2D} can be inferred directly from Eqn.3.24. Further experimental applications of the effect for the characterisation of a 2DES are given in [45].

This picture of localised and extended states is equally important for an understanding of the behaviour of the Hall resistance $R_H(= \rho_{xy})$ which is shown for the same 2D sample in Fig.3.5 as a function of the magnetic field. Again contrary to Hall's result that the Hall resistance is a linear function of B, well defined plateaus appear in R_H near integer values of ν. Furthermore, the resistance at the plateaus is precisely quantised in units of h/e^2, and remarkably, is independent of sample parameters and material. These observations, which were first made by

von Klitzing *et al.* [31] in a study of inversion layers in Si MOSFET's are termed the integer quantum Hall effect.

The existence of quantised values of the resistance can be predicted quite simply from Eqn.3.12. Substituting for the electron density in terms of the number of electrons per Landau level and the filling factor gives the Hall resistance,

$$R_H = \frac{h}{\nu e^2} \tag{3.28}$$

This suggests that R_H is only quantised at very special values of B (i.e. when the uppermost Landau level is completely occupied) and does not imply the presence of plateau regions. To understand the plateaus, again requires a return to the idea of localised and extended states. Only current carrying states (extended states in the Landau level centre) can contribute to the Hall voltage (or resistance) and hence a constant value of R_H would be expected while the Fermi level lies in the region of localised states between the Landau levels. While explaining the presence of the plateaus, this does not explain why they occur at values of h/e^2 since the localised states cannot carry current and should not influence the Hall resistance (Eqn.3.28). This problem has been the subject of much investigation (see [29] and references therein) and is partly answered in the edge state model of the quantum Hall effect which is described below.

3.4 The Edge State Picture of the Quantum Hall Effect

The above discussion of the quantum Hall effect purely in terms of localisation in a discrete density of states assumes a 2DES of infinite extent and ignores any influence the sample boundaries may have on experimental observations. To understand the role played by the sample edges in determining the properties of a real 2DES, it is necessary to return to the Schrödinger equation describing the motion of electrons in the x-y plane. The effect of the edges is to introduce a confinement potential

$V(x,y)$ which is zero at the centre of the sample but increases sharply near the boundaries. Assuming a very long sample (such as a Hall bar) enables $V(x,y)$ to be considered as one-dimensional (i.e. only a single pair of opposing edges are included). In this case the Hamiltonian is separable (as in the case of Eqn.3.18) using the wave function,

$$\Psi(x,y) = exp(ik_y y)\phi(x - x_0) \tag{3.29}$$

to produce the SE,

$$\left[\frac{-\hbar^2}{2m^*}\frac{\partial^2}{\partial x^2} + \frac{m^*\omega_c^2}{2}(x - x_0)^2 + V(x)\right]\phi(x - x_0) = (E - E_i)\phi(x - x_0) \tag{3.30}$$

In the centre of the sample where $V(x) = 0$, the eigenvalues are identical to those for an infinite system as given previously in Eqn.3.21. For non zero $V(x)$ (at the sample edge), the influence of $V(x)$ is to sharply increase the energy of the eigenvalues, which also become dependent on k_y.

A more convenient coordinate from which to plot the eigenvalue dispersion, is the centre of the cyclotron orbit x_0 where,

$$x_0 = -l^2 k_y \tag{3.31}$$

and l is the magnetic length ($l^2 = \hbar/eB$). Fig.3.6 shows a sketch of the energy dispersion of the first four (un-broadened) Landau levels across the width of a sample as a function of the orbit centre x_0 (ignoring spin splitting). The sample edges are at x_1 and x_2 and the dashed curve indicates a smooth confining potential $V(x)$. For current to flow in the sample, empty states must exist at the Fermi energy. Since all states below E_F are occupied, it can be seen from Fig.3.6 that unless the magnetic field is such that E_F coincides with a Landau level in the centre of the sample, free states at E_F only exist where it intersects with a Landau level at the edge of the sample. Thus current in the 2DES is carried by a set of one-dimensional (1D) states known as *edge*

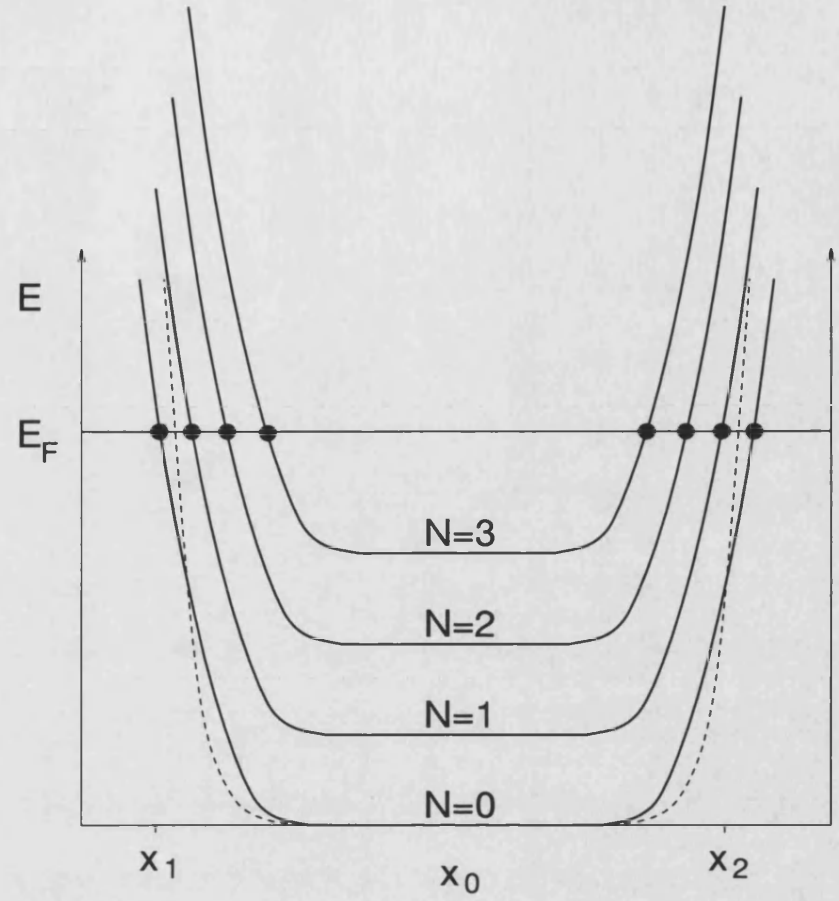

Figure 3.6: *Landau level dispersion in a 2DES with a smooth confining potential $V(x)$ (dashed line) as a function of the orbit centre x_0. x_1 and x_2 are the physical boundaries of the sample where the confining potential tends to infinity. The black dots indicate the position of free states at the Fermi energy E_F*

states or *edge channels* near the sample boundaries. Classically these edge states correspond to paths in which the electrons skip along the sample boundary, colliding elastically with the edge potential (so-called skipping orbits sketched in Fig.3.7a)). Note that the centre of mass of the electron wave function remains within the sample, even for orbit centres that lie beyond the boundary.

The motion of electrons in edge channels can be characterised by a

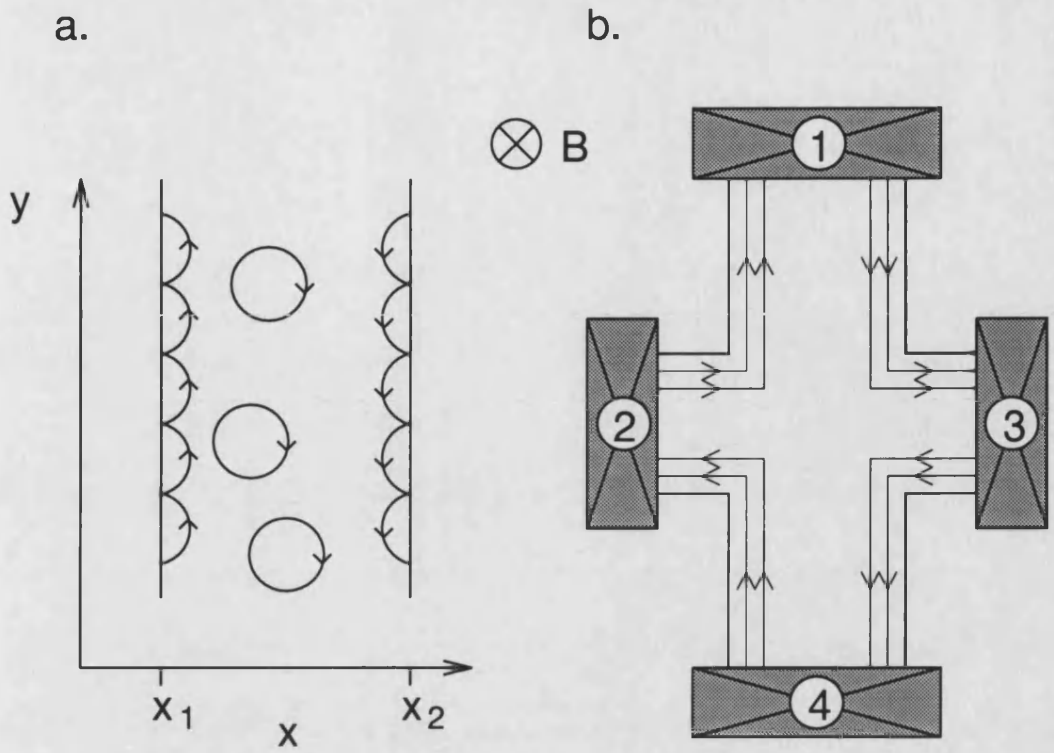

Figure 3.7: *a) Current flow via skipping orbits at the edge of a sample in a high magnetic field. Orbits in the centre of the sample are localised in the quantum Hall plateau regimes. b) Edge state paths in a Hall bar with 2 occupied Landau levels. The direction of the carrier motion is indicated by an arrow head on each channel.*

group velocity v_y in a direction along the sample, where

$$v_y = \frac{1}{\hbar}\frac{\partial E}{\partial k_y} = \frac{1}{\hbar}\frac{\partial E}{\partial x_0}\frac{\partial x_0}{\partial k_y} = \frac{1}{eB}\frac{\partial E}{\partial x_0}. \tag{3.32}$$

From Eqn.3.32 it is clear that electrons on opposing sides of the sample will have velocities with opposite signs. For each 1D channel, the density of states in $k-$space $\partial n/\partial k = 1/2\pi$. The DOS can be expressed in terms of energy as

$$D_{1D} = \frac{\partial n}{\partial E} = \frac{\partial n}{\partial k_y}\frac{\partial k_y}{\partial E} = \frac{1}{hv_y}. \tag{3.33}$$

Fig.3.7 b) shows a sketch of the edge channel paths on a Hall bar with two current contacts (1 and 4) and two voltage probes (2 and 3). In the absence of scattering, Eqn.3.32 and 3.33 can be used to express the

current flowing between two contacts (for example 1 and 2) in terms of their electrochemical potentials μ_1 and μ_2,

$$I_{1,2} = e\int_{\mu_1}^{\mu_2} D_{1D} v_y dE = \frac{e}{h}(\mu_2 - \mu_1) \tag{3.34}$$

A generalisation of Eqn.3.34, which is important for an understanding of how the edge state model can explain the quantum Hall effect, was proposed by Büttiker [46], who included the idea of reflection and transmission of the 1D channels at each contact. The Landauer-Büttiker formalism for a single contact i is written in terms of r_{ii}, the probability of a channel being reflected from contact i back to contact i and t_{ij}, the probability of the channel being transmitted from another contact j to contact i. For M 1D channels the formula for the current flowing in contact i is

$$I_i = \frac{e}{h}\left[(M - r_{ii})\mu_i - \sum_j t_{ij}\mu_j\right] \tag{3.35}$$

For the quantum Hall effect regime, where $E_F \neq E_i + (N + \frac{1}{2})\hbar\omega_c$, the absence of free states near E_F in the bulk of the sample leads to a suppression of scattering (termed back scattering) between opposite edges of the sample. For this case, $r_{ii} = 0$ and $t_{ij} = 1$. Returning to the Hall bar in Fig.3.7b), contacts 2 and 3 are voltage probes, hence $I_2 = I_3 = 0$ whereas for the current contacts, $I_1 = -I_4$. The Hall voltage $V_H = V_{2,3}$ can be written as the difference in the electrochemical potentials of contacts 2 and 3, i.e.

$$V_{2,3} = \frac{\mu_3 - \mu_2}{e}. \tag{3.36}$$

Using Eqn.3.36 for two occupied Landau levels gives the currents

$$I_1 = -I_4 = \frac{2e}{h}(\mu_3 - \mu_2). \tag{3.37}$$

Thus the Hall resistance is quantised,

$$R_{2,3} = \nu\frac{h}{e^2} \tag{3.38}$$

at all values of the magnetic field where back scattering is *suppressed.* Therefore the quantised value of the Hall plateaus *and* their finite width are explained. When E_F lies in the centre of a Landau level in the bulk, the conditions $r_{ii} = 0$ and $t_{ij} = 1$ no longer hold, since free states exist at E_F across the sample and backscattering can occur. This corresponds to the dissipative regime, between the plateaus.

Although experimental and theoretical support for the edge state picture of the quantum Hall effect is widespread, a definitive experiment, proving that current only flows at the edge of the sample has not been published to-date [47]. A number of authors have given very complete reviews on the subject [47–49]. Chapter 8 gives a detailed account of how tunnelling experiments can be used as a probe to study edge state transport in a 2DES.

4 Sample Fabrication

4.1 Introduction

In the 1950's and 60's, the early commercial semiconductor industry was based on macroscopic electronic devices with typical device dimensions being in the range of 10^{-4}-10^{-3}m. Electron transport effects were therefore dominated by bulk crystal phenomena and much of the research effort at the time was devoted to producing structures with a higher crystal purity. With the advent of semiconductor microstructures and integrated circuit technologies in the early 1970's, improvements in material quality were mirrored by a rapid advance in the lateral patterning

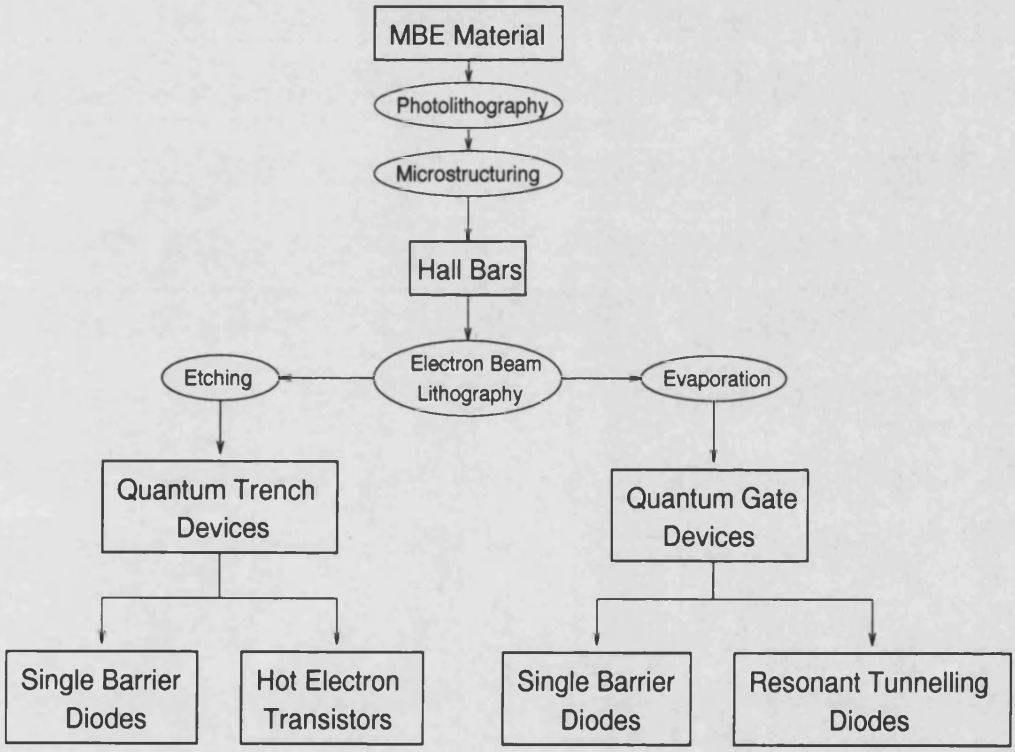

Figure 4.1: *Outline of the processing steps involved in the fabrication of lateral quantum tunnelling devices.*

techniques and a consequent rapid reduction in feature sizes which has continued until the present day.

Although microstructures with device dimensions in the range of 10^{-7}-10^{-4}m now dominate the semiconductor marketplace, researchers have become increasingly interested in semiconductor nanostructures which have made possible the observation of many quantum phenomena, and have the potential to revolutionise the electronics industry. A number of very comprehensive reviews have been written on both the lateral patterning and crystal growth of semiconductor devices with dimensions in the nanometre (10^{-10}-10^{-7}m) range. The following chapter attempts to summarise both the principles of the most important technologies used in the fabrication of lateral quantum tunnelling devices and the process parameters used for various devices. Fig.4.1 gives a brief outline of the processing steps involved, starting from the crystal material which was grown in-house by Prof. K. Ploog and co-workers (see Acknowledgements).

4.2 Modulation Doped Heterostructures Grown by MBE

Modulation doped semiconductor heterostructures play an important role in many areas of high speed electronics, the most common example of which is the high electron mobility transistor (HEMT) used as a GHz amplifier in domestic satellite receivers. The high frequency performance stems from the ultra high electron mobilities achievable in semiconductors where the electrons are spatially separated from their parent donors. Although for reasons of cost the majority of commercial structures are grown by metal-organic-chemical-vapour-deposition (MOCVD), molecular beam epitaxy (MBE) generally provides the best crystal quality (see [2] for a review) and is thus used for the growth of most research devices.

Crystal growth by MBE occurs via the thermal evaporation of the required chemical constituents in an ultra high vacuum environment. Each gaseous component is produced as a beam of atoms and/or molecules,

directed at a heated, crystalline substrate. Careful control of each beam by means of a blanking shutter allows the growth of crystal structures both with a very exact chemical content and a precision in thickness of one atomic layer or better. Such precise control is invaluable for the growth of semiconductor heterostructures where crystal and interface quality is of paramount importance.

The devices described in the following chapters, were all fabricated on modulation doped GaAs/AlGaAs heterostructure samples taken from a single, MBE grown wafer (No. 8134). The heterostructure was grown on a semi-insulating (SI) GaAs substrate wafer with a [100] crystal orientation. The MBE growth sequence consisted of a 2μm un-doped GaAs buffer followed by a 25nm un-doped $Al_xGa_{1-x}As$ spacer, a 58nm $\sim 1 \times 10^{18}cm^{-3}$ Si doped $Al_xGa_{1-x}As$ layer and an 11nm un-doped GaAs cap. The Al mole fraction x was 0.3 which gives a conduction band energy offset between GaAs and AlGaAs of approximately 300meV [50]. The mobility and carrier density of the 2DES at a temperature of 4.2K without illumination were approximately $600000cm^2V^{-1}s^{-1}$ and $2.5 \times 10^{11}cm^{-2}$ respectively.

Although MBE produces extremely pure semiconductor material, background impurities such as carbon and oxygen are generally present. This background doping plays an important role in the potential energy profile of a structure and may also influence the transport properties of the 2DES [36]. Although the exact concentration of background impurities is difficult to determine, values in the region of $1 \times 10^{14}cm^{-3}$ are generally assumed [51]. Fig.4.2 shows a sketch of the heterostructure layer sequence and the energy profile in conduction and valence bands.

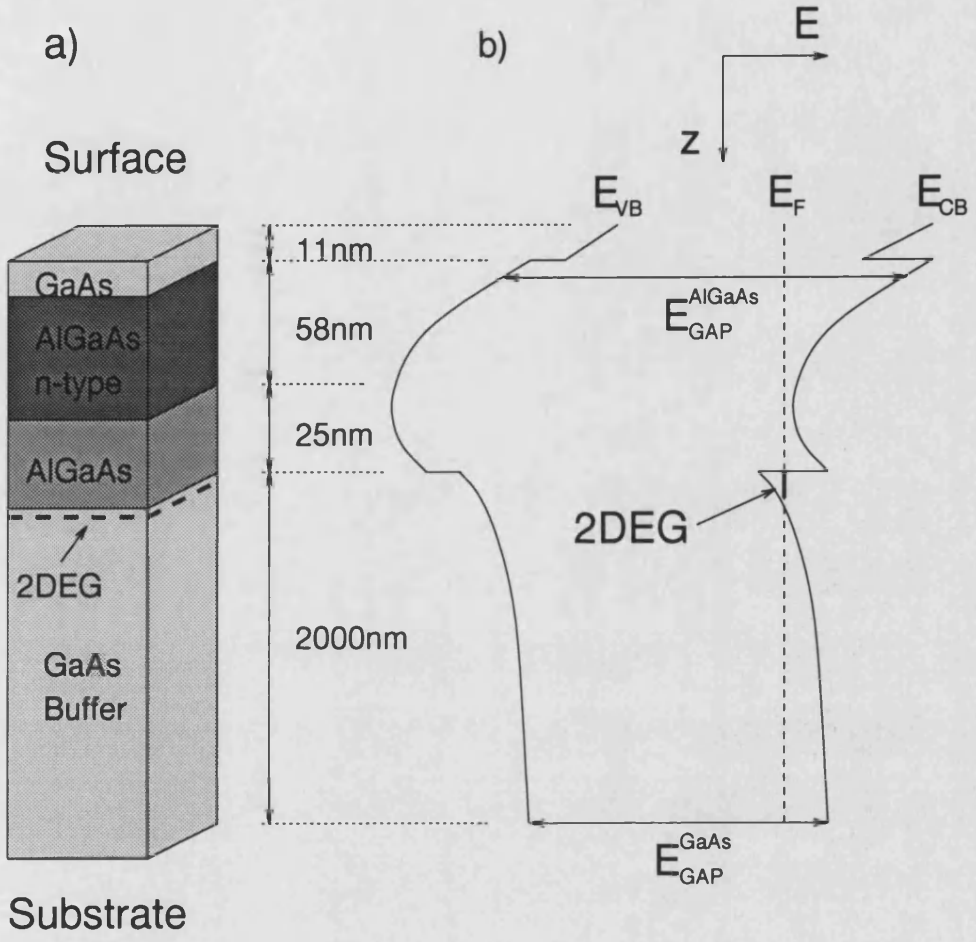

Figure 4.2: *a) Schematic diagram of the crystal layers of a modulation doped GaAs/AlGaAs heterostructure. The n-type $Al_xGa_{1-x}As$ layer is Si doped with a density of roughly $1 \times 10^{18} cm^{-3}$. The rest of the sample is not intentionally doped but a background impurities are assumed to be present with an estimated density of $1 \times 10^{14} cm^{-3}$. b) Sketch of the conduction band edge energy E_{CB} and the valence band edge energy E_{VB} for the sample in the growth direction z. The Fermi level E_F is indicated by the dashed line and the forbidden energy gaps for the materials by E_{GAP} .*

4.3 Sample Preparation

4.3.1 Lithography

Since the introduction of the first integrated circuit technologies in the early 1970's, the most successful tool for defining semiconductor microstructures has been photolithography [52]. Using wavelengths in either the ultra-violet or X-ray regimes, structures are defined by projecting photons through a mask containing the required geometrical pattern onto a radiation sensitive resist covering the wafer (sketched in Fig.4.3). Development using a chemical solution removes the resist in either exposed or un-exposed areas (depending on whether the resist is of a positive or negative type) and then resist free regions can be structured by for example etching or by material deposition.

Owing to diffraction effects however, photolithography has a reso-

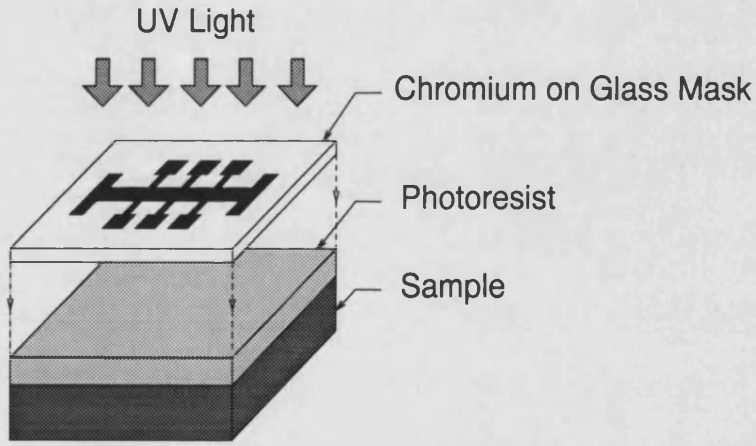

Figure 4.3: *Expanded view of photolithography using a simple contact mask*

lution limit of around 100nm [53] which in many cases is too large to observe quantum effects. Feature sizes can in principle be reduced by the use of short wavelength radiation (such as X-rays) but here the limiting factor is the availability of suitable optical systems.

A substantial improvement in lithographic resolution can be obtained

by using electrons rather than photons as the exposing radiation. Electron beam lithography (EBL) technology has advanced rapidly over the last decade and is now used extensively in both the writing of high quality masks for photolithography, and more importantly for this work, for the fabrication of devices on the nanometre scale.

The principle of EBL is different to that of photolithography in that structures are written sequentially using a thin electron beam (usually a few nanometres in diameter) rather than exposed simultaneously through a large mask. The electron resist generally consists of an organic polymer in which impacting electrons cause either the breaking or forming of bonds (again depending on whether the resist type is positive or negative), thus rendering the exposed areas more soluble in the developing solution. The major drawback with EBL lies in the time required to sequentially write large structures, hence its most common industrial application in the writing of one-off masks for photolithography.

However, for the fabrication of research orientated nanostructures, the tiny electron wavelength and high quality of electron optical systems make EBL an ideal tool. The most common hardware used for EBL is a scanning electron microscope (SEM) in which the scan coils are used to move the highly focussed electron beam in the desired pattern. Although the electron beam in a SEM can be routinely focussed to a diameter of less than 5nm, the limiting factor for EBL resolution is the area of resist in which the electrons dissipate their energy. Electrons incident on the resist undergo a number of scattering processes, some of which can cause exposure in regions adjacent to the primary beam; the so called proximity effect (explained in Fig.4.4). A range of scattering mechanisms are involved, the most important being backscattering of electrons from the semiconductor itself[1] which can cause proximity exposure at a range of

[1]In addition to backscattering, proximity exposure is caused both by forward scattering of the primary beam in the electron resist, and by low energy secondary electrons produced by ionising collisions with atoms in the sample [53].

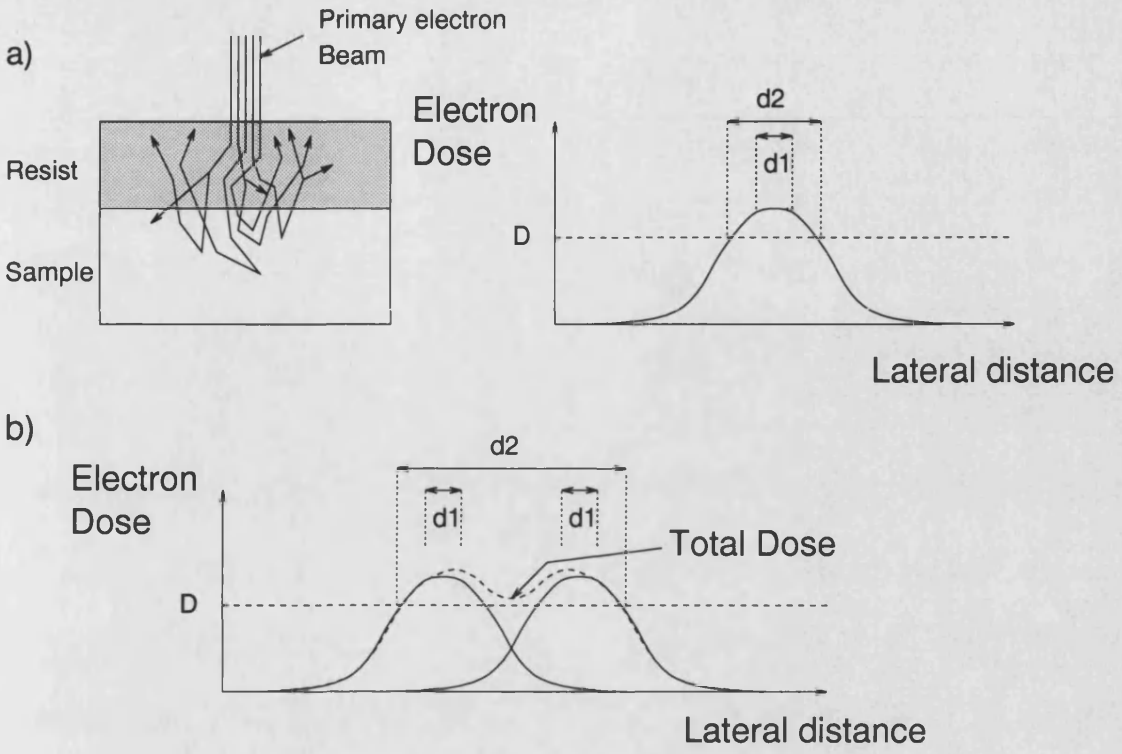

Figure 4.4: *Schematic representation of the electron scattering processes contributing to the proximity effect. a) shows how in a single written feature, the minimum dose for exposure D is reached over an area d2 much wider than the diameter of the primary beam d1. b) illustrates the way the proximity effect will tend to cause two features written close to one another to merge. Typically, this becomes a serious problem for features separated by less than 100nm*

a few microns. Some contribution from the proximity effect in EBL is usually unavoidable, particularly when working in the sub 100nm range where scattered electrons simply broaden written features. Optimisation of the electron optics, resist thickness and electron dose (the total number of electrons incident per unit area) can reduce the effect and indeed feature sizes of less than 10nm have been achieved with EBL [53].

4.3.2 Microstructuring Using Photolithography

All the measurements described in the forthcoming chapters were performed on devices patterned on samples with standard Hall bar geometries. As a first step in sample preparation, 5mm square chips were cut from the MBE wafer using a diamond scriber. During cutting, the wafer surface was protected from dust and debris with a thick layer of photo-resist which was subsequently dissolved away in acetone. Throughout the entire fabrication process, the samples were kept clean by regular washing with acetone in an ultrasound bath and by careful handling in a clean environment.

The Hall bars and Ohmic contacts were defined using the scheme outlined in Fig.4.5. Each lithographic step used a Shipley S1818 photo-resist spun onto the sample to a thickness of roughly 500nm and baked at 80°C for 20 minutes. The resists were exposed with U-V light for approximately 30 seconds through a mask in direct contact with the sample. A 1:3 ratio of Shipley Microposit MF312 to water was used as a developer with development times of approximately 60 seconds.

Where processing stages involved metal deposition (either for contacts or gate fingers), the samples were immersed in chlorobenzene (C_6H_5Cl) for 10 minutes after exposure and left to stand in air for 2 hours. This treatment produces a thin, hard crust on the photo-resist surface which dissolves more slowly than the softer under-layer during development. The resulting undercut in the resist is an important aid to "lift off" of excess metal after the evaporation process [54].

Contacts consisting of a 200nm layer of a Au/Ge alloy followed by a 40nm Ni layer were deposited on the samples using a thermal evaporation system and lift-off of the excess metal was achieved using acetone in an ultrasound bath at 80°C. Electrical contact to the 2DES was produced by thermally annealing the sample at 450°C for 2 minutes in a N_2/H_2 atmosphere. The annealing causes the diffusion of Ge (a donor

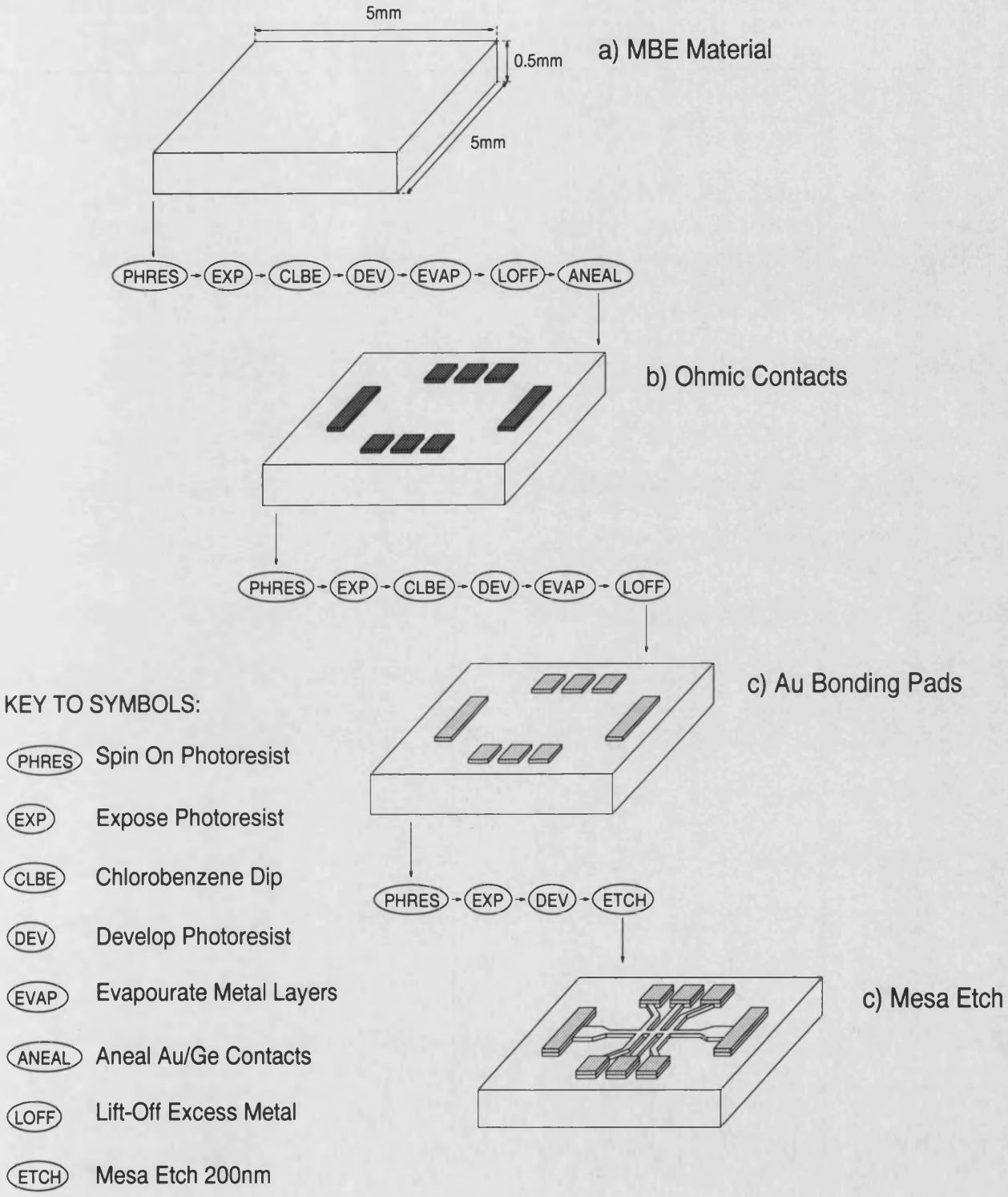

Figure 4.5: *Lithographic and patterning steps used for the definition of Hall bar structures.*

impurity in III/V semiconductors) into the sample surface, which serves to reduce the width of the Schottky barrier between metal and semiconductor to such an extent that its electrical properties are approximately Ohmic [55]. To complete the Ohmic contacts, bonding pads were de-

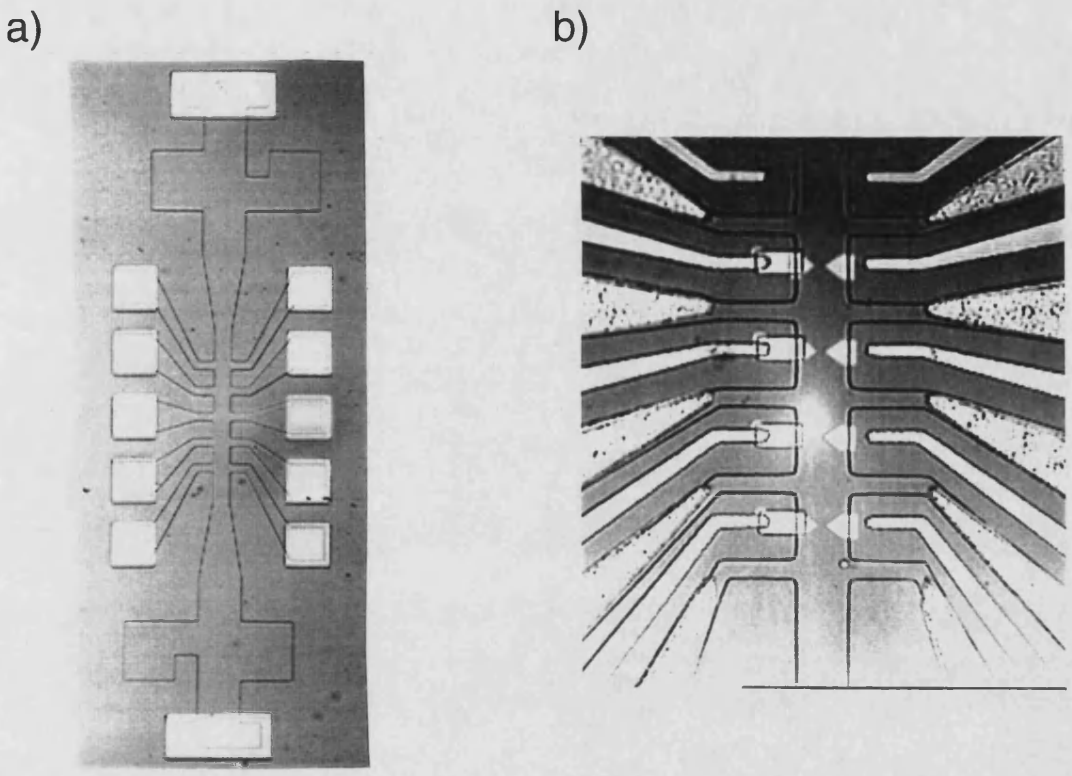

Figure 4.6: *a) Optical micrograph of a completed Hall bar sample used for quantum trench devices. b) Optical micrograph of the Hall bar geometry used for gated devices. The gate fingers are positioned between each pair of Hall bar legs. On this sample the gates themselves have already been evaporated onto the Hall bar surface.*

posited to provide a stable layer for wire bonding. These consisted of a thin, 30nm layer of Cr which acts as an adhesive film for a subsequent 200nm layer of Au.

Different Hall bar mesas were electrically isolated on the chip by wet chemical etching. A solution of H_2O:H_2O_2:H_2SO_4 in the ratio 1000:8:1 was used as the etchant, which at a temperature of $3°C$ has an etch

rate of $\sim$ 10nm/min. A relatively shallow etch depth of 200nm was chosen (c.f. 2DES depth of $\sim$100nm) so that the 100nm thick electron resist layers, applied in subsequent EBL processing would be continuous over the edges of the Hall bars. Fig.4.6a) is an optical micrograph of a completed Hall bar sample, used as a basis for quantum trench devices. The second completed Hall bar structure shown in the micrograph of Fig.4.6b) was used for devices with gates.

4.3.3 Nanostructuring Using Electron Beam Lithography

After the completion of all Hall bar microstructuring, the samples were covered in a 100nm thick layer of a PMMA (poly-methyl-mecryl-acetate, molecular weight 95000) electron resist. The resist layers were spun on in a two-stage process, using both viscosity and rotation speed to control the thickness. Two drops of PMMA diluted to a ratio of 1:40 (PMMA:chlorobenzene (C_6H_5Cl)) were applied to the stationary sample using a 5cl medical syringe. The sample was then rotated at at a speed of 3000 r.p.m for 5 seconds during which a further two drops were added. The rotation speed was then increased to 8000 r.p.m for a further 30 seconds. Finally, the samples were baked at 160°C for 60 minutes to ensure complete evaporation of chlorobenzene. Resist thicknesses were measured using a Dektak step profiler on a small scratch made in the resist and typically varied by less than 10nm. As a rule of thumb, the resist appears light blue for thicknesses around 100nm.

4.3.4 Electron Beam Lithography Using a Scanning Electron Microscope

Fig.4.8 shows a schematic diagram of the apparatus used for EBL. The system is based on a Hitachi S2300 SEM with a heated tungsten filament cathode, a beam energy of 25kV and a minimum beam diameter of

4nm. The beam position during writing is controlled by the microscope scan coils which are in turn controlled by a microcomputer via a D/A converter. "ELPHY3" from Raith Gmbh is used as controlling computer software. An important feature of the system is a beam blanking lens mounted just below the electron gun which deflects the beam from the sample when moving between features on the writing field, preventing unintentional exposure.

For writing, samples were mounted on an aluminium block and held with copper clips to ensure a good earth contact. A working distance of 10 mm allowed high microscope resolution with a depth of focus greater than the sample height variation over the $(100\mu m)^2$ writing area. Structures were written with a beam current of 5pA, measured with an electrometer via a *Faraday cup* probe prior to exposure.

To correct for proximity exposure the electron dose was varied over

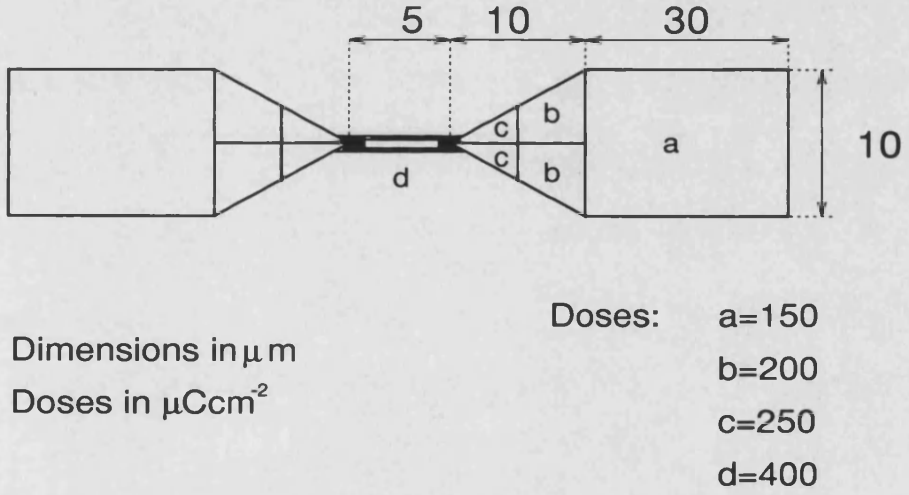

Figure 4.7: *Typical dose pattern for quantum trench diode*

the writing field. Although advanced software packages exist for the calculation of dose correction schemes, a method of trial and error on GaAs test samples was found to be a more efficient approach to the problem. Fig.4.7 shows a typical dose pattern for a 5μm wide lateral diode designed for an 80μm wide Hall bar. The large areas either side

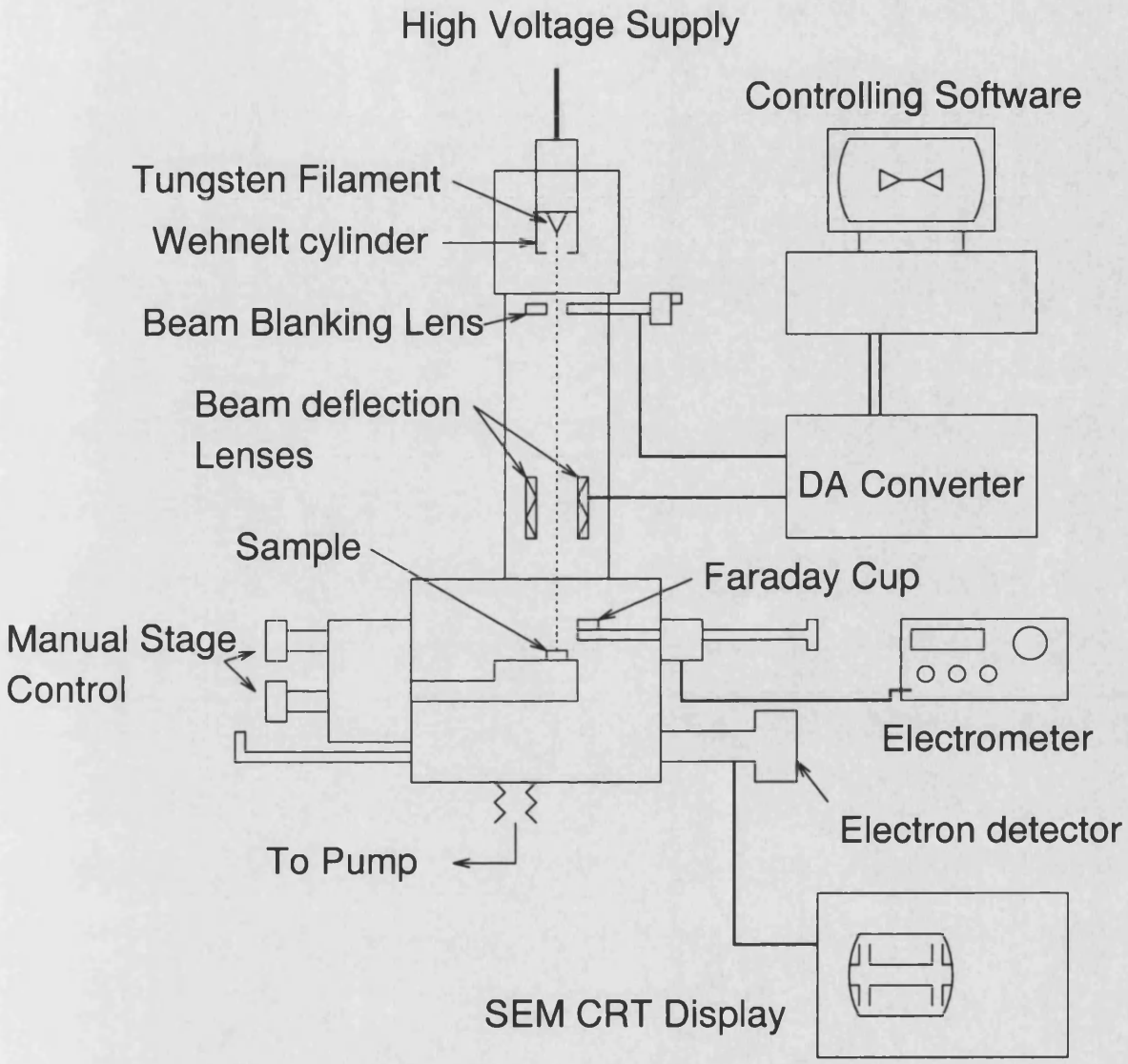

Figure 4.8: *Schematic diagram of the EBL apparatus. The system uses a tungsten heated filament as an electron source with an accelerating voltage of 25kV. Further details of the system are described in the text and in [39].*

of the quantum trench/gate region are designed to confine the electron transport to the central 5μm of the Hall bar. Extreme care was taken with the writing of the trench/gate feature to obtain the minimum possible line width. The region was exposed by scanning the electron beam twice along the same coordinates. The electron dose was chosen to *just expose* the line, i.e. to include the minimum possible amount of line broadening from scattered electrons (see Fig.4.4). Even so, owing to the absence of proximity exposure of the lines from *other* neighbouring regions, large electron doses in excess of 500μCcm^{-2} were required to completely expose the channel.

The exposed samples were developed in an slowly stirred solution of MIBK (methyl-iso-butyl-ketone) and propanol in the ratio 1:3 for 65 seconds. A 60 second dip in propanol was used as a fix.

4.4 Fabrication of Quantum Trench Diodes

Reproducible, uni-directional etching techniques are a basic requirement for the controllable etching of semiconductor crystals on a nanometre scale. In the following section, *wet* chemical and *dry* reactive ion (RIE) techniques are compared and and contrasted as a method for etching quantum trench devices.

4.4.1 Wet Chemical Etching

For wet chemical etching, a solution of H_2O, H_2O_2 (30% concentrated) and H_2SO_4 (96% concentrated) in the ratio 1000:8:1 was used at a temperature of 3°C. During etching, the samples were immersed in the solution on a small glass cradle and the solution stirred with a magnetic stirrer at a rate of 200 r.p.m. The solution temperature was controlled to an accuracy of $\pm$0.1°C by using a jacketed reaction vessel through which glycol from a constant temperature bath was pumped. Care was

taken to shield the glass vessel from light, which initialises the breakdown of H_2O_2 to H_2O and O_2 and can affect the etching rate over typical solution preparation, cooling and etching times of roughly one hour. A

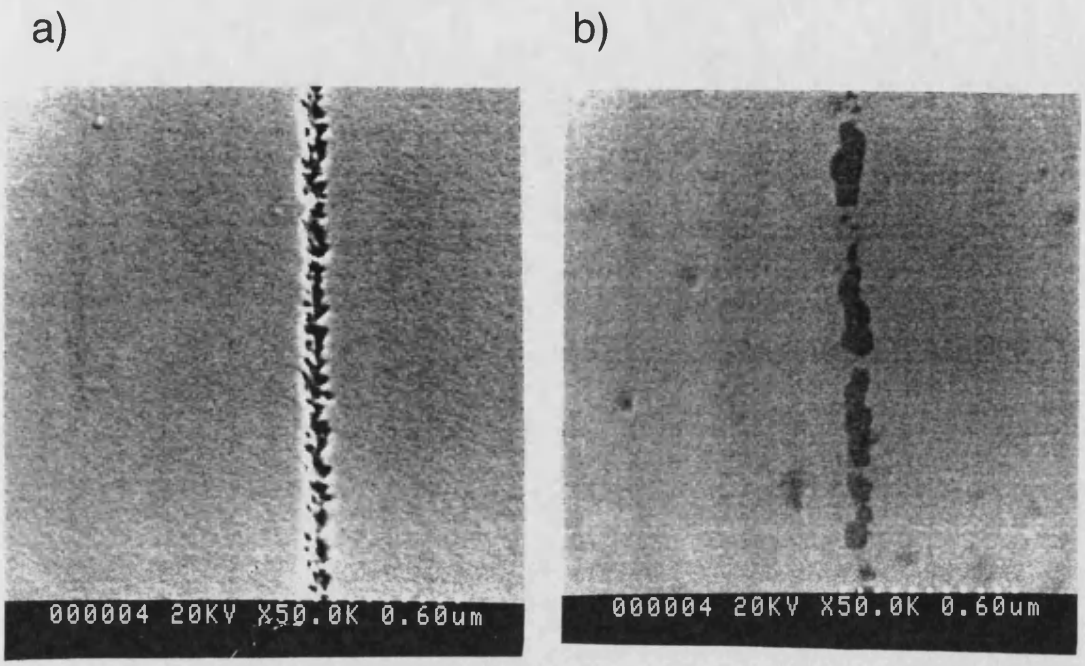

Figure 4.9: *SEM micrographs of quantum trenches, etched using the H_2O:H_2O_2:H_2SO_4 system. The jagged walls of the channel in a) indicate a strong crystal orientation dependency in the etching rate whereas the breaks in the line on b) are probably the result of a badly developed electron resist*

range of etch rate tests were performed on both GaAs substrate material and GaAs/AlGaAs MBE material using optically defined mesas with feature sizes of the order of 10μm. The etch depths were measured with a Dektak step profiler and indicate roughly the same etch rate of 10 ± 1nm/min, for both materials. For these feature sizes the technique is an efficient and highly reproducible method of etching the GaAs/AlGaAs material system.

Wet etching techniques seem however to be unsuited for structures with dimensions in the sub-micrometer range. Fig.4.9a) and b) show

SEM micrographs of two $\sim$ 70nm wide quantum trenches, etched to a depth of roughly 50nm using the above method. The left hand micrograph clearly shows an intrinsic drawback of wet etching on this feature scale, namely that the etch rate is highly dependent on the crystal orientation and that undercut will occur and tend to follow the easiest path. Such an inhomogeneous trench profile is clearly not suitable for producing high quality devices. Problems were also caused wherever small areas of electron resist in the channel remained after developing. Fig.4.9b) shows an SEM micrograph of such a case where resist protected areas have caused clear breaks in the etched line. The frequency of the breaks was reduced by treating the whole sample with an O_2 resist oxidation plasma for a few seconds after development in an attempt to clean out the channel, but this also tended to increase the line-width by more than 50%.

4.4.2 Reactive Ion Etching

The crystal orientation dependency and undercut properties shown by wet chemical etching techniques are to a large extent overcome by RIE. RIE is essentially a uni-directional process where the sample is etched by an ion plasma, generated from a basis gas by an RF field applied between two plate electrodes. During etching, the sample sits on the lower of the two plates, and a DC electric field between the electrodes accelerates positive ions towards the sample surface. The etching mechanism comprises of both a mechanical *milling* component and a chemical *reactive* component. The mechanical component is desirable in that it is uni-directional, but undesirable in that it can damage the crystal structure under the etched region if the accelerating voltage is too high. The chemical component on the other hand causes no structural damage, but is responsible for some undercut during etching.

An LE301 RIE system from Leybold Hereus was used in the experi-

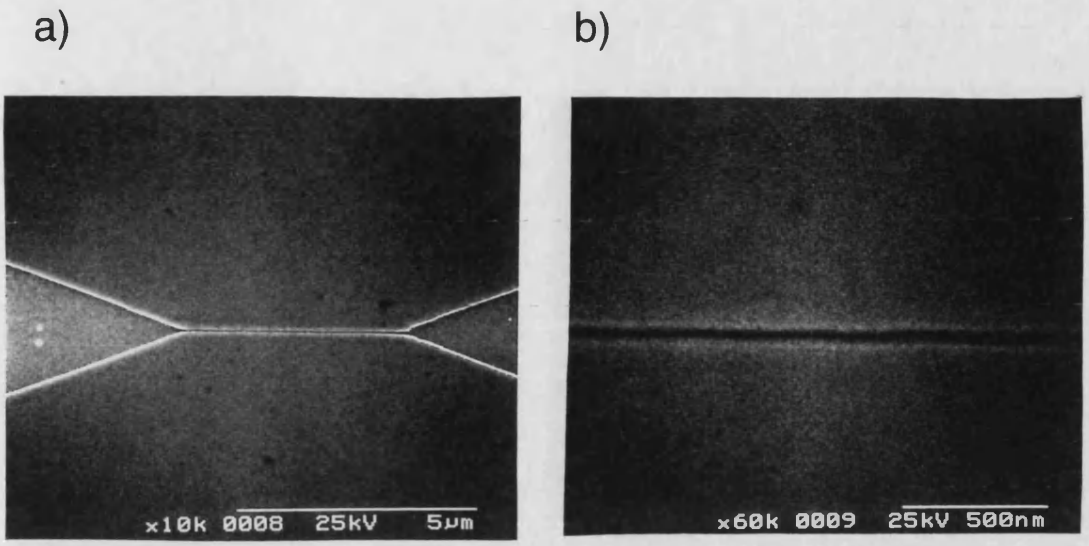

Figure 4.10: *Electron micrographs of a quantum trench diode, reactive ion etched onto a GaAs test sample.*

ments with a $SiCl_4$ gas. The process used a DC bias of 140V, a gas flow rate of 31sccm and a chamber pressure of 10^{-2}mbar which combine to give an etch rate of approximately 80nm/min. Full details of the RIE method are given in [56].

Etching depths for the trenches were inferred from depths measured on large mesas, optically defined on GaAs test samples which were etched simultaneously. This method produces only a rough approximation to the real depth since the scavenging of reacted components from the nanometre scale trenches is almost certainly inefficient compared to the large mesas and will decrease the local etch rate. This point is discussed more fully in Chapter 5.

Fig.4.10a) and b) show SEM micrographs of a reactive ion etched quantum trench diode at both low and high magnification. The quality of the trench profile is immediately apparent and is highly reproducible between different samples and etch runs. The width of the trench, which is of the order of 40nm is also impressively small and is approaching the

minimum possible value imposed by the proximity effect at electron energies of 25kV.

An interesting by-product of RIE was the apparent deposition of tiny

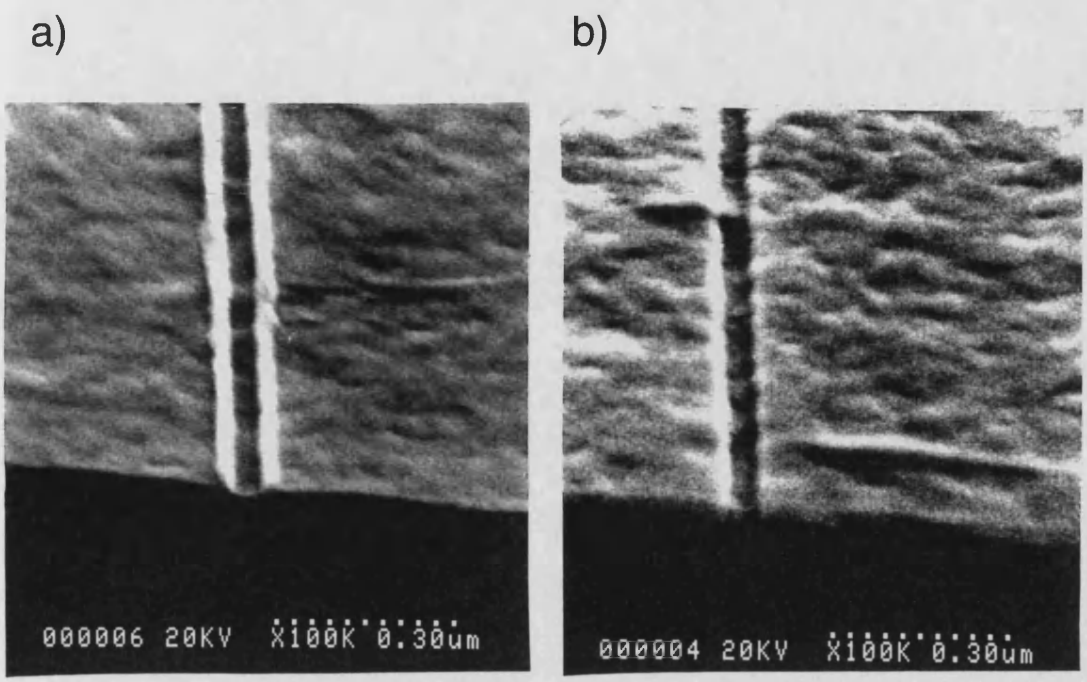

Figure 4.11: *a) Reactive ion etched quantum trench with carbon contamination on the etch walls. b) after treatment with conc.* H_2SO_4

ridges along the sides of the trench, clearly visible in Fig.4.11a) which shows a micrograph of a quantum trench on a cleaved GaAs test sample. Although no attempt was made to chemically analyse the deposited material, it is probably a carbon based polymer sputtered from the PMMA resist at the edge of the trench and insoluble in the MIBK/propanol developer. It was found that the ridges could be removed by immersing the sample in conc. H_2SO_4 in an ultrasound bath for 30 seconds, and a micrograph of the same sample after such treatment is shown in Fig.4.11b).

4.5 Fabrication of Gated Lateral Tunnelling Devices

The optical lithography scheme for gated devices involved a third processing step to define the gate fingers for wire bonding. Fig.4.12 shows a sketch of a typical gated Hall bar, on which the gate fingers (consisting of a 30nm Cr/200nm Au layer) were thermally evaporated on the mesa etched substrate of the sample and positioned to bisect pairs of Hall bar legs. An optical micrograph of a completed sample is shown in Fig.4.6

The gates themselves were defined on the Hall bar using the EBL

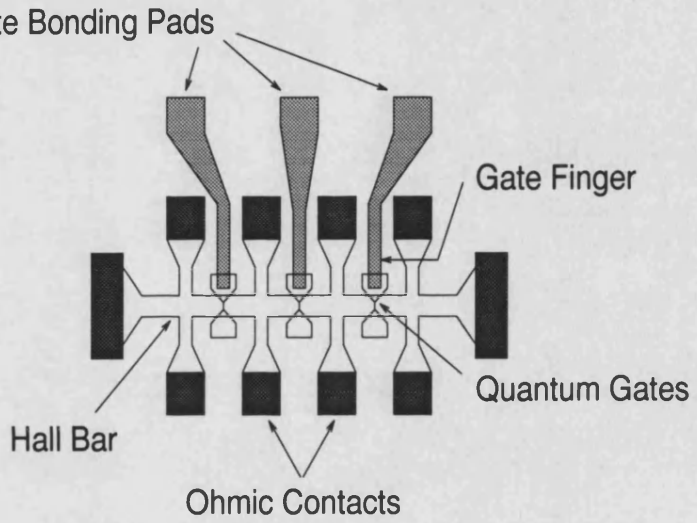

Figure 4.12: *Sketch of a Hall bar with gate fingers bisecting pairs of Hall bar legs.*

process described above with a geometry similar to that shown in Fig.4.7. The use of extremely thin gate layers was necessary in order to achieve successful metal lift-off with such a thin (100nm) electron resist layer. The metal layers (10nm Cr/25nm Au) were deposited in a thermal evaporator, using a particularly slow evaporation rate ($\sim 0.5\mathring{A}s^{-1}$ c.f. $\sim 3\mathring{A}s^{-1}$ for optically defined contacts) in an attempt to reduce the droplet size of the evaporated metal and produce a more homogeneous layer.

Fig.4.13 is an electron micrograph of a single gate on a GaAs test sam-

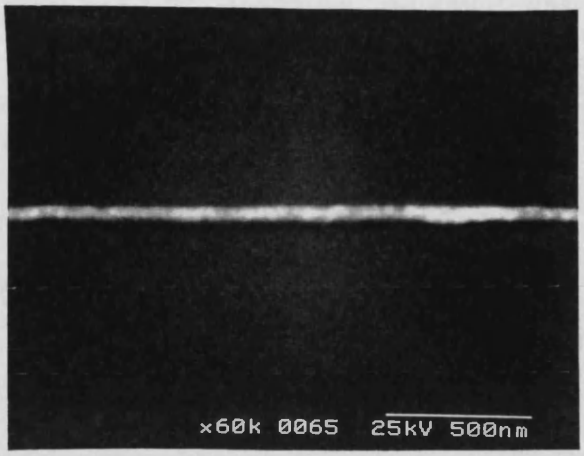

Figure 4.13: *Scanning electron micrograph of a single gated diode on a GaAs test sample. The gate is approximately 50nm long and 5μm wide.*

ple. Although at ~ 50nm the gate is very slightly wider than the etched quantum trenches, it is still within the dimensions necessary to produce a narrow tunnelling potential barrier in the 2DES. Furthermore, gates of this scale and quality were quite straightforward to reproduce on different samples with an overall yield of roughly 75%.

Some previous work has suggested that the current leakage characteristics of other gated devices are improved by evaporating onto a cooled sample. The cooling is intended to reduce the diffusion rate of metal into the sample during evaporation thus ensuring the existence of a wide Schottky barrier at the surface under the gate. Evaporation tests were therefore made on GaAs substrate material, cooled to liquid nitrogen temperature (−196°C). The resulting gates were however unacceptably wide (>100nm) and inhomogeneous compared to those evaporated at room temperature, which was attributed to a distortion of the electron resist profile occurring near the channel due to a strong contraction of the PMMA at low temperature.

Fig.4.14a) and b) show electron micrographs of a *dual* gated device where the gate width is ~ 50nm and the spacing ~ 60nm. The effects

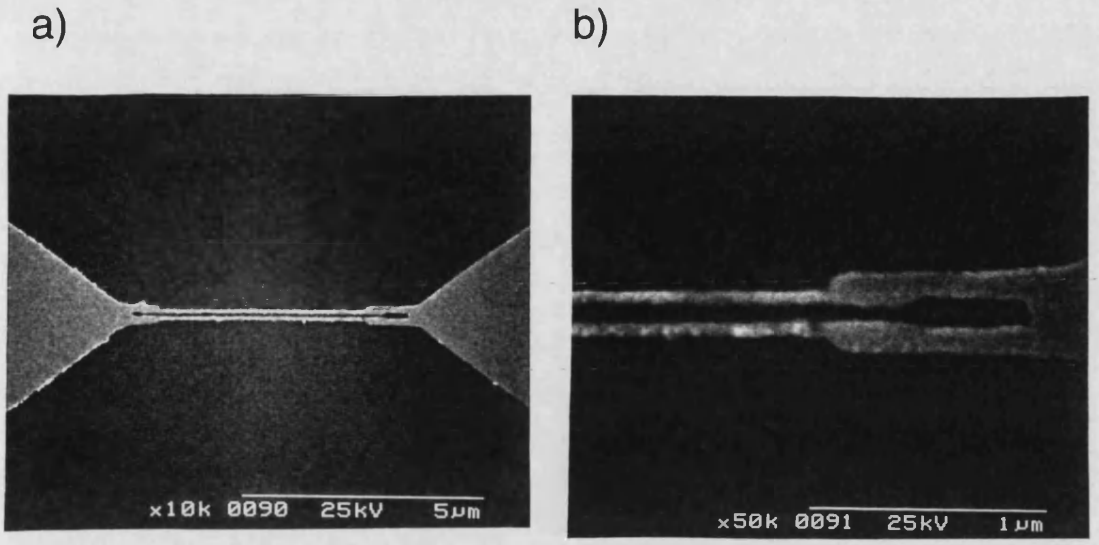

Figure 4.14: *Scanning electron micrographs of a dual gate lateral tunnelling diode, fabricated on a GaAs test sample. The gates are approximately 50nm long and 60nm apart*

of proximity scattering during EBL make the writing of such structures significantly more difficult than for single gates. Particular problems included achieving complete metal lift-off in the gap between the gates, and preventing breaks occurring at the point where they join the isolating triangular regions. In a successful effort to overcome this second problem, the gates were made slightly thicker at each end which can be clearly seen on Fig.4.14.

5 Characterisation Experiments on Quantum Trench Tunnelling Diodes

5.1 Introduction

Significant progress has been made in recent years on the physics and technology of lateral tunnelling in 2D electron systems. The majority of devices reported to-date have used reverse biased Schottky gates to induce narrow potential barriers in the plane of a 2DES confined at the interface of a GaAs/AlGaAs modulation doped heterostructure. This technique has allowed the realisation of a range of different devices, from simple single barrier diodes [57], through to resonant double barrier devices [58,59] [Chapter 7 of this thesis] and even three terminal hot electron transistors [60]. In addition to providing a sensitive probe for studying the physics of the 2DES, lateral devices also have the potential for ultra-high frequency applications (up to ~2THz with current technologies) owing to their tiny capacitances (< 5Ff) and series resistances (~ 100Ω) [7,61] . Commonly proposed applications include microwave mixer diodes and high frequency oscillators and current amplifiers.

In this chapter, data is presented on a novel type of lateral tunnelling device with the potential for enhanced, ultra-high frequency operation. The device is fabricated by etching an extremely thin *quantum trench* into the surface of a heterostructure in place of the conventional Schottky gate. The etching introduces a large density of surface states in closer proximity to the 2DES in the region of the etch and the subsequent band bending represents a tunnelling barrier to 2D electrons in the plane. This technique offers significant advantages over devices employing Schottky gates. Firstly, the barrier profile of a gated structure is to a far greater degree dependent on the applied bias voltage due to the need to reference the gate potential to either the emitter or the collector (see Chapter 7). Consequently their *I-V* characteristics lose their

antisymmetric behaviour and can display current saturation effects due to pinch-off. Such effects are not present in trenched devices which may prove advantageous for studying the physics of lateral transport through a narrow barrier.

Secondly, and more importantly for device applications, gated structures suffer from parasitic capacitances between the gate and emitter/collector which inevitably degrade high frequency performance. Such capacitances are not present in trenched structures which should exhibit enhanced frequency performance, in particular for mixer applications. In addition, trenched devices have the practical advantages being far more robust and of having inherently fewer contacts than those with gates. All these points however, are at the expense of losing the continuous tunability of the barrier potential available with gated devices, although it should be noted that such tunability is also not possible with the majority of commercially available devices based on vertical transport.

Fig.5.1 shows a sketch of a typical quantum trench diode in which

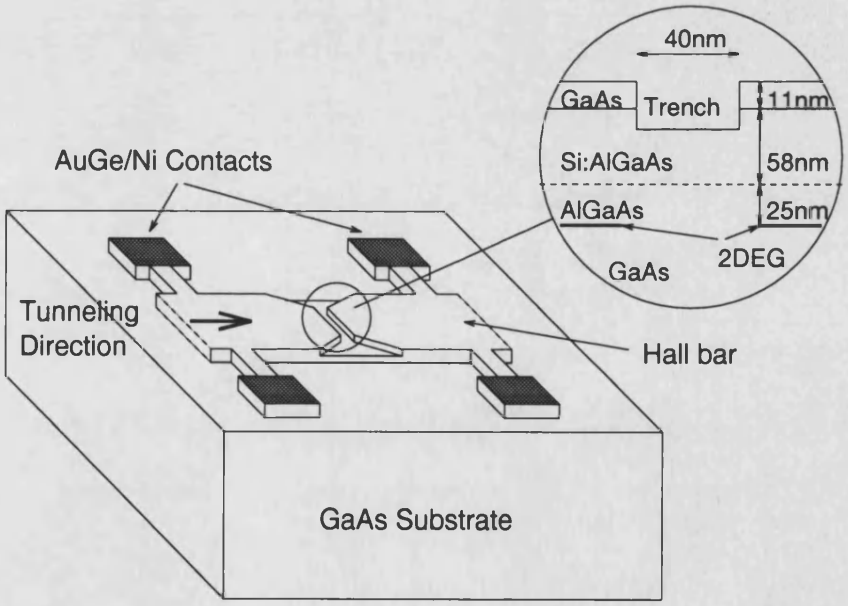

Figure 5.1: *Schematic diagram of a quantum trench device, showing the position of the trench and the transport direction.*

the trench is positioned to bisect two contact pairs of a Hall bar. Full details of the fabrication process are given in Chapter 4.

In the absence of scattering, current flow through single barrier diodes can occur via three main transport mechanisms. At zero temperature, only electronic states up to the Fermi energy E_F are occupied and thus transport can only occur via tunnelling into empty states on the other side of the barrier. At finite temperature T however, a high energy tail

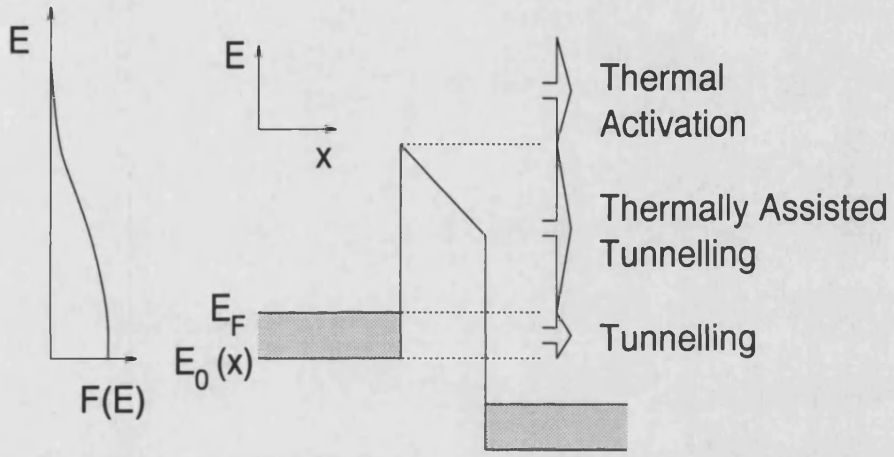

Figure 5.2: *Schematic illustration of the energy dependent transport mechanisms possible in single barrier diodes. To the left of the figure is a sketch of the energy distribution of electrons in the Fermi sea at finite temperature.*

of occupied states exist above E_F which are described by an occupation probability

$$f(E) = \frac{1}{1 + exp\left(\frac{E-E_F}{kT}\right)} \tag{5.1}$$

where k is Boltzmann's constant. Electrons from these higher energy states may either tunnel through the upper parts of the barrier (thermally assisted tunnelling) or if they possess sufficient energy, simply pass over the top (thermal activation). The three transport mechanisms are summarised in Fig.5.2. By using the appropriate temperature and bias voltage conditions, it is possible to study current dominated either by tunnelling or by thermally activated transport, in order to obtain infor-

mation about the potential barrier.

The following sections describe characterisation experiments which were performed on a range of quantum trench devices. Note that the experimental methods described apply to the measurements made not only in this chapter, but throughout the thesis.

5.2 Current-Voltage Measurements

5.2.1 Experimental Techniques

The majority of the experiments on lateral tunnelling devices described in the following chapters use a constant voltage, two-terminal method to measure either the current I as a function of the bias voltage V (the I-V characteristics), or the differential conductivity dI/dV, as as a function of V. The I-V characteristics were obtained by applying a DC voltage across the two sample contacts and measuring the resulting DC current. dI/dV was measured using an AC technique which is described below. For the characterisation of gated diodes (Chapter 7), the gate voltage V_{GD} was used as an additional variable parameter.

Fig.5.3 shows a schematic diagram of the electrical circuit used for the characterisation of devices. The principle of the system is as follows; using a voltage follower circuit as a voltage adder, a voltage signal consisting of DC (V) and AC (dV) components is applied to the emitter contact of the sample. The collector contact is grounded via a current amplifier (Ithaco model 1211) with a minimum current sensitivity of 1pA. Depending on the amplification range chosen, the drain sees a resistance of between 20 and 600Ω to ground.

A Hewlett Packard (model HP3325B) function generator was used to supply the *sweepable* DC component V of the applied voltage. Using a sawtooth waveform, and a frequency in the range $10^{-3} - 10^{-4}$Hz, (ramp time ~1000 seconds for a single branch of the sawtooth) this system has the advantage of providing a low-noise, continuously variable signal

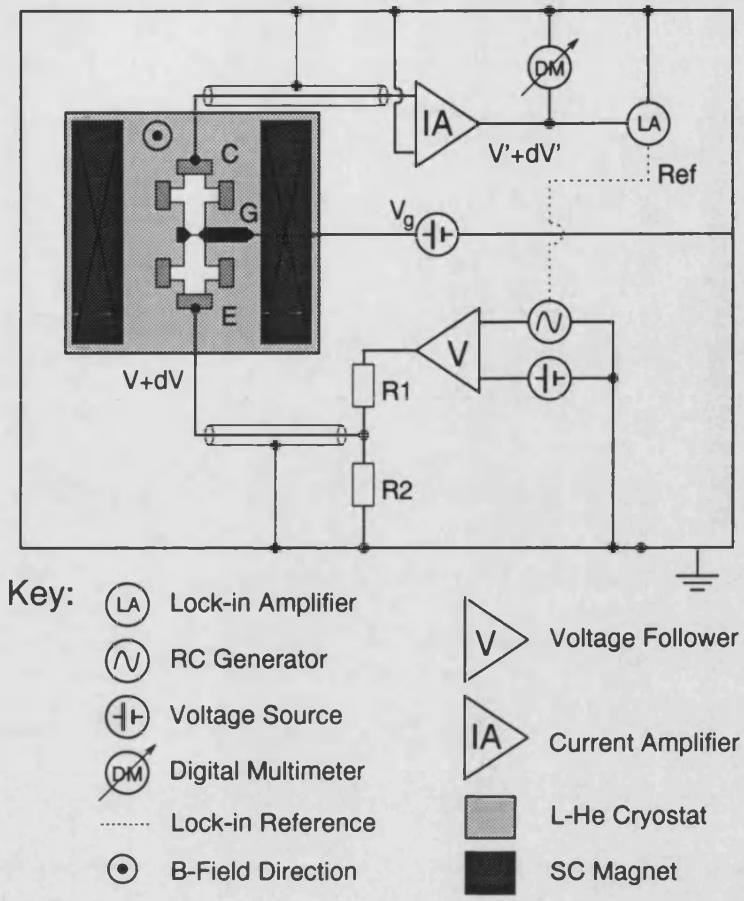

Figure 5.3: *Experimental set-up for characterisation measurements. An explanation of the system is given in the text. E and C indicate the emitter and collector contacts respectively and G represents the gate contact for gated devices.*

which is simple to control via the HP-IB bus. The resulting DC component of the current, given as a voltage signal by the current amplifier, was measured with a digital multimeter (model Keithley 230). Different bias voltage ranges were obtained using a potential divider at the voltage follower output. (R1 and R2 on Fig.5.3)

The differential conductivity dI/dV was measured using a standard AC lock-in technique. The AC component of the voltage applied to the emitter ($dV \sim 50\mu$V f=13Hz) was provided by an RC generator (model Philips PM5109). Using the lock-in amplifier (model EG&G 5210) to

detect the AC voltage signal from the current amplifier, produced at the same frequency, provides a value $dV' \propto dI$. From this AC signal, it is simple to deduce the differential conductivity dI/dV.

Care was taken to define only a single electrical earth for the measurement system via the steel cryostat and earthed pumping systems beyond. The mains earth was removed using 1:1 AC transformers and voltage spikes from the mains network were smoothed with a 50Hz band-pass filter. The whole measurement system was controlled with a Hewlett Packard HP3000 series computer using BASIC, via an HP-IB, IEEE compatible data-bus. An optical fibre data-bus link was used to avoid electrical contact between the computer and the measurement circuit.

Low temperature measurements were performed in an Oxford Instruments liquid helium (Li-He) bath cryostat (temperature range 1.5-4.2K) with a superconducting solenoid magnet (field range 0-12T). Lower temperature (0.022K) measurements were made in a dilution refrigerator and are discussed in Chapter 7

5.2.2 *I-V* Characteristics

Characterisation experiments were made on 5 quantum trench diodes (referred to in the following as A, B, C, D and E) with estimated trench depths of 14, 28, 34, 40 and 50 nm respectively (see Section 5.4.1). Fig.5.4 shows *I-V* characteristics for the five devices at a temperature of

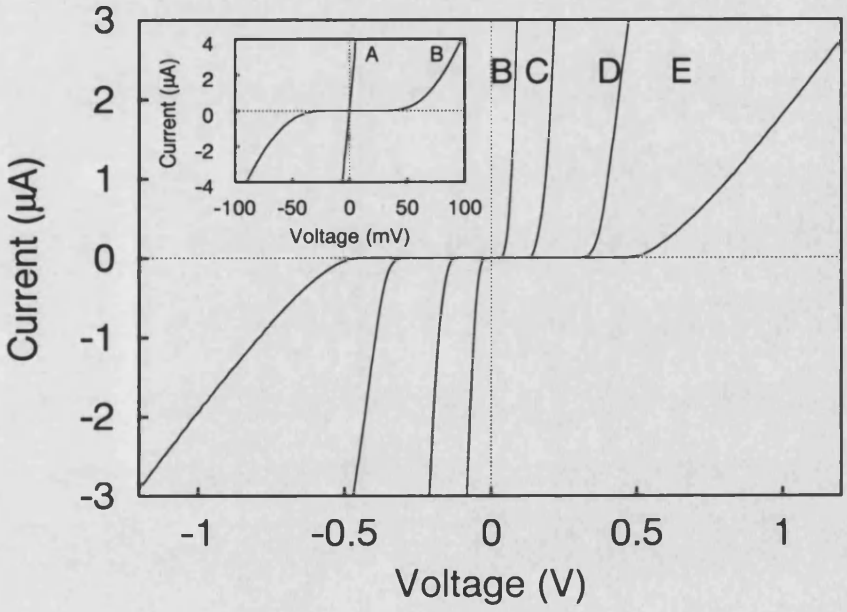

Figure 5.4: *I-V characteristics for devices A-E at 4.2K in the dark. Inset shows A and B on an enlarged scale.*

4.2K in the dark. Devices B, C, D and E display extremely non-linear behaviour with very sharp measurable current onsets. This non-linear behaviour, together with the absence of leakage currents at low bias, are indicative of a homogeneous barrier potential, where the tunnel current would be expected to be approximately exponentially dependent on the applied voltage. The characteristics are antisymmetric, and increasing the depth of the trench clearly results in a strong increase in the size of the potential barrier, with a consequent suppression of the tunnelling current. The linear behaviour of device A indicates a potential modula-

tion which is less than the Fermi energy and hence no tunnelling barrier is evident. At very high bias, the devices display a slow decrease in the differential conductivity which is discussed more fully in Chapter 6.

The device characteristics were highly reproducible over typical measurement periods of a few days, and seemed largely insensitive to any small electrical shocks received through the measurement apparatus. Temperature cycling (i.e. warming to room temperature and re-cooling to 4.2K) caused changes in the position of the measurable current onset of roughly ±20%.

Numerical calculations, outlined in Chapter 6, indicate that the tunnelling barrier potential is highly sensitive to the concentration of ionised donor impurities present in the doped AlGaAs layer of the heterostructure. Measurements performed by Schubert *et al.* [62] indicate that depending on Al content, the majority of Si donors in AlGaAs reside in deep states in the energy gap known as D-X centres. The D-X centre is believed to consist of a Si donor which undergoes a distortion from its substitutional site, resulting in a broken bond. (A complete review of the properties of D-X centres is given in [63]). The occupation probability of D-X states is strongly temperature sensitive, with an activation temperature of roughly 150K and therefore at liquid He temperatures, the occupation distribution is roughly static.

The changes that occur in the diode characteristics with temperature cycling are consistent with this picture of a temperature sensitive ionised impurity distribution which will be redefined with each cooling process. In addition, what appears to be an undesirable effect can be used to tune the properties of the device, once cold.

Ionisation of D-X states at low temperature can occur via photoexcitation, upon which the electron is given up to the 2DES at the GaAs/AlGaAs interface (see Fig.5.5). Re-capture then requires a multiphonon scattering process which is strongly suppressed at low temperature. Thus, illumination of a sample will cause both an increase in the

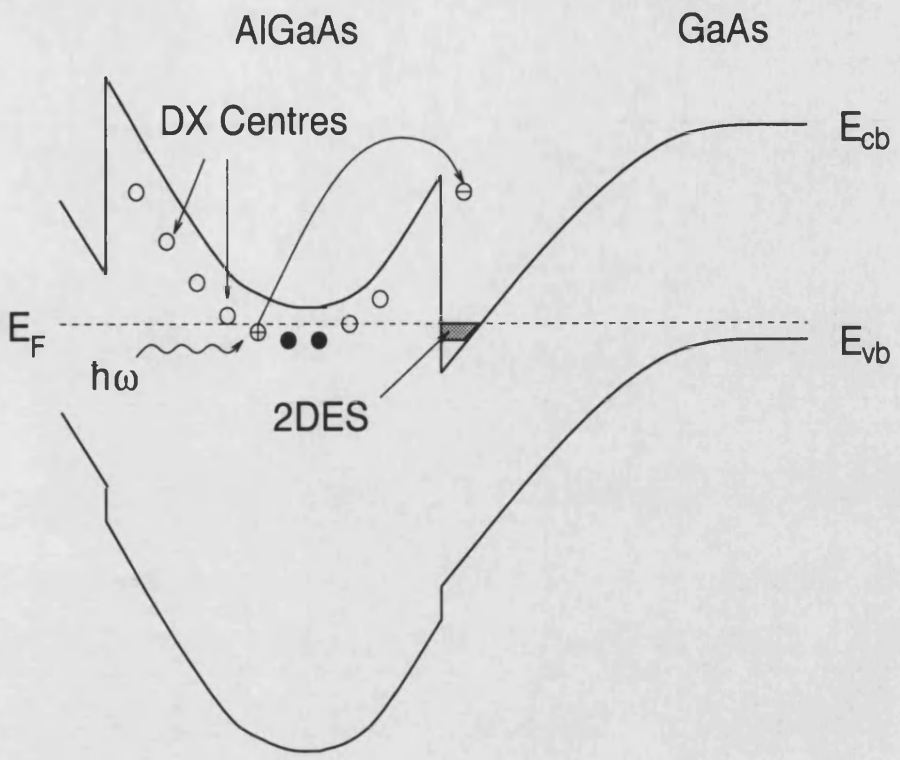

Figure 5.5: *Schematic diagram of the band profile of a heterostructure, indicating the mechanism for DX centre ionisation.*

ionised donor concentration *and* an increase in the density of electrons in the 2DES. Because the re-capture process is so slow, the latter effect is generally termed *persistent photo-conductivity* and has been the subject of a great deal of experimental investigation [64,65].

Device C was illuminated with single short pulses from a GaAs infra-red light emitting diode (LED) at a temperature of 4.2K. Each pulse was found to cause a very sharp increase in the current flow at constant bias voltage, followed by a slower reduction (over a period of seconds) to a value still many orders of magnitude greater than the original. Fig.5.6 shows the resulting *relaxed I-V* characteristics at each stage of illumination, from a single 1ms pulse through to continuous illumination.

The increase in the conductivity of the device after illumination is probably due to a combination of an increased ionised donor concentration N_D in the doped AlGaAs layer, and an increased 2D electron

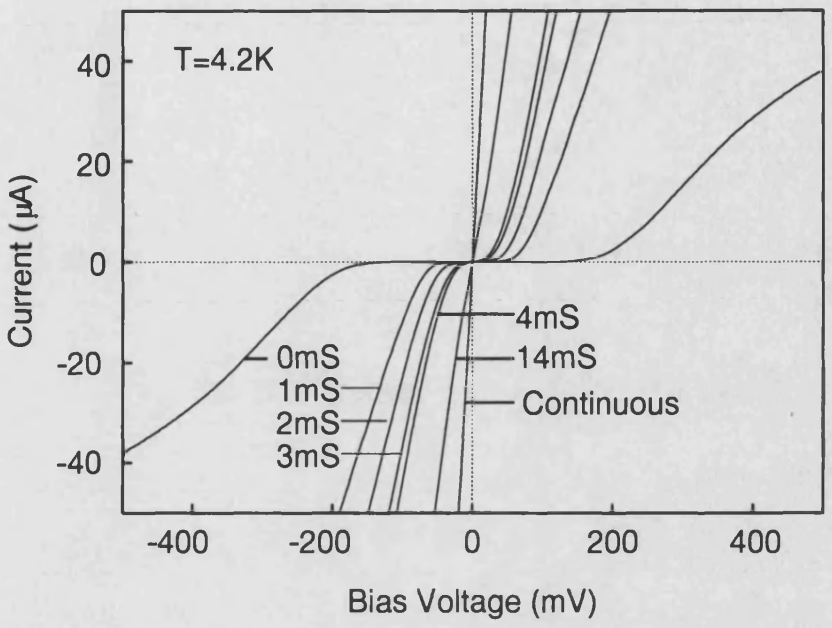

Figure 5.6: *I-V characteristics for device C under illumination. The pulse length was 1ms for the first 4 curves, increasing to 10ms (indicated) and finally continuous illumination.*

density n_{2D}. Numerical calculations from Chapter 6 indicate that donor charges in the AlGaAs layer tend to screen the 2DES from the potential at the etched surface, and that even small increases in the ionised donor concentration can result in a very strong decrease in the magnitude of the tunnelling barrier. Within this picture, a large increase in the tunnelling current would be expected, even with slight illumination of the device. Increases in n_{2D} will also act to reduce the effective barrier height since the Fermi energy will increase. Given however that illumination causes changes of $\sim 50\%$ in n_{2D}, the change in E_F ($E_F \propto n_{2D}$) will only be of the order of a few meV. Although the transmission coefficient is exponentially dependent on the position of E_F, it is difficult to see how a relatively small change, compared to a barrier height of 50meV (see Section 5.3) could be responsible for such a large increase in the tunnel

current. The origin of the relaxation in the current flow, immediately after illumination is unclear, but may be caused by re-capture at D-X centres of electrons which remain in the conduction band of the sample in the AlGaAs layer after illumination.

In summary, the influence of illumination on the properties of quantum trench diodes is believed to be dominated by changes in the ionised D-X centre concentration in the AlGaAs layer of the heterostructure.

5.3 Thermal Activation Measurements

5.3.1 The Richardson Law in 2D

Thermally activated current measurements have been used extensively for the study of potential barrier heights in semiconductor and semiconductor-metal material systems. A great deal of the early work concentrated on Schottky barriers at Si-metal and GaAs-metal interfaces (for examples see [66] and [67] respectively) and a general review of such measurements is given by Rhoderick [55]. More recently Roßmanith *et al.* [68] demonstrated how a measurement of thermally activated current could be used to investigate X-point barrier heights in $GaAs/Al_xGa_{1-x}As$ single barrier tunnelling diodes under hydrostatic pressure.

The Richardson law governing the thermally activated component of the current can be derived from the current equations discussed in Chapters 2 and 6. The expression is greatly simplified by making the approximation that for a non-zero bias voltage V, the current flow is dominated by electrons moving in the direction of the applied bias. This gives the current density flowing from the emitter to the collector for a device with 2D electrodes as

$$J = \frac{e\sqrt{2m^*}}{(2\pi\hbar)^2}\int_0^\infty\int_0^\infty [f(E) - f(E+eV)]\,T(E_x, eV)\frac{dE_x dE_y}{\sqrt{E_y}} \qquad (5.2)$$

where $E = E_x + E_y$ and E_x and E_y are the electron energies in the transport direction and parallel to the barrier respectively. Implicit in

Eqn.5.2 is the assumption that only a single occupied subband in the emitter contributes to the current. A further simplification can be obtained by ignoring the contribution to the current from tunnelling, which enables the use of the classical values for the transmission coefficients,

$$\begin{aligned} T(E_x, eV) &= 0 \qquad \text{for } E_x \leq \Phi_0 \\ T(E_x, eV) &= 1 \qquad \text{for } E_x > \Phi_0 \end{aligned} \tag{5.3}$$

for a potential barrier height Φ_0 above E_F. Combining these approximations, and positioning the Fermi energy such that $E_F = 0$, gives the activated current density for a rectangular barrier as,

$$J_{act} \approx \frac{e\sqrt{2m^*}}{(2\pi\hbar)^2} \int_0^\infty \int_{\Phi_0}^\infty exp\left[\frac{-(E_x + E_y)}{kT}\right] \frac{dE_x dE_y}{\sqrt{E_y}} \tag{5.4}$$

It is then simple to obtain the Richardson law for a device with 2D electrodes,

$$J_{act} \approx \frac{e\sqrt{m^*}}{\hbar^2} \left(\frac{kT}{2\pi}\right)^{\frac{3}{2}} exp\left[-\frac{\Phi_0}{kT}\right] \tag{5.5}$$

which shows the activated current has a $T^{\frac{3}{2}}$ dependence as opposed to a T^2 dependence for 3D electrodes. Note that in this classical picture, the activated current density is independent of the bias voltage for a rectangular barrier at high bias voltages. For the low voltage limit, the $T^{\frac{3}{2}}$ dependence in the Richardson law becomes a $T^{\frac{1}{2}}$ dependence and the thermally activated current also becomes dependent on the applied voltage.

For the high voltage limit, a measurement of the activated current over range of temperatures therefore enables the barrier height to be obtained from the gradient of a straight-line plot of $ln(J/T^{\frac{3}{2}})$ vs $1/T$.

5.3.2 Experimental Techniques

Thermally activated current measurements were made for devices B, C, D and E. The experiments were performed in a liquid He bath cryostat

with the samples mounted on a temperature controllable insert in He exchange gas at low pressure. Further thermal contact between the insert and the bath was provided by a set of copper springs which are indicated on the sketch in Fig.5.7. The temperature was set using a small resistance wire coil heater, mounted on a copper cylinder directly below the sample. The heater current was supplied by a Lakeshore Cryotronics temperature controller (Model DRC 91C) using a pre-calibrated carbon-glass temperature sensor positioned under the sample. With this method it was straightforward to achieve a temperature stability of better than $\pm$0.1K over the entire measurement range (4.2-250K). A sketch of the apparatus is shown in Fig.5.7.

The activated current was measured to an accuracy of 0.1nA over a range of temperatures, using the experimental apparatus described in section 5.2.1. Measurements were made with applied biases between 1 and 20mV for devices B and C and between 10 and 50mV for devices D and E.

5.3.3 Thermal Activation Results

Fig.5.8a) and 5.8b) are Arrhenius plots of $ln(J/T^{\frac{3}{2}})$ vs $1/T$ for devices B and C for a range of different values of the applied bias. The solid lines sketched on the plots indicate the temperature regions where the transport is dominated by thermal activation and the data obey a straight line fit. Taking the low bias limit gives values for Φ_0 of 12meV and 50meV for devices B and C respectively. At high temperature, there is a roll-off in the gradients of the plots which is attributed to the resistance of the 2DES leads in the sample ($\sim 20k\Omega$ at 200K) becoming larger than the resistance of the barrier.

The data for device B are instructive, since contrary to Eqn.5.5 they clearly indicate both a strong dependence of the gradient on the applied bias voltage *and* a non-linear dependence of $ln(J/T^{\frac{3}{2}})$ on $1/T$ in the low-

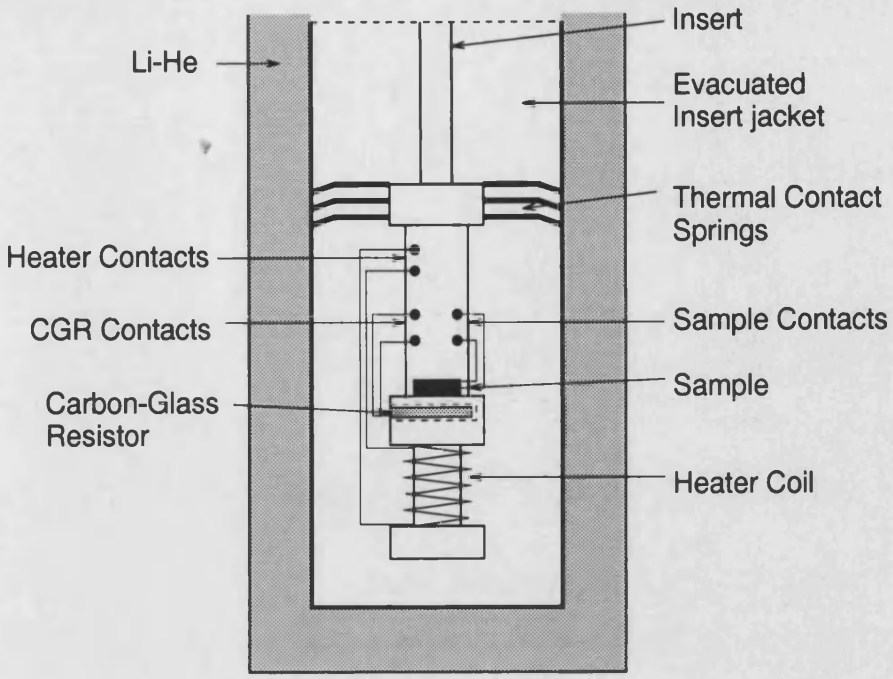

Figure 5.7: *Schematic diagram of the experimental apparatus used for controlling temperature. An explanation of the system is given in the text.*

est temperature range on Fig.5.8a). These effects both originate from a breakdown of the assumptions made in the derivation of the Richardson law which become less valid for small potential barriers. Simply speaking, this means that at low temperatures where the activated current is vanishingly small, the Richardson law can no longer be applied if $T(E_x, eV) \neq 0$ for $E_x \leq \Phi_0$ and the current flow is dominated by tunnelling. Similarly at high bias voltage ($eV \sim \Phi_0$) the tunnel current plays a significant role, and together with a reduction in the effective barrier height due to thermally assisted tunnelling near the tip, acts to reduce the gradients of the Arrhenius plots.

Fig.5.9 shows Arrhenius plots for all four devices at low applied bias. Values for Φ_0 are 12, 50, 92 and 150meV for devices B, C, D and E respectively which are consistent with the *I-V* characteristics of Fig.5.4. Note that since the barrier profiles are smooth and the barrier width is strongly correlated to the barrier height, the *I-V* characteristics cannot

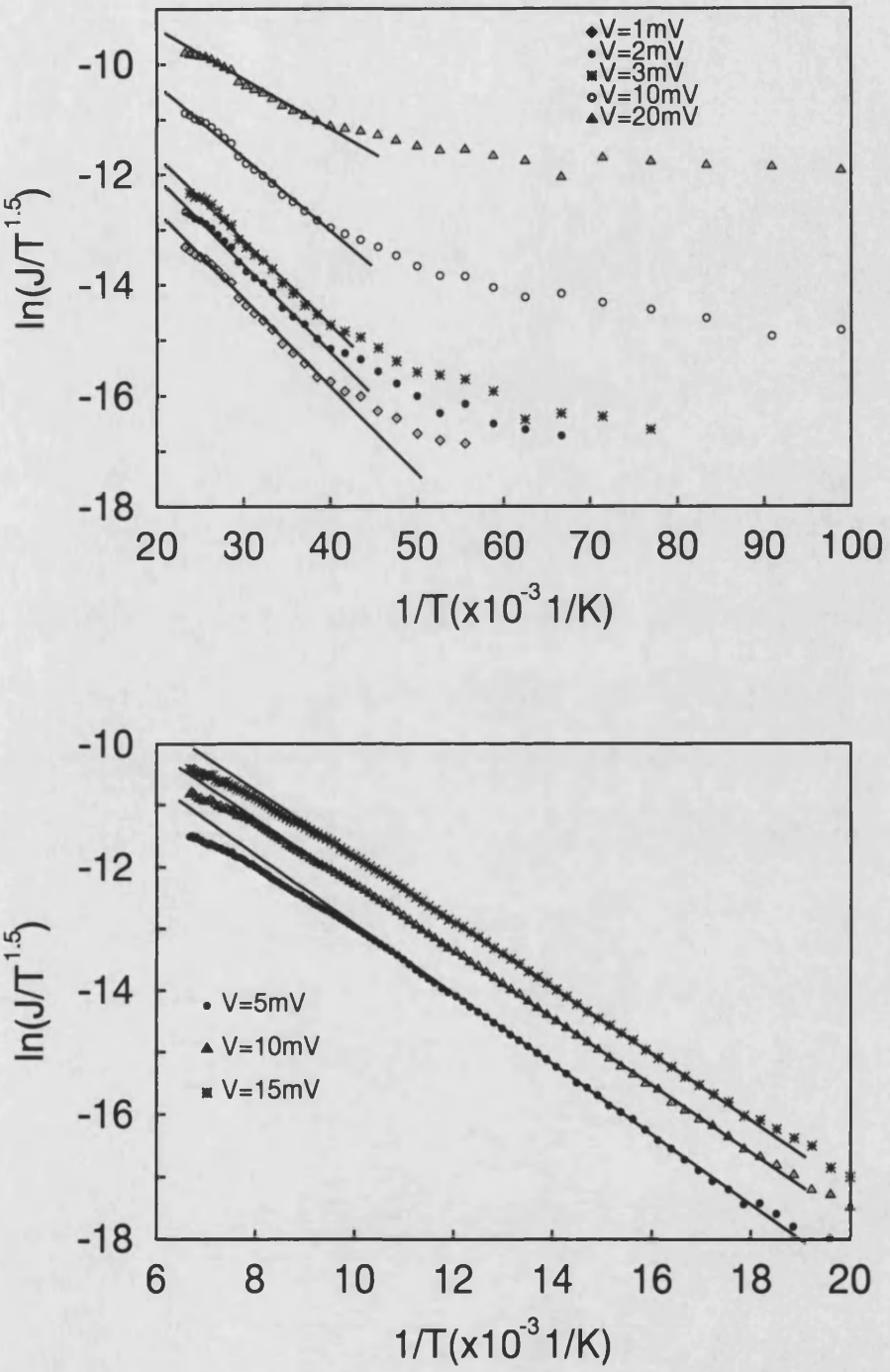

Figure 5.8: *Arrhenius plots for devices B (above) and C (below) for temperature ranges of 10-50K and 50-150K respectively. Solid lines indicate the region dominated by thermally activated transport*

be interpreted purely in terms of Φ_0.

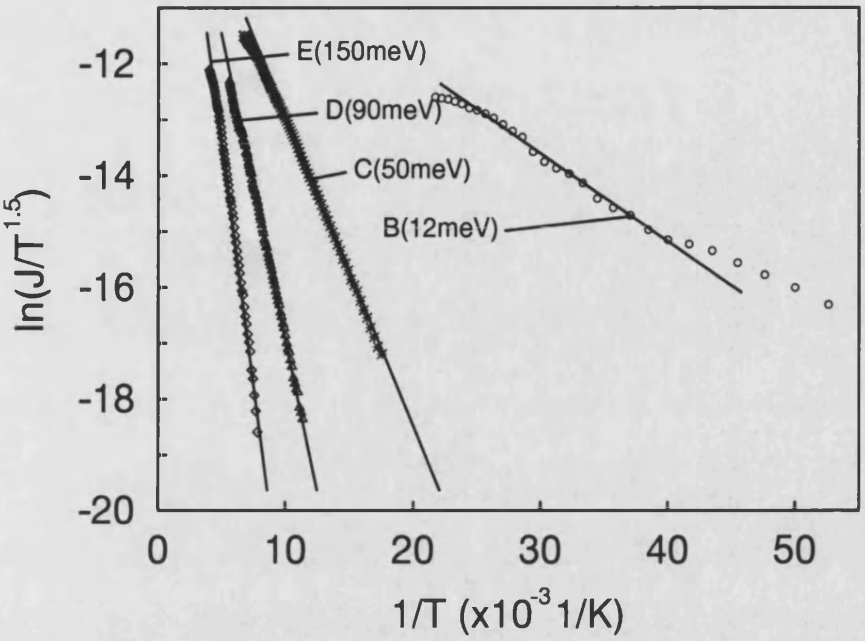

Figure 5.9: *Arrhenius plots for devices B-E in the saturated current regime. Solid lines indicate the gradients used to calculate* Φ_0

5.4 Comparison of Thermal Activation Results With Theory

5.4.1 Analysis of Quantum Trench Profiles

In order to compare the experimentally determined tunnelling barrier heights with those predicted by numerical calculations described in Chapter 6, a more detailed analysis of the trench dimensions was performed. Quantum trench widths were measured from SEM micrographs of reference structures written on unused parts of the samples. Typically, such micrographs yield feature sizes to within an accuracy of $\pm$10nm at an SEM magnification of 60000$\times$ on the system used in this work (see Section 3.3.4). When micrographs were taken directly on the real diodes,

this was found to cause a severe degradation of the 2DES mobility, thus introducing large series resistances into the devices. The exact mechanism for the damage to the 2DES is not understood and it is surprising that such an effect occurs at what are relatively low electron energies (25kV). Smith *et al.* [69] have observed similar behaviour at electron energies of around 20kV and attribute the damage to the fact that at these energies, the electrons have a penetration depth of around 100nm and thus dissipate their energy in the 2DES region.

Approximate etch depths were measured using a Dektak step pro-

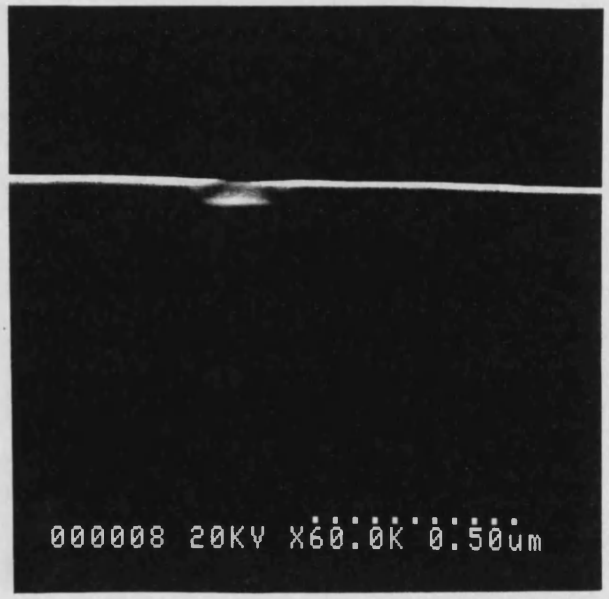

Figure 5.10: *Electron micrograph of a quantum trench on a cleaved sample*

filer on large (feature size $\sim 200\mu$m), optically defined mesa structures etched simultaneously on GaAs substrate material. To assess the accuracy of these measurements, dense, *lateral superlattice* arrays of quantum trenches (lateral spacing 10μm) were written with EBL on heterostructure samples and etched simultaneously with the GaAs references. Cleaving the heterostructures in a direction perpendicular to the trench arrays enabled SEM micrographs to be taken of the quantum trenches *end-on*.

Fig.5.10 shows an SEM micrograph of a single trench on a cleaved sample. The trench depth is estimated to be 50nm compared to a Dektak step height of roughly 70nm on the GaAs reference mesas. Measurements on a range of cleaved samples indicate that as a rough guide, step heights obtained from the GaAs reference mesas overestimate the trench depth by about 30%. This is reasonable given the contrasting lateral dimensions between the trenches and the reference mesas and to a lesser extent the chemical differences between the two materials. The trench depths given at the beginning of the Chapter for devices A-E were all estimated in this fashion.

The micrograph in Fig.5.10 also indicates that the trench profile is trapezoidal as opposed to rectangular. This is a common result of RIE, and occurs as the resist, remaining at the trench edges, is slowly removed during the etching process, allowing an increasingly wide area of the sample to be attacked.

5.4.2 Comparison of Barrier Heights

Chapter 6 details a numerical simulation of the quantum trench structure, based on a finite difference form of the Poisson equation. The calculations supply subband energy profiles (tunnelling barriers) in the plane of the 2DES from which it is straightforward to obtain values for the barrier heights above E_F. Simulations were made for a range of quantum trench depths, spanning the values estimated for the five devices A-E. The trench width was taken to be 40nm in all cases and rectangular trench profiles were used.

On Fig.5.11, the calculated and measured barrier heights are plotted as a function of the trench depth. Note the change in nomenclature for the barrier height, $E_0(0) \equiv \Phi_0$. The calculated results predict the correct trend of increasing barrier height with trench depth, but the agreement with experimental values is poor. The source of the discrepancy prob-

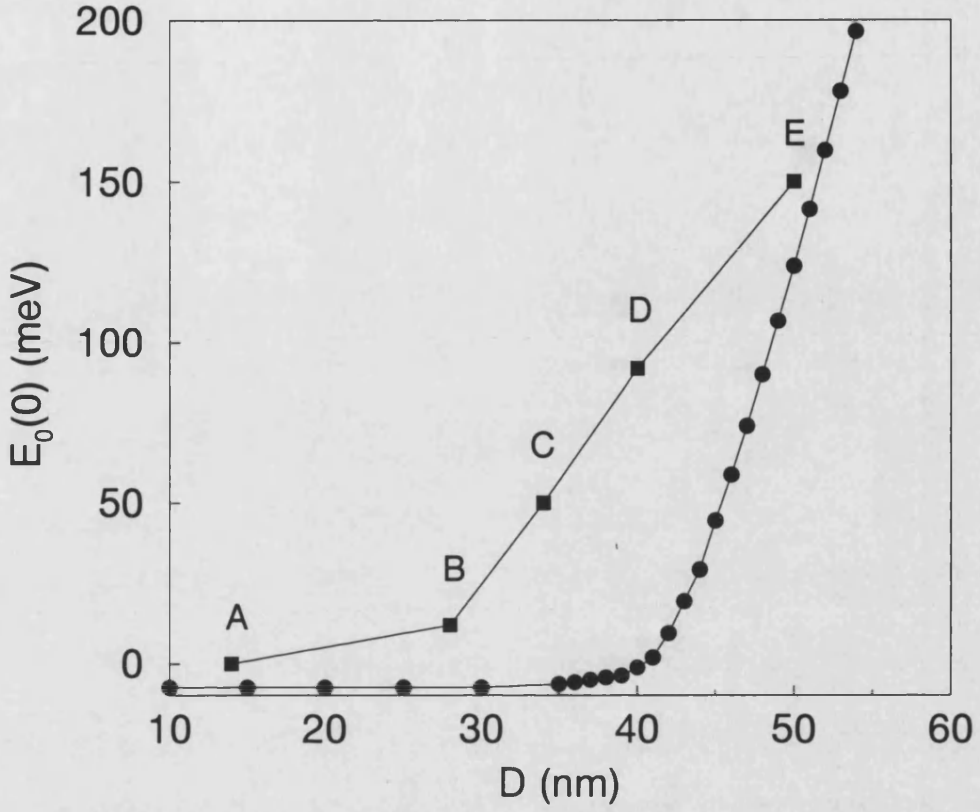

Figure 5.11: *Comparison of measured (squares) and calculated (circles) barrier heights for a range of quantum trench devices.*

ably lies both in the trench depth values assumed for the experimental devices and the choice of trench profile used in the calculation. The discussion in Section 5.4.1 demonstrates the problems involved in accurately determining both the size and shape of the quantum trench, which are clearly important parameters in the numerical simulation. In the following Chapter, a detailed comparison is made between experimental and calculated *I-V* characteristics. To avoid this problem with determining the real trench dimensions a simple fitting procedure is used for the trench depth to produce good agreement between experimental and calculated barrier heights.

5.5 Conclusions

To conclude, a range of characterisation data has been presented on a novel type of single barrier lateral tunnelling diode. The diodes were fabricated by reactive ion etching nanometre scale quantum trenches into the surface of a GaAs/AlGaAs modulation doped heterostructure. Five, 40nm wide (in the tunnelling direction) devices were studied with estimated trench depths of 14, 28, 34, 40 and 50nm. Current-voltage characteristics for all but the 14nm deep trench are very non-linear, and an increase in the trench depth results in a strong reduction in the current. The devices were found to be highly sensitive to illumination, which caused a very strong increase in the current, equivalent to a strong reduction in the size of the barrier. The influence of illumination is attributed to the ionisation of deep states in the AlGaAs layer of the heterostructure, which tend to screen the 2DES from the potential at the etched surface.

Thermal activation experiments were performed on the four non-linear devices and a fit of the activated current to a 2D form of the Richardson law indicated barrier heights above E_F of 12, 50, 92 and 150meV respectively. A numerical simulation of the devices, based on the Poisson equation strongly underestimates the size of the barrier for particular trench depths which is probably due to the assumptions made about the trench dimensions.

6 Numerical Modelling of Quantum Trench Diodes

6.1 Introduction

The physical complexity of semiconductor devices based on modulation doped heterostructures has hindered the development of theoretical models designed to simulate their electrical characteristics. Ideally, any such model should begin with a calculation of the band structure potential profile of the structure, for which the most common approach involves numerically solving the Poisson (PE) and Schrödinger equations (SE) self-consistently. In other words, this system of equations is mutually dependent; the electron wave function from the SE is required for a PE solution to the electrostatic potential at the 2DES and *vice versa.*

Clearly for a real device, where it may be necessary to consider the potential in all three dimensions, such a calculation is not only difficult to set up but may require excessive computing time. In spite of this, some notable advances have been made on the modelling of quantum point contacts [70], etched quantum wires [71] and on a range of quantum dot problems [72,73]. In [74], quantum wires are described using a purely analytical solution to the PE. This is enabled by considering the limiting case of a few confined electrons which removes the need for a self-consistent solution including the SE. Finally a numerical 2D solution to the PE, treating the 2DES as a sheet of charge with the experimentally determined charge density has been successfully implemented to describe a gated lateral tunnelling diode [57].

In this chapter, a model of the single barrier quantum trench tunnelling diode is presented. The motivation for producing such a model is many-fold. Not only does it provide support for the experimental data described in Chapter 5, but also forms a basis for many further calculations such as those predicting the device properties in a magnetic field.

Furthermore, the model has been developed in a very general form, and can in principle be applied to any device based on a heterojunction sample.

Fig.6.1 shows a schematic representation of an idealised quantum

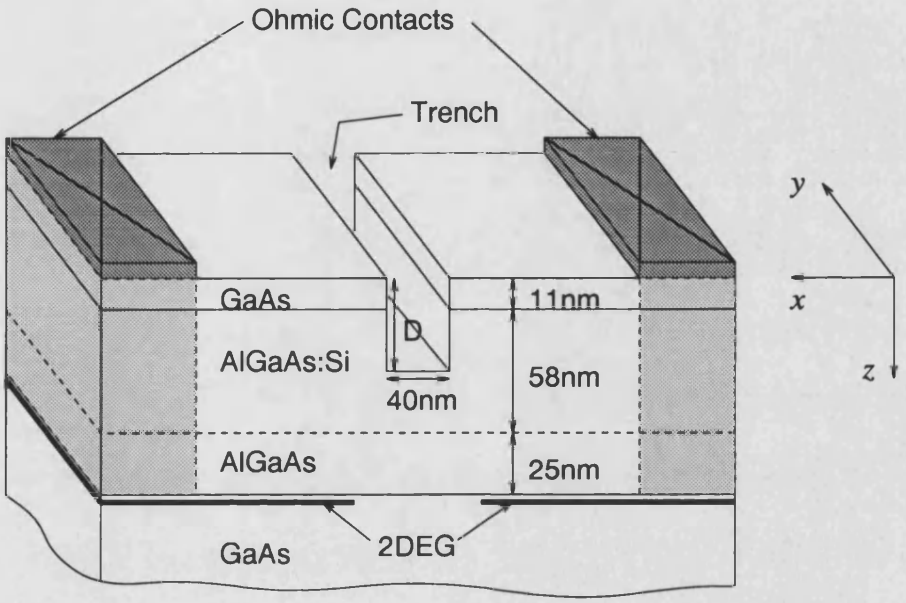

Figure 6.1: *Schematic diagram of an idealised quantum trench tunnelling diode.*

trench diode which is essentially identical to the experimental devices described in Chapter 5. The trench is assumed to be 40nm wide in the tunnelling direction throughout these calculations and is etched into the surface of the sample to a depth D.

A general outline of the model is as follows. A numerical solution of the PE is used to calculate the conduction band edge potential profile of the structures and thus to deduce the tunnelling barrier potential at zero applied bias. The electronic charge in the 2DES is taken to be distributed according to a Fang-Howard variational wave function [35] which removes the need for a self-consistent solution to the PE and SE. This is a relatively common approximation, used by a number of previous authors [73,75]. Zero temperature is assumed in all the calculations.

A further significant simplification to the problem is obtained by assuming that the trench is infinitely long in the $y-$direction, reducing the problem to only two dimensions; the growth direction (z) and the tunnelling direction (x).

Taking the calculated barrier profile as a starting point, the model is then extended to include the effect of a bias voltage across the device. Previous authors have approached this problem by assuming a linear drop of the applied potential (in the $x-$direction) across the depletion region of the device. This method represents a good approximation in the regime where the applied voltage is small compared to the tunnelling barrier height, but strongly overestimates the rate of decrease in the size of the barrier at increasingly higher bias voltages [57]. In this work, the tunnelling barrier profiles under applied voltages are calculated within the framework of the model described above, i.e. *the profiles are still solutions of the PE.*

Subsequent application of standard tunnelling theory using a WKB approximation (see Chapter 2) yields model I-V characteristics for diodes with different fabrication parameters.

Finally, the calculations are compared with experimental results and the performance of the model is evaluated in light of the approximations made.

6.2 Theory

6.2.1 Potential Profiles

To calculate the conduction band edge potential profile $\phi(x,z)$, a finite difference method is used to solve the Poisson equation,

$$\nabla^2\phi(x,z) = \frac{-\rho(x,z)}{\epsilon_0\epsilon_r(x,z)} \tag{6.1}$$

where $\rho(x,z)$ is the charge per unit volume and $\epsilon_r(x,z)$ is the relative dielectric constant (12.2 for GaAs and 13.2 for $Al_{0.3}Ga_{0.7}As$) at coordinates

(x, z) (see Fig.6.1). The potential surface of interest is considered as a 2D grid of discrete points with indices (i, j) corresponding to positions (x, z) and a cell size Δ (sketched in Fig.6.2). Considering a point (i, j),

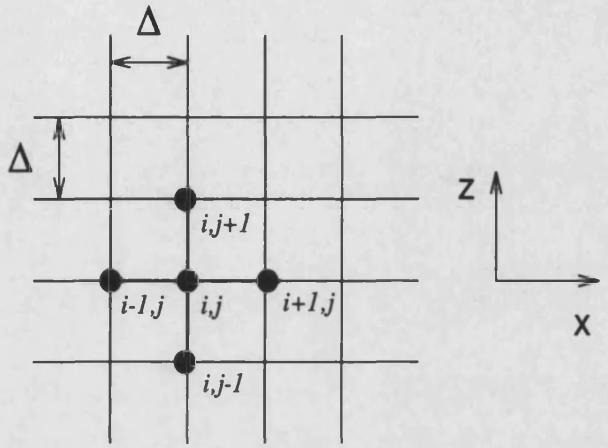

Figure 6.2: *Grid notation used for the finite difference solution to the PE*

the first derivative of the potential along the x-direction line connecting (i, j) with $(i + 1, j)$ can be written,

$$\frac{\partial \phi}{\partial x} \approx \frac{\phi_{i+1,j} - \phi_{i,j}}{\Delta} \tag{6.2}$$

whereas between (i, j) and $(i - 1, j)$,

$$\frac{\partial \phi}{\partial x} \approx \frac{\phi_{i,j} - \phi_{i-1,j}}{\Delta}. \tag{6.3}$$

The same argument applied to Eqn.6.2 and 6.3 gives the second derivative,

$$\begin{aligned} \frac{\partial^2 \phi}{\partial x^2} &\approx \frac{(\phi_{i+1,j} - \phi_{i,j})/\Delta - (\phi_{i,j} - \phi_{i-1,j})/\Delta}{\Delta} \\ &= \frac{\phi_{i+1,j} + \phi_{i-1,j} - 2\phi_{i,j}}{\Delta^2} \end{aligned} \tag{6.4}$$

Similarly in the z-direction,

$$\frac{\partial^2 \phi}{\partial z^2} \approx \frac{\phi_{i,j+1} + \phi_{i,j-1} - 2\phi_{i,j}}{\Delta^2}. \tag{6.5}$$

Combining Eqn.6.4 and 6.5 with the PE, gives the finite difference form of the PE in 2D,

$$\phi_{i+1,j} + \phi_{i-1,j} + \phi_{i,j+1} + \phi_{i,j-1} - 4\phi_{i,j} = \frac{\rho(i,j)\Delta^2}{\epsilon_0\epsilon_r(i,j)} \qquad (6.6)$$

Rearranging Eqn.6.6 results in an expression for the potential at any point on the grid in terms of its 4 neighbours and the charge $\rho(i,j)$ present in the volume Δ^3.

$$\phi_{i,j} = \frac{\phi_{i+1,j} + \phi_{i-1,j} + \phi_{i,j+1} + \phi_{i,j-1}}{4} - \frac{\rho(i,j)\Delta^2}{4\epsilon_0\epsilon_r(i,j)} \qquad (6.7)$$

A grid size of $500\times2000\text{nm}^2$ was used with a cell size Δ =1nm in the active layers of the heterostructure, rising to Δ =10nm in the substrate. The following assumptions were made about the boundary conditions (BC's) at the edges of the iteration grid;

(i) For both GaAs and AlGaAs(trench) exposed surfaces, the Fermi level E_F is pinned near the middle of the forbidden gap, i.e. $\phi(x, z = z_{surf}) = 0.8eV(1.1eV)$ for GaAs(AlGaAs) with no applied bias.

(ii) The electric field $(d\phi(x,z)/dz) \rightarrow 0$ as $z \rightarrow \infty$ due to charge neutrality in the substrate.

(iii) In the lateral (x) direction far from the trench, the electric field $(d\phi(x,z)/dx) \rightarrow 0$ as $x \rightarrow \pm\infty$ as is the case for a homogeneous 2DES.

Condition (i) is simply stating that at all the exposed surfaces, the Fermi energy becomes pinned at the energy of the surface states which for GaAs/AlGaAs sit roughly at the middle of the forbidden gap. Thermal activation experiments on Schottky barrier diodes generally indicate a barrier height (position of $\phi(x, z = z_{surf})$) of about 0.8eV [55] above E_F for GaAs.

The second condition ensures that the electric field deep in the substrate is zero, which is expected for a homogeneous semiconductor. Finally, in the $\pm x$−direction, far from the trench, the potential feels no

influence from the trench and is thus simply that of an un-etched heterostructure.

The space charge present in the device falls into two distinct categories; fixed charges, localised either at Si donors in the AlGaAs layer or at p-type background impurities in the GaAs buffer, and 'free' electrons confined to the 2DES. Clearly, depending on the position of E_F in the layers, donor and acceptor impurities will be either ionised or neutral. In order to take into account these inhomogeneities in the distribution of ionised impurities which occur in both x- and z-directions, an approach similar to that of Lier *et al.* [73] is used. The approximation is made that all Si donors exist as deep states (D-X centres) [76] lying at an energy E_d, 120meV below the AlGaAs conduction band edge. Thus the states are neutral if E_d lies below E_F and represent positive charges if E_d lies above E_F. The situation is summarised in Eqn.6.8 ,

$$\rho_{n-al}(x,z) = \begin{cases} 0 & \text{if } E_d < E_F \\ \rho_d/2 & \text{if } E_d = E_F \\ \rho_d & \text{if } E_d > E_F \end{cases} \tag{6.8}$$

where $\rho_{n-al}(x,z)$ is the charge density in the AlGaAs layer and ρ_d is the Si doping density (taken to be $1\times10^{18}\text{cm}^{-3}$). Thus values for $\rho_{n-al}(x,z)$ are re-calculated after each iteration of $\phi(x,z)$. A similar scheme is used to describe the non-intentionally-doped p-type GaAs buffer for which a density of $1\times10^{14}\text{cm}^{-3}$ and an acceptor binding energy of 1.5eV below the GaAs conduction band edge are assumed. Fig.6.3 shows a sketch of the valence and conduction band edges of the structure in the z-direction, indicating the energy positions of both donor and acceptor levels.

The electron density in the 2DES is modelled using a Fang-Howard variational function which is normalised to the total electron density n_{2D}^0 ($n_{2D}^0 = 2.5\times10^{11}cm^{-2}$) obtained from Shubnikov-de Haas measurements

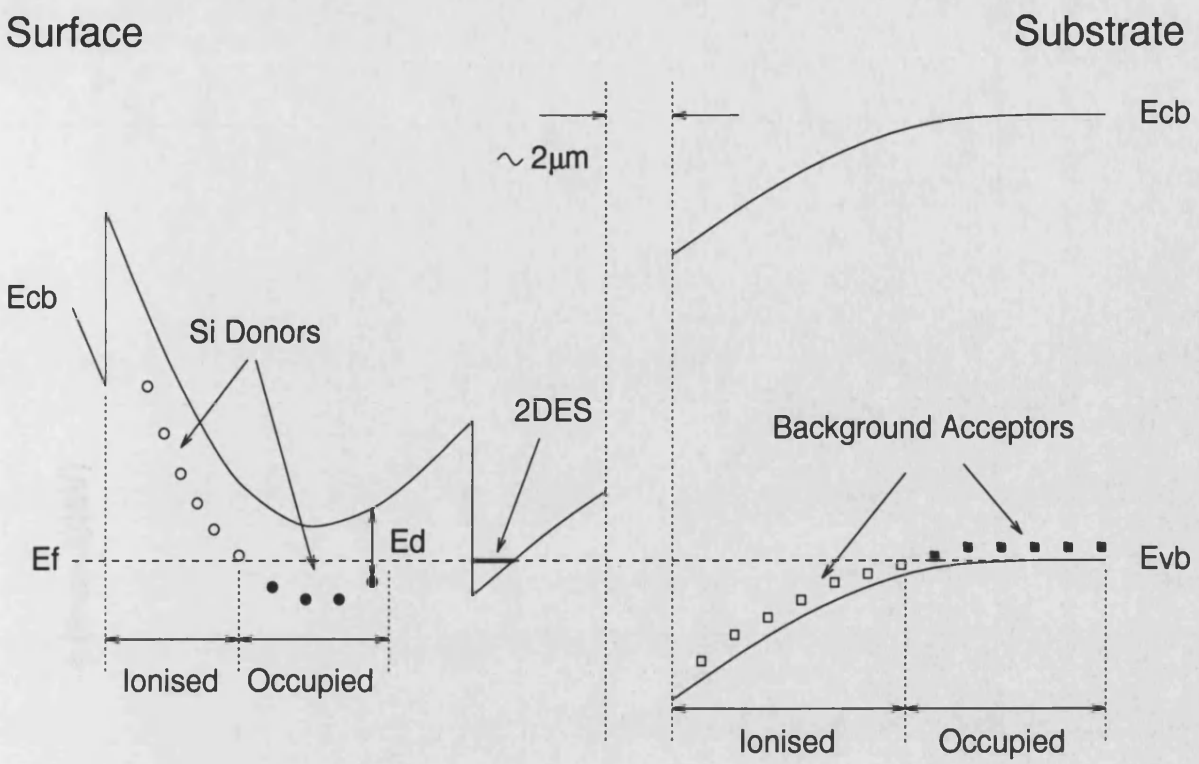

Figure 6.3: *Sketch of the donor and acceptor energy positions in the structure. The left hand portion of the figure shows only the conduction band edge energy E_{cb} near the sample surface, and indicates areas where deep Si donors are either ionised (representing positive charges) or occupied (neutral). The right hand portion of the figure shows E_{cb} and the valence band edge energy E_{vb} on the substrate side, deep in the sample. Here acceptors are ionised (representing negative charges) when below the Fermi energy E_F and occupied (neutral) when above E_F.*

(Chapter 2). Far from the trench, the electron density is given by,

$$n(x = \infty, z) = \frac{n_{2D}^0}{d^2} z exp(-z/d) \tag{6.9}$$

such that

$$\int_{-\infty}^{\infty} n(x = \infty, z) dz = n_{2D}^0. \tag{6.10}$$

where d (d =5nm) describes the half-width of the distribution. The resulting electron density as a function of z is shown in the inset of

Fig.6.4a).

Fig.6.4a) and b) show plots of the calculated $z-$direction conduction

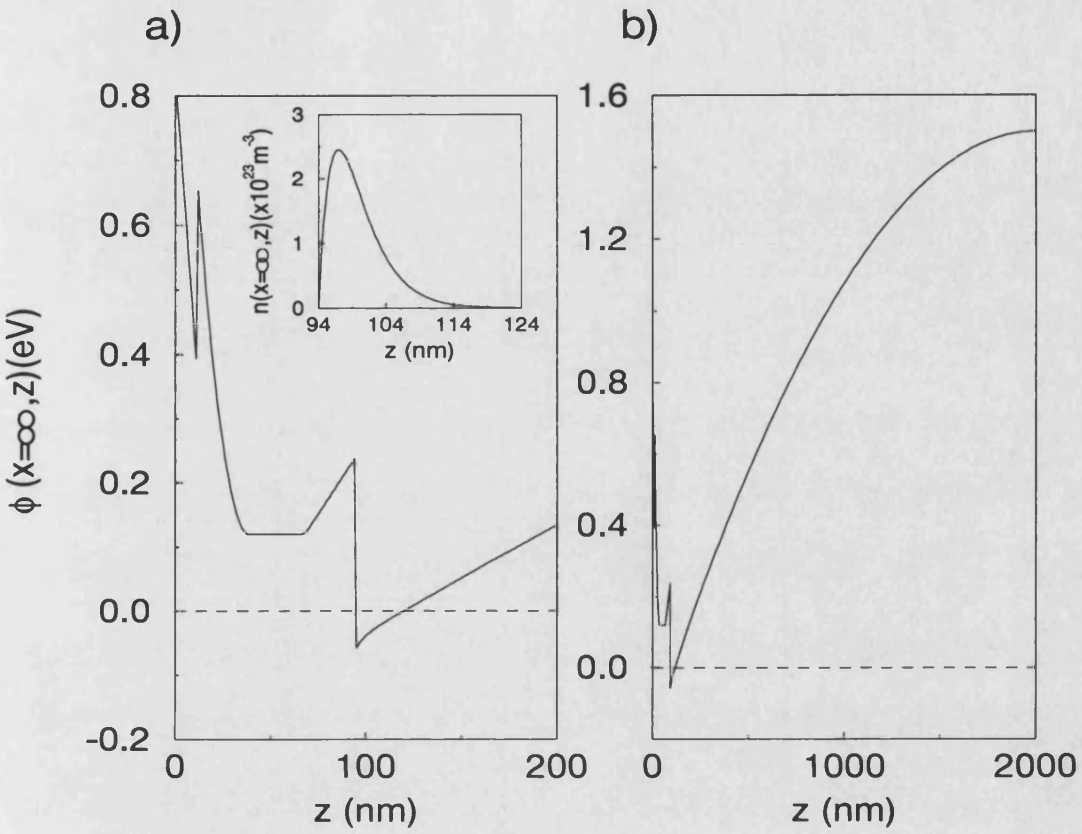

Figure 6.4: *a). Conduction band edge profile in the z-direction for a structure before etching. Inset shows the electron density distribution in the 2DES derived from a Fang Howard variational function, normalised to the experimentally determined electron concentration. b). The same energy profile over the entire calculated z range.*

band edge profile of a structure before etching. The flat portion of the potential in the doped AlGaAs region is a result of E_F becoming pinned at the Si D-X centre energy and its width is strongly influenced by the value chosen for the total Si donor concentration. The boundary conditions (i) and (ii) for the surface and substrate of the sample are also clearly seen on these plots.

This $z-$direction profile, mapped into a 2D field, is used as an initialisation for the calculation, and with E_F pinned at mid-gap where the new surfaces have been exposed by etching, solutions for $\phi(x,z)$ are iterated until convergence. Typical computing times for each trench depth were of the order of 300 minutes, using Fortran on a DEC 5000 workstation. Convergence was assumed when successive iterations yielded changes in $\phi(x,z)$ of less than 0.01meV at any point on the grid.

In areas where the band bending caused by the exposed trench sur-

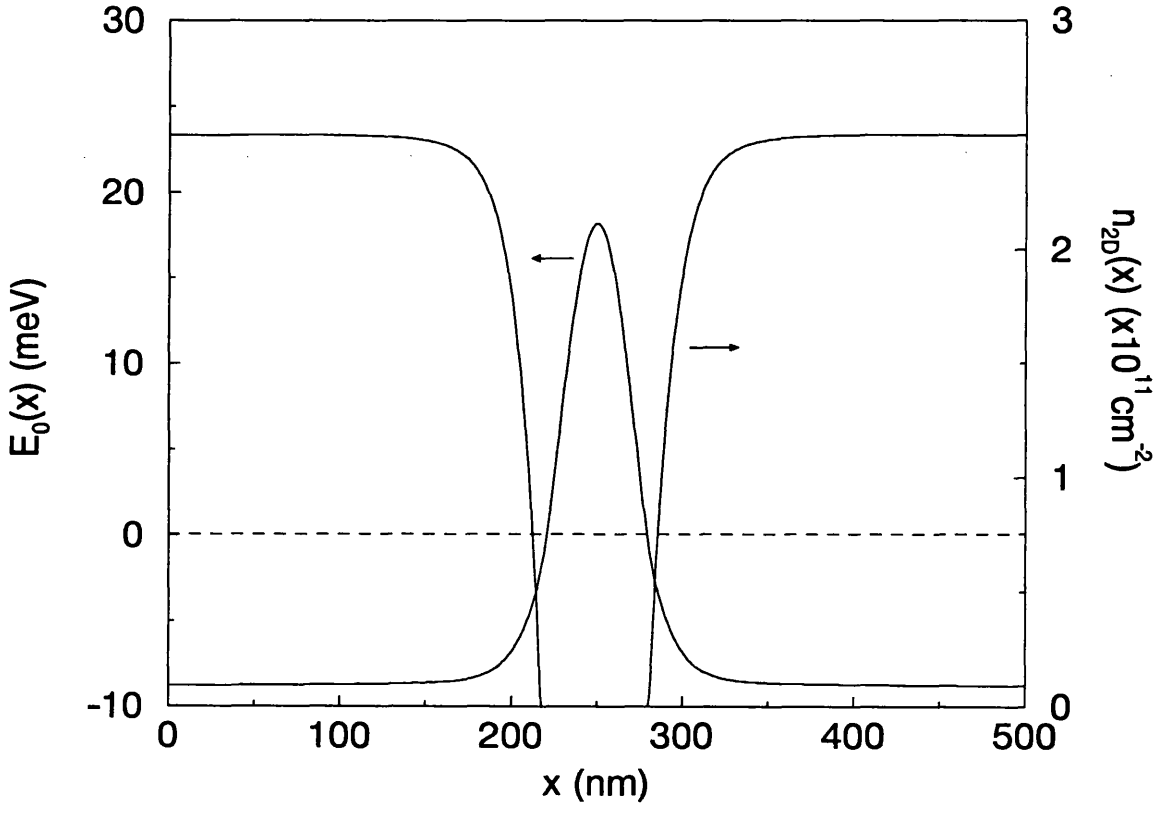

Figure 6.5: *Calculated electron density in the 2DES $n_{2D}(x)$ and subband energy profile (tunnelling barrier) $E_0(x)$ as a function of lateral distance x. The dashed line indicates the position of the Fermi energy E_F for the left hand axis. The 2DES is totally depleted ($n_{2D}(x) = 0$) in the region where $E_0(x) > E_F$.*

face results in an increase in the conduction band edge potential at the 2DES, $n(x, z)$ is sharply reduced. In the absence of a self-consistent solution to the SE, this effect is modelled using a simple algorithm based on the following assumptions.

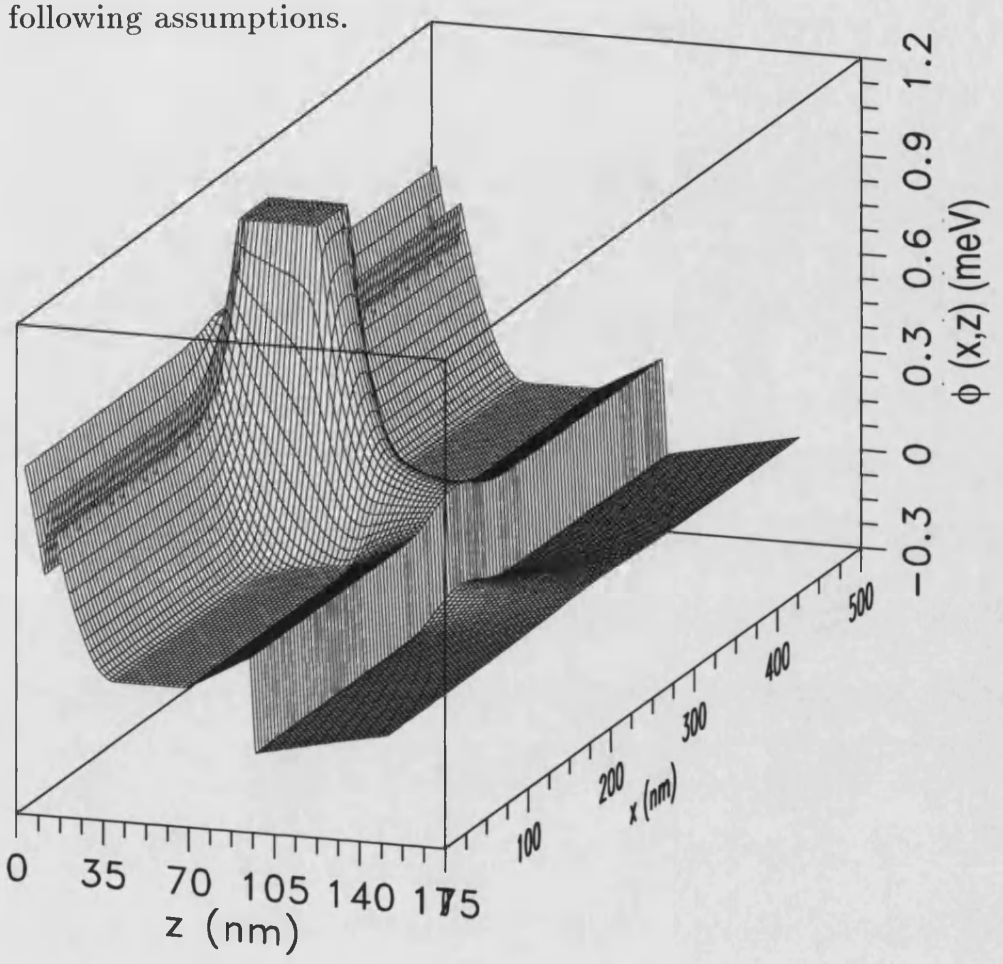

Figure 6.6: *Surface plot of the conduction band edge energy in the $x-$ and $z-$directions.*

Firstly, the energy difference between the conduction band edge potential at the interface, $\phi(x, z_i)$ and the first subband energy $E_0(x)$ is assumed constant. Simply speaking, this means that the subband profile (tunnelling barrier) mirrors the conduction band profile at the

GaAs/AlGaAs interface. Such an approximation is valid providing changes in $\phi(x, z_i)$ occur on a length scale which is large compared to the size of the electron wave-function d. The second assumption is that only one 2D subband is occupied and that the density of states is an energy independent constant. Consequently, as $E_0(x)$ increases, the local electron density $n(x, z)$ can be reduced linearly according to the following scheme,

$$n(x,z) = n(x=\infty,z)\frac{(E_F - E_0(x))}{(E_F - E_0(x=\infty))}\Theta(E_F - E_0(x)) \qquad (6.11)$$

where the step function Θ forces the density to zero if the subband energy exceeds E_F. Fig.6.5 shows the total electron density in the 2DES $n_{2D}(x)$ (where $n_{2D}(x) = \int_0^\infty n(x,z)dz$) for a model device with a trench depth $D = 43$nm.

In the following discussion, the length of the trench (in the tunnelling direction, x) is fixed at 40nm. Fig.6.6 shows a typical conduction band edge energy surface plot for a 46nm deep trench. A feature clearly seen on this plot is the steep rise in $\phi(x, z)$ in the Si doped region beneath the trench, centred around $x = 0$. Indeed the magnitude of the potential modulation in the 2DES is highly sensitive to the concentration of donors in the AlGaAs layer. Fig.6.7 shows a set of plots of the subband energy $E_0(x)$ as a function of the trench depth D. The corresponding barrier height $E_0(0)$ and the width at the Fermi energy W_{E_F} are plotted in Fig.6.8 and indicate a barrier of rapidly increasing size for trench depths greater than $\sim$ 40nm. Note that the existence of a true barrier only for etch depths greater than $\sim$ 40nm is also observed experimentally (see Chapter 5).

6.2.2 Potential Profiles Under Bias

The application of a bias voltage V to the structure involves a redefinition of the BC's at the edges of the iteration grid. Clearly, far from the

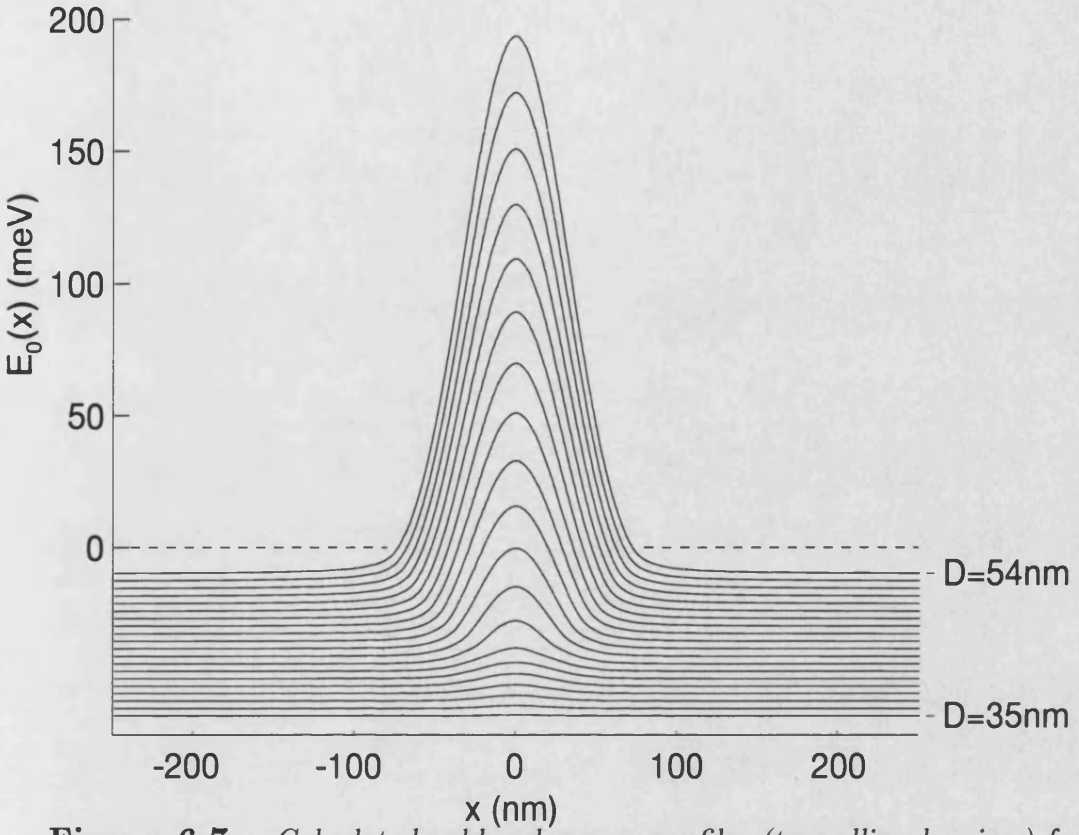

Figure 6.7: *Calculated subband energy profiles (tunnelling barriers) for devices with trench depths from 35 to 54nm (in 1nm steps). The curves have been offset on the y-axis for clarity. The dashed line indicates the position of the Fermi energy for the uppermost (D=54nm) curve.*

trench in the $\pm x$-direction, the z-direction profiles must be identical, but shifted in energy by eV. Consequently, the surface (substrate) boundary conditions must also vary through the structure with some distribution of the applied voltage. One self-consistent solution to this problem is to shift the surface (substrate) pinning energies after each iteration by the same amount as the change in the 2D subband energy at the point x.

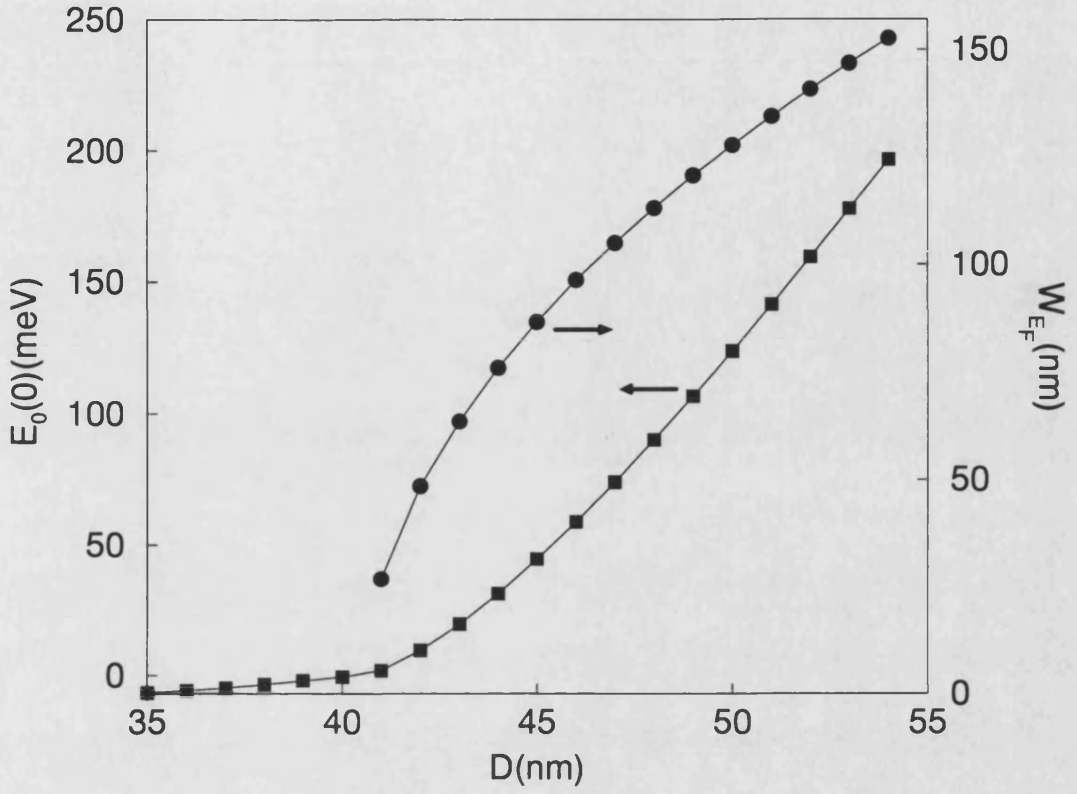

Figure 6.8: *Potential barrier height $E_0(0)$ and width at the Fermi energy W_{E_F} as a function of the trench depth D.*

i.e. for the surface,

$$\phi^{k+1}(x, z_{surf}) = \phi^{k}(x, z_{surf}) + (E_0^{k+1}(x) - E_0^{k}(x)) \tag{6.12}$$

where k represents the k^{th} iteration. The un-biased 2D solution is taken as a starting point, with an additional piecewise linear potential drop in the $x-$direction which is initially assumed to fall across the trench region. The finite element PE is then iterated once again to convergence (as with the $V = 0$ case). Convergence is defined as when $E_0^{k+1}(x) - E_0^{k}(x)$ tends to zero and a stable solution is achieved that satisfies the BC's (computing time $\sim$ 200 minutes for each bias value for the convergence criterion used for zero bias). One problem that re-

mains is a description of the distribution of ionised impurities through the structure which will be meta-stable for $V \neq 0$. It is however generally accepted that the emission and capture rates of electrons at D-X centres are extremely slow in the temperature regime where the devices are measured. For this reason the zero bias distribution of ionized D-X centres was used to model the device under bias.

Fig.6.9 shows calculated subband profiles for the 46nm deep trench

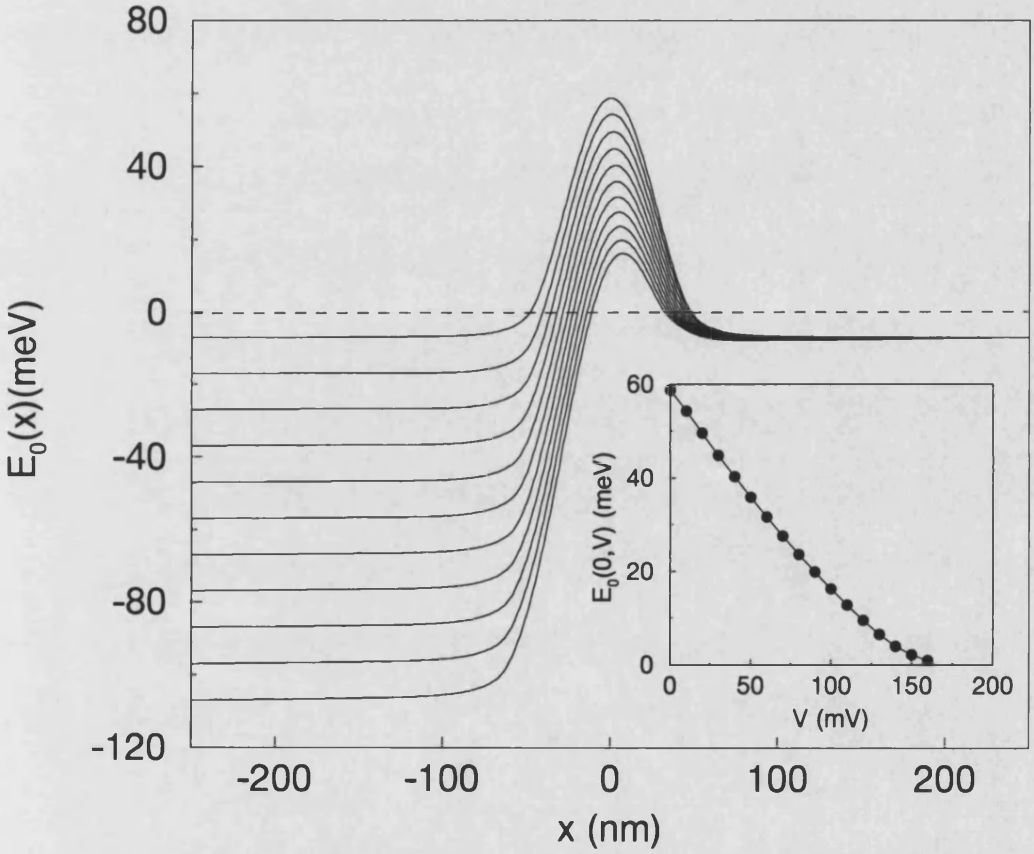

Figure 6.9: *Subband energy profiles $E_0(x)$ for a structure with a 46nm deep trench with applied biases from 0 (uppermost curve) to 100mV (lowest curve). The dashed line indicates the position of E_F in the emitter. Inset shows the barrier height ($E_0(0,V)$) above E_F for applied biases up to 160mV.*

with applied biases from 0 to 100mV in 10mV steps. Significantly, al-

though both barrier height and width are strongly reduced with increasing bias voltage, a tunnelling barrier still exists for applied bias voltages substantially in excess of the zero bias barrier height $E_0(0)$.

6.2.3 Tunnel Currents

The transmission coefficients $T(E_x, eV)$ are evaluated for the calculated profiles using the WKB approximation described in Chapter 2. The transmission coefficient was given as,

$$T(E_x, eV) \approx \exp\left(-2d\left(\frac{2m^*}{\hbar^2}\right)^{\frac{1}{2}}\sum_{l=1}^{p}(\xi_l - E_x)^{\frac{1}{2}}\right) \tag{6.13}$$

for any numerically defined barrier potential, sub-divided into p rectangular components with individual barrier heights ξ_l. The tunnelling current density per unit length, J is then evaluated from,

$$J = \int_{-\infty}^{+\infty} S(E_x)T(E_x, eV)dE_x \tag{6.14}$$

where $S(E_x)$ is the supply function and defines the number of electrons with an energy near E_x available for tunnelling (see Chapter 2). The form of $S(E_x)$ can be derived by considering the ideal rectangular potential profile shown in Fig.6.10. For 2D electrodes, the current J_{rl} flowing from right to left can be written in terms of the probability of a state on the right being occupied, and a state on the left being empty. i.e.

$$J_{rl} = \int_{-\infty}^{\infty}\int_{-\infty}^{\infty} \frac{-2edk_xdk_y}{(2\pi)^2} v_x f(E)[1 - f(E + eV)]T(E_x, eV) \tag{6.15}$$

similarly for the current from left to right,

$$J_{lr} = \int_{-\infty}^{\infty}\int_{-\infty}^{\infty} \frac{-2edk_xdk_y}{(2\pi)^2} v_x f(E + eV)[1 - f(E)]T(E_x, eV) \tag{6.16}$$

where

$$f(E) = \frac{1}{1 + exp\left(\frac{E-E_F}{kT}\right)} \tag{6.17}$$

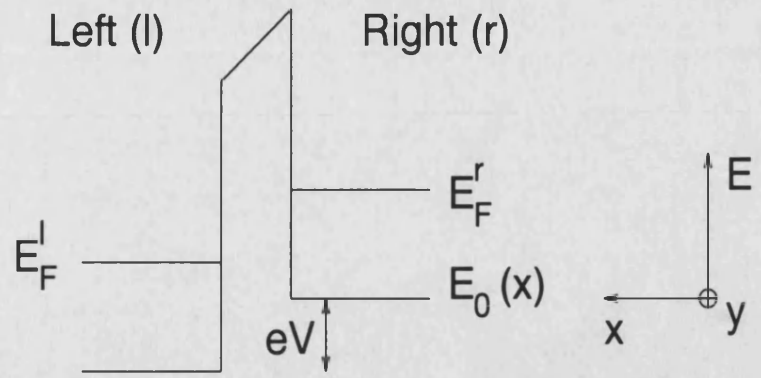

Figure 6.10: *Sketch of an ideal square barrier potential under an applied bias V. The subband energy $E_0(x)$ on the right-hand side of the barrier is defined as zero potential for the calculation and the $y-$direction runs into the page.*

and v_x is the $x-$directed electron velocity. The set of equations 6.15-6.17 are the analogue of Eqn.2.7 in Chapter 2 for 3D electrodes.

Since parallel momentum k_y and total energy E are conserved in the tunnelling process, the first differential of k_y can be written in terms of the parallel energy dispersion,

$$dk_y = \sqrt{\frac{2m^*}{\hbar^2}} \frac{dE_y}{2\sqrt{E_y}} \tag{6.18}$$

and the group velocity in the tunnelling direction from the energy in the tunnelling direction,

$$v_x = \frac{1}{\hbar} \frac{\partial E_x}{\partial k_x} \tag{6.19}$$

By substituting Eqn.6.18 and 6.19 into Eqn.6.15 and 6.16, the total current $J = J_{rl} - J_{lr}$ can be written,

$$J = \frac{e}{\hbar(2\pi)^2} \sqrt{\frac{2m^*}{\hbar^2}} \int_{-\infty}^{\infty} \int_{-\infty}^{\infty} [f(E_x + E_y) - f(E_x + E_y + eV)] T(E_x, eV) \frac{dE_y dE_x}{\sqrt{E_y}} \tag{6.20}$$

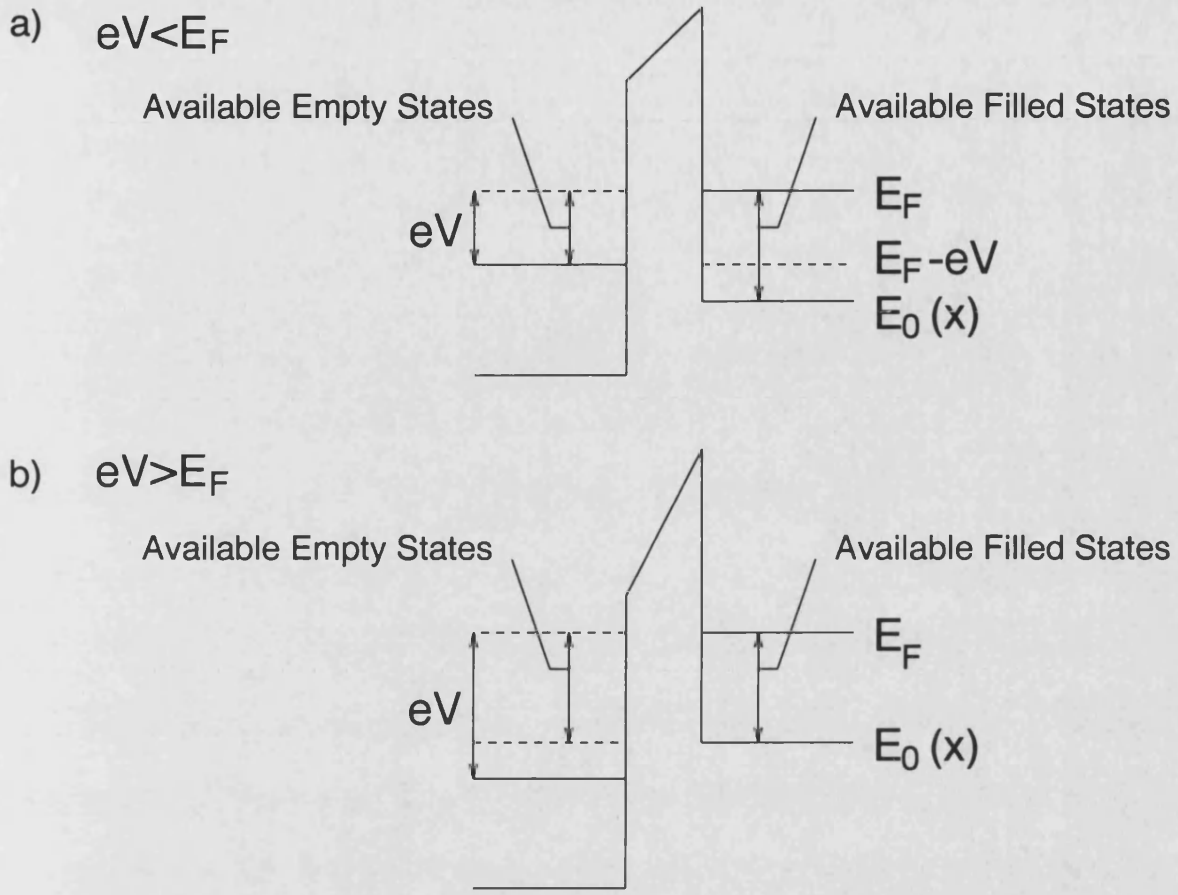

Figure 6.11: *Ideal tunnelling barrier potential profiles for a) the case $eV < E_F$ where the energies of filled states in the emitter and collector overlap, and b) for the case $eV > E_F$ where there is no overlap.*

which implies the supply function,

$$S(E_x) = \frac{e}{\hbar(2\pi)^2}\sqrt{\frac{2m^*}{\hbar^2}}\int_{-\infty}^{\infty}[f(E_x+E_y)-f(E_x+E_y+eV)]\frac{dE_y}{\sqrt{E_y}} \quad (6.21)$$

At this point the 2D nature of the tunnelling problem is accounted for in the integration of the supply function $S(E_x)$ where the parallel energy E_y is one dimensional (as opposed to being two dimensional for vertical tunnelling problems). Solving Eqn.6.21 for the supply function is drastically simplified by the assumption of zero temperature since the Fermi functions $f(E_x + E_y)$ and $f(E_x + E_y + eV)$ can only take values of 1 or 0. Thus, $S(E_x)$ must be obtained separately for the two bias volt-

age regimes for which either some or no energy overlap exists between occupied states in the emitter and collector; $eV < E_F$ and $eV > E_F$ respectively.

Considering the first case, which is sketched in Fig.6.11a), only elec-

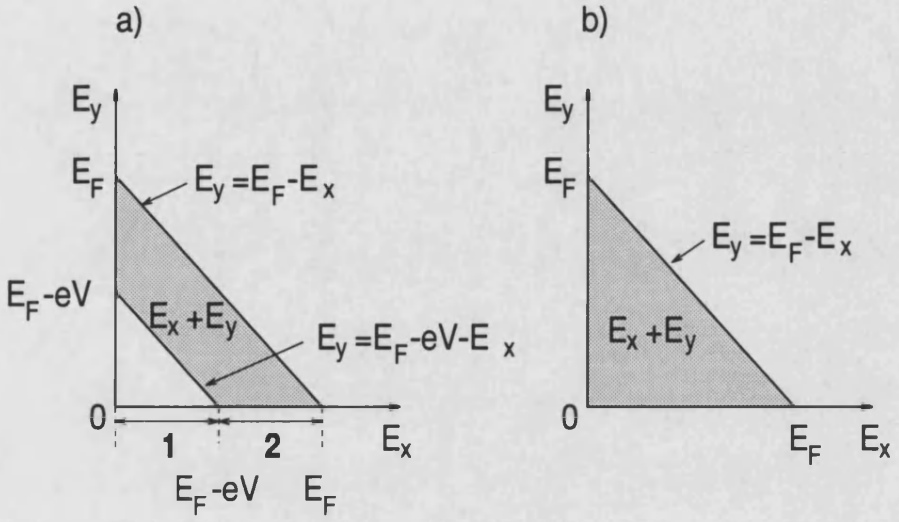

Figure 6.12: *Energy diagram for the total electron energy E plotted as a function of E_x and E_y components for the bias range $eV \leq E_F$. The shaded region indicates the energy surface used for the integration of the current density J.*

trons with a total energy $E = E_x + E_y$ in the energy range of occupied states in the emitter and free states in the collector can contribute to the supply function. Therefore, for $E_F - eV < E < E_F$,

$$f(E_x + E_y) = 1$$
$$f(E_x + E_y + eV) = 0.$$

To calculate $S(E_x)$ and J for this bias region, it is necessary to integrate over all possible values of E_x and E_y, which are sketched in Fig.6.12. Here, the problem is subdivided again into two energy regimes, $0 \leq E_x \leq E_F$ and $E_F - eV \leq E_x \leq E_F$ for regions indicated by **1** and **2** respectively on the figure. In region **1** possible values of E_y are bounded

by the lines $E_y = E_F - eV - E_x$ and $E_y = E_F - E_x$ which form the supply function integral limits, i.e.

$$S(E_x) = \frac{e}{\hbar(2\pi)^2}\sqrt{\frac{2m^*}{\hbar^2}}\int_{E_F-eV-E_x}^{E_F-E_x}\frac{dE_y}{\sqrt{E_y}} \tag{6.22}$$

The first component of the current density is then given by,

$$J_1 = 2\frac{e}{\hbar(2\pi)^2}\sqrt{\frac{2m^*}{\hbar^2}}\int_0^{E_F-eV}(\sqrt{E_F - E_x} - \sqrt{E_F - E_x - eV})T(E_x, eV)dE_x \tag{6.23}$$

In the second region, E_y is bounded by the lines $E_y = 0$ and $E_y = E_F - E_x$, which gives the supply function,

$$S(E_x) = \frac{e}{\hbar(2\pi)^2}\sqrt{\frac{2m^*}{\hbar^2}}\int_0^{E_F-E_x}\frac{dE_y}{\sqrt{E_y}} \tag{6.24}$$

The corresponding component of the current density is given by,

$$J_2 = 2\frac{e}{\hbar(2\pi)^2}\sqrt{\frac{2m^*}{\hbar^2}}\int_{E_F-eV}^{E_F}(\sqrt{E_F - E_x})T(E_x, eV)dE_x \tag{6.25}$$

Thus the total current density for the bias regime $eV \leq E_F$ can be written,

$$J = 2\frac{e}{\hbar(2\pi)^2}\sqrt{\frac{2m^*}{\hbar^2}}\left[\int_0^{E_F-eV}(\sqrt{E_F - E_x} - \sqrt{E_F - E_x - eV})T(E_x, eV)dE_x + \int_{E_F-eV}^{E_F}(\sqrt{E_F - E_x})T(E_x, eV)dE_x\right] \tag{6.26}$$

For the second bias regime where $eV > E_F$, values for the total energy E lie in the range $0 < E < E_F$ which ensure,

$$f(E_x + E_y) = 1$$
$$f(E_x + E_y + eV) = 0$$

The integration surface is sketched in Fig.6.12 b), and in this case the problem can be solved as a single surface integral. E_y is bounded by the lines $E_y = 0$ and $E_y = E_F - E_x$ and therefore the supply function is given by,

$$S(E_x) = \frac{e}{\hbar(2\pi)^2}\sqrt{\frac{2m^*}{\hbar^2}}\int_0^{E_F-E_x}\frac{dE_y}{\sqrt{E_y}} \tag{6.27}$$

The current density for $eV > E_F$ is therefore,

$$J = 2\frac{e}{\hbar(2\pi)^2}\sqrt{\frac{2m^*}{\hbar^2}}\int_0^{E_F}(\sqrt{E_F - E_x})T(E_x, eV)dE_x \tag{6.28}$$

6.3 Comparison with Experimental Results

The integrals 6.26 and 6.28 were solved numerically using a computer library routine based on Gauss-Konrad rules [77] in the two voltage regimes discussed. Fig.6.13 shows experimental *I-V* curves for two 5μm wide diodes (solid lines) measured to a sensitivity of 10pA. The barrier heights for the two devices $E_0(0)$ measured using the thermal activation technique are indicated. Also shown on the figure are the calculated *I-V* curves (dots) for two model diodes with trench depths $D_1 = 43$nm and $D_2 = 46$nm chosen to yield barrier heights as close as possible the experimental values. This was the only stage of the calculation where a fitting procedure was used and it is justified by the experimental difficulty involved in measuring both the depths of the trenches and their cross-sectional geometries (see Chapter 5). The iteration grid cell size $\Delta = 1$nm prevented a more accurate fitting of the barrier heights.

In view of the fact that the comparison is of tunnel current (which is exponentially sensitive to the form of the barrier potential), and given the large number of approximations contained in the model, agreement between the experimental and modelled *I-V* curves is impressive. In addition to the accurate reproduction of the gradients of the curves (differential conductivity) over more than four orders of magnitude in the current, the agreement in their voltage position is also good. Fur-

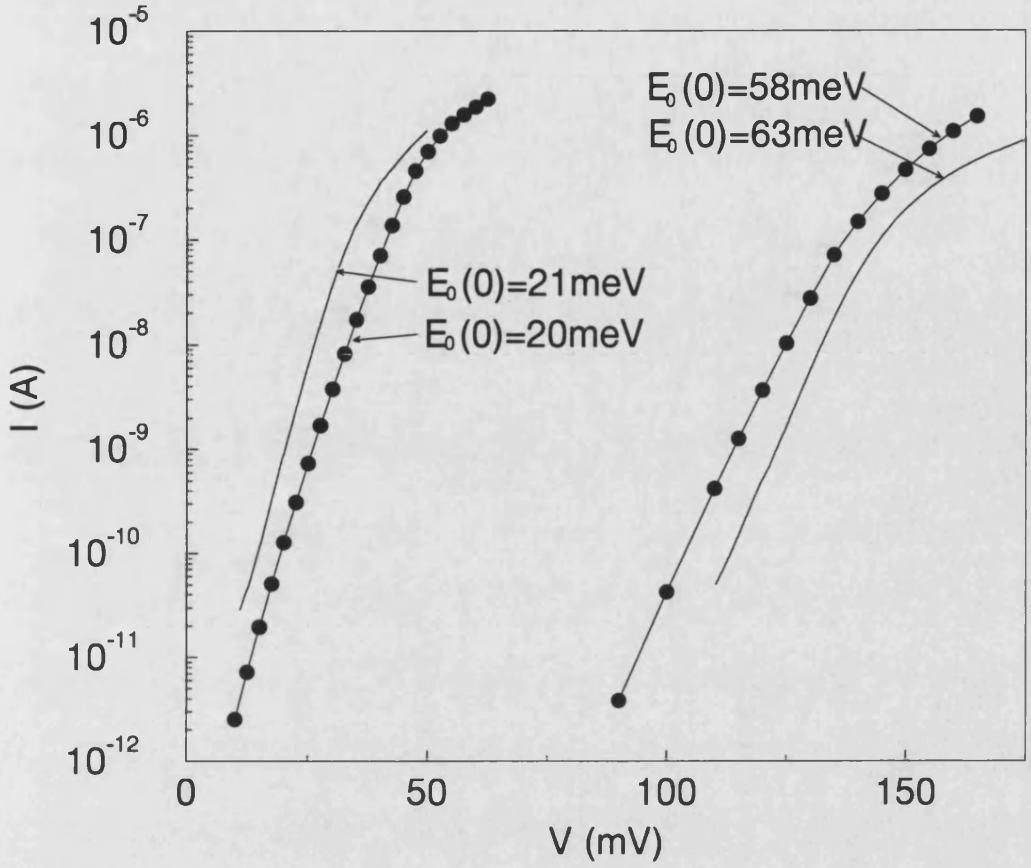

Figure 6.13: *Model (lines and points) and experimental (solid lines) I-V characteristics for 2 different diodes. The zero bias barrier heights $E_0(0)$ for the calculated (experimental) data are 20(21) and 58(63)meV respectively.*

thermore, a saturation in the barrier height with increasingly large bias voltage in the calculations (shown on the insert of Fig.6.9) leads to a roll-off in the gradient of the *I-V* characteristics (decrease in the differential conductivity). This phenomenon is also observed in the experimental data and may have a similar origin.

6.4 Conclusions

A numerical model, based on a finite difference solution to the Poisson equation has been developed to describe a single barrier quantum trench lateral tunnelling diode. The model uses a Fang-Howard variational approach to describing the electron distribution in the 2DES and takes into account variations in the impurity occupation density in both lateral and vertical directions. Computing time, in comparison to similar reported calculations, is modest. The model has been applied to obtain information about tunnelling barrier energy profiles and barrier heights as a function of the trench depth. A direct comparison between experiment and theory in this case is difficult owing to the difficulty involved in accurately measuring trench cross-sectional geometries and depths. The model also identifies the density of donor impurities in the AlGaAs barrier region as a critical parameter in determining the magnitude of the barrier potential.

A novel feature of the model involves the application of a bias voltage to the device which is achieved using a self-consistent method of boundary condition adjustment to calculate the voltage drop profile. Application of standard tunnelling theory using a form of the WKB approximation enabled the calculation of I-V properties from the biased barrier profiles.

Agreement between the experimental and modelled I-V characteristics is excellent using only the experimentally determined barrier height as a fitting parameter. This indicates that not only does the model produce a good simulation of the form of the zero bias tunnelling barrier potentials, but that the self-consistent approach to the application of the bias voltage also yields valid results. Furthermore, the author is unaware of any comparable, first principles tunnelling calculation that gives consistent order-of-magnitude agreement with experiment.

Finally, although the technique has been applied to the relatively

simple case of a single barrier diode, the principles behind it are quite general and could be applied to structures of arbitrary geometry.

7 Lateral Tunnelling in Gated Diodes

7.1 Introduction

In this chapter, attention is focussed on lateral tunnelling through potential barriers induced by field-effect metallic Schottky gates, as opposed to etched quantum trenches. Experimental data are presented for both single and double barrier devices, which were fabricated using the methods outlined in Chapter 4.

The principles behind Schottky barrier devices are quite simple, and indeed analogous to those for a field effect transistor (FET). Applying a negative bias voltage to a very narrow metallic gate on the sample surface produces an electrostatic field which causes a local depletion of the 2DES in the region under the gate. This depletion region represents a potential barrier to electrons in the electrodes of the device (which for gated structures are re-named *source* (emitter) and *drain* (collector)). Operating the device in the gate voltage range just after pinch-off (pinch-off is defined as when the barrier height equals the Fermi energy), means that at low temperature, transport can only occur via tunnelling.

In the introduction to Chapter 5, the disadvantages that gated lateral tunnel diodes have for commercial applications were highlighted and it was also suggested that etched structures may be more suitable for some experimental purposes. Clearly however, gated tunnelling devices have the significant experimental advantage that the size of the electrostatic potential can be continually changed via the externally applied gate voltage. This enables the systematic study of transport through a wide range of potential barriers, and in particular, the study of tunnelling through very small barriers, where the transmission coefficients are large enough to observe tunnelling effects at small values of the applied bias voltage.

7.2 The Effects of Disorder in Lateral Devices

Recent publications have suggested that disorder plays an important role in the properties of lateral devices, such as quantum point contacts and lateral tunnelling diodes. An early example came from McEuen *et al.* [78], who observed a small number of sharp resonances in the transconductance of a quantum point contact near pinch-off. The authors explained their data in terms of resonant tunnelling through bound states of a quantum well in the barrier, induced by a single, positively charged impurity ion. The impurity was assumed to come from the background doping density and lie near the plane of the 2DES in the region of the barrier. Similar effects were observed by Weis *et al.* [79], also using a split-gate geometry.

Quite different results were reported by Washburn *et al.* [80], who studied a single, field induced lateral tunnelling barrier, fabricated on a 1μm wide quantum wire. The devices displayed a range of transconductance fluctuations in the gate voltage regime before pinch-off, which were attributed to fluctuations in the potential profile of the barrier. Subsequent calculations by Davies *et al.* [81] demonstrated that the results could be explained in terms of potential fluctuations, induced by the random positioning of *donor* impurities in the AlGaAs layer of the heterostructure.

It is clear that as the dimensions of electronic devices are reduced, the probability that their electrical properties will become dominated by disorder such as donor or other impurities must increase. The experimental data shown in the following chapters on field induced lateral tunnelling devices reinforce this statement, and demonstrate that the effects of disorder are particularly important for an understanding of the physics involved in two-dimensional lateral problems.

7.3 Transport and Tunnelling Through Single Barrier Devices

In common with the quantum trench devices discussed in Chapters 5 and 6, the gated tunnelling devices here are described as 2D, i.e. the electrostatic potential barrier has finite extent in both the x-direction (tunnelling direction) and the $y-$direction. One of the few published experiments, concentrating solely on 2D lateral tunnelling through single, gate-induced barriers (as opposed to tunnelling through 1D split gate structures or in quantum wires) was conducted by Manion *et al.* [57], who compared their source-drain current-voltage properties at fixed gate voltage with a model based on the Poisson equation and a simple tunnelling theory involving the WKB approximation. The authors were able to show a good agreement between measurement and theory by using both the barrier height and width as fitting parameters.

In this work, a more detailed experimental study of the properties of a single 2D field induced barrier is presented. In addition to a simple investigation of the conventional current-voltage characteristics, a detailed study of the conductance properties of the barrier was made both in the *transport* (before pinch-off) and in the *tunnelling* (after pinch-off) regimes. It is shown that owing to the presence of inhomogeneities in the barrier potential, the properties of the device near and beyond pinch-off are dominated by *weak* points in the potential. Hence, the transport and tunnelling properties of this 2D barrier must be interpreted in terms of a parallel array of 1D barriers.

7.3.1 Experimental Methods

The single-barrier-lateral-tunnelling-diodes (SLTD's) were fabricated on Hall bar samples, with a geometry similar to that used for the quantum trench devices. The Schottky gates consisted of a 15nm Cr layer, followed by a 30nm layer of Au and the gate dimensions were approximately

50nm long in the tunnelling direction and 5μm wide. To ensure that no current could flow along the gate itself, contact to it was only made via a single gate finger on one side of the Hall bar. Fig.7.1 shows a sketch of an ideal SLTD and full details of the fabrication process are given in Chapter 4.

Both single and double barrier devices were studied using two vari-

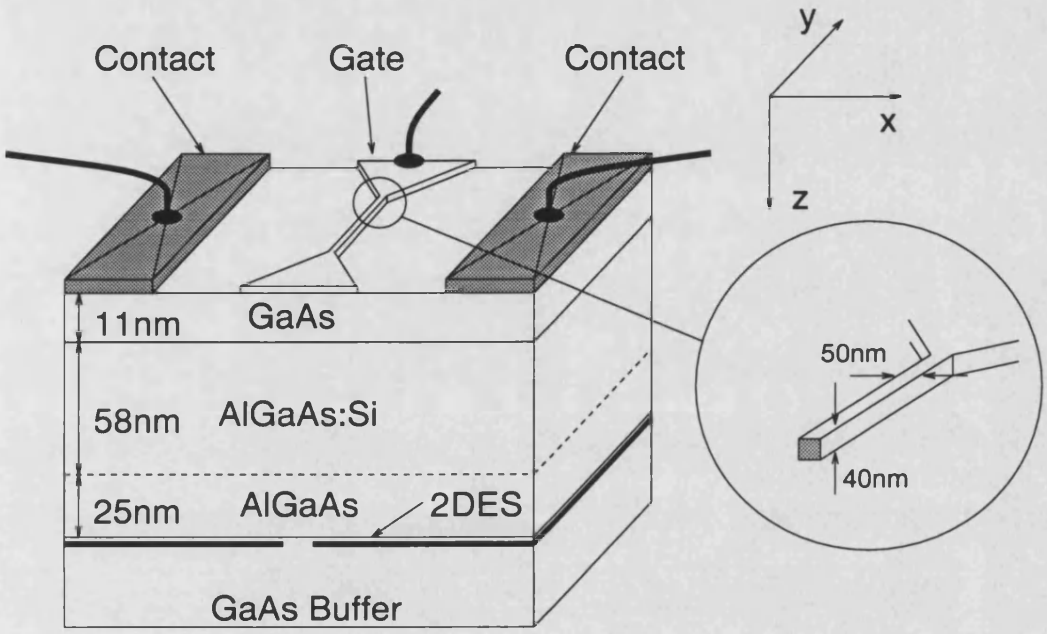

Figure 7.1: *Schematic diagram of an ideal SLTD.*

able parameters; the source drain voltage V_{SD} and the gate voltage V_{GD}. This enables two modes of operation;

1. I_{SD} or dI_{SD}/dV_{SD} measured as a function of V_{GD} for fixed V_{SD}.
2. I_{SD} or dI_{SD}/dV_{SD} measured as a function of V_{SD} for fixed V_{GD}.

Leakage currents between the gate and drain were smaller than the minimum current sensitivity of 1pA used.

Fig.7.2 shows a simplified schematic representation of the electrical circuit used in the experiments. The drain contact is always connected via the current amplifier (internal resistance $\sim 100\Omega$, which was always much smaller than the sample resistance) to ground whereas V_{GD} and

V_{SD} are referenced directly to ground. Since the electric field between gate and drain is largely independent of the source potential, current-voltage characteristics measured with this configuration are usually not antisymmetric, especially for large values of V_{SD}. All the experiments on single barrier devices were conducted in a top-loading dilution refrigerator (TLM400 System from Oxford Instruments) at a temperature of 22mK in the dark.

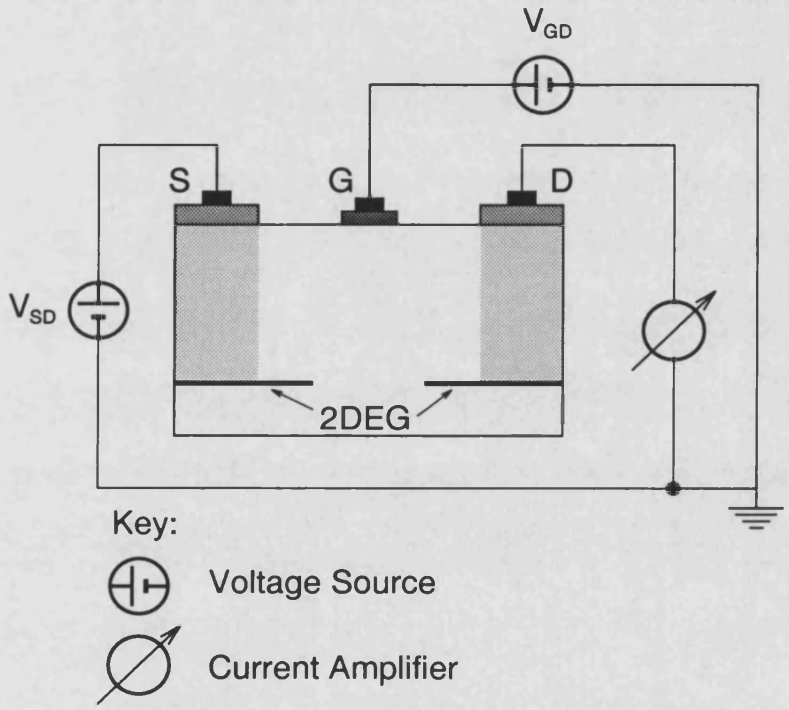

Figure 7.2: *Simplified schematic representation of the measurement circuit.*

7.3.2 Results for Zero DC Source-Drain Voltage

Data are presented for two SLTD's, which were fabricated on the same Hall bar sample and are denoted device A and device B in the following discussion. Fig.7.3a) shows a plot of the differential conductivity dI_{SD}/dV_{SD} for the two devices as a function of gate voltage V_{GD}, for zero applied DC source-drain voltage V_{SD} (the Mode 1 characteristics).

The influence of V_{GD} is small for both devices, until a threshold voltage

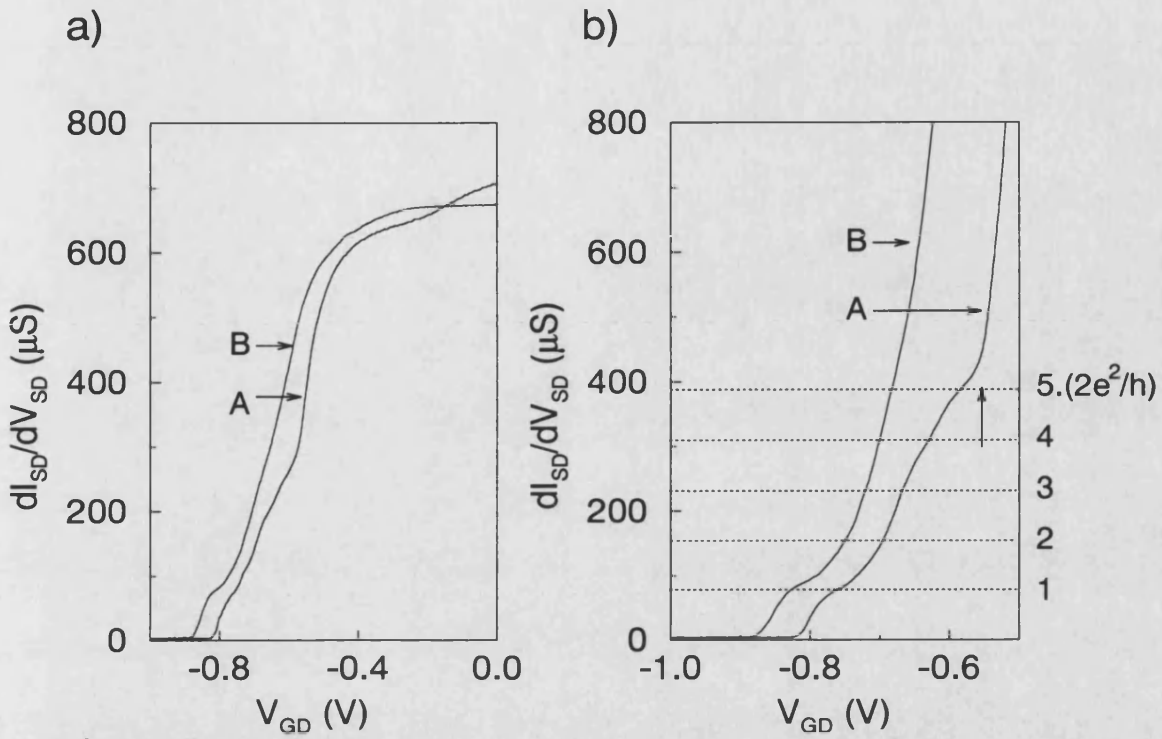

Figure 7.3: *a) Differential conductivity of devices A and B as a function of the gate voltage for zero DC source-drain voltage. b) The same curves, adjusted to remove the contribution of the 2D lead and sample contact resistances. The vertical arrow indicates the point at which the device A characteristics become dominated by 1D transport. The dotted lines indicate integer multiples of the 1D quantised conductance $2e^2/h$ given by the Landauer formula.*

of $V_{GD} \sim -0.5$V is reached, at which point dI_{SD}/dV_{SD} drops rapidly. Although for a homogeneous potential, a roughly exponential reduction in dI_{SD}/dV_{SD} would be expected with increasing $|V_{GD}|$ in this regime, device A displays a number of pronounced shoulders in dI_{SD}/dV_{SD} before pinch-off. The strongest feature, which is also observed for device B, occurs just before pinch-off. Pinch-off is assumed to be when $dI_{SD}/dV_{SD} \approx 0$ for $V_{SD} = 0$ which in this case occurs at $V_{GD} \approx$-0.82V and -0.88V for A and B respectively. The curves were found to be repro-

ducible within a single cooling cycle, with small shifts of ~ 0.01V occurring in the value of V_{GD} required for pinch-off. After warming to room temperature and re-cooling, the features in dI_{SD}/dV_{SD} remained qualitatively similar, although their gate-voltage positions, and the pinch-off gate voltage varied by up to 0.2V. The value of dI_{SD}/dV_{SD} for the pronounced shoulder before pinch-off remained roughly constant with temperature cycling.

Fig.7.3b) shows the same Mode 1 characteristics, with the resistance R_0 of the 2D leads and the sample contacts removed (R_0 was taken as the resistance of the device for zero V_{GD}). The adjusted values of dI_{SD}/dV_{SD} therefore represent the differential conductivity of the barrier *only*. It is clear from Fig.7.3b) that the first pronounced shoulder in dI_{SD}/dV_{SD}, that is observed for both devices, occurs at a value close $dI_{SD}/dV_{SD} = 2e^2/h$.

To explain the results, it is necessary to return to the Landauer model of quantised 1D conductance, which was introduced earlier in the thesis in relation to the edge state model of the quantum Hall effect, and is discussed further in the following section.

7.3.2.1 Quantised Conductance in 1D Channels

If the lateral width of a conducting channel in a 2DES is made comparable to the Fermi wavelength λ_F, then a further 1D quantisation of the electron motion occurs, in addition to that imposed by the z-direction confinement at the heterostructure interface. Assuming for example that the lateral confinement acts in the y-direction, then solving the Schrödinger equation for free motion in the x-directions [39] reveals a discrete set of energy eigenvalues E_n^0. The dispersion relation for the n^{th} subband is,

$$E_n(k_x) = E_n^0 + \frac{\hbar^2 k_x^2}{2m^*} \tag{7.1}$$

where k_x is the wave vector along the channel. Each 1D state of length L occupies an area $(2\pi/L)$ in k-space, and the number of states per unit length in an interval between k and $k + dk$ is,

$$dN_{1D}(E) = 2\frac{dk}{2\pi} = \frac{dk}{\pi} \tag{7.2}$$

where the multiplying factor of 2 is included for electron spin. The density of states per unit energy and length $D_{1D}(E)$ is sketched in Fig.7.4a) and is written for each subband as

$$D_{1D}(E) = \frac{\partial N_{1D}(E)}{\partial E} = \frac{\partial N_{1D}(k)}{\partial k}\frac{\partial k}{\partial E} = \frac{2}{\pi\hbar v_g} \tag{7.3}$$

for the group velocity $v_g = 1/\hbar(dE/dk)$ (see also Section 3.4).

Fig.7.4b) shows a schematic diagram of an ideal 1D channel, sep-

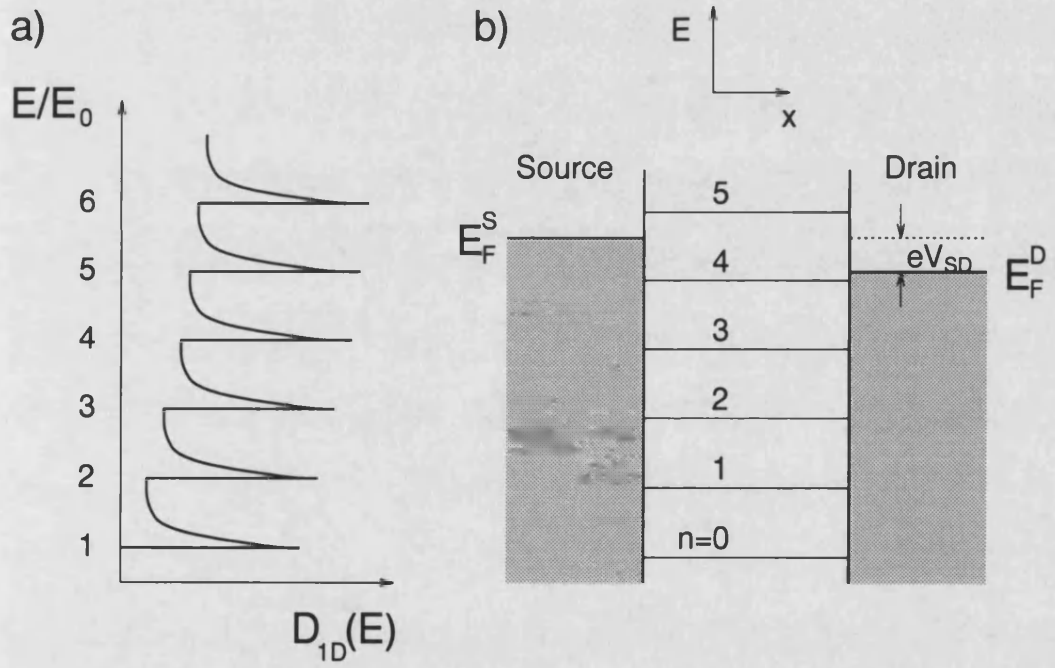

Figure 7.4: *a) Sketch of the density of states (DOS) for a 1DES as a function of energy. E_0 is the energy of the bottom of the first 1D subband. b) Schematic diagram of an ideal 1D channel connecting two electron reservoirs with a small applied source-drain voltage V_{SD}.*

arating two electron reservoirs with Fermi energies E_F^S and E_F^D. If a

small source-drain voltage V_{SD} is applied between the two ends of the 1D channel, a net current will flow between the electron reservoirs. The current per unit energy, injected into a single subband is given by the product of the density of states and the electron group velocity along the channel, which leads a general formula for the total current per subband,

$$I_{SD}(V_{SD}) = \frac{2e}{h} \int_{E_F^S - eV_{SD}}^{E_F^S} T(E_x) dE_x \tag{7.4}$$

Here $T(E_x)$ is the probability of transmission through the constriction, and for ideal 1D *transport*, $T(E) = 1$. This gives the expression for the current through the n^{th} subband as,

$$I_{SD}(V_{SD}) = \frac{2e^2}{h} V_{SD} \tag{7.5}$$

and the well know quantised value for the conductance of the n^{th} subband,

$$G = \frac{dI_{SD}}{dV_{SD}} = \frac{2e^2}{h} \tag{7.6}$$

which is independent of all material or device parameters. A more generalised form of Eqn.7.5 can be written for the current through all n subbands as,

$$I_{SD}(V_{SD}) = \sum_n \frac{2e}{h} \int_{E_F^S - eV_{SD}}^{E_F^S} \Theta(E_n - E_x) dE_x \tag{7.7}$$

where Θ is the Heaviside step function.

Conductance quantisation, in the absence of a magnetic field, was first observed in 1D split gate devices by van Wees *et al.* [82] and independently by Wharam *et al* [83] in 1988. Both authors demonstrated a step-like reduction in the conductance G of the 1D constriction in units of $2e^2/h$ as its width was reduced with increasing negative gate voltage. A very comprehensive review of many aspects of 1D transport has been given by van Houten *et al.* [6].

7.3.2.2 Discussion

Returning to the data of Fig.7.3b), it is proposed that the features observed in the differential conductivity can be explained by assuming that the 2D barrier is punctured by an array of 1D channels, caused by fluctuations in the electrostatic potential. In light of this, the data is interpreted in the following way. Transport through the 1D channels only begins to dominate when the rest of the barrier is pinched off, a point indicated for sample A by the arrow on Fig.7.3b). For more negative V_{GD}, the the conductivity is given by the parallel sum of all the 1D channels. This means that any quantisation of the conductivity in this regime is lost, although shoulders in dI_{SD}/dV_{SD} can occur, and are observed in the curve for device A. The quantised step that is observed in the curves for both devices just before pinch-off, corresponds to the situation where a single 1D subband at one weak point in the potential remains below E_F^S.

The fluctuations in the barrier potential are probably induced by the random positions of Si donor impurities in the AlGaAs layer of the heterostructure. Calculations made in [81] indicate that such fluctuations have typical widths $\sim$ 100nm which is of the correct order of magnitude to observe 1D effects (λ_F=47nm for this sample). Fig.7.5 shows a sketch of an inhomogeneous electrostatic potential barrier, based on this interpretation of the experimental data. The sketch corresponds to a gate voltage regime, just after the last 1D channel has been pinched off.

The contribution to fluctuations in the barrier potential from inhomogeneities in the gate length itself cannot be ignored. Given however that the gate length only varies by approximately $\pm$10nm and is $\sim$ 100nm from the 2DES, it is considered unlikely that such roughness could be responsible for the presence of defined 1D channels in the barrier. One alternative explanation remains; the presence of a few positively charged background donor impurities in the plane of the 2DES in the barrier re-

gion. There are however no indications in the data of *resonant* tunnelling of the type observed in [78] and [79], and therefore this interpretation of the data is considered less probable.

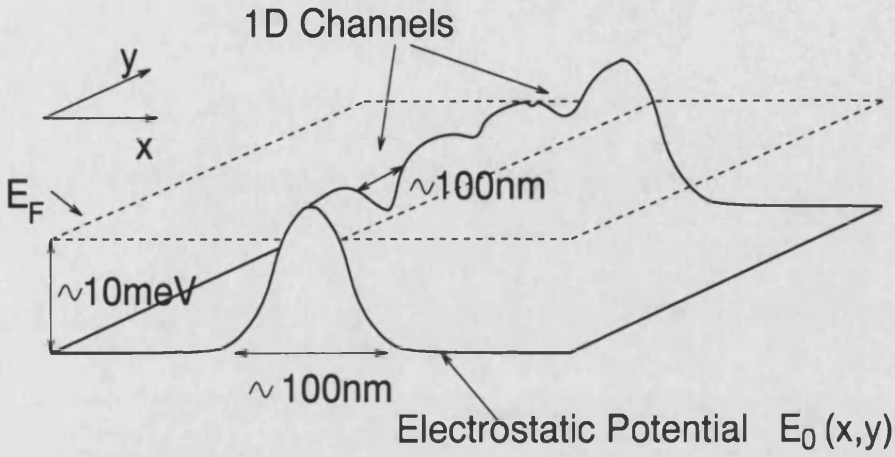

Figure 7.5: *Sketch of the electrostatic barrier potential of an SLTD after the last 1D channel has been pinched-off. The potential fluctuations in the barrier arise from the random positions of donor impurities in the AlGaAs layer. The dotted lines indicate the position of* E_F.

7.3.3 Results for Fixed Gate Voltage

This section concentrates on the Mode 2 characteristics of the SLTD's, in the two gate voltage regimes where either transport or tunnelling are expected to control the current flow. In the above, it was demonstrated that in the transport regime just before pinch-off, the device characteristics for zero DC source drain voltage are dominated by 1D channels in an inhomogeneous barrier potential. The fluctuations in the potential must however also be important in the tunnelling regime, since the transmission coefficient for the barrier is exponentially sensitive to its dimensions. Each weak point in the barrier is assumed to resemble a saddle-point potential, which is both lower than the remainder of the barrier, and thinner in the x-direction (tunnelling direction). Thus each saddle point in the potential can be considered as a quasi-1D tunnelling

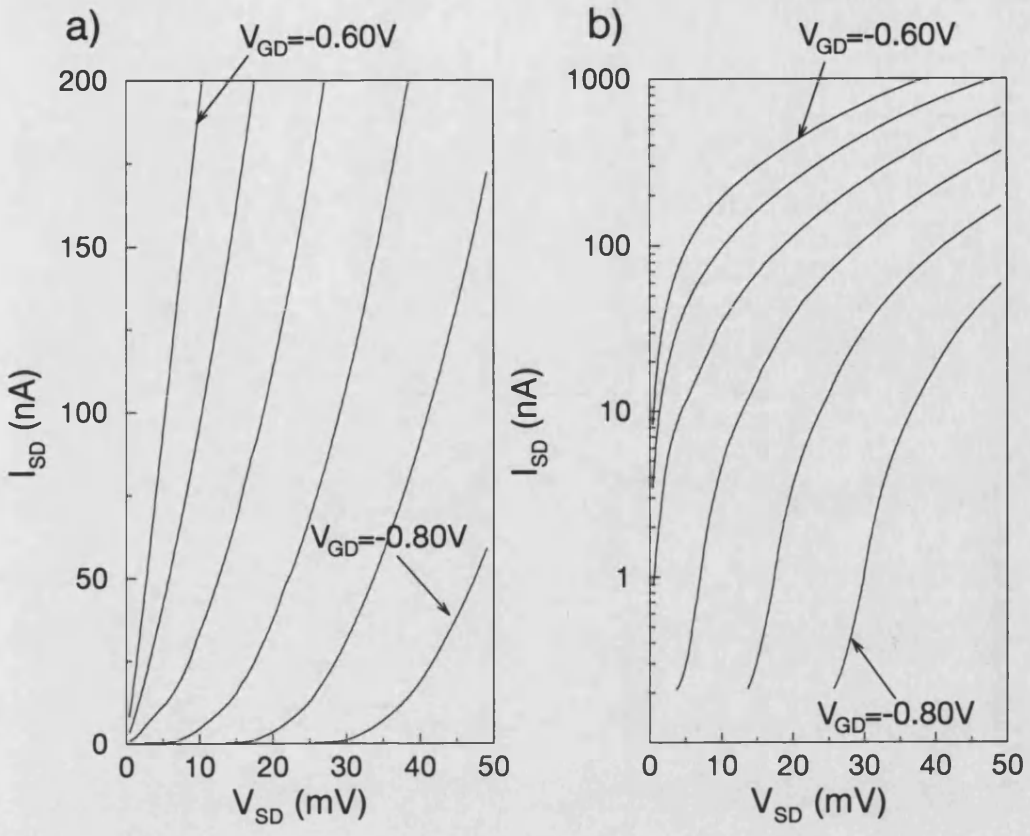

Figure 7.6: *a) Mode 2 characteristics for device A for fixed gate voltages between -0.60 and -0.8V (step 0.04V). b) The same data plotted on a logarithmic y-axis.*

barrier, and the whole device as a parallel array of quasi-1D barriers with *different heights* (see Fig.7.5).

Fig.7.6a) and b) show the Mode 2 characteristics with I_{SD} measured to an accuracy of 0.1nA for device A at *fixed* values of V_{GD} between -0.60 and -0.80V. Note that the data were taken on a different cooling cycle to that shown in Fig.7.3, and in this case the channel was completely pinched-off for $V_{GD} = -0.70$V. The data for device B were qualitatively the same. The curves show the expected transition between linear transport at low $|V_{GD}|$ and non-linear tunnelling at high $|V_{GD}|$ where the potential barrier rises above E_F across its entire width.

The curves were not antisymmetric, but the features were qualitatively the same for positive and negative V_{SD}. Clearly there is structure in the curves for $V_{GD} = -0.68$V and -0.72V at low V_{SD} and it is necessary to study the differential conductivity of the devices to obtain more precise data.

Fig.7.7 shows dI_{SD}/dV_{SD} measured in Mode 2 for device A for values of V_{GD} between 0 and -0.80V. To analyse the huge amount of information on this plot, the tunnelling and transport regimes are considered separately.

7.3.3.1 Tunnelling Regime

Concentrating first on the tunnelling regime ($V_{GD} < -0.70V$), it can be seen from Fig.7.7 that two pronounced shoulders appear in dI_{SD}/dV_{SD} with increasing V_{SD}. The positions of the shoulders shift monotonically to higher V_{SD} with increasing $|V_{GD}|$ and become weaker for the highest values of $|V_{GD}|$ shown. A subsection of these data is plotted in Fig.7.8 for positive V_{SD} in the gate voltage range between -0.71V and -0.77V and indicate that the values of dI_{SD}/dV_{SD} at which the shoulders occur, decrease slightly with increasing $|V_{GD}|$. For this plot, the resistance of the contacts and 2D leads of the devices has been subtracted. The data for device B were similar, although only a single shoulder was clearly resolvable in both directions of V_{SD}. After warming to room temperature and re-cooling, the second shoulder in the device A characteristics was also no longer clearly resolvable (see Section 8.4).

The shoulders present in dI_{SD}/dV_{SD} are surprising, since from a simple tunnelling picture, the current and thus conductivity should show an approximately exponential dependence on the applied source-drain voltage. To explain the data it is necessary to return to the idea that the barrier potential is strongly inhomogeneous, and that the potential fluctuations represent 1D channels between source and drain. Although in

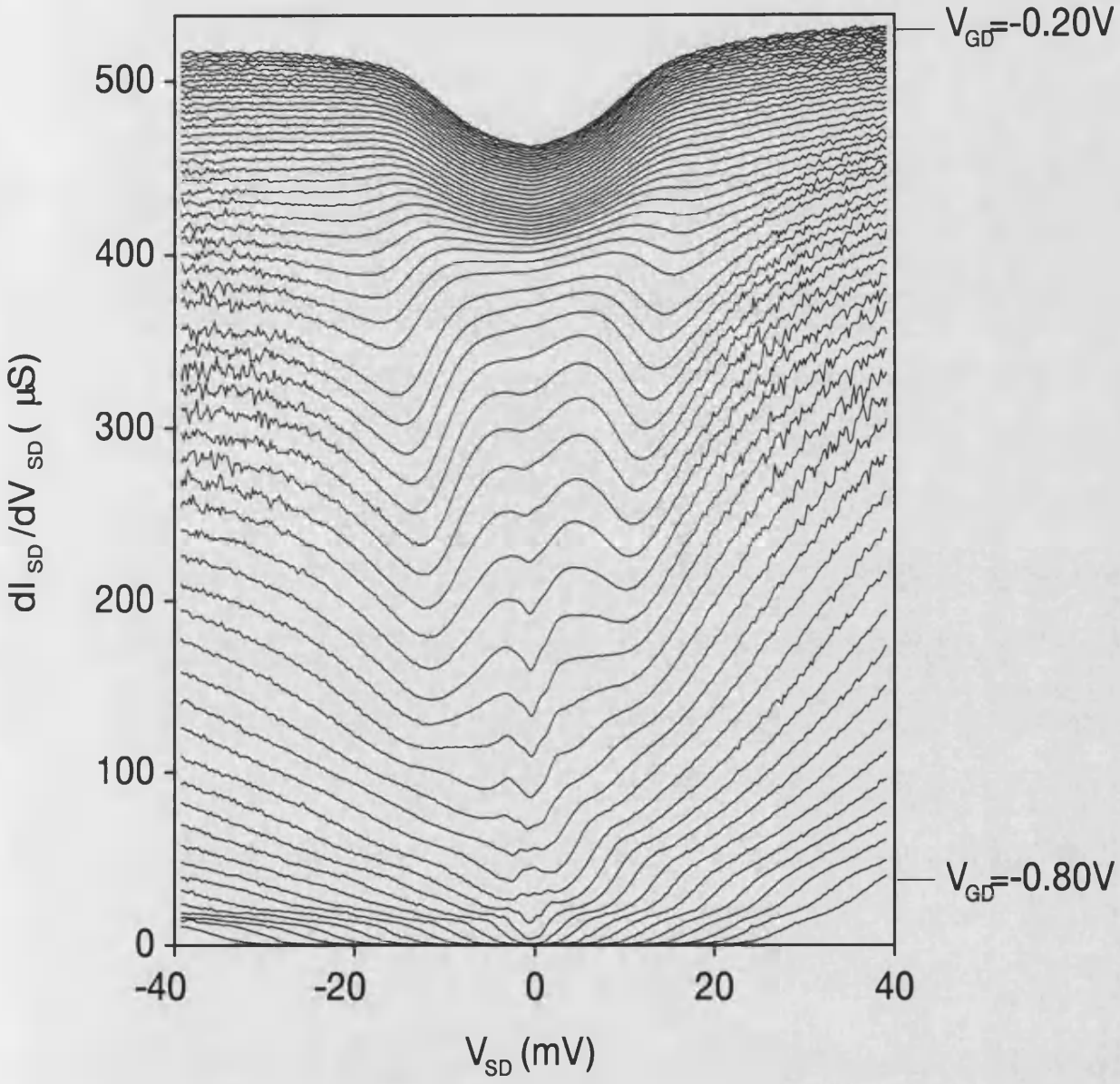

Figure 7.7: *Differential conductivity of device A measured as a function of the source-drain voltage V_{SD} for fixed values of the gate voltage V_{GD} between 0 and -0.80V (Mode 2). The gate voltage step is 0.01V and the curves have not been shifted on the y-axis*

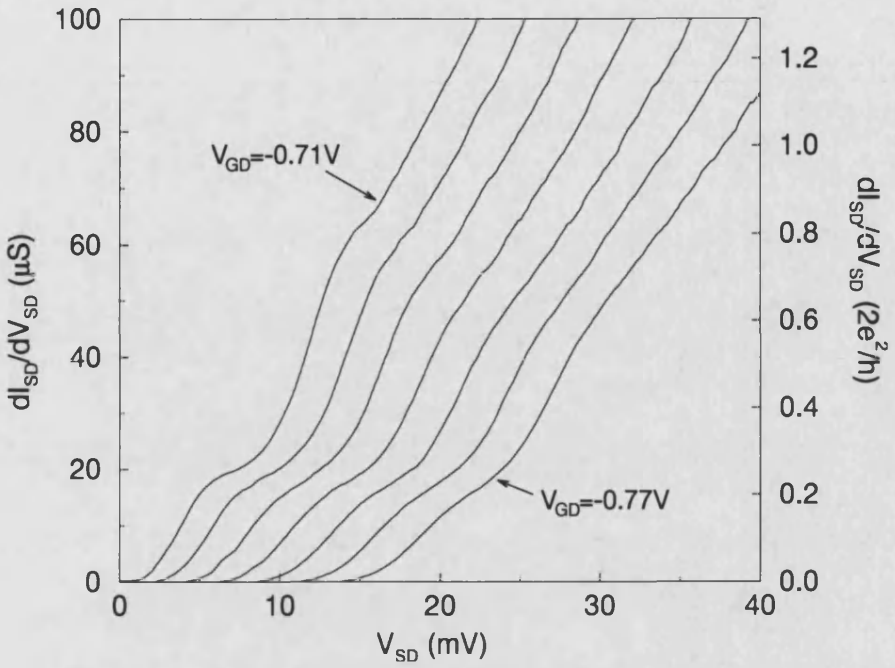

Figure 7.8: *Differential conductivity of device A as a function of the source-drain voltage V_{SD} for a range of fixed gate voltages V_{GD}. The curves have been adjusted to remove the influence of the 2D lead and contact resistances. The right hand y-axis is scaled in units of quantised 1D conductance ($2e^2/h$).*

this gate voltage regime beyond pinch-off, the 1D subbands lie above E_F^S for $V_{SD} = 0$, with increasing V_{SD} the subbands are expected to move down in energy, relative to E_F^S, and at some critical voltage V_{SD}^c, 1D transport will play a role in the conductivity of the device. It is proposed therefore that the results of Fig.7.8 can be explained as a combination of tunnelling, *and* of transport through 1D subbands at weak points in the barrier potential at high V_{SD}.

7.3.3.2 Model of 1D Transport at Large Source-Drain Voltage

One of the few experimental models of 1D transport at large source-drain voltage ($eV_{SD} > (E_n - E_{n-1})$) was published by Kowenhoven *et*

al. [84], who studied the I_{SD}-V_{SD} characteristics of a split gate device that was pinched off for zero source-drain voltage. That structure is analogous to a single weak point in the barrier potential of the device measured in this work, and therefore the simple model, outlined in [84] is used as a starting point for a discussion of the data.

The analysis is based on an idealised representation of a saddle point in the potential as a low, asymmetric triangular barrier in the x-direction, with high confining walls in the $\pm y$-directions. For $V_{SD} = 0$, the barrier is higher in energy than E_F. An applied x-direction source-drain bias V_{SD} is assumed to fall linearly across the barrier region only, and 1D subbands remain above the barrier due to the lateral confinement in the y-direction. Fig.7.9a) and b) show sketches of this ideal device for zero and finite V_{SD}.

With increasing V_{SD}, the energy of the n^{th} subband E_n differs from its equilibrium position E_n^0 due to the tilting of the potential barrier, and is given as $E_n = E_n^0 - meV_{SD}$. Here, m is a phenomenological parameter which describes the fraction of V_{SD} that falls across the left hand side of the barrier and is dependent on the *shape* of the barrier. Consequently a fraction $(1-m)$ falls on the right hand side. Ignoring any current due to tunnelling, the current flow across the barrier will be zero, until the bottom of the first subband falls below E_F^S at the critical source-drain voltage V_{SD}^c. For $V_{SD} > V_{SD}^c$, the current through the n^{th} subband is given by Eqn.7.4 as,

$$I_{SD}(V_{SD}) = \frac{2e}{h} \int_{E_n}^{E_F^S} dE \tag{7.8}$$

for $T(E_x) = 1$. This gives a contribution to the total conductivity G from the n^{th} subband as,

$$\frac{\partial I_{SD}}{\partial V_{SD}} = \frac{2e^2}{h} m\Theta(V_{SD} - V_{SD}^c) \tag{7.9}$$

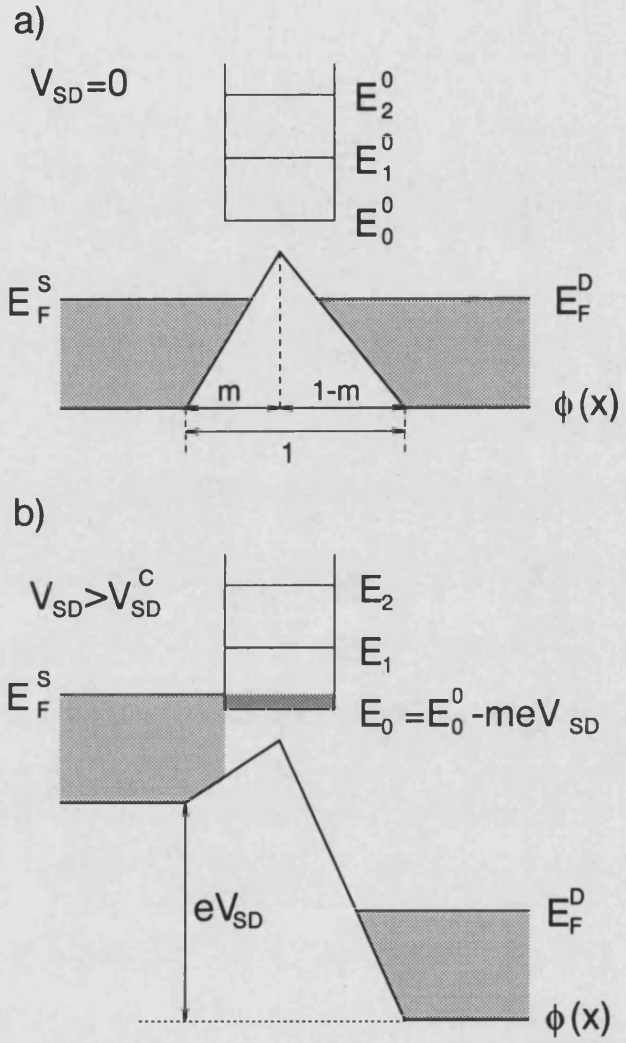

Figure 7.9: *Schematic diagram of the x-direction potential $\phi(x)$ for an asymmetric 1D triangular barrier in a y-direction constriction. a) Potential for zero source-drain voltage V_{SD}. The 1D subbands above the barrier are indicated by their equilibrium energies E_n^0. b) Potential for finite V_{SD}. The voltage drop across the left hand portion of the barrier is meV_{SD} and the new subband energies are given by $E_n = E_0^n - meV_{SD}$*

for a critical voltage,

$$V_{SD}^{c} = \frac{(E_n - E_F^S)}{me} \tag{7.10}$$

Eqn.7.9 implies that although no longer quantised, the contribution to the conductivity from each subband should remain constant, if m is independent of V_{SD}. Within the framework of this model, a step-like increase in the conductivity would be expected for increasing source-drain voltage as an increasing number of 1D subbands contribute to the overall conductivity.

7.3.3.3 Discussion

The conductivity data of Fig.7.8 are explained using a model involving both tunnelling through the barrier, and transport though 1D constrictions, formed by fluctuations in the potential. For low source-drain voltage, the energies of all the 1D subbands in the barrier lie above E_F^S and hence the only mechanism for current flow is tunnelling. This is reflected by the approximately exponential onset in dI_{SD}/dV_{SD}, observed on Fig.7.8, which is associated with tunnelling processes occurring at the smallest point in the barrier potential. The current in this case is still governed by Eqn.7.4 but $T(E_x) < 1$ for 1D tunnelling. At the critical voltage V_{SD}^{c} which for $V_{GD} = -0.71V$ is estimated as $V_{SD}^{c} \approx 5$mV, the first subband E_0 of a single 1D channel above a weak point in the barrier falls below E_F^S. In this voltage regime, the current becomes dominated by transport through the single 1D subband which contributes a constant value of $m(2e^2/h)$ towards dI_{SD}/dV_{SD}. This is seen as the first shoulder in the curves on Fig.7.8 where the value of $dI_{SD}/dV_{SD} \approx 20\mu$S implies $m \approx 0.25$. For a roughly symmetric potential, a value of $m \sim 0.5$ would be expected, but it should be stressed that this is a purely phenomenological model. Similar observations were made by the authors in [84]. Increasing $|V_{GD}|$ causes a slow reduction in the value of dI_{SD}/dV_{SD} at the first shoulder, suggesting a slight decrease in the value of m. Given

that m depends on the *shape* of the barrier, this is consistent with the model.

Increasing V_{SD} above V_{SD}^{c} results in a rapid increase in dI_{SD}/dV_{SD}, which is associated with a further contribution to the current from tunnelling. The second shoulder that is resolved for device A is assumed to arise from the presence of a second $1D$ subband below E_F^S. Whether this is the second subband E_1 of the same 1D constriction, or the first subband at another weak point in the barrier is unclear from the data.

7.3.3.4 Transport Regime

One of the most striking features of the data shown in Fig.7.7 is the strong minima that develop in dI_{SD}/dV_{SD} in the range of V_{GD} between -0.40 and -0.60V. The same minima are also observed for device B, and are surprising, since the conductivity of a simple single barrier, which in this case is lower than E_F, would be expected to show a roughly monotonic increase with increasing V_{SD}. The data for device A in this region are also plotted in Fig.7.10a) on an expanded scale and indicate that the minima positions shift to *lower* V_{SD} with *increasing* $|V_{GD}|$. Again this is surprising, since any resonance feature associated with the barrier itself would be expected to shift to *higher* V_{SD} as the barrier size increases. The logical conclusion from this is that the minima arise from a phenomenon associated with the 2D electrodes of the device, rather than with the barrier itself.

The data are explained with an analogy to the Gunn effect [4] which can be seen for example in GaAs n^{++}-n-n^{+} diode samples. The Gunn effect describes the reduction in conductivity that occurs when the electric field across the device is strong enough to allow carriers to scatter into the X and L valleys of the conduction band, where their effective mass is much higher. In the SLTD's it is proposed that the reduction in dI_{SD}/dV_{SD} occurs when the electrons have sufficient energy to transfer

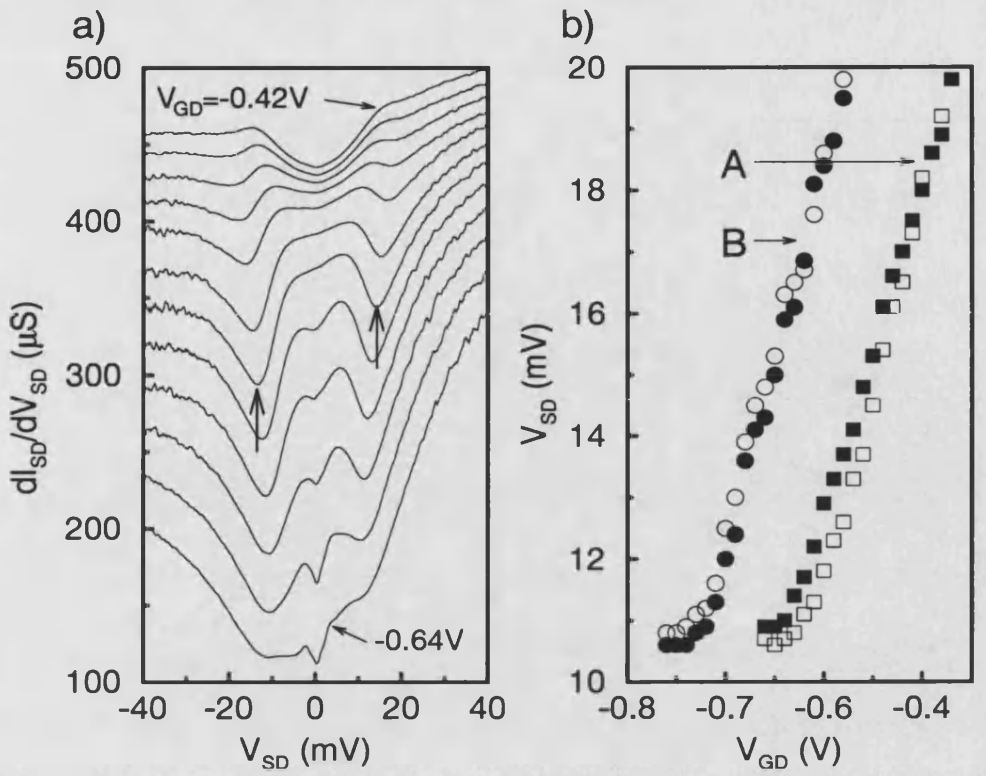

Figure 7.10: *a) Differential conductivity dI_{SD}/dV_{SD} of device A as a function of the source-drain voltage V_{SD} for fixed values of the gate voltage V_{GD}. b) Source-drain voltage positions of the minima in dI_{SD}/dV_{SD} (indicted by the arrows on a)) as a function of V_{GD} for devices A (squares) and B (circles). The solid and open symbols refer to minima at positive and negative V_{SD} respectively.*

to the *second subband* of the 2DES itself. Although the effective electron mass in the second subband is of the same order as that of the first subband ($\sim 0.07m_0$), previous authors have demonstrated theoretically [85] and experimentally [86,87] that a sharp drop in the 2DES mobility occurs with the occupation of the second subband, owing to the presence of strong interband scattering. In addition, the velocity of the electrons transferred to the second subband is reduced, since part of their kinetic energy becomes the potential energy of the second subband itself.

The model for this transfer of electrons to the second subband is sketched in Fig.7.11. In order for the transfer to occur, empty states in the second subband of the drain must be aligned in energy with filled states in the first subband of the source. To achieve this, a voltage V_{SD}^T, equal to the energy difference between E_F^S and the second subband energy E_1 must fall across the barrier region. Given typical subband energy spacings of $E_1 - E_0 \sim 20$meV [88], and the position of the Fermi energy as $E_F - E_0 \sim$10meV, implies a value $V_{SD}^T = E_1 - E_F \sim$10meV. Assuming an electron in the second subband has a maximum kinetic energy $\sim$1meV, and taking an average interband scattering time of 100ps (based on the acoustic phonon scattering time [89]), implies that electrons will remain in the second subband for an average distance of $\sim 1\mu$m after passing the barrier. Hence the reduction in conductivity with increasing V_{SD} can be understood as the formation of a low mobility, $\sim 1\mu$m wide *stripe* on the drain side of the barrier.

The transfer of carriers to the second subband in the drain however only accounts for the *reduction* in dI_{SD}/dV_{SD} with increasing $|V_{SD}|$. The reason for the subsequent increase, which defines the minimum in dI_{SD}/dV_{SD} with increasing V_{SD} is not obvious. It is plausible that dI_{SD}/dV_{SD} rises as the barrier height is reduced by the increasing electric field, and an increasing number of states in the source are available for transport without tunnelling.

The requirement of a specific voltage drop $V_{SD}^T = E_1 - E_F$ across the barrier to enable the transfer of source electrons into the second subband in the drain explains the shift in the minima positions to lower V_{SD} with increasing $|V_{GD}|$. The minima positions for both devices are plotted as a function of $|V_{GD}|$ in Fig.7.10b). At low $|V_{GD}|$, the resistance of the barrier is comparable to that of the 2D electrodes, and only a percentage of the applied V_{SD} falls across the barrier region. As $|V_{GD}|$ increases, an increasing proportion of the source-drain voltage falls across the barrier, and the value of V_{SD} required to inject carriers into the second subband

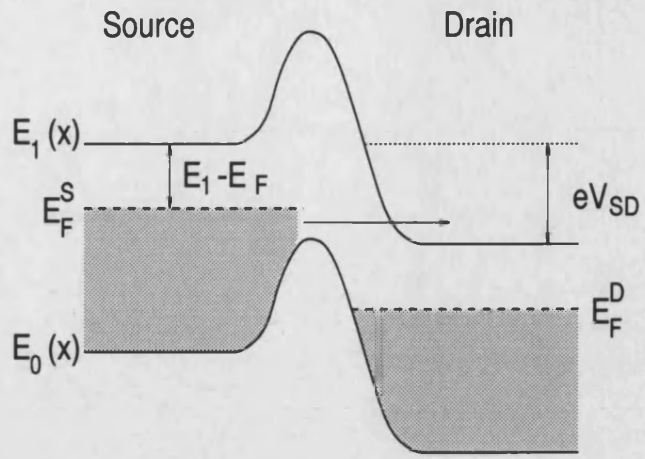

Figure 7.11: *Schematic diagram of the potential energy profiles of the first and second 2D subbands for a barrier height less than the Fermi energy E_F. The applied source-drain voltage V_{SD} is large enough to energetically align empty states in the second subband in the drain, with filled states in the first subband of the source. The transport path between the two subbands is indicated by the arrow.*

is reduced, causing the observed shift in the minima position. For high $|V_{GD}|$, the voltage drop across the barrier is approximately equal to V_{SD}, and the minima positions should precisely reflect the energy difference $E_1 - E_F$. However, since the conductivity of the devices in this regime is determined by an interplay between reduced carrier mobility and velocity in the second subband and increasing applied source-drain voltage, the relationship between the minima positions and $E_1 - E_F$ is not clear. However, the data of Fig.7.10 do show that the minima positions for both devices and both bias directions converge to the *same* value of $V_{SD} \approx 10$mV, which is of the same order as the estimate of V_{SD}^T.

To confirm this interpretation of the data would require the study of devices with different subband spacings. Attempts were made to achieve this by applying a voltage to a gate on the substrate side of the sample, but failed owing to the presence of leakage currents between this back-gate and drain. A further possibility would be to simulate the de-

vice characteristics with an appropriate theoretical model. However, in addition to the requirement of a self-consistent calculation of the subband energies for zero source-drain voltage, the presence of both current flow and the occupation of a second subband in the drain would require further self-consistent modifications to the calculated potential of the device. In light of this, such a calculation was considered to be outside the scope of this work.

7.4 Conclusions

Lateral transport and tunnelling have been investigated in single barrier diodes, induced by nanometre-scale Schottky gates. The devices display quantisation in the transconductance before pinch-off in units of $2e^2/h$, which indicates that disorder in the sample leads to the presence of a number of 1D channels in the barrier potential. The channels are believed to arise from fluctuations in the barrier potential, caused by the random positions of donor impurities in the AlGaAs layer of the heterostructure. The influence of potential fluctuations are also observed in the tunnelling regime, where pronounced shoulders appear in the differential conductivity with increasing source-drain voltage for fixed gate voltage. The shoulders occur at conductivity values lower than the conductance quantum, and the results are explained in terms of a phenomenological model, involving both tunnelling through the barrier at low source-drain voltage and transport through a few 1D subbands at high source-drain voltage.

In the transport regime at low fixed gate voltage, strong minima are observed in the differential conductivity with increasing source-drain voltage. This reduction in the conductivity is attributed to the injection of electrons into the second subband of the 2DES, which results in a decrease in the carrier velocity *and in addition*, a decrease in the mobility due to interband scattering.

7.5 Resonant Lateral Tunnelling in Dual-Gate Devices.

7.5.1 Introduction

The concept of using nanometre-scale Schottky gates to induce narrow tunnelling barriers in a 2DES can be extended to produce the lateral analogues of a number of more complicated vertical devices. A variety of structures have been proposed, which include dual-gate resonant tunnelling diodes [90,59,58], lateral-superlattice-field-effect-transistors with either uni-directional or grid-like lattices [91,92], and three terminal devices such as the tunnelling-hot-electron-transistor (THETA) [60]. Although these types of devices have many advantages over their vertical counterparts (discussed elsewhere in this thesis) the inherently poor precision of lithography as compared to epitaxial growth techniques means that quantum phenomena such as resonant tunnelling are often difficult to observe. In addition, the tiny current densities, low operating voltages and requirements of low temperature operation lead to the conclusion that conventional commercial applications are unrealistic, at least with current technologies. Despite this slightly pessimistic outlook, multi-barrier lateral devices provide a useful opportunity to study both lateral tunnelling and the physics of a 2DES. A simple example of this is to use the confined energy levels present in a double barrier device to perform spectroscopy on the 2DES itself.

In this section, a study of a dual-gate, lateral resonant tunnelling diode (LRTD) is presented. The device is fabricated using an identical process to the single gate device described above except that the gate is replaced by two, 50nm long (in the tunnelling direction) Cr/Au gates, separated by a 60nm wide gap. The gates are both connected to a single gate finger on one side of the Hall bar, and are thus electrically shorted. A sketch of the structure is given in Fig.7.12. Similar devices have been reported by Ismail *et al.* [58] and Chou *et al.* [59] who used 60:60:60nm and 80:100:80nm (gate:gap:gate) geometries re-

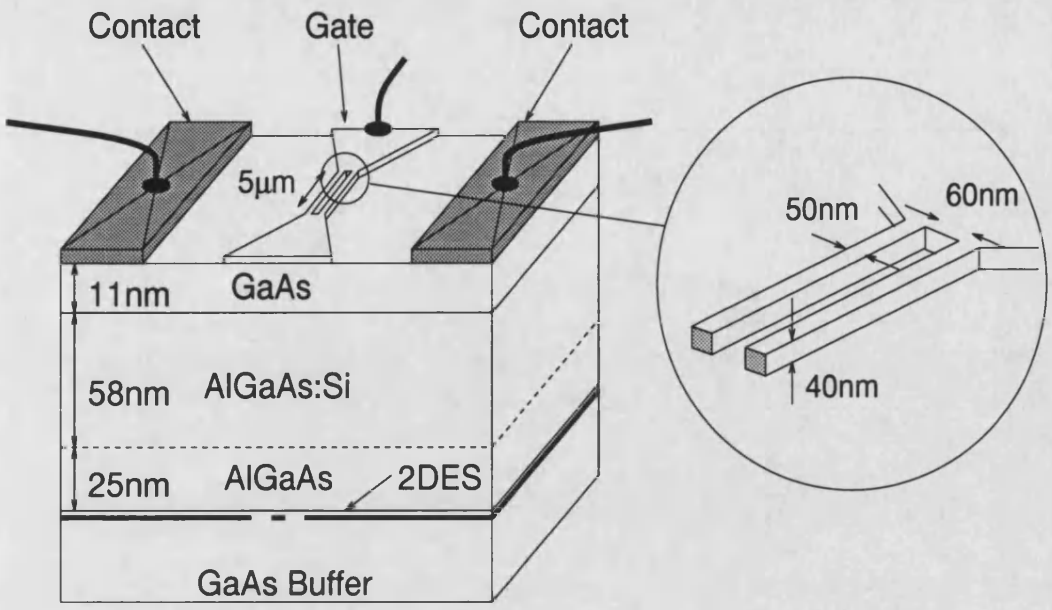

Figure 7.12: *Schematic diagram of the RLTD structure.*

spectively and Ti/Pt and Ti/Au gate materials respectively. In both the reported devices, resonant tunnelling effects were observed as peaks in either I_{SD} or dI_{SD}/dV_{SD} as a function of V_{GD} for constant V_{SD} at low temperature. Neither device displayed negative differential resistance (NDR) in the I_{SD}-V_{SD} characteristics at constant V_{GD}, although weak features were observed in the source-drain current.

It is important to outline the differences, particularly in the energy scales and physical dimensions involved, between vertical and lateral resonant tunnelling devices. Resonant tunnelling was discussed in detail in Chapter 2, with particular reference to the vertical case. To recap, typical vertical structures use rectangular barriers, a few nanometres wide, separated by a similarly sized well. Barrier heights are generally of the order of a few hundred meV above the conduction band edge in the electrodes and at zero applied bias, depend only on the material combination chosen. For a rectangular well with width l, the bound

state energies E_n can be estimated by assuming infinitely high barriers,

$$E_n = \frac{\hbar^2 \pi^2 n^2}{2m^* l^2} \tag{7.11}$$

which shows that the energy spacing of the levels decreases rapidly for an increasing well width. It is common for vertical structures with narrow wells to contain only a single bound state, a few hundred meV above the bottom of the well.

In contrast, field effect lateral devices rely on smooth potential barriers, where both the barrier height and the width of the barriers and the well are strongly dependent on the gate-voltage. Exact dimensions and energy scales are difficult to measure, but heights of the order of 10meV above E_F and dimensions at half height of $\sim$ 50nm for both the barriers and the well are probably typical. Assuming a roughly parabolic shape for the potential well means that the energy level spacing is approximately *constant* for a particular value of V_{GD}. Numerical calculations in [59] suggest typical energy level spacings in the range of a few meV under normal operating conditions.

Since the energy of the first confined state in a vertical diode is generally much larger than E_F, empty states for tunnelling in the collector exist over the whole energy range of the Fermi sea in the emitter, if the device is biassed to the resonance condition. This means that the collector can essentially be ignored in understanding the resonant tunnelling process. This is not the case for lateral diodes where the wide well and low barriers mean that many of the bound states may lie below E_F at zero source-drain bias. This leads to the addition of a further constraint to the resonance condition described in Chapter 2, namely that the bound state must lie below E_F in the source (E_F^S) *and* above E_F in the drain (E_F^D) for resonant current to flow. Fig.7.13a) shows a sketch of potential energy profile of a typical device, biassed to the resonant condition.

In light of the results for single barrier devices, it must be assumed

that any 2D double barrier device can also be considered to be a parallel array of quasi-1D barriers. Given that the expected dimensions of the potential fluctuations ($\sim$ 100nm [81]) are of the same order as the length of the device (in the tunnelling direction), it is assumed that the two barriers in each quasi-1D potential are roughly similar in size. In addition, the inhomogeneity in the barriers will result in a broadening in the quasi-bound state energies in the quantum well.

7.5.2 Experimental Results

Experimental results are presented for a single LRTD with the dimensions described above. The device is one of three that were patterned on the same Hall bar sample; of the other two devices, one had a break in the gates, preventing the closure of the channel, and the second displayed only very weak resonant tunnelling characteristics. Electron micrographs of a typical LRTD, fabricated on a GaAs test sample are shown in Chapter 4. All the measurements presented in the following were performed at a temperature of 1.5K without illumination of the sample, using the methods described above and in Chapter 5.

Resonant tunnelling was studied in the LRTD by using the two variable parameters V_{SD} and V_{GD} to move the quasi-bound state energies in the quantum well relative to E_F^S, the Fermi level in the source. As with the single barrier devices, data were taken in two different modes of operation,

1. I_{SD} measured as a function of V_{GD} for fixed V_{SD}.
2. I_{SD} measured as a function of V_{SD} for fixed V_{GD}.

In common with the SLDT samples, leakage currents between the gate and drain were found to be smaller than minimum current sensitivity of 1pA in the voltage ranges used. Note that all the measurements are of source-drain *current* I_{SD} and not differential conductivity as was generally shown for the single gated devices.

7.5.3 Characteristics for Constant Source-Drain Voltage

Fig.7.13b) and c) show characteristics for the LRTD operated in Mode 1 with V_{SD} =0.1mV. The device exhibits a very sharp reduction in I_{SD} for negative gate voltages larger than -0.25V, and the 2D channel is pinched-off for $V_{GD} \approx$-0.4V. In the gate voltage region just after pinch-off, a number of strong current resonances are observed, of which three show negative transconductance. The peaks become sharper and more clearly defined for the largest negative values of V_{GD} and the magnitude of the peak current decreases. The last two peaks (shown in Fig.7.13c)) are almost symmetric in V_{GD} and have very large peak-to-valley ratios (PVR's) of 12.9 and 30.3. These data were qualitatively reproducible after warming to room temperature and re-cooling to 1.5K.

The characteristics are interpreted purely in terms of resonant tunnelling through quasi-bound states in the quantum well. With increasing $|V_{GD}|$, the states in the well move upwards in energy as the height of the barriers increases. As each state passes the energy range of filled source states and empty drain states ($E_F^S > E_n > E_F^D$), resonant current can flow, resulting in a peak in I_{SD}. For small barrier heights above E_F^S (small $|V_{GD}|$ above pinch-off), the component of the current due to non-resonant tunnelling is relatively large and the peaks are not well defined. As the barrier height increases, the non-resonant current is suppressed and the valley current drops almost to zero. The reduction in the peak height with increasing $|V_{GD}|$ can be attributed to a decrease in the transmission coefficients of the barriers with increasing barrier height. Further current peaks would be expected at still more negative gate voltages, but were below the resolution of the measurement apparatus.

The results are consistent with the picture of an inhomogeneous barrier potential, and it is probable that the majority of the resonant current flows at the lowest saddle points in the potential. In support of this, at-

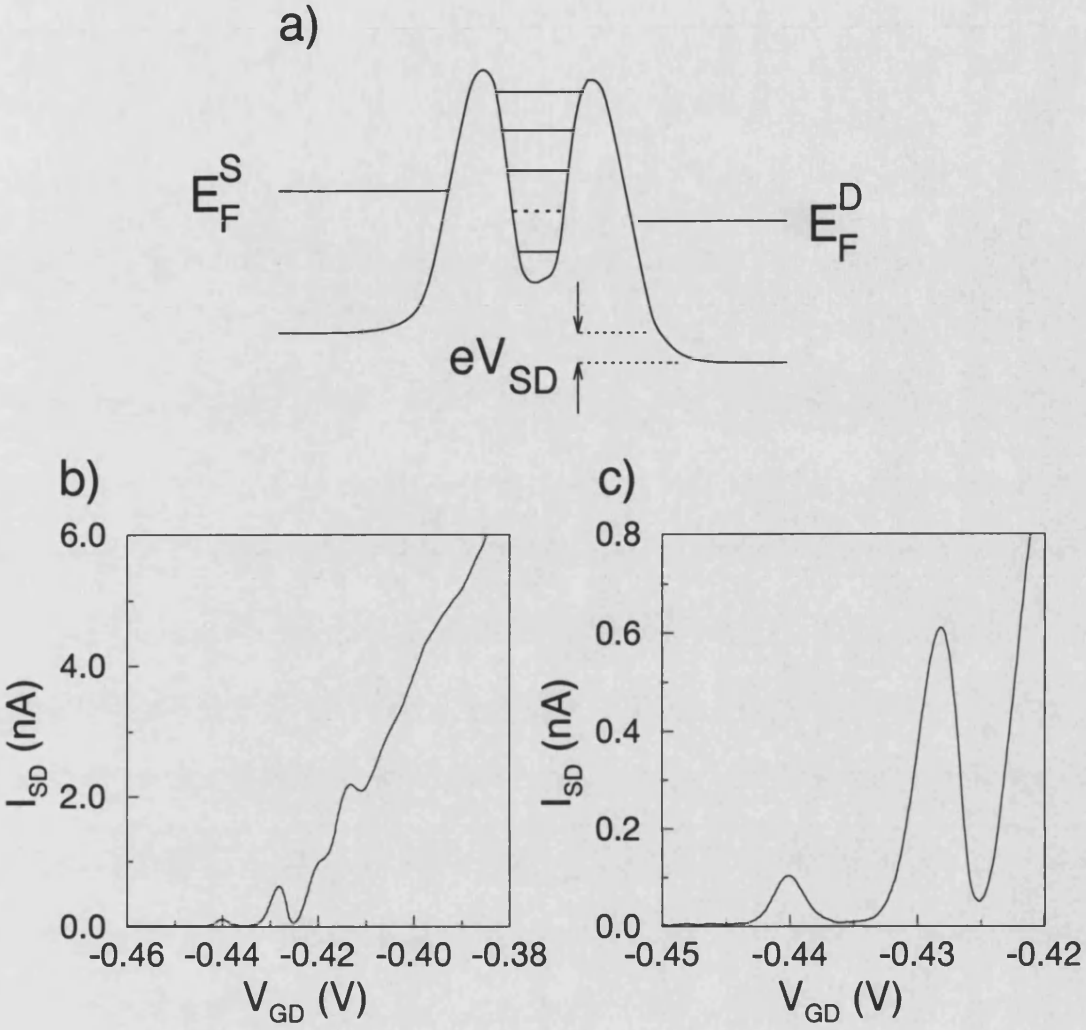

Figure 7.13: a). *Sketch of the subband energy profile for a LRTD for fixed* V_{GD} *and small* V_{SD}. *For this profile, resonant tunnelling can occur through the bound state indicated by the dotted line. Tunnelling via lower energy states is blocked by the filled states in the drain.* b). *Source-drain current* I_{SD} *as a function of the gate voltage* V_{GD} *for a constant source-drain voltage* V_{SD}=0.1mV. c) *The same data on an expanded current scale. The two peaks have PVR's of 12.9 and 30.3*

tention is drawn to the very tiny resonant currents flowing (< 1nA). These values are of the same order as those measured in some quantum dot structures [93] whose dimensions ($\sim$ 100nm) are of the order as the estimated width of the potential fluctuations here.

An alternative explanation for the data needs to be considered; resonant tunnelling through a dot-like quantum well in the barriers, induced by a positively charged background donor impurity, as was observed in a split gate device by McEuen *et al.* [78]. Although there are qualitative similarities between the two sets of data, this interpretation is considered unlikely for the following reasons. Firstly, assuming the impurity is situated within the z-direction extent of the electron wave function in the 2DES, and taking a background impurity density of $\sim 10^{14}\text{cm}^{-3}$, the number of impurities under the gate area can be calculated as ~ 1. A quantum well induced by the electric field from a charged impurity would need to lie at roughly the geometric centre of the two barriers to support a significant resonant current. Given the small number of impurities in the plane of the 2DES under the gate, this is considered highly improbable. In addition, although resonant effects were only seen in one of three devices measured, the data were reproducible over warming and cooling cycles, which is generally not the case for effects associated with impurities [78].

The influence of the source-drain voltage on the Mode 1 characteristics is shown in Fig.7.14 for values of V_{SD} between 0.1 and 5mV. As V_{SD} is increased, both the peak current and the non-resonant current rise sharply, leading to a strong reduction in the PVR's. As an example, for V_{SD} =0.5mV the PVR's for the two most sharply defined peaks fall to 3.5 and 13.7 compared to 12.9 and 30.3 for V_{SD} =0.1mV. This can be understood in terms of the transmission coefficients for both resonant and non-resonant current, which increase as the potential profile becomes tilted down in energy. Tilting the potential profile will also reduce the bound state energies in the well in relation to E_F^S. This effect

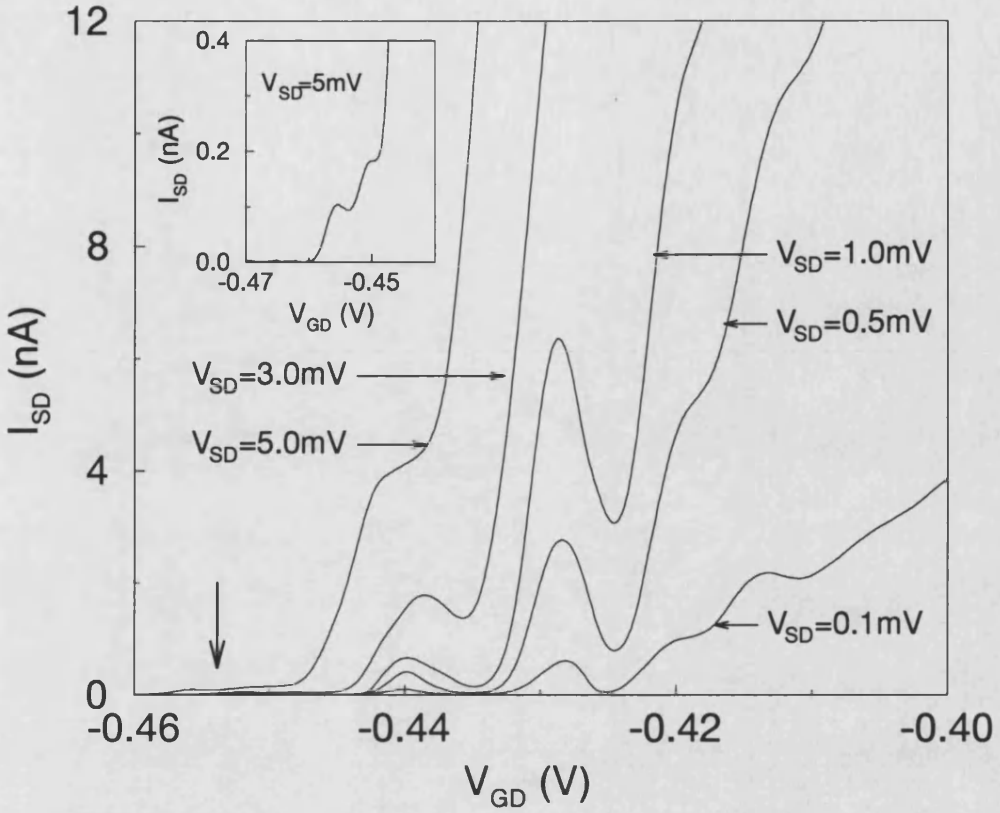

Figure 7.14: *Source-drain current I_{SD} as a function of the gate voltage V_{GD} for different values of the source-drain voltage V_{SD}. Inset shows a magnified view of the curve for V_{SD} =5mV in the region of the arrow, indicating two additional current resonances that occur at large $|V_{GD}|$.*

can be observed in Fig.7.14 where the peak positions tend to slightly more negative values of V_{GD} with increasing V_{SD}. A further influence of increasing V_{SD} is to increase the offset between E_F^S and E_F^D, i.e. the energy window in which a bound state can remain in resonance becomes wider. It is plausible that this accounts for the broadening of the current peaks that occurs with increasing V_{SD} in the experiment, although the broadening does not increase monotonically with V_{SD} as would be expected from this simple model.

At the highest source-drain voltage studied (V_{SD} =5mV), the first

three peaks are no longer observed, and the fourth remains only as a shoulder. This is attributed to the strong asymmetry that exists in the potential profile at high V_{SD}, where the upper energy levels are no longer confined in the well and no longer support resonant tunnelling. For V_{SD} =5mV however, two small *additional* peaks are resolved (shown on the inset of Fig.7.14) at more negative gate voltages. These are assigned to resonant tunnelling via states low down in the quantum well. At low V_{SD}, tunnelling via these states is suppressed, since the large gate voltages required to bring them close to E_F^S result in a vanishingly small transmission coefficient.

7.5.4 Characteristics for Constant Gate Voltage

Previous authors have shown that the negative differential resistance (NDR) features, characteristic of the *I-V* properties of vertical RTD's (see Chapter 2), are difficult to resolve in the Mode 2 characteristics of their LRTD analogues. As examples, in both [59] and [58], evidence for resonant tunnelling in the I_{SD}-V_{SD} characteristics is only seen as weak shoulders in the current.

Fig.7.15a) shows an I_{SD}-V_{SD} characteristic of the LRTD studied here, for a single value of V_{GD} chosen to lie between the two well defined current peaks in the Mode 1 characteristics. For this device a *strong* resonance exists in the current, which shows pronounced NDR (Fig.7.15b)) and a PVR of 1.15. The current increased roughly exponentially for higher values of V_{SD}, and no further features were observable in either I_{SD} or the numerical derivative dI_{SD}/dV_{SD}. Note that as with the Mode 1 data, the magnitude of the resonant current is small, indicating that the current may be flowing at a single quasi-1D point in the electrostatic potential.

Fig.7.16 shows the Mode 2 characteristics over the range of V_{GD} in which this single current resonance was observed. For the smallest

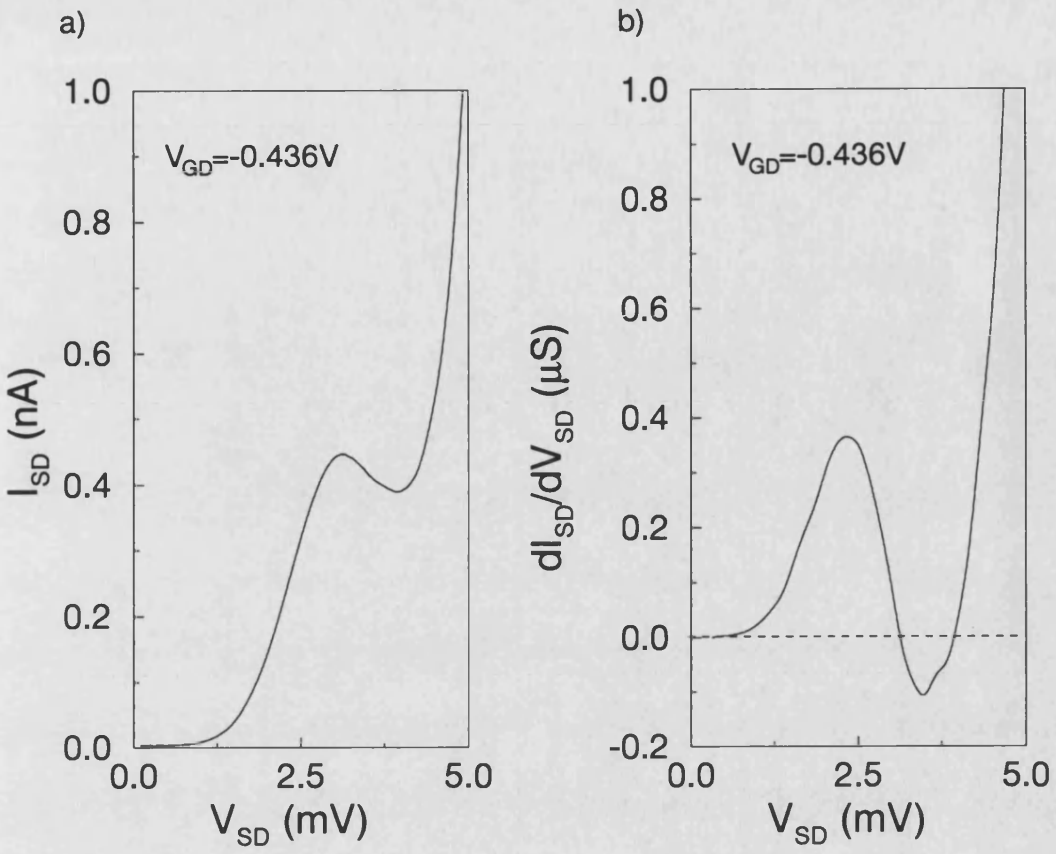

Figure 7.15: *a) I_{SD}-V_{SD} characteristic for the device at a gate voltage V_{GD}=-0.436V, showing a strong current resonance and pronounced NDR. b) Numerical derivative of the I_{SD}-V_{SD} characteristic.*

value V_{GD}=-0.432V, the current shows a straightforward non-linear dependence on V_{SD}. With an increase of *only* 2mV in $|V_{GD}|$ the current resonance is strongly resolved, with an onset at $V_{SD} \approx 0$. Subsequent small increases in $|V_{GD}|$ shift the resonance to higher V_{SD} where it finally becomes smeared out and remains as only a weak shoulder in the current. The onset of the exponentially increasing, non-resonant current in each case shows the expected monotonic shift to higher V_{SD} with increasing $|V_{GD}|$. No resonant features were observed in the current in other gate voltage ranges.

These data can be explained within the picture of resonant tunnelling

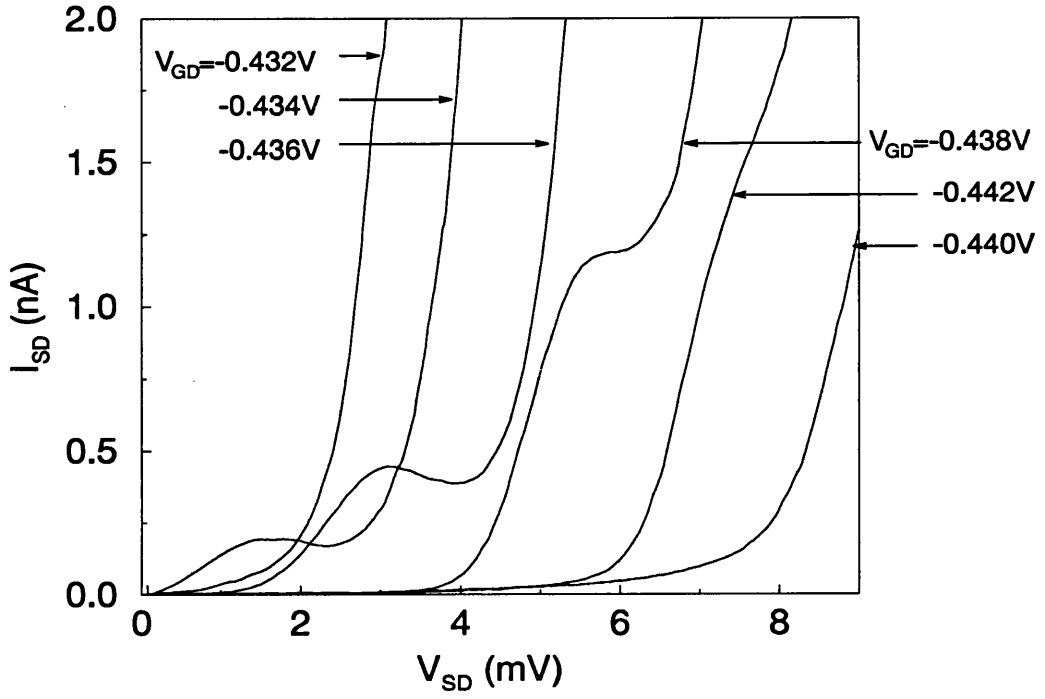

Figure 7.16: *Mode 2 characteristics for the LRTD for six values of the gate voltage V_{GD} between -0.432V and -0.440V.*

through a single quasi-bound state (with energy E_N^0 at equilibrium) in the quantum well. Given that non resonant tunnelling is observed for $V_{SD} \approx 0$ and $V_{GD} = -0.432V$ it is assumed that E_N^0 lies below E_F^S, and therefore the state is occupied in equilibrium. This situation has been studied previously for a vertical resonant tunnelling diode with a triangular quantum well [94]. The authors in [94] proposed that owing to the presence of strong electron-electron scattering, that resonant tunnelling through an occupied bound state in a quantum well is only poorly resolved in the current. This picture is consistent with the data of Fig.7.16 where no current resonance is observed for $V_{GD} = -0.432$V. With a small increase in $|V_{GD}|$, the peak in I_{SD} appears, with an onset at $V_{SD} \approx 0$, which implies that the E_N^0 is situated *at* the Fermi energy. For $E_N^0 \geq E_F^S$, the quasi-bound state state is not occupied and hence the electron scattering mechanism no longer exists.

Subsequent increases in $|V_{GD}|$ cause a monotonic increase in the size of the barriers and result in a shift of E_N^0 to higher energies. This is manifested in the observed shift in the resonance position to higher V_{SD} with increasing $|V_{GD}|$. For the highest values of $|V_{GD}|$ shown it is assumed that resonant component of the current becomes small, due to the strong asymmetry that exists in the two barriers at large V_{SD}. For this case the current resonance becomes obscured by the non-resonant component of the current.

7.6 Conclusions

In conclusion, lateral resonant tunnelling in a 2DES has been demonstrated in a double barrier device, induced by nanometre-scale Schottky gates. The device exhibits strong resonances in the source-drain current as a function of the gate voltage near pinch-off for constant source-drain voltage. The two strongest resonances show peak-to-valley ratios of 12.9 and 30.3. Pronounced negative differential resistance is observed in the source-drain current-voltage characteristics in only a narrow range of fixed gate voltages.

The results can be explained within a standard model of resonant tunnelling. Taking into account the results for single barrier structures and the small magnitude of the peak currents measured, it is probable that resonant tunnelling only occurs at weak points in the barrier potential.

8 Lateral Tunnelling in a Perpendicular Magnetic Field

8.1 Introduction

Experimental evidence supporting the edge state picture of the integer quantum Hall effect has been widely published (see [47] for a review) since Büttiker's proposal that quantum Hall plateaus could be explained in terms of perfect reflection and transmission of 1D channels at the sample contacts. Many of the reported experiments have confirmed the validity of the Landauer-Büttiker (LB) formalism by modifying the transmission or reflection coefficients for different edge channels in the sample itself with the introduction of a potential barrier to the current flow.

An elegant demonstration of this kind was reported by Haug *et al.* [95,96] who studied a Hall bar sample with a 10μm wide Schottky gate bisecting the two voltage probes (see Fig.8.1a)). Applying a negative voltage to the gate causes a local electron depletion of the 2DES under the gate, which can be regarded as a low potential barrier to electron transport. In a perpendicular magnetic field, partial depletion of the 2DES under the gate will result in different filling factors ν in gated and ungated regions of the sample. In the edge state picture, when integer values of ν exist in both regions, edge states will either be completely reflected or transmitted at the barrier (Fig.8.1b)) and the sample resistance can be simply predicted using the LB formalism. This approach is verified in the experiment where the four terminal resistance R_{23} was measured as a function of the gate voltage (sketched in Fig.8.1c)) for a constant current I_{14} at fixed magnetic field. R_{23} displays quantised values in particular gate voltage regimes which correspond to near integer filling factors under the gate. The quantised values agree exactly with those predicted by the LB formula.

Although such experiments have confirmed a large number of predictions made by the edge state model, definitive proof that the current flows only at the edges of the sample does not exist to date [47].

In general, experiments using wide potential barriers, can only be

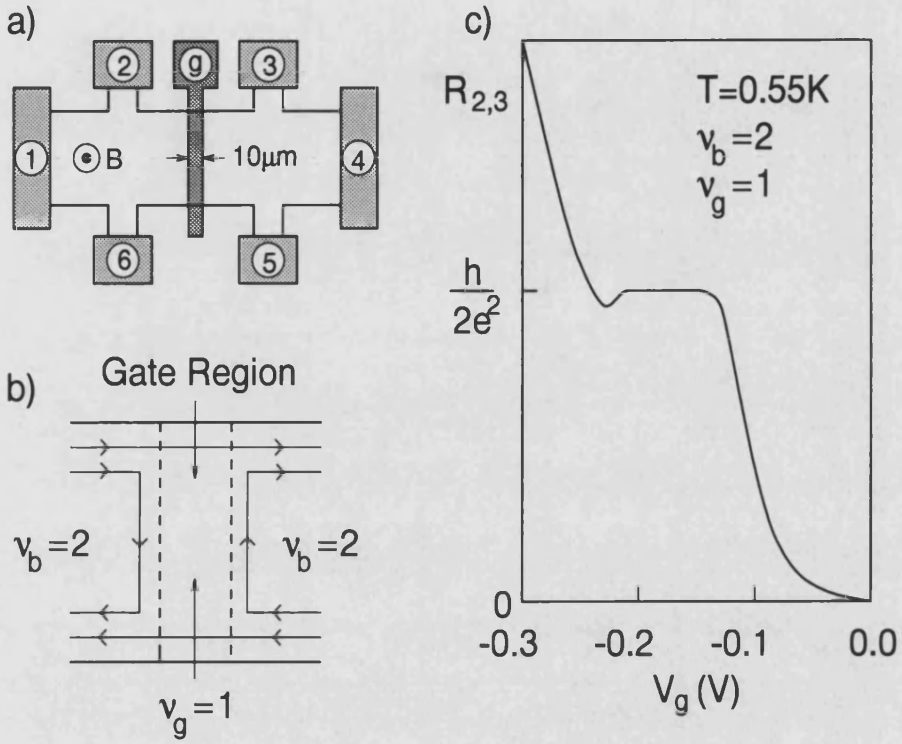

Figure 8.1: *Edge state reflection and transmission at a wide potential barrier in a strong perpendicular magnetic field. a). The sample geometry with a 10μm wide Schottky gate across the Hall bar. b). Schematic diagram of the edge state trajectories in the gate region (indicated by the dashed line) for a bulk filling factor $\nu_b = 2$ and a filling factor under the gate $\nu_g = 1$. c). Sketch of experimental data from Haug et al. [96]. The plateau at $R_{2,3} = h/2e^2$ occurs for the gate voltage range where the filling factor under the gate $\nu_g = 1$.*

used to study effects involving complete reflection or transmission of edge states. If, on the other hand the potential barrier is made high ($> E_F$), but also very thin ($<$ 100nm), then the only transport mechanism available to electrons at low temperature is tunnelling between edge states

on both sides of the barrier. Since tunnelling processes are sensitive to the density of states in the electrodes, tunnelling experiments should provide a useful method for studying edge states in a 2DES.

In the following sections, a model of lateral tunnelling between edge states is presented and used to predict the properties of both SLTD's and quantum trench diodes in a perpendicular magnetic field. The predictions are then compared to experimental data for both types of device, and the comparison is used to discuss the validity of the edge state picture in relation to this kind of tunnelling problem.

8.2 Model of Tunnelling Between Edge States

The model of lateral tunnelling between edge states described in the following sections was first proposed by Tejedor *et al.* [97], who considered the ideal case of two, 2D electrodes, separated by a trapezoidal barrier with a barrier height much larger than the Fermi energy. In a perpendicular magnetic field, the trajectories of all edge states incident on the barrier are deflected to the opposite edge of the sample, a situation sketched in Fig.8.2. A longitudinal current can therefore only

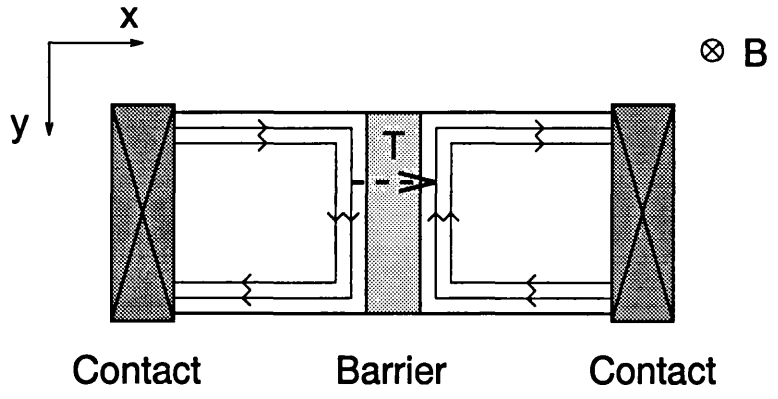

Figure 8.2: *Schematic representation of ideal 2D electrodes separated by a thin barrier. The arrowed lines indicate the trajectories of the reflected edge states. The dashed arrow represents a possible tunnelling path between two edge states with a transmission probability T*

be supported by electrons which tunnel between edge states on opposite sides of the barrier and *cannot* be described using the LB scheme. Working within the Landau gauge (see Chapter 3) with a vector potential $\vec{A} = (0, Bx, 0)$ gives solutions to the Schrödinger equation (SE) which are plane waves in the y-direction. Thus, in common with tunnelling in zero magnetic field, tunnelling processes between edge states on either side of the barrier *must* conserve parallel momentum k_y in the absence of scattering.

Tejedor's model is based on the idea that for a finite barrier height, when edge states in the source and drain are only very weakly coupled, the edge states dispersions from the source and drain can be considered independently and will intersect in the barrier region at well defined *crossing energies.* This is outlined schematically in Fig.8.3 which shows the edge state dispersion as a function of the orbit centre coordinate x_0 in the barrier region. It is important to note that while the orbit centres can lie within the barrier, *classically, the electrons themselves perform skipping orbits along its outer edge.* The crossing points indicate states from source and drain which have the same energy *and* parallel momentum ($k_y \sim x_0$) and hence tunnelling processes via these states (generally referred to as tunnelling channels) can conserve total energy and parallel momentum. All other tunnelling paths require a scattering event such as phonon emission or capture and are thus strongly suppressed. Spin splitting is ignored in this part of the model, as is any broadening of the Landau levels in the barrier region, and it is therefore convenient to define a new spin-degenerate filling factor ν' where $\nu' = \nu/2$. Furthermore, zero temperature is assumed in all the calculations.

Increasing the magnetic field in such a system, at a constant source-drain bias V_{SD}, increases the energies of the tunnelling channels in the barrier. As each channel rises above the Fermi energy in the source $E_F^S(B)$ it will no longer be available for tunnelling and the current will decrease in a step-like manner. Conversely, increasing V_{SD} at constant

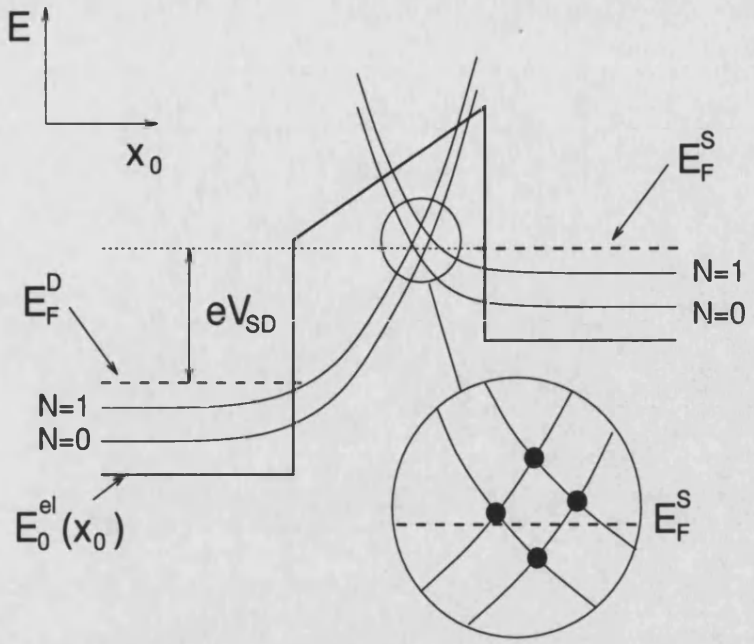

Figure 8.3: *Energy dispersion of the N=0 and N=1 edge states as a function of the orbit centre coordinate x_0 (spin splitting ignored). $E_0^{el}(x_0)$ is the electrostatic barrier potential with an applied bias V_{SD} and E_F^S and E_F^D are the Fermi energies in the source and drain respectively. The black circles in the blown up region indicate crossings between edge states.*

magnetic field will cause new channels to fall below the $E_F^S(B)$, resulting in step-like *increases* in the current. In addition, for the magnetic field range where $\nu' < 1$ in the source, no tunnelling channels exist below $E_F^S(B)$ and the model predicts that no current should flow if broadening and spin splitting are ignored in the Landau levels.

Based on this model, the current-voltage properties of a lateral diode in a perpendicular magnetic field should exhibit a very detailed spectrum of current resonances. The observation and evaluation of such a resonance spectrum would add strong support to the edge state picture of a 2DES in a perpendicular magnetic field.

8.3 Theory

The aim of the following analysis is to develop a basis for the calculation of the resonance spectra for both SLTD's and quantum trench diodes in a perpendicular magnetic field, within the framework of Tejedor's model. Unlike the discussion in [97] however, the starting point for both calculations is a smooth electrostatic potential barrier profile. For the gated devices, the potential is modelled phenomenologically as a simple inverted parabola for reasons discussed in later sections. For the quantum trench structures, the numerical potentials, calculated in Chapter 6 are used.

Making the approximation once again that the barrier is infinitely long in the $y-$direction means that the edge state dispersion in the barrier region can be obtained from a 1D Schrödinger equation as a function of the magnetic field for different values of the applied bias. The crossing points between source and drain edge states can then be calculated as a function of the magnetic field and compared to $E_F^S(B)$ which *oscillates* in a perpendicular magnetic field. In this way, a detailed spectrum can be developed, showing values of B and V_{SD} for which the crossing points and $E_F^S(B)$ are coincident in energy, and hence where resonances should occur. Although methods for calculating the tunnelling current exist [97] they go beyond the scope of this work.

8.3.1 Method for Calculating the Edge State Dispersion

The 1D Schrödinger equation (SE) in the plane of a 2DES was given in Chapter 3 in the Landau gauge $\vec{A} = (0, Bx, 0)$ as,

$$\left[-\frac{\hbar^2}{2m^*}\frac{\partial^2}{\partial x^2} + \frac{e^2B^2}{2m^*}(x - x_0)^2 + E_0^{el}(x)\right]\psi(x - x_0) = E_{N,k_y}\psi(x - x_0). \tag{8.1}$$

Solutions take the form,

$$\Psi(x, y) = exp(ik_y y)\psi(x - x_0) \tag{8.2}$$

where the orbit centre coordinate $x_0 = \hbar k_y/eB$ and $E_0^{el}(x)$ is the electrostatic potential.

The edge state calculation treats the left and right hand sides of the potential barrier separately. Far from the barrier, solutions to the SE are simple bulk Landau levels with eigenvalues $E_N = (N+1/2)\hbar\omega_c$. Within roughly a magnetic length of the barrier region, where the electrons feel the electrostatic potential, the eigenvalues increase sharply and the SE is solved numerically assuming that the wavefunction has a node at the maximum of the electrostatic barrier.

Taking the right hand side as an example, values for E_N are cal-

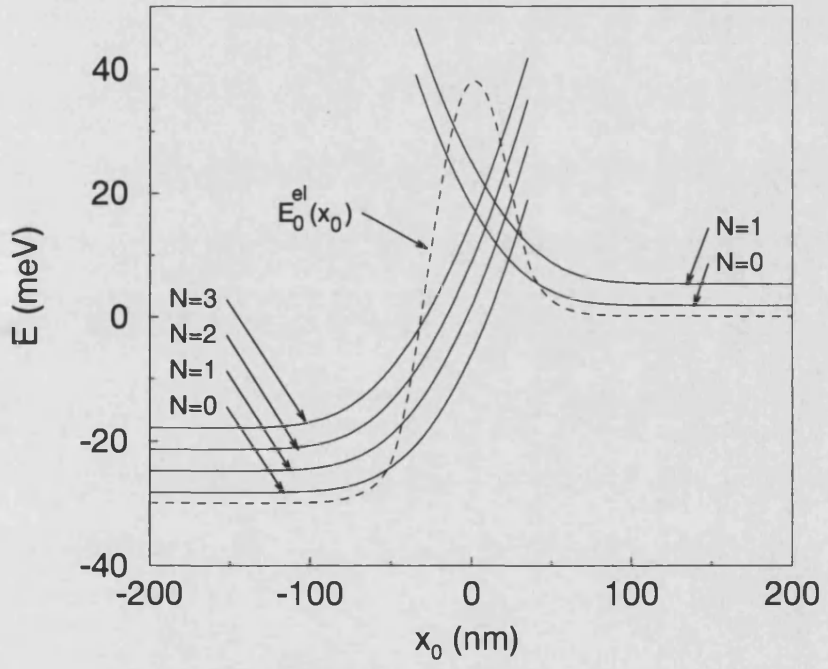

Figure 8.4: *Calculated edge state dispersion as a function of x_0 for a 45meV high quantum trench potential barrier under an applied bias of 30mV. The magnetic field is 2T and the dashed line indicates the electrostatic potential $E_0^{el}(x_0)$*

culated for orbit centres x_0 lying at 0.1nm intervals underneath the

geometric centre of the barrier up to a point three magnetic lengths beyond its outer edge. To calculate values for E_N, the following iterative method is used for each value of the magnetic field B. Starting at the outer edge of the x_0 range, an initial value is chosen for E_N, based on the corresponding bulk Landau level energy. For this eigenvalue and using an electrostatic potential $E_0^{el}(x_0)$, the SE is solved for the electron wave function $\psi(x)$ over an x-range of three magnetic lengths either side of the x_0 coordinate. The eigenvalue is assumed to be correct if the calculated wave function has the correct number of turning points ($M = 2(N+1)$) for the particular edge state index N *and* if

$$\begin{aligned} \Psi(x) &\rightarrow 0 \qquad \text{for } x << x_0 \\ \Psi(x) &\rightarrow 0 \qquad \text{for } x >> x_0 \end{aligned} \tag{8.3}$$

If these conditions for $\Psi(x)$ are not fulfilled, E_N is updated and the procedure repeated.

Fig.8.4 shows the calculated edge state dispersion for a model potential barrier of a typical quantum trench diode in a magnetic field of 2T. The zero bias barrier height was 45meV, and the calculation was made for an applied bias of 30mV.

8.3.2 The Fermi Energy in a Perpendicular Magnetic Field

The oscillatory behaviour of the Fermi energy $E_F(B)$ in a 2DES under the influence of a perpendicular magnetic field has been widely studied both experimentally and theoretically (see for example [98] and [99] respectively). At zero temperature, $E_F(B)$ is defined as the energy of the uppermost occupied state in the Fermi sea, and can therefore be calculated for a 2DES from the set of equations,

$$E_F(B) = E_0 + \int_0^{\Delta E} D_{2D}(E)dE \tag{8.4}$$

where

$$n_{2D} = \int_0^{\Delta E} D_{2D}(E)dE \tag{8.5}$$

for n_{2D} electrons and a 2D density of states (DOS) $D_{2D}(E)$. The form of the DOS was discussed in some detail in Chapter 3, and can be modelled as a sum of Gaussian functions,

$$D_{2D}(E) = n_L \sum_N \frac{1}{\sqrt{2\pi\Gamma^2}} exp\left[-\frac{1}{2}\left(\frac{E - E_{N,s}}{\Gamma}\right)^2\right] \tag{8.6}$$

where n_L is the number of electrons in each Landau level and Γ is the level broadening,

$$\Gamma = \hbar\sqrt{\frac{2eB}{\pi m^* \tau_B}} \tag{8.7}$$

The splitting of the Landau levels due to the electron spin is included as the Zeeman term in the level energy,

$$E_{N,s} = (N + \frac{1}{2})\hbar\omega_c + sg^*\mu_B B \tag{8.8}$$

where g^* is the *enhanced* Landé g-factor. g^* contains many-body corrections due to the Coulomb interaction between electrons in spin-up and spin-down states. A simple model for calculating the g^* was published by Berg *et al.* [100] as,

$$g^* = g + \frac{1}{g\mu_B} E_{xc} \frac{N_\uparrow - N_\downarrow}{N_\uparrow + N_\downarrow} \tag{8.9}$$

where $N_\uparrow$ and $N_\downarrow$ are the numbers of electrons in spin-up and spin-down states respectively and $g = -0.44$ for GaAs. E_{xc} is an electrostatic exchange interaction energy between electrons and $E_{xc} = 6$meV. From Eqn.8.9 it can be clearly seen that the enhanced g-factor is proportional to the difference in the number of spin-up and spin-down electrons in the uppermost occupied Landau level. More exact methods for calculating g^* are given in [101].

Fig.8.5 shows the Fermi energy, calculated using Eqn.8.4-8.9 as a function of B for a 2DES with $n_{2D} = 2.5 \times 10^{11}\text{cm}^{-2}$. Also plotted on the

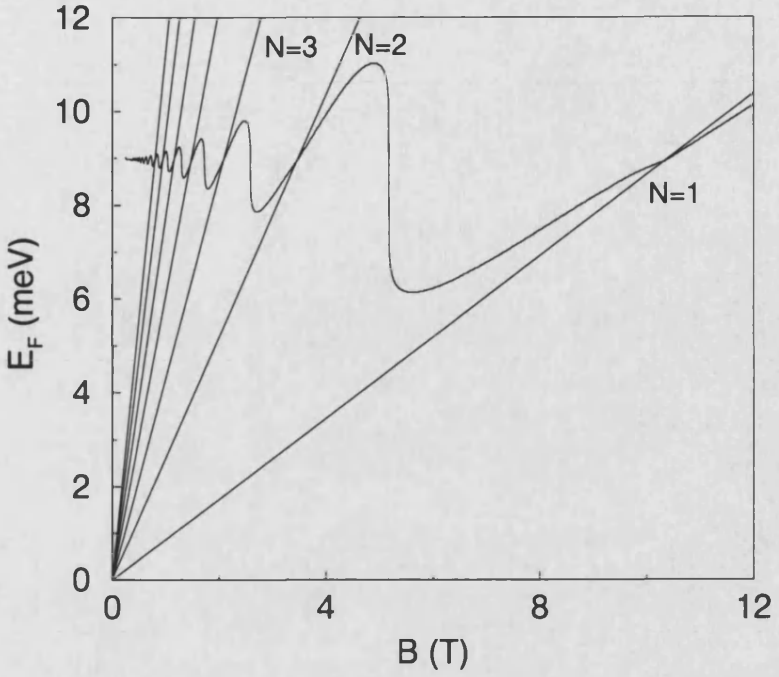

Figure 8.5: *Calculated Fermi energy as a function of magnetic field for an electron density* $n_{2D} = 2.5 \times 10^{11} cm^{-2}$ *and a scattering time* $\tau_B = 5 \times 10^{-12}$ *seconds.*

figure are the delta function Landau level dispersions $E_N = (N+1/2)\hbar\omega_c$ for values of N from 0 to 6. A value $\tau_B = 5 \times 10^{-12}$ seconds was taken for the mean time between scattering events, which effectively defines the Landau level broadening. This value of τ_B was chosen to give a good fit between $E_F(B)$ and experiments described in [99].

The calculated data in Fig.8.5 show the well known *sawtooth* oscillations which occur in E_F with increasing magnetic field. For most values of B, $E_F(B)$ is *pinned* at the large density of states in the centre of the uppermost occupied Landau level. The sharp drops occur during the rapid depopulation of the small DOS that exists between each Landau level. Note that with the value of τ_B taken for the calculation, drops in $E_F(B)$ at odd-integer values of the filling factor (spin states) are only observed as a weak feature for $\nu = 1$. The inclusion of spin effects is

however justified as they have a strong influence on the DOS and therefore the magnitude of the sawtooth oscillations.

8.3.3 Method for Calculating Resonance Positions

Within the framework of the model outlined above, resonances in the differential conductivity of a lateral tunnelling device are expected whenever the source-drain voltage and magnetic field conditions are such that a tunnelling channel passes the Fermi energy in the source of the device. To illustrate the mechanism for calculating resonant values of B and V_{SD}, the model barrier potential for a quantum trench device from Fig.8.4 with an applied bias of 70mV is used as an example. Taking in this case a range of magnetic field values between 1.5 and 5T, the edge state dispersion is calculated in both the source and the drain to give defined energies at which the states intersect.

The energies at which the N=0 level in the source and the N=0...3 levels in the drain cross are plotted on Fig.8.6 for each value of the magnetic field. The label "S0D0" denotes the intersection between N=0 in the source and N=0 in the drain and so on. Also plotted on Fig.8.6 is the position of $E_F^S(B)$, the Fermi energy in the bulk of the source electrode. For this value of the source-drain voltage V_{SD}, the four tunnelling channels pass $E_F^S(B)$ (indicated on the figure by open circles) at magnetic field values of 2.75, 2.59, 2.56 and 2.41T for channels S0D0 to S0D3 respectively. At these points a step in the current and a peak in the differential conductivity would be expected. Note however that the size of each resonance will depend strongly on the transmission coefficient for the respective tunnelling channel, and hence measurable tunnelling effects will not necessarily be observed for every channel predicted by the model. This point is discussed in more detail below.

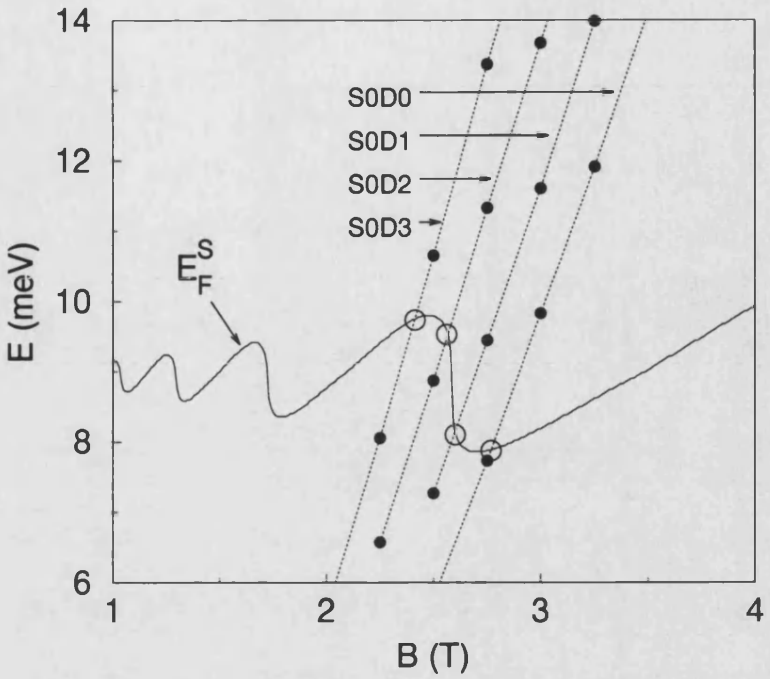

Figure 8.6: *Calculated edge state crossing energies as a function of magnetic field for the electrostatic potential of Fig.8.4 with an applied source-drain voltage $V_{SD} = 70mV$. Data shown are for the the $N = 0$ source level and $N = 0...3$ levels in the drain and the points at which the crossings pass the Fermi energy are indicated by the large open circles.*

8.4 Results for Gated Single Barrier Diodes

The following sections describe a comparison between calculations based on the theoretical analysis described above, and experimental magnetic field data for the two SLTD devices A and B whose zero field properties were described in Chapter 7. To reiterate the experimental details and results so far, the gates were roughly 50nm long in the x-direction (tunnelling direction) and 5μm wide in the y-direction, and were fabricated on a single Hall bar, patterned on a heterostructure sample. The zero magnetic field data indicated that the barriers are strongly inhomogeneous and that current flows through the lowest and thinnest regions in

the potential. The goal here is to study tunnelling effects, and hence the devices were operated in the gate voltage regime after pinch-off, where the barrier height is larger than $E_F(B = 0)$ over the whole active width of the device, for zero source-drain voltage V_{SD}. In contrast to the work on quantum trench tunnelling diodes, a quantitative description of the electrostatic barrier was not attempted for the SLTD devices. Therefore the intention of the following sections is to make a purely qualitative comparison between experiment and theory, and the electrostatic potential is modelled as a simple inverted parabola.

8.4.1 Calculated Resonance Spectrum

As a basis for an interpretation of the experimental results shown later in the chapter, this section presents a calculated resonance fan diagram for a model barrier. As a starting point, the x-direction electrostatic barrier potential for the model device in equilibrium was chosen as an inverted parabola with height $E_0^{el}(0)$ and width $2d$. For the calculations, the geometric origin $x = 0$ lies at the centre of the parabola and zero energy is defined as the 2DES subband energy at the source. In Chapter 7, the characteristics of the devices for finite V_{SD} were discussed in terms of a phenomenological model in which a fraction m of the applied V_{SD} falls across the source-half of the barrier potential and correspondingly a fraction $(1-m)$ falls across the drain-half. The same approach is used here, and assuming that none of the voltage falls across the 2D leads, the electrostatic barrier potential $E_0^{el}(x)$ is given by,

$$-d < x < 0 \qquad E_0^{el}(x) = E_0^{el}(0)\left(1 - \frac{x^2}{d^2}\right) - meV_{SD} + (1-m)eV_{SD}\left(\frac{x}{d}\right)$$

$$0 < x < d \qquad E_0^{el}(x) = E_0^{el}(0)\left(1 - \frac{x^2}{d^2}\right) + meV_{SD}\left(\frac{x-d}{d}\right) \qquad (8.10)$$

where a value $m = 0.25$ was chosen to agree roughly with the experimental data shown for $B = 0$ in Chapter 7.

Calculations were made for a model potential barrier using the following parameters;

$n_{2D} = 2.85 \times 10^{15}\mathrm{m}^{-2}$

d =7nm

$E_0^{el}(0) = 25\mathrm{meV}$

The value of n_{2D} was taken to agree with the experimental electron density obtained from magnetoresistance measurements shown later, and the chosen value for $E_0^{el}(0)$ corresponds to a barrier height above the Fermi energy of $(E_0^{el}(0) - E_F^S(B=0)) \approx 15\mathrm{meV}$. To reduce the computing time, the calculation was restricted to involve only the the first three edge state indices (N =0,1,2) in both the source and in the drain. Note that although spin splitting effects are not included in the calculation of the edge state dispersion near the barrier, the calculation of $E_F^S(B)$ does include spin. Hence for this model, tunnelling channels involving the $N = 0$ edge state in the source can exist below $E_F^S(B)$ in the magnetic field regime where $1 < \nu < 2$ (or $0.5 < \nu' < 1$).

The resonance spectrum for the model barrier was calculated for a range of magnetic field values between 1 and 9T at different, fixed values of the source-drain voltage V_{SD}. Edge states that intersect at an energy above the barrier no longer represent *tunnelling* channels and were therefore not included in the results. Thus for each tunnelling channel, the maximum value of the source-drain voltage V_{SD} used, corresponded to the point at which the crossing point energy $E^C(N_S, N_D)$ of the constituent source and drain edge state dispersions (with indices N_S and N_D respectively) rose above the maximum in the effective potential energy of the barrier $E_0^{eff}(x)$. $E_0^{eff}(x)$ consists of terms due to the electrostatic potential barrier $E_0^{el}(x)$ and the magnetic potential $E_0^B(x, x_0)$, and for a tunnelling channel with an orbit centre coordinate positioned at x_0,

$$E_0^{eff}(x) = E_0^{el}(x) + E_0^B(x, x_0) \tag{8.11}$$

where,

$$E_0^B(x, x_0) = \frac{e^2B^2}{2m^*}(x - x_0)^2. \tag{8.12}$$

The maximum in $E_0^{eff}(x)$ is assumed to occur on the source side of the barrier, at a position x_{max}. Thus, the value of x_{max} for a particular tunnelling channel can be obtained from the turning point,

$$\left(\frac{\partial E_0^{eff}}{\partial x}\right)_{xmax} = 0 \tag{8.13}$$

in the expression for the total effective potential,

$$E_0^{eff}(x) = E_0^{el}(0)\left(1 - \frac{x^2}{d^2}\right) + meV_{SD}\left(\frac{x-d}{d}\right) + \frac{e^2B^2}{2m^*}(x - x_0)^2$$

$$\text{for } 0 < x < d. \tag{8.14}$$

This gives the position of the maximum effective potential for a tunnelling channel with a centre of orbit coordinate x_0 as

$$x_{max} = ed\left(\frac{edx_0B^2 - mV_{SD}m^*}{e^2d^2B^2 - 2E_0^{el}(0)m^*}\right) \tag{8.15}$$

and therefore the condition for the maximum value of V_{SD} used for each tunnelling channel can be written mathematically as

$$E^C(N_S, N_D) < E_0^{eff}(x_{max}). \tag{8.16}$$

For this initial discussion of the model, the influence of the individual transmission coefficients on the various tunnelling channels has been ignored. Fig.8.7 shows the calculated crossing point energies $E^C(B, V_{SD})$ for the S0D0 edge state intersection, as a function of the magnetic field for five values of V_{SD} between 2mV and 10mV. Also plotted on the figure is $E_F^S(B)$. Each intersection between $E_F^S(B)$ and $E^C(B, V_{SD})$ represents a single point for the resonance fan diagram. A simple straight line extrapolation to $E_F^S(B)$ was performed for values of V_{SD} where no intersection with $E_F^S(B)$ occurred in the magnetic field range studied.

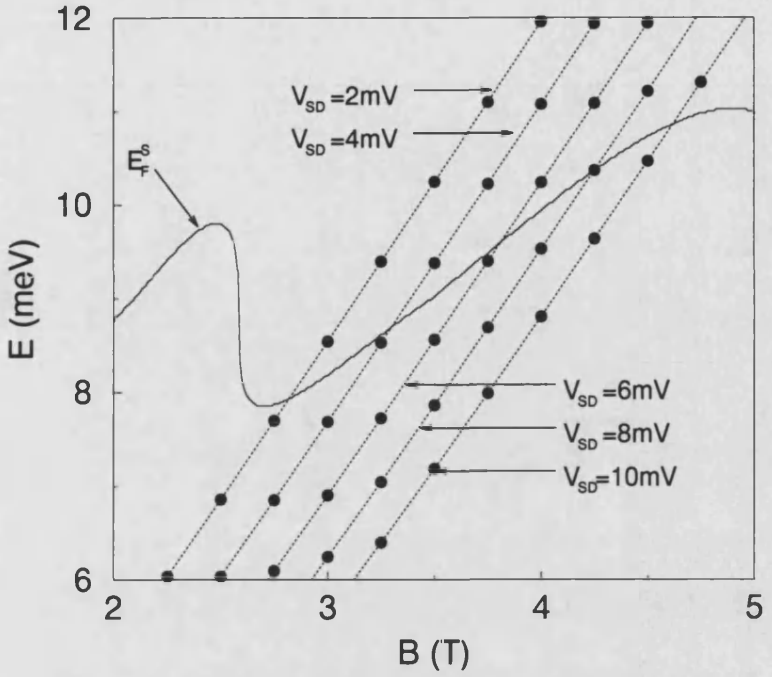

Figure 8.7: *Calculated crossing energies of the S0D0 edge state intersection for a 14nm wide, 25meV high parabolic barrier, as a function of the magnetic field B for five values of the source-drain voltage V_{SD}. Also plotted is the Fermi energy in the source $E_F^S(B)$.*

Fig.8.8a) shows a subsection of the resulting calculated fan diagram involving only the N =0 edge state in the source. Each branch of the fan shows a monotonic increase in resonant source-drain voltage V_{SD} with increasing magnetic field B. The diverging gradients of the three branches reflect the increase in the energy spacing between the three tunnelling channels with increasing B. An interesting feature of the data is the *steps* which occur in each curve at integer values of ν', where there is a rapid change in $E_F^S(B)$ within a small range of the magnetic field. The origin of this effect can be seen clearly in Fig.8.8b) which shows a plot of the S0D1 edge state crossing energies $E^C(B, V_{SD})$ as a function of B in the $\nu' = 2$ region, for a closely spaced range of V_{SD}.

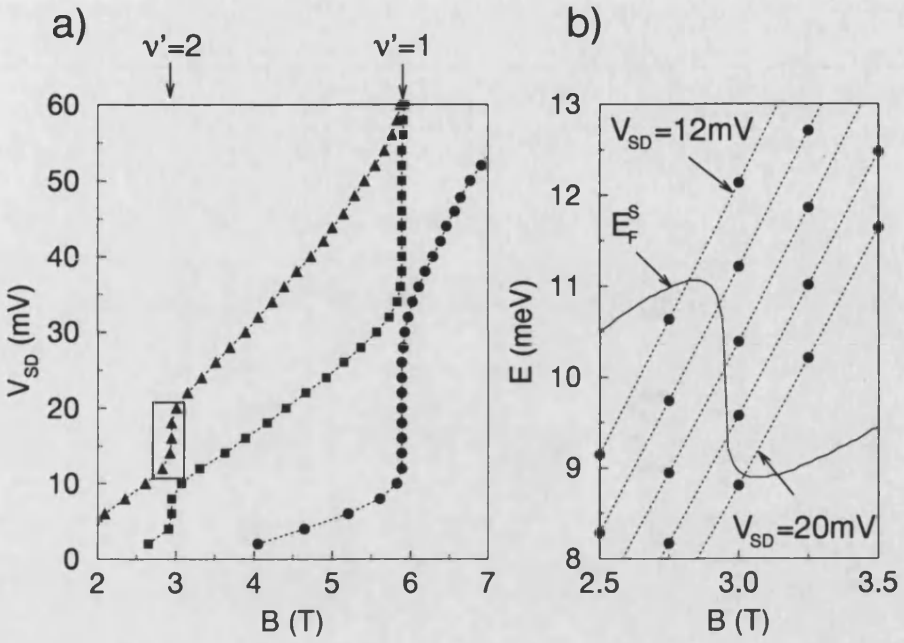

Figure 8.8: *a) Calculated fan chart for the S0D0 (solid circles) S0D1 (solid squares) and S0D2 (solid triangles) edge state intersections. The magnetic field positions of the filling factors ν' are indicated by the arrows. b) Calculated crossing energies of the S0D1 edge states as a function of the magnetic field B for five values of the source-drain voltage V_{SD}. For this range of V_{SD} the intersections with $E_F^S(B)$ occur at a roughly constant value of B and are indicated by the enclosed region on the fan diagram in a).*

From the figure, it can be seen that despite the increasing source-drain voltage, the intersections with $E_F^S(B)$ occur at an almost constant value of the magnetic field, leading to a step in the corresponding branch of the fan chart. In this way the fan chart is like an *inverse* signature of $E_F^S(B)$, i.e. drops in the position of $E_F^S(B)$ lead to an increase in the source-drain voltage position of each resonance.

To conclude this preliminary discussion of the model results, Fig.8.9 shows the full calculated fan diagram including the N =0,1,2 edge states in both the source and the drain. The model predicts a very dense range

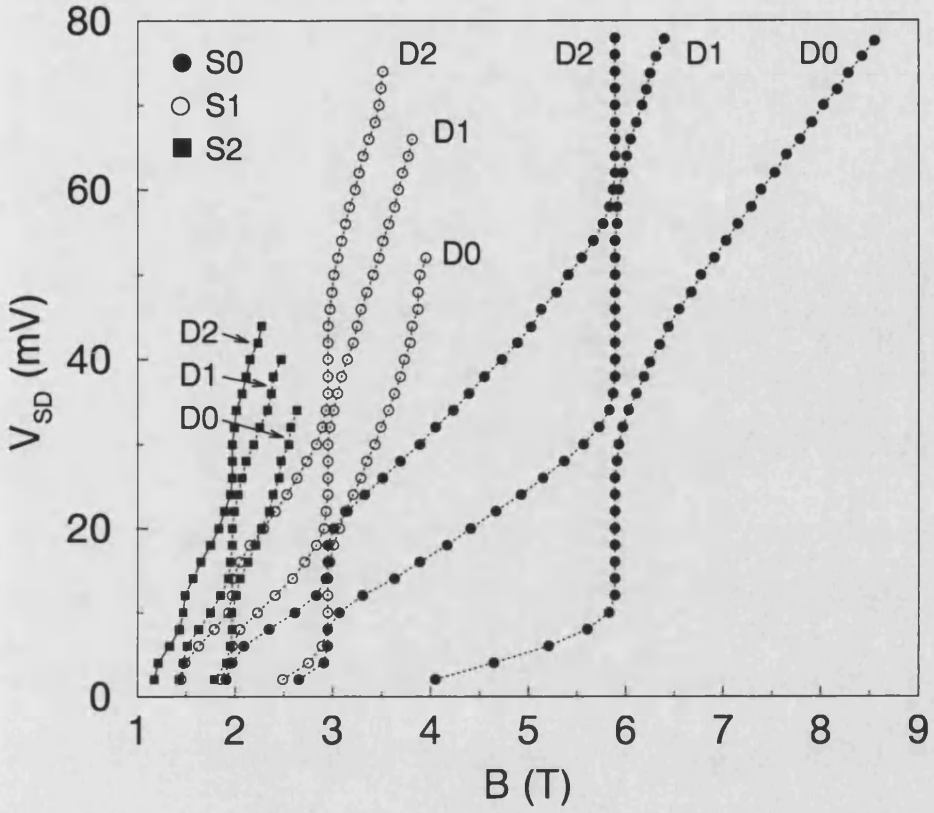

Figure 8.9: *Calculated fan diagram for tunnelling channels involving the $N = 0, 1, 2$ edge states from the source and drain. Each branch of the fan is calculated for the range where the corresponding edge state crossing energy lies below the maximum of the total effective potential barrier $E_0^{eff}(x)$*

of resonant values of V_{SD}, particularly for small values of B ($\nu' > 2$). The inclusion of edge states with indices $N > 2$ would clearly contribute further branches to the fan diagram, although for large values of B it is assumed that the energy of these edge state intersections would lie above $E_0^{eff}(x)$, and hence they would not represent *tunnelling* channels.

8.4.2 Transmission Coefficients

The model of tunnelling between edge states has until now been simplistic in that it ignores the individual transmission coefficient associated

with each particular tunnelling channel, which will strongly influence the respective resonance strength. Here again it is important to stress that the tunnelling channels relate parallel momentum and total energy of electrons on both sides of the barrier and do not represent electronic states *in* the barrier itself. The transmission coefficient for a particular

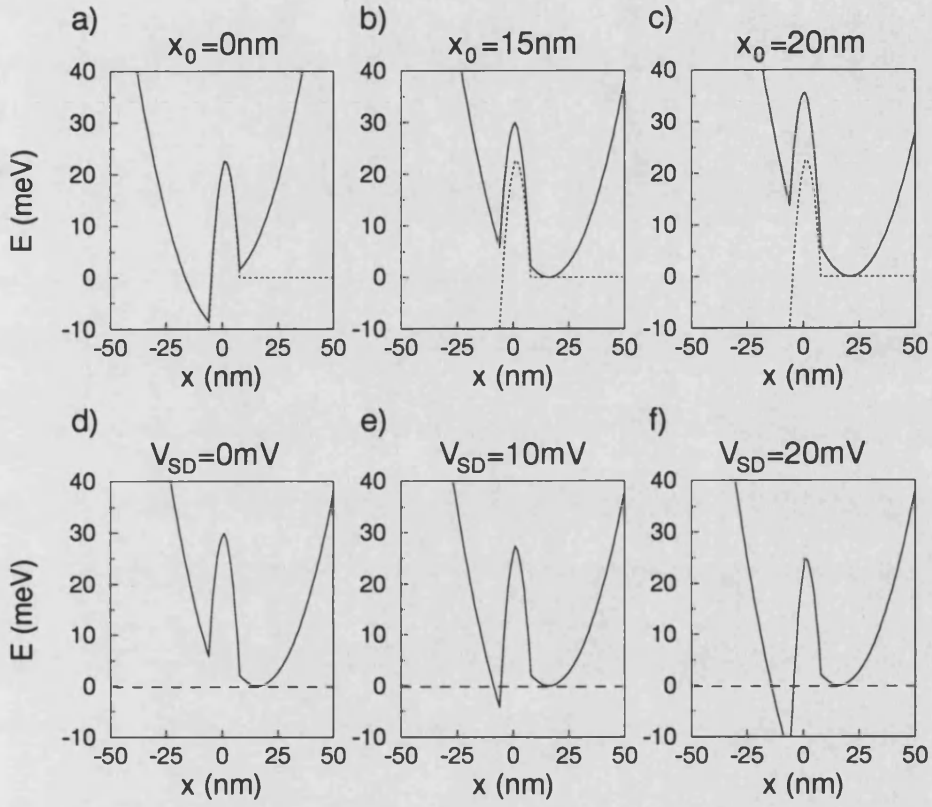

Figure 8.10: *a)-c). Total effective potential $E_0^{eff}(x)$ (solid lines) for a magnetic field B =5T for three tunnelling channels with different orbit centres x_0. The electrostatic potential $E_0^{el}(x)$ (dotted lines) is also indicated on each panel and the source-drain voltage V_{SD}=10mV. d)-f) Total effective potential for the same magnetic field for a single tunnelling channel (x_0=15nm) for three values of the source-drain voltage V_{SD}.*

tunnelling channel is therefore determined by the total effective potential barrier $E_0^{eff}(x)$ seen by electrons in the corresponding source edge

state. Panels a) to c) on Fig.8.10 show example calculations of the total effective potential $E_0^{eff}(x)$, derived from Eqn.8.11, for three notional tunnelling channels at a magnetic field $B = 5T$. The tunnelling channels have orbit centre coordinates x_0 positioned at 0, 15 and 20nm on the source side of the barrier (panels a) to c) respectively) and the applied source drain voltage V_{SD}=10mV. From the figure it can be seen clearly that the maximum of the effective potential barrier is minimised for tunnelling channels with orbit centres near the geometric centre of the electrostatic barrier. The orbit centre coordinate is however not the only important parameter with a bearing on the transmission coefficient. For a particular value of the magnetic field B, the size of the effective potential barrier is also reduced with increasing V_{SD}, owing to the reduction in the height of the electrostatic barrier. This can be seen in the lower panels of Fig.8.10, which show the calculated effective potential for a tunnelling channel with x_0 =15nm, for source drain voltages V_{SD}=0, 10 and 20mV (panels d) to f) respectively) at a magnetic field $B = 5$T. The transmission coefficients are therefore maximised for tunnelling channels involving drain edge states with high indices, since these tunnelling channels only fall below $E_F^S(B)$ for large values of V_{SD}.

Based on these assumptions, it is possible to state that as a general rule, the transmission coefficient for a particular tunnelling channel is determined by a trade-off between the indices of the component edge states, and the orbit centre coordinates at which they cross. To obtain the relative weighting of each partner in this trade-off would require a detailed calculation of the transmission coefficients for each tunnelling channel which lies beyond the scope of this work. In addition, given that for an experimental device, the transmission coefficients are determined by the quantitative details of the electrostatic barrier potential $E_0^{el}(x)$, such calculations for this simple parabolic model would provide only limited agreement with the experiment. However, these numerical studies show that for low, narrow barriers such as those studied here,

the orbit centre coordinate for each tunnelling channel is only weakly dependent on the indices of the edge states involved, and thus higher index crossings will dominate if available.

8.4.3 Experimental Results

In common with the zero field data, the measurements described in this section were taken at a temperature of 22mK without illumination of the sample. Initially, magnetotransport experiments were performed on an unstructured region of the Hall bar to determine the magnetic field positions of the integer filling factors ν, and hence to infer the electron density n_{2D} in the 2DES. Fig.8.11 shows a plot of the magnetoresistance ρ_{xx} as a function of the magnetic field B (the Shubnikov-de Haas oscillations), measured using a four-terminal, AC lock-in method. The

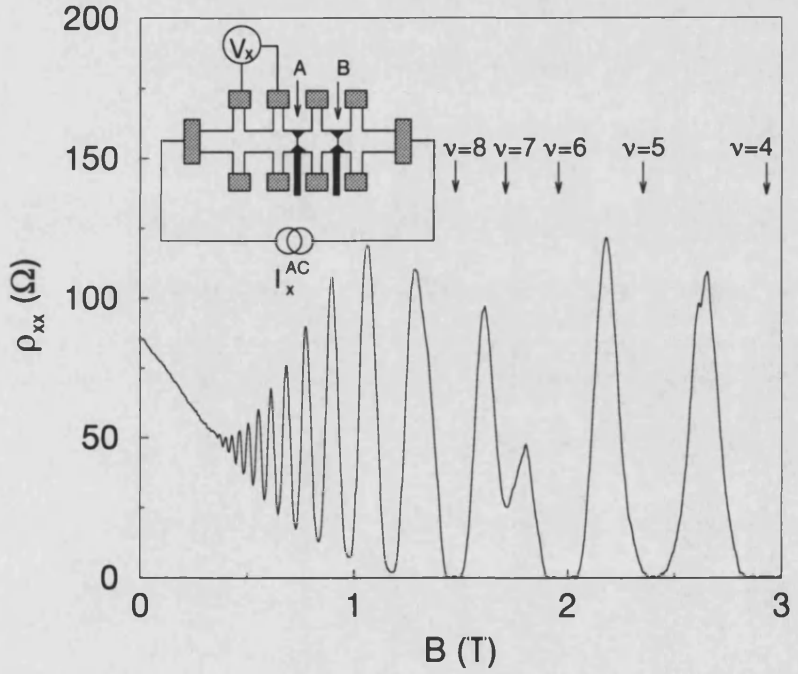

Figure 8.11: *Shubnikov-de Haas oscillations in the magnetoresistance ($\rho_{xx} = V_x/I_x$), obtained from an ungated region of the Hall bar at a temperature of 22mK. The curve was measured using an AC lock-in technique, with the measurement configuration shown in the inset. The magnetic field positions of some of the integer filling factors are indicated by the arrows.*

electron density can be calculated using Eqn.2.24, from the gradient of

a plot of the magnetic field positions of the minima in ρ_{xx} against the corresponding filling factor ν. This gives a value $n_{2D} = 2.85 \times 10^{11}\text{cm}^{-2}$, which is assumed to be constant over the whole Hall bar area.

8.4.3.1 Magnetic Field Data

Experimental data are presented for devices A and B at constant values of the magnetic field B between 0 and 12T. As indicated earlier, the magnetic field direction was always perpendicular to the plane of the 2DES. The devices were characterised in Mode 2, in which the differential conductivity dI_{SD}/dV_{SD} was measured as a function of the source-drain voltage V_{SD}, for a fixed value of the gate voltage V_{GD} (V_{GD} =-0.75V and -0.85V for A and B respectively). This mode of operation was chosen to enable a direct comparison with the calculated results described earlier in which V_{SD} is also the varied parameter.

Fig.8.12 shows a subset of the results for device A for values of the magnetic field B between 0 and 7T. In the zero field trace, a single weak shoulder in each source-drain bias direction can be resolved in dI_{SD}/dV_{SD}. These features were discussed in detail in Chapter 7 and are associated with transport through a 1D subband above a saddle point minimum in the barrier potential. Note that these data were taken on a different cooling cycle to that shown for device A in Chapter 7, where the shoulders in dI_{SD}/dV_{SD} were more pronounced. Based on the analysis of Section 7.3.2, the voltage position and magnitude of the shoulder imply a critical voltage $V_{SD}^{c} \approx 6\text{mV}$ and a value $m \approx 0.25$. This enables a rough estimate of the barrier height at the lowest part of the electrostatic potential from Eqn.7.10 as $(E_0^{el}(0) - E_F^S) \approx 1.5\text{meV}$ for $B = 0$. The same analysis, performed for device B indicates a minimum barrier height $(E_0^{el}(0) - E_F^S) \approx 1.3\text{meV}$. Note however, that the total effective potential barrier height $E_0^{eff}(x)$ *rises* rapidly with an applied magnetic field B, due to the addition of the magnetic potential $E_0^B(x, x_0)$.

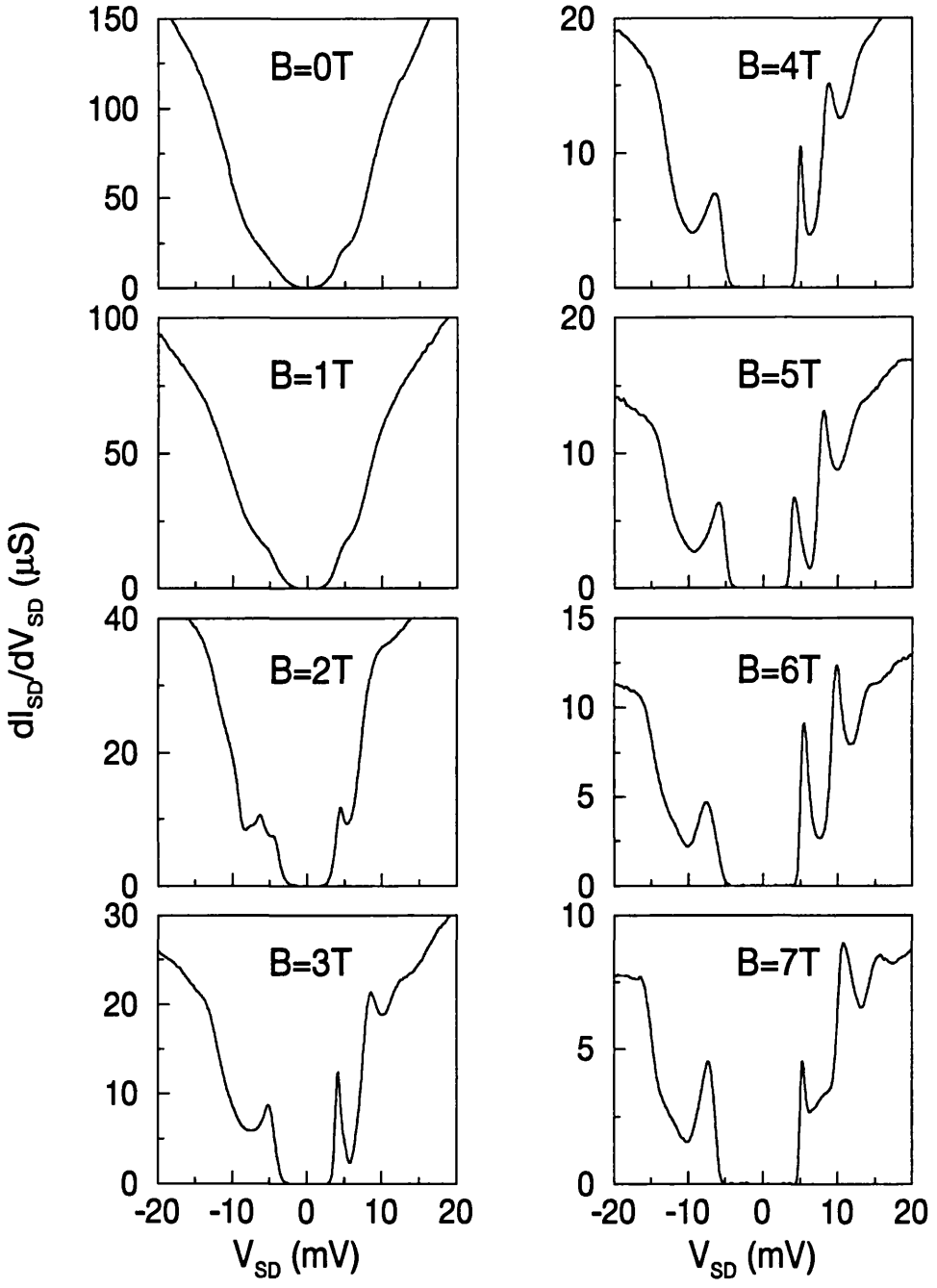

Figure 8.12: *Differential conductivity of device A for an applied gate voltage of -0.75V at fixed perpendicular magnetic fields between 0 and 7T. The data were taken at a temperature T=25mK.*

Returning to Fig.8.12, as the magnetic field is increased, the overall conductivity is strongly reduced, and a number of very sharp resonances develop in both directions of V_{SD}. Up to three peaks are resolvable for positive V_{SD} at high magnetic field, whereas only a single, broader peak can be seen for negative V_{SD}. For values of B above 7T (not shown), the curves remain qualitatively the same, although both the peak height and background conductivity decrease slowly. Increasing the value of $|V_{GD}|$ resulted in a shift in all the peak positions to higher values of V_{SD}

The results for device B, were similar, although only a *single* resonance in dI_{SD}/dV_{SD} was observed in both directions of V_{SD}. Warming the devices to room temperature and re-cooling produced quantitative changes in both the peak heights and voltage positions, but the basic features of the data remained the same.

Fig.8.13 shows a further subset of the device A results, for positive V_{SD}, at a dense range of magnetic field values between 6.2 and 7.5T. These data show clearly that with increasing magnetic field in this range, both peaks in dI_{SD}/dV_{SD} disappear, and are replaced by new resonances at lower values of V_{SD}. In other words, a clear transition occurs, which is observed for both directions of V_{SD}, and furthermore, in a number of other magnetic field regimes. These transitions can also be seen as discontinuities in the V_{SD} positions of the resonances, which are plotted for device A as a fan diagram in Fig.8.14a), for both directions of V_{SD}. Also indicated on the figure are the magnetic field values at which integer filling factors occur in the source electrode (inferred from the Shubnikov-de Haas oscillations shown in Fig.8.11). Note that for this two terminal measurement configuration, a proportion of the applied source-drain voltage will fall across any series resistances present in the contacts, or in the 2D leads of the Hall bar, resulting in a modification to the true voltage positions of each peak in dI_{SD}/dV_{SD}. Although for this Hall bar the contact resistances are small ($\sim 100\Omega$), for large magnetic fields the 2D lead resistance, which is dominated by the Hall resistance,

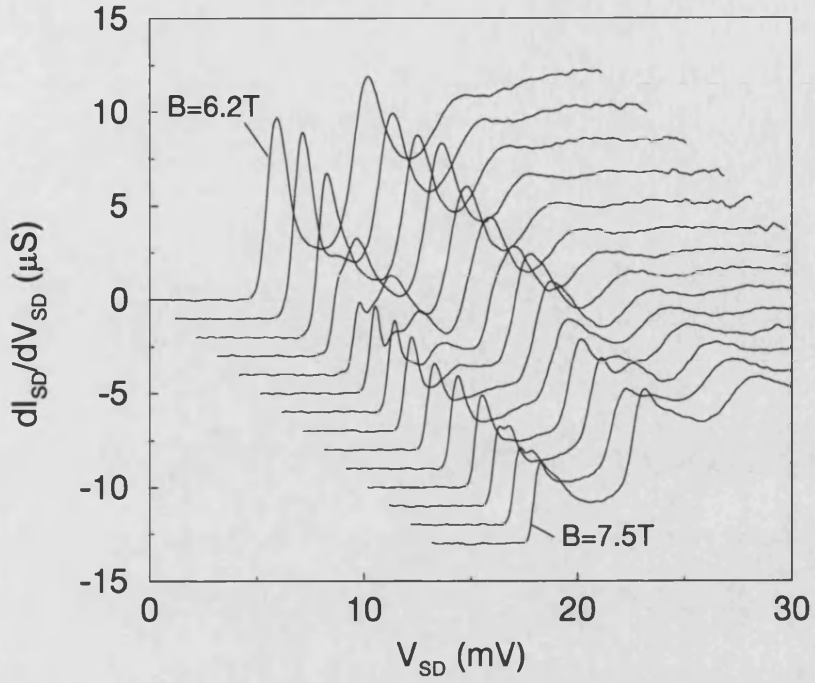

Figure 8.13: *Differential conductivity for device A as a function of the source-drain voltage V_{SD} at a range of magnetic field values between 6.2 and 7.5T. The magnetic field step is 0.1T, and the curves have been offset on the x- and y-axes for clarity.*

can become quite large. However, a simple analysis of the classical 2D Hall effect suggests a value for this series resistance of $R_S \sim B/n_{2D}e$, which is more than an order of magnitude less than the resistance of the barrier over the magnetic field range used in the experiment. Therefore, in the following analysis, the influence of the lead resistance is assumed to represent a negligible correction to the resonance positions, in view of the qualitative nature of the comparison between experiment and theory.

Returning to the fan diagram of Fig.8.14a), a number of important points emerge. Firstly, the shifts in the peak positions with increasing magnetic field for positive and negative source-drain voltage are qualitatively very similar, although for negative V_{SD}, a scattered range of ad-

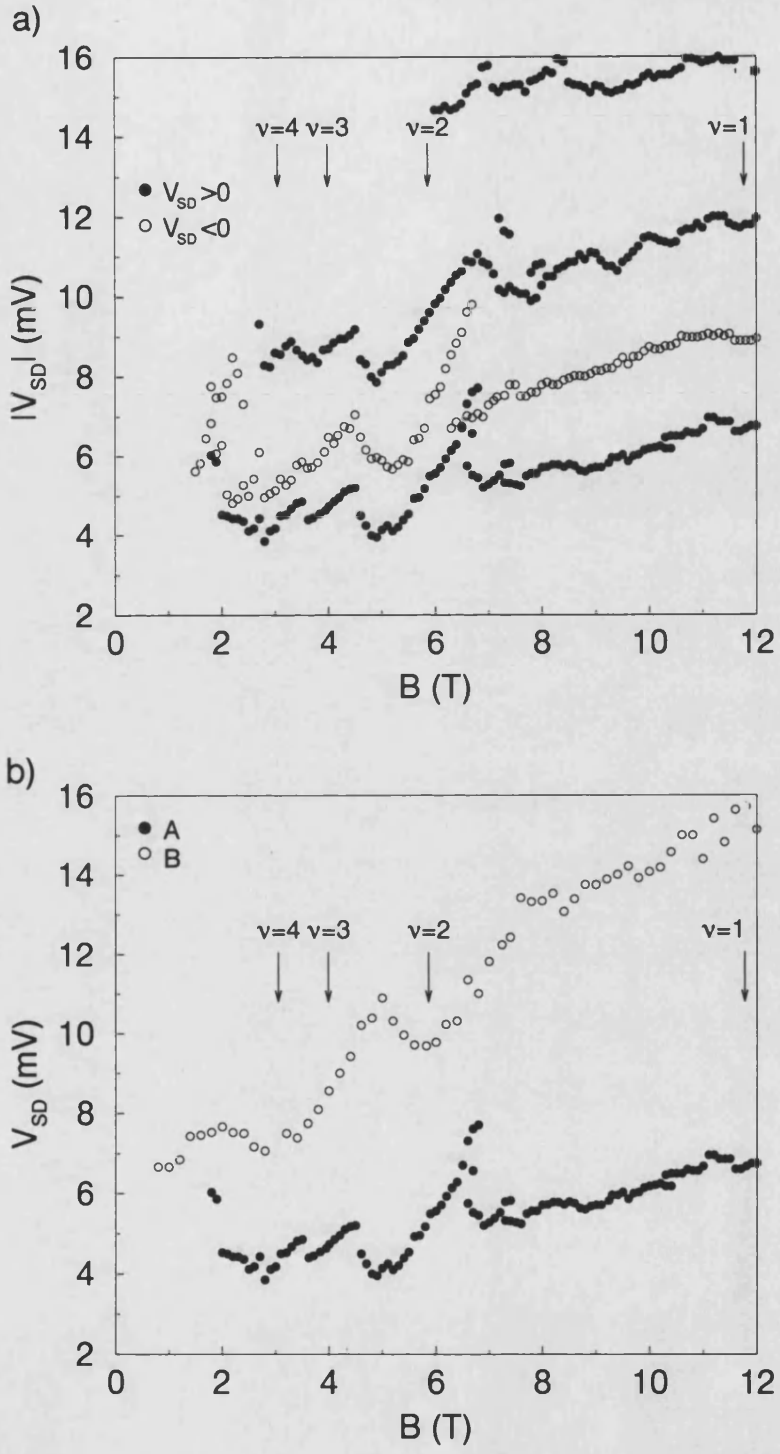

Figure 8.14: *a) Source-drain voltage positions of the conductivity resonances as a function of the magnetic field for device A. b) Comparison of a single branch of the fan diagram for devices A and B for positive V_{SD}.*

ditional resonances exist at magnetic fields around 2T. These additional resonances can also be seen in-part on the B =2T trace on Fig.8.12. Furthermore, the dispersions of the peaks for positive V_{SD} are roughly *parallel* with increasing magnetic field. The data also indicate that the discontinuities in the peak positions occur at magnetic field values just *after* the measured integer filling factors in the source electrode. It should be stressed that each discontinuity in the fan diagram represents the arrival of a new resonance, as opposed to an oscillation in the existing peak position.

Fig.8.14b) shows the fan diagram for the single peak for positive V_{SD} for device B which displays only a single strong transition in the peak position with increasing magnetic field. For comparison, a single branch of the fan digram for device A is also included on the figure. Note that in contrast to device A, the transition for device B occurs in a magnetic field range just *before* the integer filling factor $\nu = 2$ in the source electrode.

8.4.3.2 Discussion

As a starting point for this discussion of the experimental data, it is proposed that the measured spectra of conductivity resonances are a direct consequence of tunnelling between magnetic edge states on each side of the barrier, and can be explained within the framework of the theory presented earlier. To develop this interpretation of the results, attention is focussed initially on the lowest energy peak in the conductivity that was observed for both devices. For a particular value of the magnetic field, this resonance is attributed to the influence of a single tunnelling channel falling below $E_F^S(B)$. In light of the fact that the barriers are strongly inhomogeneous, this dominant tunnelling process is assumed to occur at the thinnest and lowest part of the barrier. Based on the

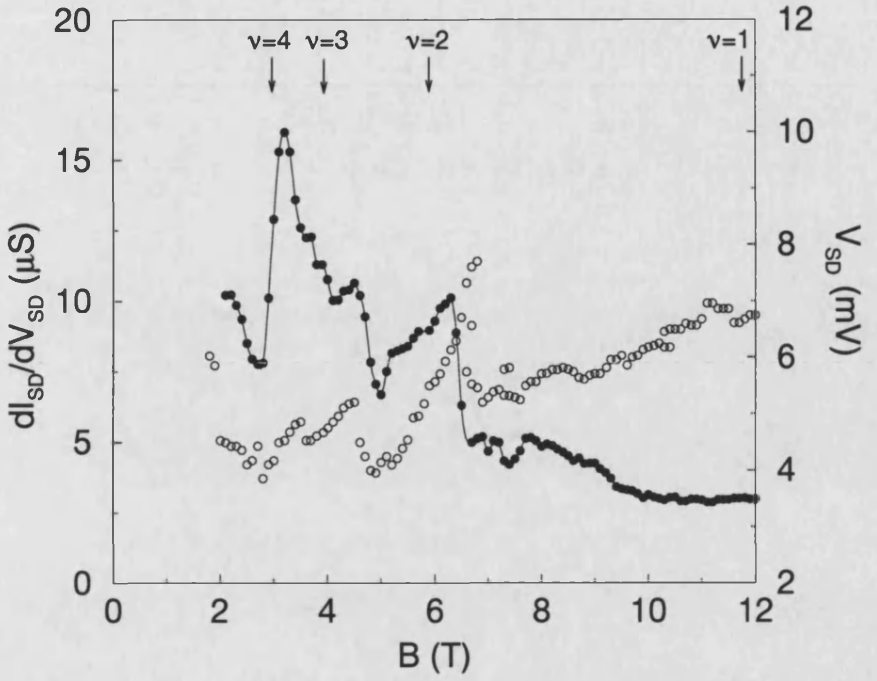

Figure 8.15: *Peak heights as a function of the magnetic field for the first positive V_{SD} resonance for device A (filled circles). Also plotted are the corresponding peak positions (empty circles), showing that maxima in the peak height occur at each discontinuity in the peak position. The arrows indicate the magnetic field values at which integer filling factors occur in the source.*

previous assumptions about transmission coefficients, the resonance is associated with a tunnelling channel made up from the occupied edge state in the source with the highest energy (which would see the smallest effective potential barrier), and a single edge state in the drain. As an example, for the B =3T trace of Fig.8.12, the low energy resonance could be assigned to a tunnelling channel involving the $N = 1$ edge state in the source. Exactly which edge state from the drain takes part is unclear, but it is assumed that for a large transmission coefficient, the x_0 coordinate at the intersection between the two edge state energy dispersions must occur near the geometric centre of the barrier. Note that this interpretation of the data implies that for the majority of the magnetic

field values studied, only a *single* tunnelling channel has a transmission coefficient, large enough for the corresponding resonance to lie within the sensitivity of the measurement apparatus.

The logical extension of this argument, is that the transitions observed in the conductivity resonances can be attributed to transitions between tunnelling channels involving different pairs of edge states from the source and drain. Fig.8.15 shows a plot of the measured *amplitudes* of the low energy resonance in the device A characteristics for positive V_{SD}. Also plotted on the figure are the corresponding peak positions, which indicate that a maximum in the peak amplitude and hence a maximum in the transmission coefficient for the tunnelling channel involved occurs just before each transition.

The transitions between different tunnelling channels can be partly understood in terms of the behaviour of edge states in the source of the device. With increasing magnetic field near an integer value of the filling factor ν, the uppermost edge state in the source will become depopulated, and in the absence of scattering, tunnelling via a channel involving this state will cease. At this point an edge state intersection involving the next lower source edge state will become the strongest tunnelling channel and its transmission coefficient will gradually increase with B as $E_F^S(B)$ slowly rises again. In this way, the succession of transitions which are observed in the experiment could be assigned to transitions between tunnelling channels involving successive source edge states.

This argument is consistent with the measured maxima in the peak amplitudes before each transition, since the occupied source edge state will have maximum energy near integer values of ν, and hence the corresponding tunnelling channel will see the smallest effective potential barrier. Clearly, transitions of this kind should occur for magnetic field values at, or near integer filling factors in the source electrode. However, although the majority of the transitions in the experimental data do oc-

cur near integer filling factors, there appears to be no clear systematic dependence on filling factor position, particularly when comparing the results for the two different devices. One possible explanation for this is that given the inhomogeneous nature of the potential in the region of the barrier, the local filling factor may be perturbed from the bulk average value of the Hall bar. In addition it is important to remember that the influence of additional factors, such as the x_0 coordinate of each tunnelling channel may maximise the respective transmission coefficient at a magnetic field value, independent of the filling factor in the source.

In spite of the fact that the calculated resonance spectrum of Fig.8.9 is intended to represent only a qualitative simulation of the experimental data, it still enables the identification of the component edge state indices associated with some of the measured resonances. Again, concentrating on the low energy peak for device A, a comparison with Fig.8.9 suggests that for $B > 6.3$T, the peak is due to the S0D0 tunnelling channel and that for $4.5 < B < 6.3$T, the S0D2 tunnelling channel is observed. For $B < 4.5$T, identification of the component edge states associated with each peak becomes more difficult, but for $3.5 < B < 4.5$T, the resonance could be assigned to the S1D0 channel. To identify the tunnelling channels in the low field regime would require a calculation based on an accurate model of the electrostatic potential barrier. Fig.8.16 shows a comparison between the calculated fan diagram and the experimental fan diagram for the lowest positive V_{SD} resonance for device A.

A puzzling feature of the data that remains is the presence of the two additional peaks in the conductivity for device A, at higher values of positive V_{SD}. It is considered unlikely that these resonances simply represent the contribution from tunnelling channels involving edge states with higher indices, since the dispersions of the two peak positions are roughly parallel to that of the low energy resonance over the whole range of the magnetic field. The calculated fan diagram of Fig.8.8 indicates that in contrast, the V_{SD} positions of resonances based on tunnelling

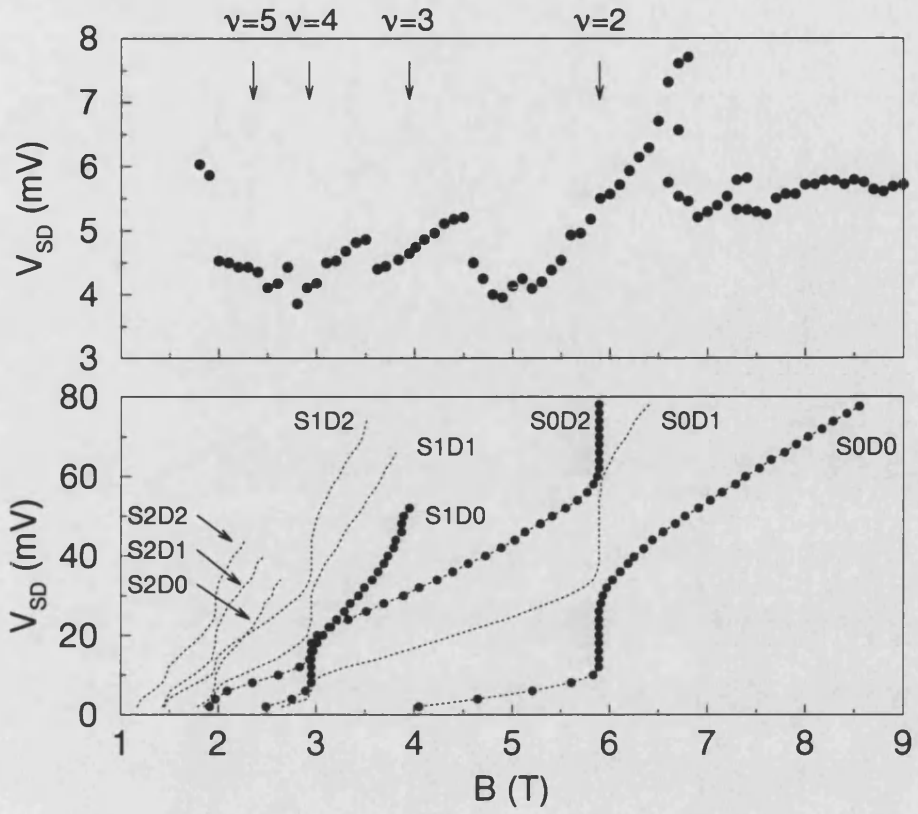

Figure 8.16: *Comparison of the experimental (upper panel) and calculated (lower panel) fan diagrams. The experimental data is for the low positive V_{SD} peak for device A. Branches of the calculated fan diagram which best reproduce the experimental data are indicated by the full circles.*

channels involving differing edge state pairs, tend to *diverge* with increasing magnetic field.

A more plausible explanation is that the additional resonances represent tunnelling processes involving tunnelling channels with the same edge state pairs but occurring at separate local saddle point minima in the inhomogeneous barrier potential. If the difference in the barrier size between each minimum in the potential is small, then as a first approximation one might expect that the difference in the source-drain voltages required to bring a particular tunnelling channel below $E_F^S(B)$ at each

individual minimum would remain largely independent of the magnetic field, as observed in the experiment. This would also explain the differing numbers of peaks observed for the two devices, since the number of dominant minima in the barrier potential depends on the microscopic details of the inhomogeneity in the 2DES.

Finally it is important to assess the possibility that the resonances observed in the conductivity have an origin other than tunnelling between edge states. An alternative explanation of the data that has been suggested is that the measured resonances arise from the transmission of edge states *over the top* of the barrier, at a saddle point minimum in the potential. At first glance this model seems plausible, given the fact that the resonances in dI_{SD}/dV_{SD} occur in a range of V_{SD} in which transport through 1D subbands above the barrier was observed for $B = 0$. This interpretation of the data is however considered unlikely for the following reason. Experiments by Nieder [39] and by Haug *et al.*[95] have indicated that edge states transmitted over the top of a potential barrier contribute only a monotonically increasing amount to the total conductivity, up to a maximum of a conductance quantum ($2e^2/h$). The situation is similar to that for transport through 1D subbands in zero magnetic field. Therefore in contrast to the sharp resonances observed in these experiments, a step-like increase in the conductivity would be expected as each state above the barrier became populated. Although transport via edge states above the barrier is discounted as an explanation for the resonances observed in the experiment, for large values of the source-drain voltage, where $E_0^{eff}(x_{max}) < E_F^S(B)$, edge state transport above the barrier will dominate the conductivity of the devices.

8.4.4 Conclusions

In summary, lateral tunnelling in single barrier gated diodes has been investigated in a perpendicular magnetic field. Theory, based on the

edge state model of a 2DES in a high magnetic field, predicts that tunnelling can occur between edge states on each side of the barrier that have the same values of total energy and parallel momentum. This condition is represented by the intersection in energy and momentum space of the edge state dispersions from the source and drain. A peak in the conductivity is expected when each edge state intersection or *tunnelling channel* falls below the Fermi energy in the source electrode of the device.

A numerical solution to the Schrödinger equation was used to calculate the tunnelling channel energies for a range of source and drain edge states for a simple parabolic potential barrier as a function of the source-drain voltage and the magnetic field. Including a model of the Fermi energy, which undergoes saw-tooth oscillations with increasing magnetic field, enabled the calculation of a fan diagram of predicted resonance positions. The results predict a monotonic increase in the resonance voltage for each tunnelling channel with increasing magnetic field. A sharp increase in the resonance voltage occurs for each tunnelling channel at integer values of the non-spin split filling factor ν', due to the corresponding rapid change in the Fermi energy.

Tunnelling channels with high energies and with centre of motion coordinates near the centre of the electrostatic potential see the smallest effective potential barrier and are assumed therefore to have the largest transmission coefficients for tunnelling. From the large number of possible resonances, only those with large transmission coefficients are expected to be observable in the experiment.

In the experiments, the two SLTD devices studied displayed a range of extremely sharp resonances in the differential conductivity as a function of the source-drain voltage at very low temperatures (22mK). Each resonance is attributed to a single, tunnelling channel coinciding with the Fermi energy in the source of the device. Given the known inhomogeneous nature of the devices, the dominant tunnelling process is

assumed to occur at the lowest part of the potential barrier. Additional resonances observed for one of the devices at higher source-drain voltages can be interpreted as the influence of the same tunnelling processes at secondary minima in the electrostatic potential barrier.

At a range of magnetic field values which show an approximate dependence on the spin-split filling factor ν, transitions are observed between tunnelling channels based on different edge state pairs. These transitions are probably due to the combination of the successive de-population of the highest occupied edge state in the source at integer values of the filling factor *and* the influence of the individual transmission coefficient of each tunnelling channel. A comparison of the experimental data with the calculated fan diagram enables the identification of the edge state indices involved in the tunnelling channels observed for large values of the magnetic field.

We believe that these measurements represent the first experimental evidence for lateral tunnelling between magnetic edge states, and furthermore give strong experimental support to the edge state picture of a 2DES in a strong perpendicular magnetic field.

8.5 Results for Quantum Trench Diodes

To complete this chapter, a similar analysis has been performed for tunnelling in quantum trench structures in a perpendicular magnetic field. Calculations based on the edge state model discussed earlier are compared to experimental data obtained for two quantum trench tunnelling diodes which were fabricated on a single Hall bar sample. The estimated depth of the etched trench for the sample was 55nm and the two diodes are referred to in the following as device X and device Y. Details of the

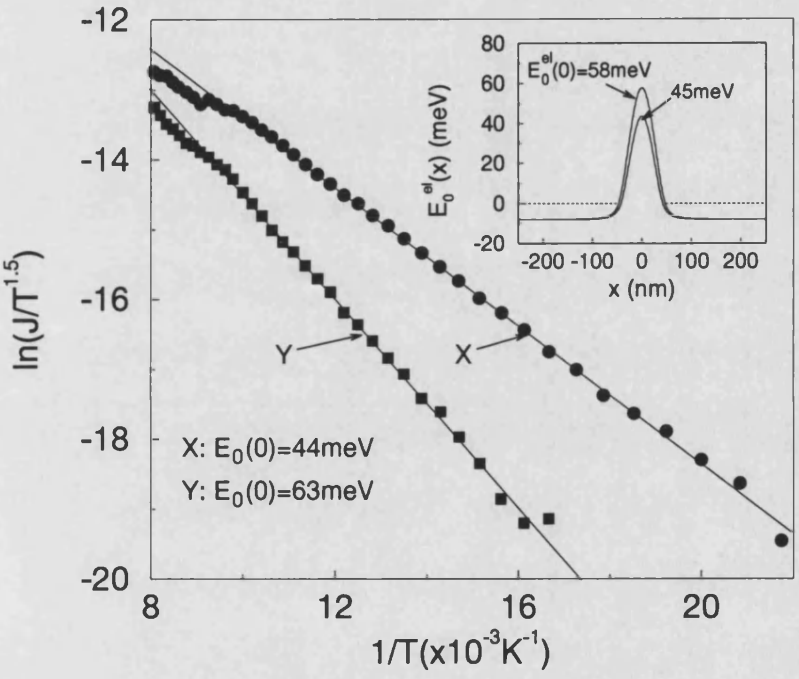

Figure 8.17: *Arrhenius plots of the thermally activated current as a function of temperature for devices X (circles) and Y (squares). The solid lines indicate the gradients used in the calculation of the barrier heights $E_0^{el}(0)$. The inset shows the numerically calculated electrostatic potential barrier profiles for two model devices with barrier heights comparable to X and Y.*

fabrication method were given in Chapter 4, and note that devices X and Y were part of a more recent batch than those described in Chapters

5 and 6.

As a starting point, the zero magnetic field barrier heights for the two devices were obtained from a measurement of the thermally activated current, using the method described in Chapter 5. Fig.8.17 shows the resulting Arrhenius plots for low source-drain voltage, indicating a good agreement with the Richardson law over a temperature range in excess of 50K. For X and Y, the inferred barrier heights are $(E_0^{el}(0) - E_F) = 44\text{meV}$ and $(E_0^{el}(0) - E_F) = 63\text{meV}$ respectively.

Calculations of the edge state dispersions for the edge state tunnelling model were based on electrostatic barrier potentials obtained using the numerical methods discussed in Chapter 6. To fit the model potentials to the experimental data, trench depths of 45nm and 46nm were chosen for devices X and Y to give calculated barrier heights of 45meV and 58meV respectively. The two model barrier profiles are plotted on the inset of Fig.8.17.

8.5.1 Experimental Magnetic Field Data

The differential conductivity dI_{SD}/dV_{SD} was measured as a function of the source-drain voltage V_{SD} for devices X and Y at a range of fixed magnetic fields between 0 and 12T. The magnetic field direction was perpendicular to the plane of the 2DES and the experiments were conducted without sample illumination at a temperature of 1.5K. Magnetoresistance measurements performed on an unstructured region of the Hall bar indicate an electron concentration in the 2D electrodes, $n_{2D} = 2.52 \times 10^{11}\text{cm}^{-2}$.

The differential conductivity dI_{SD}/dV_{SD} of device X is shown in Fig.8.18 as a function of the source-drain voltage V_{SD} for a range of magnetic field values B between 0 and 12T. The zero magnetic field trace indicates a measurable onset in dI_{SD}/dV_{SD} at $V_{SD} \approx 80\text{mV}$, with a subsequent, roughly exponential increase with increasing V_{SD}. The

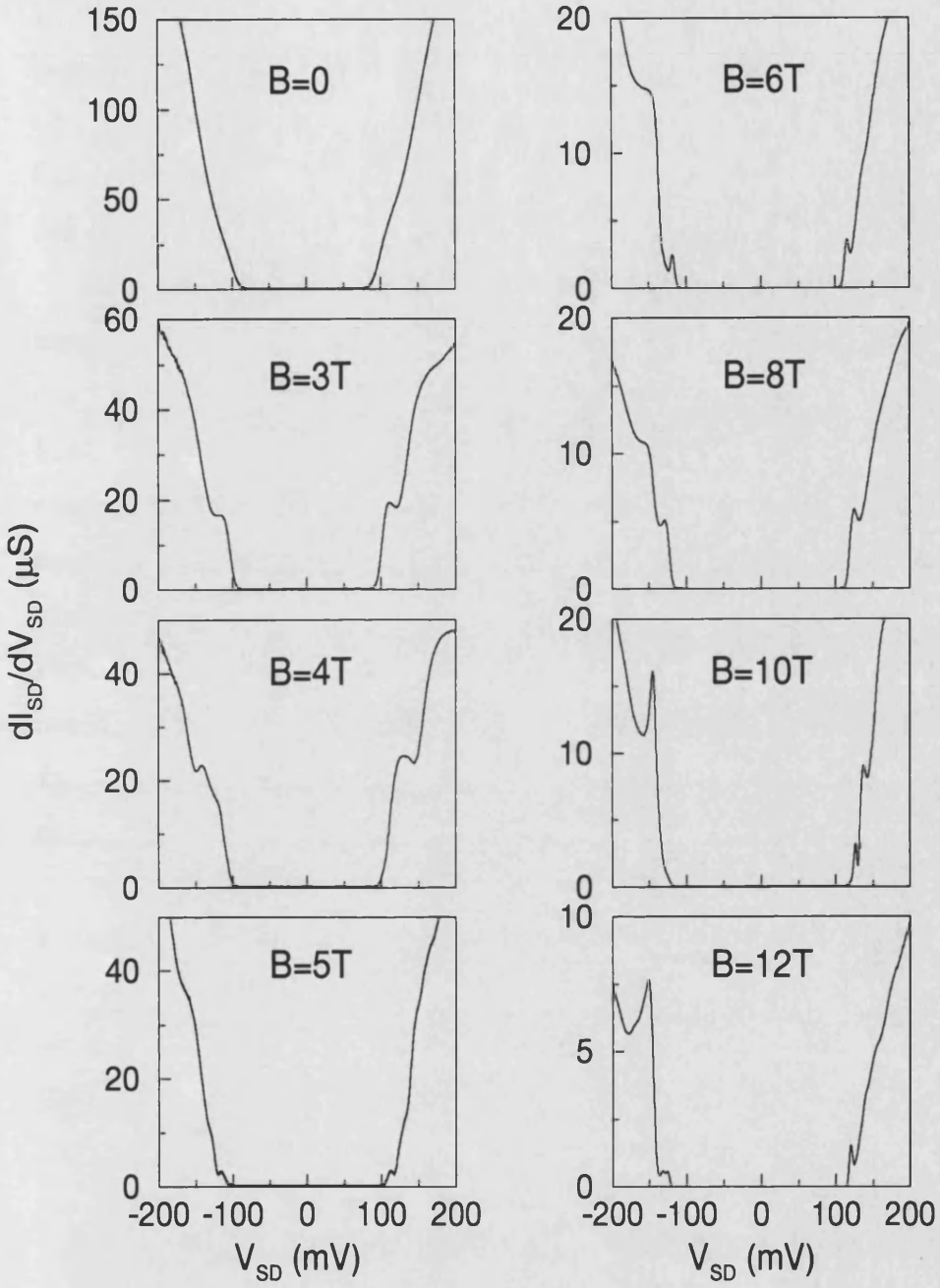

Figure 8.18: *Differential conductivity dI_{SD}/dV_{SD} as a function of the source-drain voltage V_{SD} for device X at fixed magnetic field values between 0 and 12T. The measurements were made at temperature of T=1.5K.*

data for device Y were similar, showing an onset in the conductivity for $V_{SD} \approx$100mV, which is consistent with the larger value for the measured barrier height. The characteristics for the devices were approximately symmetric in positive and negative V_{SD} both at zero and finite magnetic field, and were reproducible over different cooling cycles, and over typical measurement periods of a few days.

Returning to Fig.8.18, in common with the gated devices discussed earlier, increasing the magnetic field causes a strong reduction in the conductivity, and a shift in the measurable onset to higher values of V_{SD}. For B=2T (not shown), a number of shoulders can be resolved in the curve for both directions of V_{SD} which evolve to a single pronounced resonance for B=3T. The resonance positions shift to higher $|V_{SD}|$ with increasing B, and these resonances finally become smeared out for $B \approx$ 5T. For $B >$ 5T, *additional* resonances in dI_{SD}/dV_{SD} become resolved at lower $|V_{SD}|$ which again shift strongly to higher $|V_{SD}|$ with increasing B. Comparable results were also obtained for device Y, although the resonances were weaker over the whole range of the magnetic field.

A fan diagram of the resonance positions for device X is plotted in Fig.8.19 for both directions of V_{SD}. For the magnetic field range $B <$8T, two distinct branches can be resolved on the fan diagram for both V_{SD} directions, which show a strong qualitative similarity to data shown earlier for the SLTD devices. At high magnetic fields ($B >$ 8T) the diagrams are no longer symmetric in $\pm V_{SD}$. For $V_{SD} > 0$, additional branches evolve near the filling factor $\nu = 1$, whereas for $V_{SD} < 0$ a strong resonance is observed at high $|V_{SD}|$ which does not shift monotonically to larger values of $|V_{SD}|$ with increasing B.

8.5.2 Comparison With the Edge State Tunnelling Model

The experimental results and analysis of the earlier part of this chapter demonstrated the success of using the edge state tunnelling model to in-

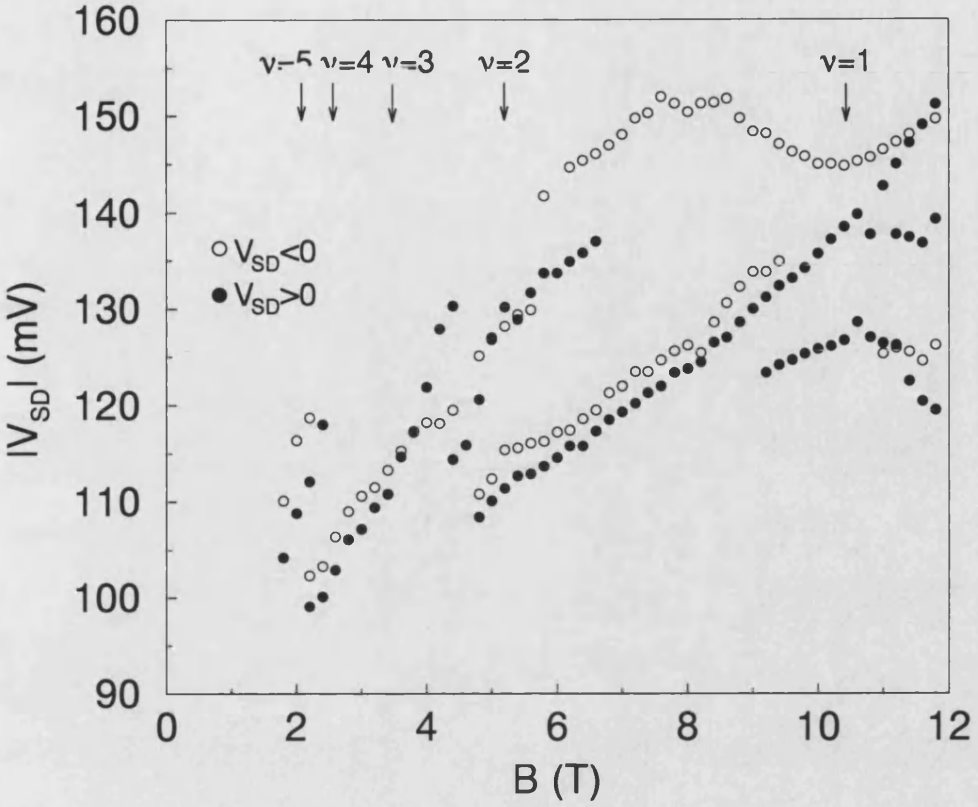

Figure 8.19: *Source-drain voltage V_{SD} positions of the conductivity resonances for positive and negative V_{SD} for device X (empty and filled circles respectively).*

terpret the characteristics of lateral tunnelling diodes in a perpendicular magnetic field. Therefore the same analysis is used in the interpretation of these data and the resonances observed in the conductivity are attributed to tunnelling channels involving source and drain edge states, falling below $E_F^S(B)$. The separate branches on the fan diagram shown in Fig.8.19 are again associated with tunnelling channels involving different edge state pairs. Also common with the results for the SLTD's is the strong transition observed near B=5T ($\nu \approx 2$), which can be explained as a transition between tunnelling channels involving the highest and next highest source edge states, due to the de-population of the high-

est state near the integer filling factor in the source. Moreover there is strong evidence in the fan diagram for the presence of a third tunnelling channel near B=5T for positive V_{SD}.

To gain further insight into the results, it is instructive to compare and contrast the properties of the electrostatic potential barriers of the quantum trench devices and the gated SLTD's. Firstly there exists a difference of more than an order of magnitude in the height of the electrostatic barrier between the two sets of devices ($\sim$ 50meV for the quantum trench diodes compared with $<$ 5meV for the SLTD's) and a corresponding difference in the barrier width. In view of this, and the smaller transmission coefficients expected for tunnelling through large barriers, it is not surprising that the resonant effects for these quantum trench devices are weaker than those observed for the SLTD's. Calculations shown earlier indicate that the transmission coefficients are maximised for tunnelling channels with orbit centre coordinates near the geometric centre of the barrier; for these large barriers such a criterion will be even more important if resonant effects are to exist within the sensitivity of the measurement apparatus.

Secondly, based on the results for the gated diodes, it must be assumed that the electrostatic barriers for the quantum trench devices are strongly inhomogeneous. Given the highly disordering nature of the reactive ion etching process, it is likely that an even denser range of fluctuations exist in the barrier potential for these devices. Clearly the dominant tunnelling process will occur at the lowest and thinnest part of the barrier.

To identify some of the tunnelling channels responsible for the resonances observed in the characteristics of devices X and Y, the model electrostatic potentials shown in the inset of Fig.8.17 were used as a basis for a calculation of the fan diagram. The calculations were restricted to the low magnetic field regime (B < 5T), where a single strong resonance was observed in the experiment for both devices and in both directions of

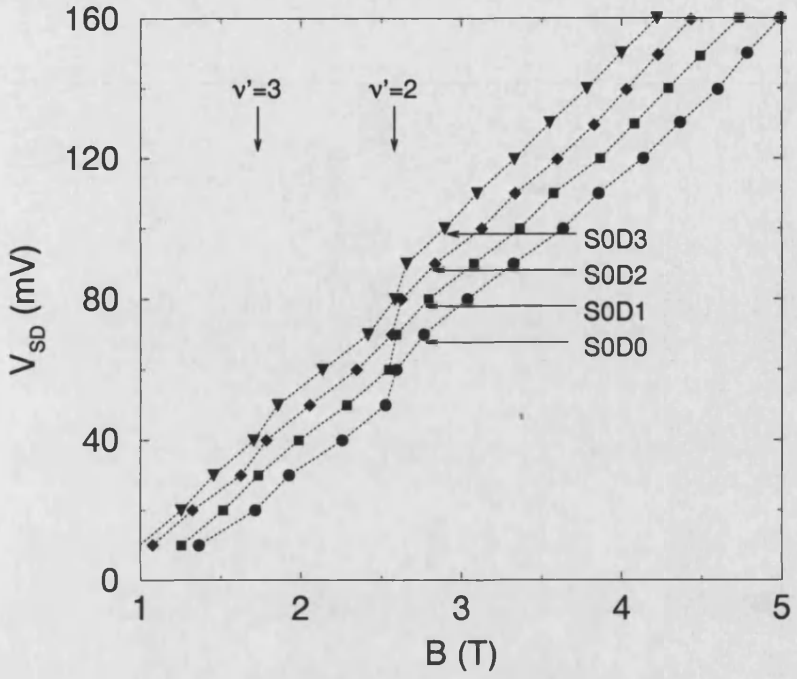

Figure 8.20: *Calculated fan diagram for device X, based on the numerical electrostatic potential shown in Fig.8.17. The four tunnelling channels used in the calculation are indicated.*

V_{SD} and involved tunnelling channels consisting of the $N = 0$ edge state in the source and the $N = 0..3$ edge states in the drain. The resulting fan diagram is plotted in Fig.8.20 for device X for the four tunnelling channels. Note that for these large electrostatic potential barriers that the dispersions for the tunnelling channels are approximately parallel with increasing magnetic field.

Since the model electrostatic potentials are believed to represent a fair approximation to the potential barriers of the experimental devices, it is possible to make a direct comparison between the calculated and experimental fan diagrams. The calculated results indicate that orbit centres for the S0D3 tunnelling channel lie consistently closest to the geometric centre of the barriers for these voltage and magnetic field ranges, and therefore the S0D3 branches of the calculated fan diagrams

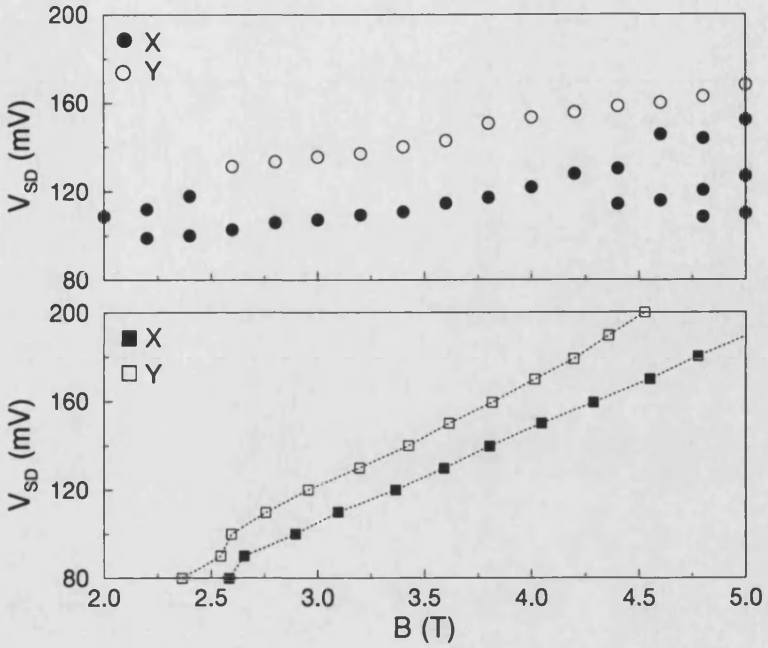

Figure 8.21: *Comparison of the experimental (upper panel) and calculated (lower panel) fan diagrams for device X (filled symbols) and device Y (empty symbols) for the low magnetic field regime. The calculated data is for the S0D3 tunnelling channel*

are compared with the single branch observed for each device in the experimental data in this magnetic field regime.

Fig.8.21 shows a plot of the S0D3 branches for both model devices, together with the experimental peak positions for devices X and Y in the $B < 5$T magnetic field regime. The theory correctly predicts the monotonic increase in the resonant source-drain voltage with increasing magnetic field in this range, and also the shift in the resonance position to higher V_{SD} for the larger tunnelling barrier of device Y. However, the agreement between the slopes of the experimental and calculated data is clearly poor. A possible source for this discrepancy lies in the choice of barrier height for the numerical electrostatic potentials. It is probable that experimental values for the barrier height obtained from thermal

activation measurements are far less sensitive to fluctuations in the potential than a measurement of tunnelling current. One reason for this is that the thermal activation result is itself modified by tunnelling through the upper parts of the barrier. Furthermore, from a simple consideration of the transmission coefficients $T(\Phi_0)$, the sensitivity of a thermal activation measurement to the barrier height Φ_0 is given approximately by,

$$\frac{\partial T(\Phi_0)}{\partial \Phi_0} \sim T(\Phi_0)\left(\frac{-e}{kT}\right) \tag{8.17}$$

where T is the temperature. For tunnelling,

$$\frac{\partial T(\Phi_0)}{\partial \Phi_0} \sim \frac{T(\Phi_0)d}{\sqrt{\left(\frac{2m^*}{\hbar^2}\right)(\Phi_0 - E_x)}} \tag{8.18}$$

for a barrier width d and an electron energy E_x. Clearly when the factor $(\Phi_0 - E_x)$ in the tunnelling transmission coefficient becomes small, as is the case for a finite source-drain voltage, then $T(\Phi_0)$ becomes extremely sensitive to Φ_0 and hence the overall transmission coefficient will be dominated by fluctuations in the potential barrier. For thermal activation however, the sensitivity remains roughly constant and depends only on the temperature.

To achieve more quantitative agreement between the experimental and calculated data, future work will involve using the electrostatic barrier height in the edge state calculations as a simple fitting parameter.

8.5.3 Conclusions

Lateral tunnelling in quantum trench diodes has been studied in a perpendicular magnetic field. Pronounced resonances were observed in the differential conductivity of the devices as a function of the source-drain voltage, at low temperature (1.5K). The results showed strong qualitative similarities with those for the gated tunnelling diodes, and are interpreted in terms of the model of tunnelling between magnetic edge

states on each side of the barrier. The resonances for quantum trench diodes are weaker than those for the gated devices, which is attributed to the larger barriers and correspondingly smaller transmission coefficients. A model of the experimental data based on a numerical calculation of the electrostatic potential shows some qualitative agreement with the data, but the quantitative agreement is poor. This is attributed to the influence of fluctuations in the potential which dominate the tunnel current, but are not included in the model for the electrostatic potential barrier.

References

[1] L. L. Chang, L. Esaki and R. Tsu, Appl. Phys. Lett. **25**, 593 (1974).

[2] K. Ploog, in *Physics and the Applications of Quantum Wells and Superlattices*, edited by E. E. Mendez and K. von Klitzing, (Plenum Press, New York, 1987), p. 43-70.

[3] M. Razeghi, M. A. Poisson, J. P. Larivain, B. de Cremoux, J. P. Duchemin and M. Voos, Electron. Lett. **18**, 340 (1982).

[4] M. Jaros, *"Physics and Applications of Semiconductor Microstructures"*, Oxford University Press (1989)

[5] K. von Klitzing, in *Physics and Applications of Quantum Wells and Superlattices*, edited by E. E. Mendez and K. von Klitzing, (Plenum Press, New York, 1987), p. 229-248.

[6] H. van Houten, C. W. J Beenakker and B. J. van Wees, in *Semiconductors and Semimetals, vol.35, Nanostructured Systems*, edited by M. Reed, (Academic Press, San Diego, 1990), p. 9.

[7] L. P. Kouwenhoven, A. T. Johnson, N. C. van der Vaart, C. J. P. M. Harmans, and C. T. Foxon, Phys. Rev. Lett. **67**, 1626 (1991).

[8] J. Smoliner, E. Gornik and G. Weimann, Phys. Rev. B **39**, 12937 (1989).

[9] J. Smoliner, W. Demmerle, G. Berthold, E. Gornik, G. Weimann, Phys. Rev. Lett. **63**, 2116 (1989).

[10] J. Cooper, Private Communication , (1993).

[11] J. E. Lillenfield, Z. Physik **23**, 506 (1922).

[12] R. H. Fowler and L. Nordheim, Proc. Roy. Soc (London) **A119**, 173 (1928).

[13] J. R. Oppenheimer, Phys. Rev. **31**, 66 (1928).

[14] G. Gamow, Z. Physik **51**, 204 (1928).

[15] C. Zener, Proc. Roy. Soc. (London) **145**, 523 (1934).

[16] E. W. Muller, Z. Physik **106**, 541 (1937).

[17] L. Esaki, Phys. Rev. **109**, 603 (1958).

[18] I. Giaever, in *Tunnelling Phenomena in Solids*, edited by E. Burnstein and S. Lundquist, (Plenum Press, New York, 1969), p. 19-30.

[19] J. G. Simmons, J. Appl. Phys.. **34**, 793 (1963).

[20] L. Esaki and L. L. Chang, Phys. Rev. Lett. **33**, 495 (1974).

[21] M. Heiblum, M. I. Nathan, C. C. Thomas and C. M. Knoedler, Phys. Rev. Lett. **55**, 2200 (1985).

[22] C. B. Duke, *"Tunnelling in Solids"*, Academic Press (1969)

[23] E. Burnstein and S. Lundqvist, *"Tunneling Phenomena in Solids"*, Plenum Press (1969)

[24] D. K. Roy, *"Quantum Mechanical tunnelling and its Applications"*, World Scientific (1986)

[25] N. W. Ashcroft and N. D. Mermin, *"Solid State Physics"*, Holt Saunders (1976)

[26] E. E. Mendez, in *Physics and Applications of Quantum Wells and Superlattices*, edited by E. E. Mendez and K. von Klitzing, (Plenum Press, New York, 1987), p. 159-188.

[27] D. Bohm, *"Quantum Theory"*, Prentice Hall (1951)

[28] S. Luryi, Appl. Phys. Lett. **47**, 490 (1985).

[29] C. Weisbuch and B. Vinter, *"Quantum Semiconductor Structures"*, Academic Press (1991)

[30] E. R. Brown, T. C. G. L. Sollner, C. D. Parker, W. D. Goodhue and C. L. Chen, Appl. Phys. Lett. **55**, 1977 (1989).

[31] K. von Klitzing, G. Dorda and M. Pepper, Phys. Rev. Lett. **45**, 494 (1980).

[32] G. Abstreiter, K. Eberl, E. Friess, U. Menczigar, W. Wegscheider and R. Zachai, J. Cryst. Grow. **95**, 431 (1989).

[33] H. L. Störmer, R. Dingle, A. C. Gossard and W. Wiegmann, Appl. Phys. Lett. **33**, 665 (1978).

[34] L. N. Pfeiffer, K. W. West, H. L. Störmer and K. Baldwin, Appl. Phys. Lett. **55**, 1888 (1989).

[35] T. Ando, A. B. Fowler and F. Stern, Rev. Mod. Phys. **54**, 437 (1982).

[36] F. Stern and S. Das Sarma, Phys. Rev. B **30**, 840 (1984).

[37] J. J. Harris, J. A. Pals and R. Woltjer, Rep. Prog. Phys. **52**, 1217 (1989).

[38] E. H. Hall, Am. J. Math. **2**, 287 (1879).

[39] J. Nieder. *Magnetotransportuntersuchungen an eindimensionalen Transistoren.* PhD Thesis, Universität Stuttgart, (1992).

[40] H. Aoki, J. Phys. C **10**, 2583 (1977).

[41] T. Ando amd Y. Uemura, J. Phys. Soc. Jpn **36**, 959 (1974).

[42] E. Stahl, D. Weiss, G. Weinmann, K. von Klitzing and K. Ploog, J. Phys. C **18**, L783 (1985).

[43] J. P. Eisenstein, H. L. Störmer, V. Narayanamurti, A. Y. Cho, A. C. Gossard and C. W. Tu, Phys. Rev. Lett. **55**, 875 (1985).

[44] R. R. Gerhardts and V. Gudmundsson, Phys. Rev. B **34**, 2999 (1986).

[45] R. J. Nicholas, in *Physics and Applications of Quantum Wells and Superlattices*, edited by E. E. Mendez and K. von Klitzing, (Plenum Press, New York, 1987), p. 217-228.

[46] M. Büttiker, Phys. Rev. B **38**, 9375 (1986).

[47] R. J. Haug, Semicond. Sci. Technol. **8**, 131 (1993).

[48] M. Büttiker, in *Festkörperprobleme, Vol.30*, edited by U. Rössler, (Vieweg, Braunschweig, 1990), p. 41.

[49] C. W. J. Beenakker and H. van Houten, Phys. Rev. B **43**, 12066 (1991).

[50] M. Missous, in *Properties of Gallium Arsenide* (INSPEC, London and New York, 1990), p. 453.

[51] H. Sakaki, in *Physics of Nanostructures*, edited by J. H. Davies and A. R. Long, (IOP Publishing, Bristol, 1991), p. 1.

[52] D. K. Ferry and R. O. Grondin, *"Physics of Submicron Devices"*, Plenum Press (1991)

[53] H. Craighead, in *Physics of Nanostructures*, edited by J. H. Davies and A. R. Long, (IOP Publishing, Bristol, 1992), p. 21.

[54] P. Grambow. *Technologie und Untersuchung nanostrukturierter Halbleitersysteme.* PhD Thesis, Technischen Hochschule Darmstadt, (1993).

[55] E. H. Rhoderick and R. H. Williams, *"Metal Semiconductor Contacts"*, Wiley New York (1981)

[56] T. Demel, D. Heitman, P. Grambow, and K. Ploog, Appl. Phys. Lett. **53**, 2176 (1989).

[57] S. J. Manion, L. D. Bell, W. J. Kaiser, P. D. Maker, and R. E. Muller, Appl. Phys. Lett. **59**, 213 (1991).

[58] K. Ismail, D. A. Antoniadis, and H. I. Smith, Appl. Phys. Lett. **55**, 589 (1989).

[59] S. Y. Chou, D. R. Allee, R. F. W. Pease, and J. S. Harris, Jr, Appl. Phys. Lett. **55**, 176 (1989).

[60] A. Palevski, M. Heiblum, C. P. Umbach, C. M. Knoedler, A. N. Broers, and R. H. Koch, Phys. Rev. Lett. **62**, 215 (1989).

[61] X. Liu and Q. Niu, Phys. Rev. B **46**, 10215 (1992).

[62] E. F. Schubert, J. Knecht, and K. Ploog, J. Phys. C **18**, L215 (1985).

[63] P. M. Mooney, in *Festkörperprobleme, Vol.29*, edited by U. Rössler, (Vieweg, Braunschweig, 1989), p. 215.

[64] R. J. Nelson, Appl. Phys. Lett. **31**, 351 (1977).

[65] N. Chand, T. Henderson, J. Clem, W. T. Masselink, R. Fisher, Y. C. Chang, and H. Morkoc, Phys. Rev. B **30**, 4481 (1984).

[66] M. J. Turner and E. H. Rhoderick, Solid. Stat. Electron. **11**, 291 (1968).

[67] B. L. Smith, Electron. Lett. **4**, 332 (1968).

[68] M. Rossmanith, K. Syasson, E. Bökenhof, K. von Klitzing, and K. Ploog, Phys. Rev. B **44**, 3168 (1991).

[69] D. D. Smith, T. Fink, W. D. Braddock, M. Saunders, J. Electron. Mat. **19**, 757 (1990).

[70] S. E. Laux, D. J. Frank, and F. Stern, Surf. Sci. **196**, 101 (1988).

[71] S. Thoms, I. McIntyre, S. P. Beaumont, M. Al-Mudares, R. Cheung, and C. D. W. Wilkinson, J. Vac. Sci. Technol **B6**, 127 (1988).

[72] A. Kumar, Surf. Sci. **263**, 335 (1992).

[73] K. Lier and R. R. Gerhardts, sub. Phys. Rev. B , (1993).

[74] J. Davies, Semicond. Sci. Technol **3**, 995 (1988).

[75] F. C. Zhang and S. Das Sarma, Phys. Rev. B **33**, 2903 (1986).

[76] P. M. Mooney, J. Appl. Phys. **67**, R1 (1990).

[77] *IMSL Math/Library*1.1 edition1989

[78] P. L. McEuen, B. W. Alphenaar, R. G. Wheeler and R. N. Sacks, Surf. Sci. **229**, 312 (1990).

[79] J. Weis, R. J. Haug, K. v. Klitzing and K. Ploog, Phys. Rev. B **46**, 12837 (1992).

[80] S. Washburn, A. B. Fowler, H. Schmid and D. Kern, Phys. Rev. B **38**, 1544 (1988).

[81] John H. Davies and John A. Nixon, Phys. Rev. B **39**, 3423 (1989).

[82] B. J. van Wees, H. van Houten, C. W. J. Beenakker, J. G. Williamson, L. P. Kouwenhoven, D. van der Marcel, and C. T. Foxon, Phys. Rev. Lett. **60**, 848 (1988).

[83] D. A. Wharam, T. J. Thornton, R. Newbury, M. Pepper, H. Ahmed, J. E. F. Frost, D. G. Hasko, D. C. Peacock, D. A. Ritchie and G. A. C. Jones, J. Phys. C **21**, L209 (1988).

[84] L. P. Kouwenhoven, B. J. van Wees, C. J. P. M. Harmans, J. G. Williamson, H. van Houten, C. W. J. Beenakker, C. T. Foxon and J. J. Harris, Phys. Rev. B **39**, 8040 (1989).

[85] S. Mori and T. Ando, Phys. Rev. B **19**, 6433 (1979).

[86] H. L. Störmer, A. C. Gossard and W. Wiegmann, Solid Stat. Comm. **10**, 707 (1982).

[87] Th. Englert, J. C. Mann, D. C. Tsui and A. C. Gossard, Solid Stat. Comm. **11**, 989 (1983).

[88] F. Stern and S. Das Sarma, Phys. Rev. B **30**, 840 (1984).

[89] J. Cooper, Private Communication , (1994).

[90] S. Y. Chou, J. S. Harris, Jr and R. F. W. Pease, Appl. Phys. Lett. **52**, 1982 (1988).

[91] K. Ismail, W. Chu, A. Yen, D. A. Antoniadis, and H. I. Smith, Appl. Phys. Lett. **55**, 460 (1989).

[92] K. Ismail, W. Chu, D. A. Antoniadis, and Henry I. Smith, Appl. Phys. Lett. **52**, 1071 (1988).

[93] J. Weis. *Einzelelektron-Tunneltransistor: Transportspektroskopie von electronischen Grund- und Anregungszuständen in einem $GaAs/Al_xGa_{1-x}As$-Quantentopf bis zu hohen Magnetfeldern.* PhD Thesis, Universität Stuttgart, (1994).

[94] S. J. Bending, C. Zhang, K. von Klitzing and K. Ploog, Phys. Rev. B **39**, 1097 (1989).

[95] R. J. Haug, A. H. MacDonald, P. Streda and K. von Klitzing, Phys. Rev. Lett. **61**, 2797 (1988).

[96] R. J. Haug, J. Kucera, P Streda and K. von Klitzing, Phys. Rev. B **39**, 10892 (1988).

[97] C. Tejedor, and J. J. Palacios, Physica Scripta **T35**, 121 (1991).

[98] E. Böckenhoff and K. von Klitzing, Surf. Sci. **229**, 182 (1990).

[99] K. D. Weiss. *Untersuchungen zur Zustandsdichte eines zweidimensionalen Elektronengases in starken Magnetfeldern.* PhD Thesis, Universität München, (1987).

[100] A. Berg, M. Dobers, R. R. Gerhardts and K. von Klitzing, Phys. Rev. Lett. **64**, 2563 (1990).

[101] A. Berg. *Der Spin in zweidimensionalen Elektronensystemen.* PhD Thesis, Universität Stuttgart, (1992).